Mathematical Problems in Engineering

Mathematical Modeling and Optimization of Functionally Graded Structures

Guest Editors: Abdelouahed Tounsi, El Abbes Adda Bedia, S. R. Mahmoud, and Sofiane Amziane

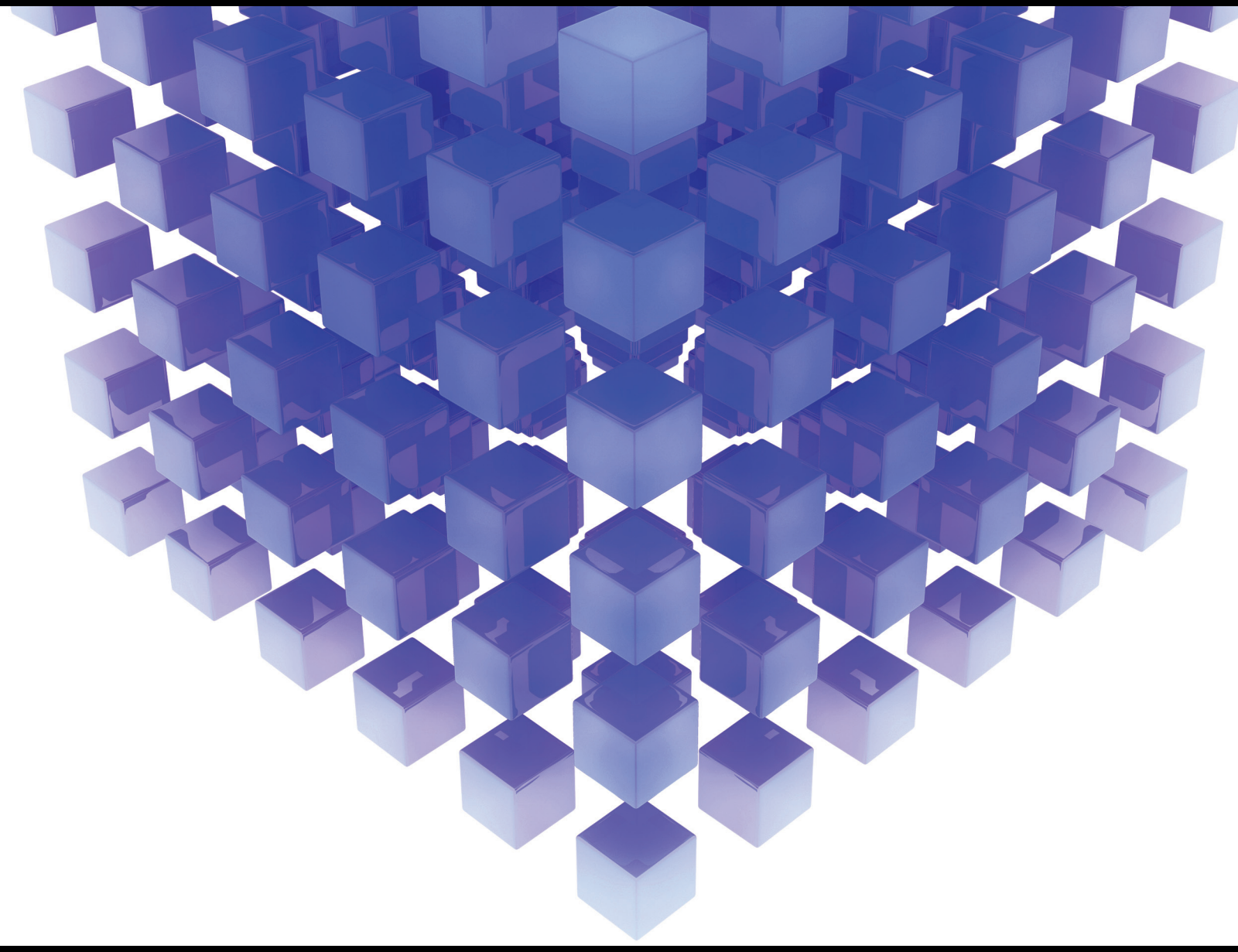

Mathematical Modeling and Optimization of Functionally Graded Structures

Mathematical Problems in Engineering

Mathematical Modeling and Optimization of Functionally Graded Structures

Guest Editors: Abdelouahed Tounsi, El Abbes Adda Bedia, S. R. Mahmoud, and Sofiane Amziane

Copyright © 2013 Hindawi Publishing Corporation. All rights reserved.

This is a special issue published in "Mathematical Problems in Engineering." All articles are open access articles distributed under the Creative Commons Attribution License, which permits unrestricted use, distribution, and reproduction in any medium, provided the original work is properly cited.

Editorial Board

M. Abd El Aziz, Egypt
E. M. Abdel-Rahman, Canada
R. K. Abu Al-Rub, USA
Sarp Adali, South Africa
Salvatore Alfonzetti, Italy
Igor Andrianov, Germany
Sebastian Anita, Romania
W. Assawinchaichote, Thailand
Erwei Bai, USA
Ezzat G. Bakhoum, USA
José M. Balthazar, Brazil
R. K. Bera, India
C. Bérenguer, France
Jonathan N. Blakely, USA
Stefano Boccaletti, Spain
Stephane P.A. Bordas, USA
Daniela Boso, Italy
M. Boutayeb, France
Michael J. Brennan, UK
Salvatore Caddemi, Italy
Piermarco Cannarsa, Italy
Jose E. Capilla, Spain
Carlo Cattani, Italy
Marcelo M. Cavalcanti, Brazil
Diego J. Celentano, Chile
Mohammed Chadli, France
Arindam Chakraborty, USA
Yong-Kui Chang, China
Michael J. Chappell, UK
Kui Fu Chen, China
Xinkai Chen, Japan
Kue-Hong Chen, Taiwan
Jyh-Horng Chou, Taiwan
Slim Choura, Tunisia
Cesar Cruz-Hernandez, Mexico
Swagatam Das, India
Filippo de Monte, Italy
Antonio Desimone, Italy
Yannis Dimakopoulos, Greece
Baocang Ding, China
Joao B. R. Do Val, Brazil
Daoyi Dong, Australia
B. Dubey, India
Horst Ecker, Austria
M. Onder Efe, Turkey
Elmetwally Elabbasy, Egypt
A. Elías-Zúñiga, Mexico
Anders Eriksson, Sweden
Vedat S. Erturk, Turkey
Moez Feki, Tunisia
Ricardo Femat, Mexico
Robertt A. Valente, Portugal
C. Fuerte-Esquivel, Mexico
Zoran Gajic, USA
Ugo Galvanetto, Italy
Furong Gao, Hong Kong
Xin-Lin Gao, USA
Behrouz Gatmiri, Iran
Oleg V. Gendelman, Israel
Didier Georges, France
Paulo B. Gonçalves, Brazil
Oded Gottlieb, Israel
Fabrizio Greco, Italy
Quang Phuc Ha, Australia
M. R. Hajj, USA
Tony S. W. Hann, Taiwan
Thomas Hanne, Switzerland
K. R. (Stevanovic) Hedrih, Serbia
M.I. Herreros, Spain
Wei-Chiang Hong, Taiwan
Jaromir Horacek, Czech Republic
Huabing Huang, China
Chuangxia Huang, China
Gordon Huang, Canada
Yi Feng Hung, Taiwan
Hai-Feng Huo, China
Asier Ibeas, Spain
Anuar Ishak, Malaysia
Reza Jazar, Australia
Zhijian Ji, China
Jun Jiang, China
J. J. Judice, Portugal
Tadeusz Kaczorek, Poland
Tamas Kalmar-Nagy, USA
Tomasz Kapitaniak, Poland
Hamid Reza Karimi, Norway
Metin O. Kaya, Turkey
Nikolaos Kazantzis, USA
Farzad Khani, Iran
K. Krabbenhoft, Australia
Ren-Jieh Kuo, Taiwan
Jurgen Kurths, Germany
Claude Lamarque, France
Usik Lee, Korea
Marek Lefik, Poland
Stefano Lenci, Italy
Roman Lewandowski, Poland
Shanling Li, Canada
Ming Li, China
Jian Li, China
Shihua Li, China
Teh-Lu Liao, Taiwan
Panos Liatsis, UK
Shueei M. Lin, Taiwan
Yi-Kuei Lin, Taiwan
Jui-Sheng Lin, Taiwan
Yuji Liu, China
Wanquan Liu, Australia
Bin Liu, Australia
Paolo Lonetti, Italy
V. C. Loukopoulos, Greece
Junguo Lu, China
Chien-Yu Lu, Taiwan
Alexei Mailybaev, Brazil
Manoranjan K. Maiti, India
O. D. Makinde, South Africa
R. Martinez-Guerra, Mexico
Driss Mehdi, France
Roderick Melnik, Canada
Xinzhu Meng, China
Yuri V. Mikhlin, Ukraine
G. Milovanovic, Serbia
Ebrahim Momoniat, South Africa
Trung Nguyen Thoi, Vietnam
Hung Nguyen-Xuan, Vietnam
Ben T. Nohara, Japan
Sotiris K. Ntouyas, Greece
Gerard Olivar, Colombia
Claudio Padra, Argentina
Bijaya Ketan Panigrahi, India
Francesco Pellicano, Italy
Matjaz Perc, Slovenia
Vu Ngoc Phat, Vietnam
M. do Rosário Pinho, Portugal
A. Pogromsky, The Netherlands

Seppo Pohjolainen, Finland
Stanislav Potapenko, Canada
Sergio Preidikman, USA
Carsten Proppe, Germany
Hector Puebla, Mexico
Justo Puerto, Spain
Dane Quinn, USA
K. R. Rajagopal, USA
Gianluca Ranzi, Australia
Sivaguru Ravindran, USA
G. Rega, Italy
Pedro Ribeiro, Portugal
J. Rodellar, Spain
R. Rodriguez-Lopez, Spain
A. J. Rodriguez-Luis, Spain
Ignacio Romero, Spain
Hamid Ronagh, Australia
Carla Roque, Portugal
Rubén R. García, Spain
Manouchehr Salehi, Iran
Miguel A. Sanjuán, Spain
Ilmar F. Santos, Denmark
Nickolas S. Sapidis, Greece
E. J. Sapountzakis, Greece
Bozidar Sarler, Slovenia
Andrey V. Savkin, Australia
Massimo Scalia, Italy
Mohamed A. Seddeek, Egypt
A. P. Seyranian, Russia
Leonid Shaikhet, Ukraine
Cheng Shao, China
Bo Shen, Germany
Jian-Jun Shu, Singapore
Zhan Shu, UK
Dan Simon, USA
Luciano Simoni, Italy
Grigori M. Sisoev, UK
Christos H. Skiadas, Greece
Davide Spinello, Canada
Sri Sridharan, USA
Rolf Stenberg, Finland
Changyin Sun, China
Jitao Sun, China
Xi-Ming Sun, China
Andrzej Swierniak, Poland
Yang Tang, Germany
Allen Tannenbaum, USA
Cristian Toma, Romania
Irina N. Trendafilova, UK
Alberto Trevisani, Italy
Jung-Fa Tsai, Taiwan
K. Vajravelu, USA
Victoria Vampa, Argentina
Josep Vehi, Spain
Stefano Vidoli, Italy
Xiaojun Wang, China
Dan Wang, China
Youqing Wang, China
Yongqi Wang, Germany
Cheng C. Wang, Taiwan
Moran Wang, China
Yijing Wang, China
Gerhard-Wilhelm Weber, Turkey
J. A. S. Witteveen, The Netherlands
Kwok-Wo Wong, Hong Kong
Ligang Wu, China
Zhengguang Wu, China
Gongnan Xie, China
Wang Xing-yuan, China
Xi Frank Xu, USA
Xuping Xu, USA
Jun-Juh Yan, Taiwan
Xing-Gang Yan, UK
Suh-Yuh Yang, Taiwan
Mahmoud T. Yassen, Egypt
Mohammad I. Younis, USA
Bo Yu, China
Huang Yuan, Germany
S.P. Yung, Hong Kong
Ion Zaballa, Spain
Ashraf M. Zenkour, Saudi Arabia
Jianming Zhan, China
Xu Zhang, China
Yingwei Zhang, China
Lu Zhen, China
Liancun Zheng, China
Jian Guo Zhou, UK
Zexuan Zhu, China
Mustapha Zidi, France

Contents

Hindawi Publishing Corporation
Mathematical Problems in Engineering
Volume 2013, Article ID 536867, 2 pages
http://dx.doi.org/10.1155/2013/536867

Editorial

Mathematical Modeling and Optimization of Functionally Graded Structures

Abdelouahed Tounsi,[1] El Abbes Adda Bedia,[1] S. R. Mahmoud,[2,3] and Sofiane Amziane[4]

[1] *Laboratoire des Matériaux et Hydrologie, Département de Génie Civil, Faculté de Technologie, Université de Sidi Bel Abbes, Algeria*
[2] *Department of Mathematics, Faculty of Science, King Abdulaziz University, Saudi Arabia*
[3] *Mathematics Department, Faculty of Science, University of Sohag, Egypt*
[4] *Clermont Université, Polytech'Clermont-Ferrand, EA 3867, LaMI, BP 10448, 63000 Clermont-Ferrand, France*

Correspondence should be addressed to Abdelouahed Tounsi; tou_abdel@yahoo.com

Received 26 September 2013; Accepted 26 September 2013

Copyright © 2013 Abdelouahed Tounsi et al. This is an open access article distributed under the Creative Commons Attribution License, which permits unrestricted use, distribution, and reproduction in any medium, provided the original work is properly cited.

Functionally graded structures such as beams, plates, and shells are those in which the volume fractions of two or more materials are varied continuously as a function of position along certain direction(s) of the structure to achieve a required function. Due to the dramatic increase in the use of functionally graded materials (FGMs) in a variety of engineering structures (e.g., mechanics, aerospace, automotive, nuclear, civil engineering, and medical prosthetics), as typical and principal mathematical issues, modeling and optimization of functionally graded structures have attracted the attention of many scientists in recent years for predicting the mechanical behavior of such structures [1–9].

This special issue collects selected papers on modeling aspects and the analysis of structures embedding functionally graded materials (FGMs).

S. Topal and S. Dag presented in their paper two different J_k-integral-based computational techniques, which can be used to conduct fracture mechanics analysis of orthotropic functionally graded materials subjected to hygrothermal stresses. The methods presented in this paper are shown to be effective ways of taking into account hygrothermal effects and evaluating fracture mechanics parameters and thus can be used to solve fracture and fatigue problems involving complex geometric configurations and loading conditions.

In the paper by S. R. Mahmoud et al., the effect of nonhomogeneity and rotation on the free vibrations for elastodynamic problem of orthotropic hollow sphere is discussed. Comparisons are made with the result in the presence and absence of nonhomogeneous and rotation in cases of orthotropic hollow sphere. An analytic solution method, without integral transformation, is developed in the paper by S. Y. Lee and C. C. Huang to find the exact solutions for transient heat conduction in functionally graded circular hollow cylinders with time-dependent boundary conditions. Limiting studies and numerical analyses are given to illustrate the efficiency and the accuracy of the analysis. Y. Yilmaz et al. introduced a localized differential quadrature method (LDQM) for buckling analysis of axially functionally graded nonuniform columns with elastic restraints. To the best of these authors' knowledge, in the open literature, LDQM has not been applied before to solutions of generalized eigenvalue problems governed by fourth-order variable coefficient differential equations. Comparison of the results obtained by Y. Yilmaz et al. shows the potential of the LDQM for solving such generalized eigenvalue problems governed by fourth-order variable coefficient differential equations with high accuracy and less computational effort.

Nonlocal elasticity model for bending analysis of sigmoid functionally graded materials (S-FGMs) nanoscale plates is presented in the paper by W. Y. Jung and S. C. Han using a first-order shear deformation theory and Hamilton's principle. The material properties of S-FGM nanoscale plate are assumed to vary according to sigmoid function (two power law distributions) of the volume fraction of the constituents. The effects of nonlocal parameters, power law index, aspect ratio, elastic modulus ratio, side-to-thickness ratio, and loading type on bending and vibration response are investigated in detail. The work presented in the paper

by W. Y. Jung and S. C. Han can be helpful while designing nanoelectromechanical system and microelectromechanical system devices using the S-FGM nanoscale plates. In the paper of F. Tornabene and A. Ceruti, the generalized differential quadrature method has been presented as a means, to investigate the static and dynamic analysis of functionally graded and laminated composite doubly curved shells and panels. The mechanical models presented by F. Tornabene and A. Ceruti, is based on the so-called first-order shear deformation theory (FSDT). Three different optimization schemes and methodologies are implemented. The particle swarm optimization, Monte Carlo, and genetic algorithm approaches have been applied to define the optimum volume fraction profile for optimizing the first natural frequency and the maximum static deflection of the considered shell structure.

In the paper presented by A. E. Alshorbagy et al., the boundary value problem of the uncoupled thermoelastic behavior of functionally graded plate is formulated and solved. First, the temperature distribution is predicted to be used in the thermoelastic analysis of functionally graded plate. Then, a finite element model based on the first-order shear deformation plate (FSDT) theory is proposed, accounting for the exact neutral plane position, for modeling the functionally graded plates. A comparative study is performed to illustrate the effect of considering the neutral plane position.

The paper presented by S. Kim et al. deals with the thermoelastic characteristics of circular disk TBC specimens with and without a functionally graded layer between the top and bond coats. Two partial differential equations are derived based on thermoelastic theory, and the thermoelastic characteristics, such as temperature distribution profiles, displacement, and stresses, are determined through mathematical approaches. Because of the complexity of the governing equations, a finite volume approach is adopted to analyze the thermoelastic characteristics.

The papers published in this special issue only discuss some of the most significant topics about the mathematical modeling and optimization of functionally graded structures. However, the included papers present significant contributions and promising methods.

Acknowledgments

We, the guest editors, would like to take this opportunity to thank all the authors for their valuable contributions as well as the anonymous reviewers for their comments and suggestions. The authors acknowledge the Deanship of Scientific Research (DSR), King Abdulaziz University, Jeddah, for the research grant and the technical and financial support. The support for this special issue by University of Sidi Bel Abbes (Algeria), and Clermont University, Institut Pascal, Clermont-Ferrand (France), is gratefully acknowledged.

Abdelouahed Tounsi
El Abbes Adda Bedia
S. R. Mahmoud
Sofiane Amziane

References

[1] A. Bessaim, M. S. A. Houari, A. Tounsi, S. R. Mahmoud, and E. A. Adda Bedia, "A new higher-order shear and normal deformation theory for the static and free vibration analysis of sandwich plates with functionally graded isotropic face sheets," *Journal of Sandwich Structures and Materials*, vol. 15, pp. 671–703, 2013.

[2] H. Hebali, A. Tounsi, M. S. A. Houari, A. Bessaim, and E. A. Adda Bedia, "A new quasi-3D hyperbolic shear deformation theory for the static and free vibration analysis of functionally graded plates," *Journal of Engineering Mechanics (ASCE)*. In press.

[3] A. Tounsi, M. S. A. Houari, S. Benyoucef, and E. A. Adda Bedia, "A refined trigonometric shear deformation theory for thermoelastic bending of functionally graded sandwich plates," *Aerospace Science and Technology*, vol. 24, pp. 209–220, 2011.

[4] H. Saidi, M. S. A. Houari, A. Tounsi, and E. A. Adda Bedia, "Thermo-mechanical bending response with stretching effect of functionally graded sandwich plates using a novel shear deformation theory," *Steel and Composite Structures*, vol. 15, pp. 221–245, 2013.

[5] K. Bakhti, A. Kaci, A. A. Bousahla, M. S. A. Houari, A. Tounsi, and E. A. Adda Bedia, "Large deformation analysis for functionally graded carbon nanotube-reinforced composite plates using an efficient and simple refined theory," *Steel and Composite Structures*, vol. 14, no. 4, pp. 335–347, 2013.

[6] N. Ziane, S. A. Meftah, H. A. Belhadj, A. Tounsi, and E. A. Adda Bedia, "Free vibration analysis of thin and thick-walled FGM box beams," *International Journal of Mechanical Sciences*, vol. 66, pp. 273–282, 2013.

[7] L. Ould Larbi, A. Kaci, M. S. A. Houari, and A. Tounsi, "An efficient shear deformation beam theory based on neutral surface position for bending and free vibration of functionally graded beams," *Mechanics Based Design of Structures and Machines*, vol. 41, pp. 421–433, 2013.

[8] M. S. A. Houari, A. Tounsi, and O. Anwar Bég, "Thermoelastic bending analysis of functionally graded sandwich plates using a new higher order shear and normal deformation theory," *International Journal of Mechanical Sciences*, vol. 76, pp. 102–111, 2013.

[9] A. Fekrar, N. El Meiche, A. Bessaim, A. Tounsi, and E. A. Adda Bedia, "Buckling analysis of functionally graded hybrid composite plates using a new four variable refined plate theory," *Steel and Composite Structures*, vol. 13, no. 1, pp. 91–107, 2012.

Hindawi Publishing Corporation
Mathematical Problems in Engineering
Volume 2013, Article ID 315176, 11 pages
http://dx.doi.org/10.1155/2013/315176

Research Article

Hygrothermal Fracture Analysis of Orthotropic Functionally Graded Materials Using J_k-Integral-Based Methods

Serra Topal[1] and Serkan Dag[2]

[1] *Department of Mechanical Engineering, Gazi University, 06570 Ankara, Turkey*
[2] *Department of Mechanical Engineering, Middle East Technical University, 06800 Ankara, Turkey*

Correspondence should be addressed to Serkan Dag; sdag@metu.edu.tr

Received 21 April 2013; Accepted 1 August 2013

Academic Editor: Abdelouahed Tounsi

Copyright © 2013 S. Topal and S. Dag. This is an open access article distributed under the Creative Commons Attribution License, which permits unrestricted use, distribution, and reproduction in any medium, provided the original work is properly cited.

This paper puts forward two different J_k-integral-based methods, which can be used to perform mixed-mode fracture analysis of orthotropic functionally graded materials subjected to hygrothermal stresses. The first method requires the evaluation of both components of J_k-integral, whereas the second method employs the first component J_1 and the asymptotic crack tip displacement fields. Plane orthotropic hygrothermoelasticity is the basic theory behind the J_k-integral formulation, which is carried out by assuming that all material properties are functions of the spatial coordinates. Developed procedures are implemented by means of the finite element method and integrated into a general purpose finite element analysis software. Temperature and specific moisture concentration fields needed in the fracture analyses are also computed through finite element analysis. Each of the developed methods is utilized in conjunction with the superposition technique to calculate the hygrothermal fracture parameters. An inclined crack located in a hygrothermally loaded orthotropic functionally graded layer is examined in parametric analyses. Comparisons of the results generated by the proposed methods do indicate that both methods lead to numerical results of high accuracy and that the developed form of the J_k-integral is domain independent. Further results are presented so as to illustrate the influences of crack inclination angle, crack length, and crack location upon the modes I and II stress intensity factors.

1. Introduction

Functionally graded materials (FGMs) are heterogeneous composite materials, which were originally proposed to be employed in high temperature applications as protective coatings [1]. However, since then, the concept of introducing gradations in certain physical properties has been realized in a number of other technological applications such as biomedical materials [2], high-performance cutting tools [3], surfaces possessing improved contact-damage resistance [4], and solid oxide fuel cells [5]. The heterogeneity of FGMs stems from the fact that volume fractions of the constituents vary along a particular direction in a predetermined manner. Certain kinds of functionally graded materials are known to be orthotropic in addition to being heterogeneous. For example, FGMs generated by means of plasma spray forming have a lamellar structure and thus contain weak cleavage planes parallel to the bounding planes [6]. Graded materials produced through the use of electron beam physical vapor deposition technique on the other hand have a columnar structure with weak cleavage planes perpendicular to the boundaries [7]. Moreover, fiber-reinforced composites possessing a variable fiber volume fraction can be considered as orthotropic functionally graded materials [8].

Considerable emphasis has been placed on fracture mechanics in research studies pertaining to orthotropic functionally graded materials due to the low fracture toughness of commonly used constituents such as ceramics and plastics. Both analytical and computational methods have been set forth for the purpose of evaluating fracture parameters for orthotropic FGMs. Analytical methods presented are almost invariably based on the approach of singular integral equations [9, 10]. Among the computational methods applied for fracture analysis of orthotropic FGMs, we can mention displacement correlation technique [11], modified crack closure method [12], interaction integral method [13], continuum shape sensitivity technique [14], and the J_k-integral approach [15]. In the studies on fracture analysis of orthotropic FGMs

in the literature, the graded medium is assumed to be under either mechanical or thermal loading. However, for certain types of orthotropic functionally graded materials, such as polymer-matrix FGMs with variable fiber spacing, in addition to the mechanical and thermal effects, hygroscopic stresses are also critical. Hygroscopic stresses are induced due to changes in moisture concentration within the polymeric matrix; and when these stresses are sufficiently large they may lead to fracture mechanics-related problems such as cracking, delamination, or fatigue. In many instances, thermal and hygroscopic effects act simultaneously on the structure. In these cases, the combined loading due to changes in temperature and moisture concentration is generally referred to as hygrothermal loading.

This paper presents two different J_k-integral-based computational techniques, which can be used to conduct fracture mechanics analysis of *orthotropic* functionally graded materials subjected to *hygrothermal stresses*. The first method developed makes use of both components J_1 and J_2 of the J_k-integral vector, whereas in the second method the first component J_1 is utilized in conjunction with the asymptotic crack tip displacement fields. The formulation of the J_k-integral is carried out by considering the constitutive relations of plane orthotropic hygrothermoelasticity. All material properties are assumed to be functions of the spatial coordinates in the derivations. The formulation yields a domain independent form for the J_k-integral, which comprises area and line integrals. Developed procedures are implemented by means of the finite element method and integrated into the general purpose finite element analysis software ANSYS [16]. Parametric analyses are performed by considering a hygrothermally loaded orthotropic functionally graded layer that contains an inclined edge crack. Comparisons of the hygrothermal fracture parameters computed by the proposed methods indicate that both techniques are capable of producing numerical results of high accuracy. Additional numerical results presented illustrate the influences of factors such as crack length, crack location, and inclination angle on modes I and II stress intensity factors (SIFs).

The organization of the paper is as follows: In Section 2, we outline the formulation of J_k-integral; Section 3 provides the details of the two different fracture analysis methods; finite element analysis techniques used in the implementation are elucidated in Section 4; and numerical results are presented in Section 5. Finally, the paper concludes with Section 6, which contains our final remarks.

2. Formulation of the J_k-Integral for Orthotropic FGMs Subjected to Hygrothermal Loading

Figure 1 depicts an inclined edge crack located in an orthotropic functionally graded material that is subjected to hygrothermal stresses. The medium is assumed to be in a state of either plane stress or strain. x and y axes are aligned along the principal directions of orthotropy; and the x_1 and x_2 axes lie parallel and perpendicular to the crack plane, respectively. Thus, ϕ in the figure represents the angle of inclination of the edge crack with respect to the principal direction of orthotropy x. A is an arbitrary area enclosing the crack tip. All material properties are assumed to be functions of the spatial coordinates. Thus, the medium possesses the property of being both orthotropic and inhomogeneous.

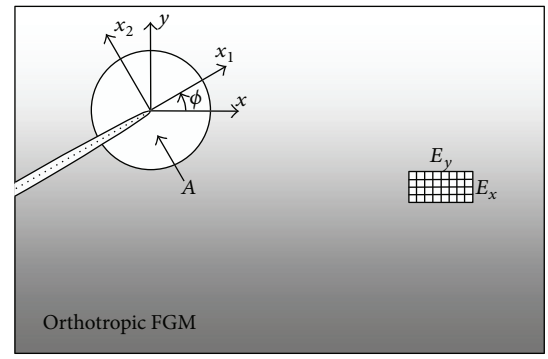

Figure 1: An inclined edge crack in an orthotropic functionally graded medium.

Constitutive relations of plane orthotropic hygrothermoelasticity are expressed as follows in the principal coordinate system:

$$\begin{bmatrix} \varepsilon_{xx} \\ \varepsilon_{yy} \\ 2\varepsilon_{xy} \end{bmatrix} = \begin{bmatrix} c_{11} & c_{12} & 0 \\ c_{12} & c_{22} & 0 \\ 0 & 0 & c_{66} \end{bmatrix} \begin{bmatrix} \sigma_{xx} \\ \sigma_{yy} \\ \sigma_{xy} \end{bmatrix} + \begin{bmatrix} d_1 \\ d_2 \\ 0 \end{bmatrix} \Delta T + \begin{bmatrix} e_1 \\ e_2 \\ 0 \end{bmatrix} \Delta c. \tag{1}$$

In this equation, ε_{ij} and σ_{ij}, respectively, stand for strain and stress; $\Delta T = T - T_r$ and $\Delta c = c - c_r$, where T is the temperature, c is the specific moisture concentration, T_r is the reference temperature, and c_r designates the reference specific moisture concentration. For plane stress, entries of the matrices are given by

$$c_{11} = \frac{1}{E_x}, \quad c_{12} = -\frac{\nu_{xy}}{E_x}, \quad c_{22} = \frac{1}{E_y}, \quad c_{66} = \frac{1}{G_{xy}}, \tag{2a}$$

$$d_1 = \alpha_x, \quad d_2 = \alpha_y, \quad e_1 = \beta_x, \quad e_2 = \beta_y, \tag{2b}$$

and for plane strain

$$c_{11} = \frac{1 - \nu_{zx}\nu_{xz}}{E_x}, \quad c_{12} = -\frac{\nu_{xy} + \nu_{xz}\nu_{zy}}{E_x}, \quad c_{22} = \frac{1 - \nu_{yz}\nu_{zy}}{E_y}, \quad c_{66} = \frac{1}{G_{xy}}, \tag{3a}$$

$$d_1 = \nu_{zx}\alpha_z + \alpha_x, \quad d_2 = \nu_{zy}\alpha_z + \alpha_y, \quad e_1 = \nu_{zx}\beta_z + \beta_x, \quad e_2 = \nu_{zy}\beta_z + \beta_y. \tag{3b}$$

In (2a), (2b), (3a), and (3b), E_i, ν_{ij}, and G_{xy} are material parameters of plane orthotropic elasticity, and α_i and β_i are

thermal and moisture expansion coefficients, respectively. In general, all material parameters are functions of the spatial coordinates in a graded medium. Moreover, the following relations are valid for an orthotropic material:

$$\frac{\nu_{yx}}{E_y} = \frac{\nu_{xy}}{E_x}, \qquad \frac{\nu_{zx}}{E_z} = \frac{\nu_{xz}}{E_x}, \qquad \frac{\nu_{zy}}{E_z} = \frac{\nu_{yz}}{E_y}. \tag{4}$$

Constitutive relations in the crack tip coordinate system comprising the axes x_1 and x_2 are derived by considering coordinate transformation rules valid for the strain and stress tensors. These constitutive relations are obtained as

$$\begin{bmatrix} \varepsilon_{11} \\ \varepsilon_{22} \\ 2\varepsilon_{12} \end{bmatrix} = \begin{bmatrix} a_{11} & a_{12} & a_{16} \\ a_{12} & a_{22} & a_{26} \\ a_{12} & a_{26} & a_{66} \end{bmatrix} \begin{bmatrix} \sigma_{11} \\ \sigma_{22} \\ \sigma_{12} \end{bmatrix} + \begin{bmatrix} g_1 \\ g_2 \\ g_{12} \end{bmatrix} \Delta T + \begin{bmatrix} h_1 \\ h_2 \\ h_{12} \end{bmatrix} \Delta c. \tag{5}$$

The entries of the compliance, thermal expansion, and moisture expansion matrices are provided in the appendix. Note that all of the entries are derived in terms of the inclination angle ϕ shown in Figure 1.

The structure of the constitutive relation (5) indicates that the principle of superposition can be used to generate the mixed-mode stress intensity factors corresponding to hygrothermal loading. The results due to thermal loading can be found by assuming $\Delta c = 0$, and the results corresponding to hygroscopic loading can be calculated by taking $\Delta T = 0$. Utilizing the principle of superposition, these two separate sets of results can be combined to evaluate the results for hygrothermal loading. Thus, it suffices to formulate the problem in terms of ΔT and thermal expansion matrix entries g_1, g_2, and g_{12}. When the results for hygroscopic loading are to be calculated, these quantities need to be replaced by Δc, h_1, h_2, and h_{12}. The respective sums of the modes I and II stress intensity factors are the final results valid for hygrothermal loading. In what follows, we provide the formulation for thermal loading, which can be used to generate the numerical results for both thermal and hygroscopic loading cases.

For the crack depicted in Figure 1, the J_k-integral is derived to be in the following form:

$$J_k = \iint_A \left\{\sigma_{ij} u_{i,k} - W\delta_{kj}\right\} q_{,j} dA - \iint_A \left(W_{,k}\right)_{\text{expl}} q\, dA - \int_{\Gamma_c} \left(W^+ - W^-\right) \delta_{2k} q\, ds, \quad (i, j, k = 1, 2). \tag{6}$$

This equation is valid in the local coordinate system x_1-x_2. u_i here stands for the displacement vector; W designates the mechanical strain energy density function; δ_{kj} is Kronecker delta; q is a piecewise smooth function that is equal to unity at the crack tip and zero on the circumference of area A; $(W_{,k})_{\text{expl}}$ denotes the explicit derivative of W; and s is the arc length. Γ_c is the straight line that is initiated at the point where A intersects crack faces and terminates at the origin. The outcome of the analysis is independent of the size and shape of area A used around the crack tip. In the present study, A is specified as a circular area with its center lying at the crack tip. The q-function utilized is in the form

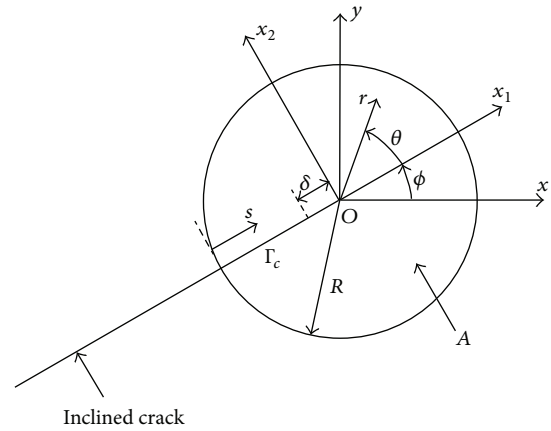

Figure 2: Integration domains used in the evaluation of the J_k-integral.

$$q(x_1, x_2) = 1 - \frac{\sqrt{x_1^2 + x_2^2}}{R}, \tag{7}$$

where R is the radius of area A. The integration domains A and Γ_c are depicted in Figure 2.

Although (6) is to be evaluated in the local coordinate system x_1-x_2, the scalar quantities W and $(W_{,k})_{\text{expl}}$ can be computed in any coordinate system since they are independent of coordinate transformation. In this study, these two quantities are computed in the principal coordinate system for the sake of simplicity. For plane stress, the expression of W in the principal coordinate system is derived as

$$W = \frac{E_x^2 \left(\varepsilon_{xx} - \alpha_x \Delta T\right) + \nu_{xy} E_x E_y \left(\varepsilon_{yy} - \alpha_y \Delta T\right)}{2\left(E_x - \nu_{xy}^2 E_y\right)} \times \left(\varepsilon_{xx} - \alpha_x \Delta T\right) + 2G_{xy}\varepsilon_{xy}^2 + \frac{\nu_{xy} E_x E_y \left(\varepsilon_{xx} - \alpha_x \Delta T\right) + E_x E_y \left(\varepsilon_{yy} - \alpha_y \Delta T\right)}{2\left(E_x - \nu_{xy}^2 E_y\right)} \times \left(\varepsilon_{yy} - \alpha_y \Delta T\right), \tag{8}$$

and for plane strain W reads

$$W = \frac{E_x \bar{\varepsilon}_{xx}}{2D} \times \left\{\left(1 - \frac{E_y \nu_{xz} \nu_{zy}^2}{E_x \nu_{zx}}\right) E_x \bar{\varepsilon}_{xx} + \left(\nu_{xy} + \nu_{xz}\nu_{zy}\right) E_y \bar{\varepsilon}_{yy}\right\} + 2G_{xy}\varepsilon_{xy}^2 + \frac{E_x E_y \bar{\varepsilon}_{yy}}{2D}$$

$$\times \left\{\left(\nu_{xy} + \nu_{xz}\nu_{zy}\right)\bar{\varepsilon}_{xx} + \left(1 - \nu_{zx}\nu_{xz}\right)\bar{\varepsilon}_{yy}\right\} + \frac{E_x \nu_{zx}}{2\nu_{xz}}\alpha_z^2 (\Delta T)^2, \tag{9a}$$

$$D = E_x\left(1 - \nu_{zx}\nu_{xz}\right) - E_y\left(\frac{\nu_{zy}^2\nu_{xz}}{\nu_{zx}} + \nu_{xy}^2 + 2\nu_{xy}\nu_{xz}\nu_{zy}\right), \tag{9b}$$

$$\bar{\varepsilon}_{xx} = \varepsilon_{xx} - \left(\nu_{zx}\alpha_z + \alpha_x\right)\Delta T, \qquad \bar{\varepsilon}_{yy} = \varepsilon_{yy} - \left(\nu_{zy}\alpha_z + \alpha_y\right)\Delta T. \tag{9c}$$

The explicit derivatives of the mechanical strain energy density function are derived by considering (8), (9a), (9b), and (9c). For the cases of plane stress and strain, these derivatives are given by

$$\left(\frac{\partial W}{\partial x_k}\right)_{\text{expl}} = \frac{\partial W}{\partial E_x}\frac{\partial E_x}{\partial x_k} + \frac{\partial W}{\partial E_y}\frac{\partial E_y}{\partial x_k} + \frac{\partial W}{\partial \nu_{xy}}\frac{\partial \nu_{xy}}{\partial x_k} + \frac{\partial W}{\partial G_{xy}}\frac{\partial G_{xy}}{\partial x_k} + \frac{\partial W}{\partial \alpha_x}\frac{\partial \alpha_x}{\partial x_k} + \frac{\partial W}{\partial \alpha_y}\frac{\partial \alpha_y}{\partial x_k} + \frac{\partial W}{\partial (\Delta T)}\frac{\partial (\Delta T)}{\partial x_k}, \quad (k = 1, 2) \text{ for plane stress,} \tag{10a}$$

$$\left(\frac{\partial W}{\partial x_k}\right)_{\text{expl}} = \frac{\partial W}{\partial E_x}\frac{\partial E_x}{\partial x_k} + \frac{\partial W}{\partial E_y}\frac{\partial E_y}{\partial x_k} + \frac{\partial W}{\partial \nu_{zy}}\frac{\partial \nu_{zy}}{\partial x_k} + \frac{\partial W}{\partial \nu_{xz}}\frac{\partial \nu_{xz}}{\partial x_k} + \frac{\partial W}{\partial \nu_{xy}}\frac{\partial \nu_{xy}}{\partial x_k} + \frac{\partial W}{\partial \nu_{zy}}\frac{\partial \nu_{zy}}{\partial x_k} + \frac{\partial W}{\partial G_{xy}}\frac{\partial G_{xy}}{\partial x_k} + \frac{\partial W}{\partial \alpha_x}\frac{\partial \alpha_x}{\partial x_k} + \frac{\partial W}{\partial \alpha_y}\frac{\partial \alpha_y}{\partial x_k} + \frac{\partial W}{\partial \alpha_z}\frac{\partial \alpha_z}{\partial x_k} + \frac{\partial W}{\partial (\Delta T)}\frac{\partial (\Delta T)}{\partial x_k}, \quad (k = 1, 2) \text{ for plane strain.} \tag{10b}$$

Derivatives of W with respect to the material parameters and the temperature difference in (10a) and (10b) are found in closed form. The remaining partial derivatives in these equations, that is, the derivatives of the material properties and the temperature difference with respect to spatial coordinates, are calculated numerically during the finite element computations.

3. J_k-Integral-Based Methods

In this section, we elucidate two different J_k-integral-based methods, which can be employed to compute mixed-mode stress intensity factors for orthotropic functionally graded materials under hygrothermal stresses. For both thermal and hygroscopic loading cases, the formulation given in the previous section is applicable provided that the appropriate loading function (i.e., ΔT or Δc) and material properties are considered. Once mixed-mode stress intensity factors are computed for thermal or hygroscopic loading cases, the resultant SIFs can be obtained by combining the separate stress intensity factors evaluated for these loads. The methods presented in this section allow the evaluation of the mixed-mode SIFs for both thermal and hygroscopic types of loading. The first method makes use of both components of the J_k-integral, J_1 and J_2, whereas in the second method we utilize the first component J_1 and the asymptotic displacement fields.

3.1. Method I. In this method, we use the relations between the components of the J_k-integral and the mixed-mode stress intensity factors K_{I} and K_{II}. Equation (6) indicates that the first component of the J_k-integral comprises solely area integrals, while the second component J_2 involves both area and line integrals. The expression of J_2 is further simplified by separating the line integral into two parts, one evaluated over a region away from the crack tip and the other evaluated near the crack tip. The integral evaluated over a domain near the crack tip is determined in closed form. Then, the components of the J_k-integral are written as follows:

$$J_1 = \iint_A \left\{\sigma_{ij}u_{i,1} - W\delta_{1j}\right\} q_{,j}\, dA - \iint_A \left(W_{,1}\right)_{\text{expl}} q\, dA \quad (i, j = 1, 2), \tag{11a}$$

$$J_2 = \iint_A \left\{\sigma_{ij}u_{i,2} - W\delta_{2j}\right\} q_{,j}\, dA - \iint_A \left(W_{,2}\right)_{\text{expl}} q\, dA - \int_0^{R-\delta} \left(W^+ - W^-\right) q\, ds - \sqrt{\frac{2\delta}{\pi}}C \quad (i, j = 1, 2), \tag{11b}$$

where δ is the length of the domain over which the line integral is evaluated analytically. This length is also depicted in Figure 2. The term C in (11b) is derived in the form

$$C = -2a_{11}^{\text{tip}}\sigma_{11}^0 \left\{\left(\alpha_1\eta_2 + \alpha_2\eta_1\right)K_{\text{I}} + \left(\eta_1 + \eta_2\right)K_{\text{II}}\right\}, \tag{12}$$

where σ_{11}^0 is the constant term in the asymptotic expansion of the stress component σ_{11} and a_{11}^{tip} is the value of a_{11} at the crack tip. a_{11} is given by (A.1a) for plane stress and by (A.2a) for plane strain in the appendix. α_i and η_i are the real and imaginary parts of the two roots of the characteristic equation

$$a_{11}^{\text{tip}}s^4 - 2a_{16}^{\text{tip}}s^3 + \left(2a_{12}^{\text{tip}} + a_{66}^{\text{tip}}\right)s^2 - 2a_{26}^{\text{tip}}s + a_{22}^{\text{tip}} = 0, \tag{13}$$

whose imaginary parts are positive. a_{ij}^{tip} in this equation are the crack-tip values of a_{ij}. The expressions of a_{ij} are provided in the appendix for both plane stress and strain.

J_1 given by (11a) consists of only area integrals and can be evaluated numerically in a straightforward manner by using the Gauss-quadrature methods. However, the expression of J_2 given by (11b) contains σ_{11}^0, K_{I}, and K_{II}, which are unknowns.

In order to be able to evaluate J_2, we define a new variable $\widehat{J}_2$ as follows:

$$\widehat{J}_2 = \iint_A \left\{\sigma_{ij}u_{i,2} - W\delta_{2j}\right\} q_{,j}\,dA - \iint_A (W_{,2})_{\text{expl}}\, q\,dA - \int_0^{R-\delta} \left(W^+ - W^-\right) q\,ds. \tag{14}$$

For a given loading condition, $\widehat{J}_2$ is calculated for two different values of δ. Denoting these δ values by δ_1, δ_2, the corresponding $\widehat{J}_2$ values by $\widehat{J}_2^1$, $\widehat{J}_2^2$ and considering (11b), J_2 is expressed as

$$J_2 = \frac{1}{\sqrt{\delta_2/\pi} - \sqrt{\delta_1/\pi}} \left\{ \sqrt{\frac{\delta_2}{\pi}}\widehat{J}_2^1 - \sqrt{\frac{\delta_1}{\pi}}\widehat{J}_2^2 \right\}. \tag{15}$$

Once J_1 is calculated using (11a) and J_2 using (15), mixed-mode stress intensity factors can be evaluated by the following equalities that relate the components of the J_k-integral to K_{I} and K_{II} [17]:

$$J_1 = \frac{a_{11}^{\text{tip}}}{2}\left\{c_{11}K_{\text{I}}^2 + c_{12}K_{\text{I}}K_{\text{II}} + c_{22}K_{\text{II}}^2\right\}, \tag{16a}$$

$$J_2 = -\frac{a_{11}^{\text{tip}}}{4}\left\{d_{11}K_{\text{I}}^2 + d_{12}K_{\text{I}}K_{\text{II}} + d_{22}K_{\text{II}}^2\right\}, \tag{16b}$$

where

$$c_{11} = \alpha_1^2\eta_2 + \alpha_2^2\eta_1 + \eta_1^2\eta_2 + \eta_1\eta_2^2, \tag{17a}$$

$$c_{12} = 2\left(\alpha_1\eta_2 + \alpha_2\eta_1\right), \tag{17b}$$

$$c_{22} = \eta_1 + \eta_2, \tag{17c}$$

$$d_{11} = \alpha_1\eta_2 + \alpha_2\eta_1, \tag{17d}$$

$$d_{12} = 4\left\{\eta_1^2\eta_2 + \eta_1\eta_2^2 - \alpha_1\alpha_2\left(\eta_1 + \eta_2\right)\right\}, \tag{17e}$$

$$d_{22} = 2\left\{\alpha_1^2\eta_2 + \alpha_2^2\eta_1 + \alpha_1\alpha_2\left(\eta_1 + \eta_2\right)\right\} - \alpha_1\eta_2 - \alpha_2\eta_1. \tag{17f}$$

The nonlinear equation set (16a) and (16b) is solved by employing the Newton-Raphson method. Although in general the outcome of the Newton-Raphson method is sensitive to the initial guesses, it is found that convergence is assured by initially specifying K_{I} as an arbitrary positive number and K_{II} as zero.

3.2. Method II. The second method we developed is based on the use of the first component of the J_k-integral J_1 and the asymptotic crack tip displacement fields. Referring to Figure 2, asymptotic relative displacements of the crack faces can be written as follows [18]:

$$u_1(r,\pi) - u_1(r,-\pi) = 2\sqrt{\frac{2r}{\pi}}\left\{D_{11}K_{\text{I}} + D_{12}K_{\text{II}}\right\}, \tag{18a}$$

$$u_2(r,\pi) - u_2(r,-\pi) = 2\sqrt{\frac{2r}{\pi}}\left\{D_{21}K_{\text{I}} + D_{22}K_{\text{II}}\right\}, \tag{18b}$$

where

$$D_{11} = \text{Im}\left\{\frac{s_2P_{11} - s_1P_{12}}{s_1 - s_2}\right\}, \quad D_{12} = \text{Im}\left\{\frac{P_{11} - P_{12}}{s_1 - s_2}\right\}, \tag{19a}$$

$$D_{21} = \text{Im}\left\{\frac{s_2P_{21} - s_1P_{22}}{s_1 - s_2}\right\}, \quad D_{22} = \text{Im}\left\{\frac{P_{21} - P_{22}}{s_1 - s_2}\right\}, \tag{19b}$$

$$P_{1i} = a_{11}^{\text{tip}}s_i^2 + a_{12}^{\text{tip}} - a_{16}^{\text{tip}}s_i \quad (i = 1,2), \tag{19c}$$

$$P_{2i} = a_{12}^{\text{tip}}s_i + \frac{a_{22}^{\text{tip}}}{s_i} - a_{26}^{\text{tip}} \quad (i = 1,2), \tag{19d}$$

and s_1 and s_2 are the roots of the characteristic equation (13) with positive imaginary parts. We define a ratio involving the relative displacements of the crack faces at a radial location r_a in the following form:

$$A_r = \frac{u_2(r_a,\pi) - u_2(r_a,-\pi)}{u_1(r_a,\pi) - u_1(r_a,-\pi)}. \tag{20}$$

From (18a), (18b), and (20) it then follows that

$$\frac{K_{\text{I}}}{K_{\text{II}}} = \frac{A_rD_{12} - D_{22}}{D_{21} - A_rD_{11}} = B. \tag{21}$$

Substituting this result into (16a), K_{I} is derived as

$$K_{\text{I}} = \sqrt{\frac{2J_1}{a_{11}^{\text{tip}}\left(c_{11} + (c_{12}/B) + (c_{22}/B^2)\right)}}. \tag{22}$$

In this second method, once J_1 is determined through (11a), K_{I} and K_{II} can be computed by the use of (22) and (21), respectively.

4. Numerical Implementation

The methods described in Section 3 are implemented by means of the finite element method. The proposed procedures are integrated into the general purpose finite element analysis software ANSYS [16]. In thermal fracture analysis, the first step is the determination of the temperature field. In the case of hygroscopic loading, specific moisture concentration distribution needs to be determined at the outset. These fields are computed by solving the governing partial differential equations through the use of finite element method. The governing partial differential equation for the temperature distribution is the heat equation, which is given by

$$\frac{\partial}{\partial x}\left(k_x(x,y)\frac{\partial T}{\partial x}\right) + \frac{\partial}{\partial y}\left(k_y(x,y)\frac{\partial T}{\partial y}\right) = 0, \tag{23}$$

where T denotes the temperature; x and y are the principal coordinates of orthotropy shown in Figure 1; and k_x and

k_y are the principal thermal conductivities. The governing partial differential equation for the specific moisture concentration is

$$\frac{\partial}{\partial x}\left(D_x(x,y)\frac{\partial c}{\partial x}\right)+\frac{\partial}{\partial y}\left(D_y(x,y)\frac{\partial c}{\partial y}\right)=0. \quad (24)$$

c in this equation is specific moisture concentration and D_x and D_y are the principal mass diffusivities.

The temperature and specific moisture concentration distributions computed through the solutions of (23) and (24) are used to calculate the components of the J_k-integral and the modes I and II stress intensity factors K_{I} and K_{II} for each type of loading, that is, for thermal and hygroscopic loadings. The SIFs generated for these separate loads are then superposed to determine the results valid for hygrothermal loading. Smooth spatial variations of the hygrothermomechanical properties of orthotropic FGMs are taken into account in the finite element analyses by specifying the material properties of each finite element at its centroid. This approach is generally referred to as homogeneous finite element approach and leads to computational results of high accuracy provided that there is an appropriate degree of mesh refinement in the finite element model [11, 19]. The finite element meshes employed in the analyses are constructed by utilizing 6-node triangular elements.

The area and line integrals required to be evaluated in J_k-integral computations are calculated by using the Gauss quadrature in conjunction with the isoparametric finite element concept. Area integrals are computed over circular domains centered at the tip of the crack. The accuracy of the outcome of the numerical procedures developed is influenced by certain parameters needed in the solution. For instance, δ_1 and δ_2 values used in (15) and r_a value used in (20) have to be set sufficiently small to evaluate the hygrothermal fracture parameters within a high degree of accuracy. It is found that for both thermal and hygroscopic loading cases, highly accurate results can be obtained by setting δ_1, δ_2, and r_a, respectively, as $a/2000$, $a/1000$, and $a/8000$, where a is the length of the inclined crack.

5. Numerical Results

Hygrothermal fracture analysis methods developed in this study are used to compute the fracture parameters for the problem depicted in Figure 3. The figure illustrates both the geometry and hygrothermal boundary conditions. A graded orthotropic layer of length L contains an inclined edge crack whose length is denoted by a. The axes x and y are the principal axes of orthotropy, and the angle of inclination between the crack plane and x-axis is symbolized by ϕ. We suppose that the medium is in a state of plane strain. T_0 and c_0 values used in hygrothermal loading are also the reference values for the temperature and the specific moisture concentration. In all analyses T_0 and c_0 are, respectively, set as 20°C and 0.005. As also mentioned in the previous sections, the modes I and II stress intensity factors for the considered hygrothermal loading are determined by superposing the results calculated for thermal and hygroscopic loads.

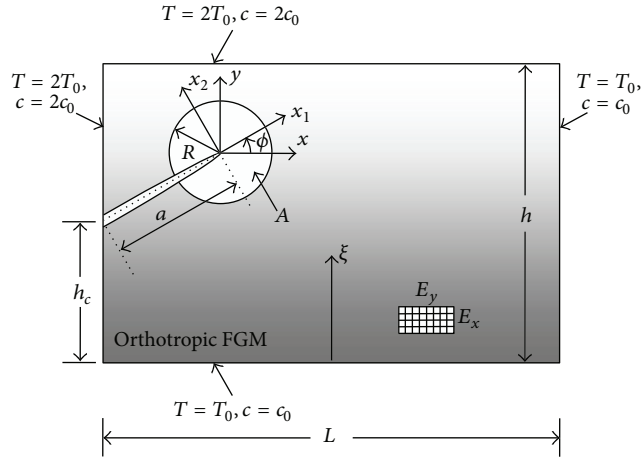

Figure 3: Problem geometry and hygrothermal boundary conditions.

Table 1: Material properties at $\xi = 0$ and $\xi = h$ and the exponents.

		$\xi = 0$	$\xi = h$	Exponent
E_x	(GPa)	80	80	γ_x
E_y	(GPa)	80	40	γ_y
G_{xy}	(GPa)	32	26.7	γ_{xy}
ν_{xy}		0.25	0.25	ω_{xy}
ν_{xz}		0.25	0.25	ω_{xz}
ν_{zx}		0.25	0.3	ω_{zx}
ν_{zy}		0.25	0.3	ω_{zy}
α_x	(1/°C)	$3(10)^{-5}$	$3(10)^{-5}$	λ_x
α_y	(1/°C)	$3(10)^{-5}$	$6(10)^{-5}$	λ_y
α_z	(1/°C)	$3(10)^{-5}$	$4.5(10)^{-5}$	λ_z
β_x		0.33	0.33	κ_x
β_y		0.33	0.66	κ_y
β_z		0.33	0.495	κ_z
k_x	(W/m·°C)	0.5	0.5	η_x
k_y	(W/m·°C)	0.5	1	η_y
D_x	(m^2/s)	$3(10)^{-15}$	$3(10)^{-15}$	ρ_x
D_y	(m^2/s)	$3(10)^{-15}$	$6(10)^{-15}$	ρ_y

The layer is assumed to be a fiber-reinforced composite with a fiber volume fraction decreasing as ξ increases from 0 to h. As a result, all of the material properties of the layer become functions of the thickness coordinate ξ. Each of the material property required in the analysis is represented by a power function in the following form:

$$M(\xi) = M_0 + (M_h - M_0)\left(\frac{\xi}{h}\right)^p, \quad (25)$$

where M_0 and M_h are the values of the material property at $\xi = 0$ and $\xi = h$, respectively, and p is the exponent of the power function characterizing the nature of the property distribution across the thickness. The properties of the orthotropic FGM layer at $\xi = 0$ and $\xi = h$ and the symbols designating the exponents are provided in Table 1.

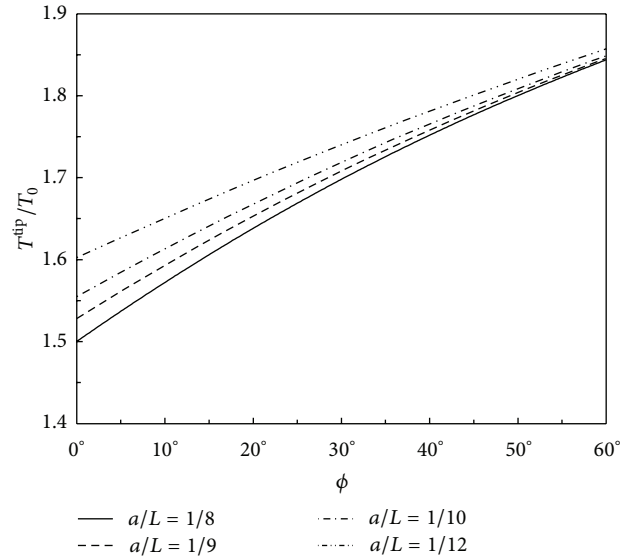

FIGURE 4: Normalized crack tip temperature versus inclination angle ϕ and a/L. $\eta_x = \eta_y = 2.5$, $h_c/h = 0.25$, and $h/L = 0.4$.

Temperature and specific moisture concentration fields for the layer are computed by solving (23) and (24) through the finite element method. Normalized crack tip temperature variations are provided in Figure 4. This figure shows the normalized crack tip temperature as functions of the crack inclination angle ϕ and normalized crack length a/L. It is seen that crack tip temperature is an increasing function of the inclination angle. This is the expected result since the crack tip gets closer to the boundaries at the higher temperature as ϕ becomes larger. The figure also indicates that at a given inclination angle, crack tip temperature is a decreasing function of a/L. The trends observed for the crack tip specific moisture concentration are very similar to those presented in Figure 4.

In order to be able to verify the developed computational methods, in Table 2 we provide comparisons of the normalized mixed-mode stress intensity factors computed for the hygrothermal loading shown in Figure 3. Normalized stress intensity factors are defined as

$$K_{\text{I}n} = \frac{K_{\text{I}}}{\alpha(0)\, E_x(0)\, T_0 \sqrt{\pi a}},$$
$$K_{\text{II}n} = \frac{K_{\text{II}}}{\alpha(0)\, E_x(0)\, T_0 \sqrt{\pi a}}. \tag{26}$$

The hygrothermal mixed-mode stress intensity factors are calculated by considering four different values of the inclination angle ϕ, and for each inclination angle the results are given for four different values of the normalized domain radius R/a. Examining the results, it is seen that the SIFs generated by each method are independent of the domain radius. Hence, it can be deduced that the developed form of the J_k-integral is domain independent. Furthermore, the results obtained by methods I and II are in excellent agreement, which is indicative of the high level of accuracy of the results generated by means of the developed techniques. Deformed shape of the finite element mesh under thermal loading is provided in Figure 5.

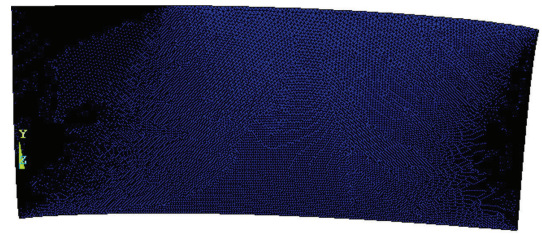

FIGURE 5: Deformed shape of the finite element mesh under thermal loading. $\gamma_x = \gamma_y = \gamma_{xy} = 2$, $\omega_{xy} = \omega_{xz} = \omega_{zx} = \omega_{zy} = 2$, $\lambda_x = \lambda_y = \lambda_z = 2.5$, $\kappa_x = \kappa_y = \kappa_z = 1.5$, $\eta_x = \eta_y = 2.5$, $\rho_x = \rho_y = 1.5$, $h_c/h = 0.25$, $h/L = 0.4$, and $a/L = 0.1$.

Further results are provided in Figures 6 and 7, which illustrate the influences of inclination angle, crack length, and crack location upon the mixed-mode stress intensity factors. Since both methods are shown to be capable of producing highly accurate numerical results, it is deemed as sufficient to use method I in the generation of the further results presented in these figures. Normalized domain radius R/a is set as 0.1 in the pertaining calculations.

Figure 6 shows the variations of the normalized mixed-mode SIFs with respect to ϕ for four different values of normalized crack length a/L. It is seen that $K_{\text{I}n}$ curves go through maximums at ϕ values close to 60°, while $K_{\text{II}n}$ attains maximums at ϕ values between 0° and 30°. $K_{\text{I}n}$ decreases as a/L is increased from 1/12 to 1/8. On the other hand, $K_{\text{II}n}$ is found to be an increasing function of a/L except for relatively small values of ϕ. We also note that $K_{\text{I}n}$ is positive and the crack is open for all ϕ considered, whereas $K_{\text{II}n}$ can be positive or negative depending on the value of the inclination angle.

In Figure 7, we present plots of normalized modes I and II SIFs as functions of the inclination angle ϕ and the relative crack location h_c/h. h_c is the height of crack mouth and h stands for the height of the orthotropic FGM layer. For ϕ values approximately less than 45°, $K_{\text{I}n}$ is an increasing function of h_c/h; that is, $K_{\text{I}n}$ increases as h_c/h is increased from 0.15 to 0.3. When ϕ is close to 60°, $K_{\text{I}n}$ is not that sensitive to the variations in the relative crack location. For relatively small values of ϕ, normalized mode II stress intensity factor is an increasing function of h_c/h. However, for larger values of the inclination angle $K_{\text{II}n}$ drops with a corresponding increase in h_c/h.

6. Closure

This study sets forth two different J_k-integral-based methods, which can be employed to conduct fracture mechanics analysis of orthotropic functionally graded materials that are under the influence of *hygrothermal stresses*. In the first of these methods, both components of the J_k-integral are evaluated, whereas the second technique requires the computation of only the first component. Proposed procedures are implemented by means of the finite element method

Table 2: Comparisons of the mixed-mode stress intensity factors. $\gamma_x = \gamma_y = \gamma_{xy} = 2$, $\omega_{xy} = \omega_{xz} = \omega_{zx} = \omega_{zy} = 2$, $\lambda_x = \lambda_y = \lambda_z = 2.5$, $\kappa_x = \kappa_y = \kappa_z = 1.5$, $\eta_x = \eta_y = 2.5$, $\rho_x = \rho_y = 1.5$, $h_c/h = 0.25$, $h/L = 0.4$, and $a/L = 0.1$.

ϕ	R/a	Method I		Method II	
		K_{In}	K_{IIn}	K_{In}	K_{IIn}
0°	0.1	0.0098	0.0122	0.0098	0.0119
	0.2	0.0099	0.0122	0.0098	0.0120
	0.3	0.0099	0.0123	0.0098	0.0120
	0.4	0.0099	0.0123	0.0097	0.0119
30°	0.1	0.0251	0.0080	0.0250	0.0076
	0.2	0.0252	0.0080	0.0251	0.0077
	0.3	0.0253	0.0080	0.0252	0.0077
	0.4	0.0253	0.0081	0.0252	0.0077
45°	0.1	0.0296	−0.0006	0.0296	−0.0008
	0.2	0.0298	−0.0006	0.0298	−0.0008
	0.3	0.0300	−0.0006	0.0300	−0.0007
	0.4	0.0301	−0.0008	0.0301	−0.0007
60°	0.1	0.0287	−0.0081	0.0288	−0.0089
	0.2	0.0292	−0.0083	0.0292	−0.0090
	0.3	0.0297	−0.0086	0.0296	−0.0091
	0.4	0.0301	−0.0086	0.0299	−0.0092

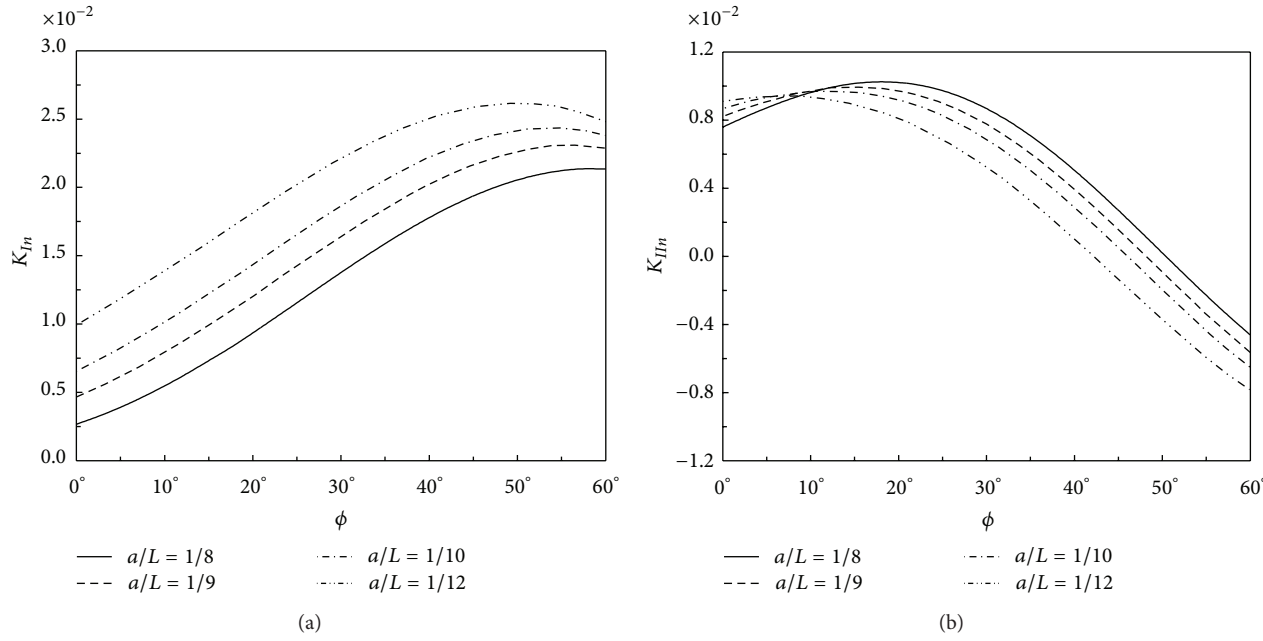

Figure 6: Normalized mixed-mode stress intensity factors versus inclination angle ϕ and a/L: (a) mode I SIFs; (b) mode II SIFs. $\gamma_x = \gamma_y = \gamma_{xy} = 2$, $\omega_{xy} = \omega_{xz} = \omega_{zx} = \omega_{zy} = 2$, $\lambda_x = \lambda_y = \lambda_z = 2$, $\kappa_x = \kappa_y = \kappa_z = 2$, $\eta_x = \eta_y = 2$, $\rho_x = \rho_y = 2$, $h_c/h = 0.25$, and $h/L = 0.4$.

and integrated into a general purpose finite element analysis software. Superposition technique is utilized in the extraction of the hygrothermal modes I and II stress intensity factors.

The comparisons provided do indicate that the derived form of the J_k-integral possesses the required domain independence and that both methods are capable of producing numerical results of high accuracy. Further results are presented to illustrate the impacts of inclination angle, normalized crack length, and relative crack location on the normalized mixed-mode stress intensity factors. In general, the influence of each of these parameters on the fracture behavior is significant. Especially, the effect of the crack inclination angle is seen to be rather pronounced. Under hygrothermal stresses, both K_{I} and K_{II} go through maximum values as the inclination angle is increased from zero.

In studies on fracture mechanics and fatigue of orthotropic functionally graded materials, correct evaluation of the mixed-mode stress intensity factors is a basic

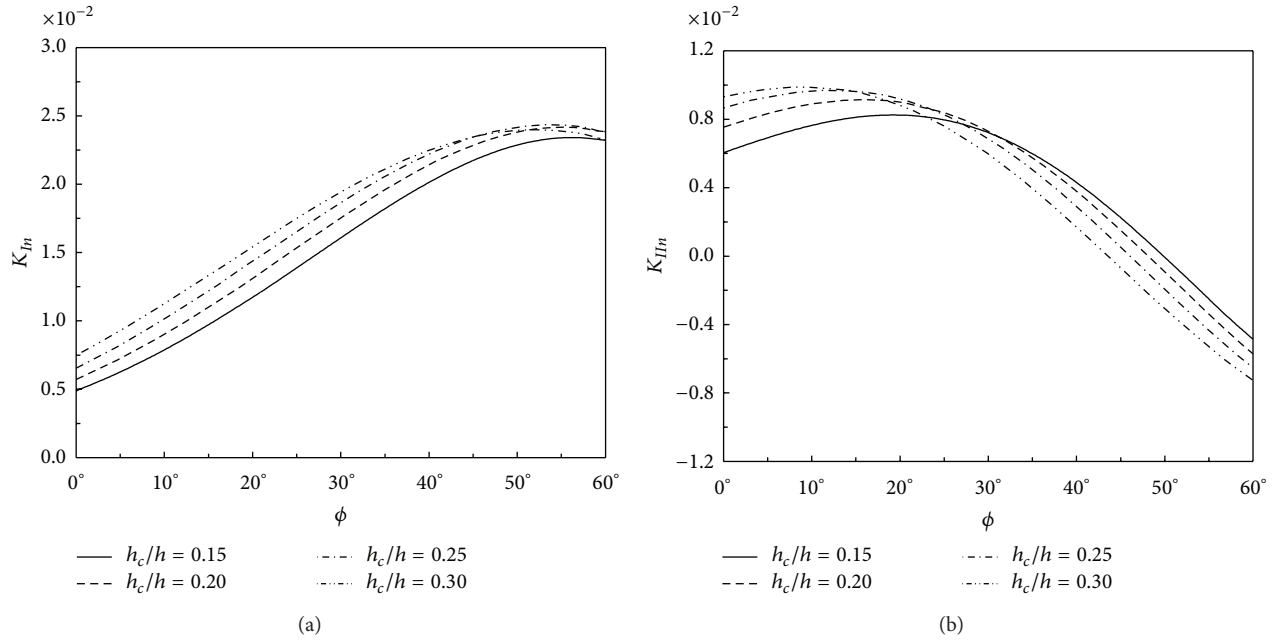

FIGURE 7: Normalized mixed-mode stress intensity factors versus inclination angle ϕ and h_c/h: (a) mode I SIFs; (b) mode II SIFs. $\gamma_x = \gamma_y = \gamma_{xy} = 2$, $\omega_{xy} = \omega_{xz} = \omega_{zx} = \omega_{zy} = 2$, $\lambda_x = \lambda_y = \lambda_z = 2$, $\kappa_x = \kappa_y = \kappa_z = 2$, $\eta_x = \eta_y = 2$, $\rho_x = \rho_y = 2$, $h/L = 0.4$, and $a/L = 0.1$.

requirement. Moreover, existence of thermal and hygroscopic effects in the examined problems makes it necessary to incorporate these loadings into the computational framework. The methods presented in this paper are shown to be effective ways of taking into account hygrothermal effects and evaluating fracture mechanics parameters and thus can be used to solve fracture and fatigue problems involving complex geometric configurations and loading conditions.

Appendix

The Entries of the Compliance, Thermal Expansion, and Moisture Expansion Matrices

The elements of the compliance, thermal expansion, and moisture expansion matrices used in (5) are derived by coordinate transformation. For the case of plane stress, these elements are given by

$$a_{11} = S_{11}, \qquad a_{12} = S_{12}, \qquad a_{16} = 2S_{16}, \tag{A.1a}$$

$$a_{22} = S_{22}, \qquad a_{26} = 2S_{26}, \qquad a_{66} = 2\left(S_{66} + S_{69}\right), \tag{A.1b}$$

$$g_1 = \alpha_1, \qquad g_2 = \alpha_2, \qquad g_{12} = 2\alpha_6. \tag{A.1c}$$

$$h_1 = \beta_1, \qquad h_2 = \beta_2, \qquad h_{12} = 2\beta_6, \tag{A.1d}$$

and for plane strain

$$a_{11} = S_{11} - \frac{S_{13}^2}{S_{33}}, \qquad a_{12} = S_{12} - \frac{S_{13}S_{23}}{S_{33}}, \qquad a_{16} = 2\left(S_{16} - \frac{S_{36}S_{13}}{S_{33}}\right), \tag{A.2a}$$

$$a_{22} = S_{22} - \frac{S_{23}^2}{S_{33}}, \qquad a_{26} = 2\left(S_{26} - \frac{S_{23}S_{36}}{S_{33}}\right), \qquad a_{66} = 2\left(S_{66} + S_{69} - \frac{2S_{36}^2}{S_{33}}\right), \tag{A.2b}$$

$$g_1 = \alpha_1 - \frac{S_{13}}{S_{33}}\alpha_3, \qquad g_2 = \alpha_2 - \frac{S_{23}}{S_{33}}\alpha_3, \qquad g_{12} = 2\left(\alpha_6 - \frac{S_{36}}{S_{33}}\alpha_3\right), \tag{A.2c}$$

$$h_1 = \beta_1 - \frac{S_{13}}{S_{33}}\beta_3, \qquad h_2 = \beta_2, \qquad h_{12} = 2\left(\beta_6 - \frac{S_{36}}{S_{33}}\beta_3\right). \tag{A.2d}$$

S_{ij}, α_i, and β_i in these equalities are derived as follows:

$$S_{11} = \frac{1}{E_x}\left(\cos^2\phi - \sin^2\phi\nu_{xy}\right)\cos^2\phi + \left(\frac{\sin^2\phi}{E_y} - \frac{\nu_{xy}}{E_x}\cos^2\phi\right)\sin^2\phi + \frac{\cos^2\phi\sin^2\phi}{G_{xy}}, \tag{A.3a}$$

$$S_{12} = \frac{1}{E_x}\left(\cos^2\phi - \sin^2\phi\nu_{xy}\right)\sin^2\phi + \left(\frac{\sin^2\phi}{E_y} - \frac{\nu_{xy}}{E_x}\cos^2\phi\right)\cos^2\phi - \frac{\cos^2\phi\sin^2\phi}{G_{xy}}, \tag{A.3b}$$

$$S_{16} = \frac{1}{E_x}\left(\nu_{xy}\sin^2\phi - \cos^2\phi\right)\cos\phi\sin\phi + \left(\frac{\sin^2\phi}{E_y} - \frac{\nu_{xy}}{E_x}\cos^2\phi\right)\cos\phi\sin\phi + \frac{1}{2G_{xy}}\left(\cos^3\phi\sin\phi - \cos\phi\sin^3\phi\right), \quad (A.3c)$$

$$S_{22} = \frac{1}{E_x}\left(\sin^2\phi - \nu_{xy}\cos^2\phi\right)\sin^2\phi + \left(\frac{\cos^2\phi}{E_y} - \frac{\nu_{xy}}{E_x}\sin^2\phi\right)\cos^2\phi + \frac{\cos^2\phi\sin^2\phi}{G_{xy}}, \quad (A.3d)$$

$$S_{26} = \frac{1}{E_x}\left(\nu_{xy}\cos^2\phi - \sin^2\phi\right)\cos\phi\sin\phi + \left(\frac{\cos^2\phi}{E_y} - \frac{\nu_{xy}}{E_x}\sin^2\phi\right)\cos\phi\sin\phi + \frac{1}{2G_{xy}}\left(\cos\phi\sin^3\phi - \cos^3\phi\sin\phi\right), \quad (A.3e)$$

$$S_{66} = \frac{1}{E_x}\left(\nu_{xy} + 1\right)\cos^2\phi\sin^2\phi + \left(\frac{\nu_{xy}}{E_x} + \frac{1}{E_y}\right)\cos^2\phi\sin^2\phi + \frac{1}{2G_{xy}}\left(\cos^4\phi + \sin^4\phi\right), \quad (A.3f)$$

$$S_{69} = \frac{1}{E_x}\left(\nu_{xy} + 1\right)\cos^2\phi\sin^2\phi + \left(\frac{\nu_{xy}}{E_x} + \frac{1}{E_y}\right)\cos^2\phi\sin^2\phi - \frac{\cos^2\phi\sin^2\phi}{G_{xy}}, \quad (A.3g)$$

$$S_{13} = -\frac{\nu_{xz}}{E_x}\cos^2\phi - \frac{\nu_{yz}}{E_y}\sin^2\phi, \quad (A.3h)$$

$$S_{23} = -\frac{\nu_{xz}}{E_x}\sin^2\phi - \frac{\nu_{yz}}{E_y}\cos^2\phi, \quad (A.3i)$$

$$S_{33} = \frac{1}{E_z}, \quad (A.3j)$$

$$S_{36} = \left(\frac{\nu_{xz}}{E_x} - \frac{\nu_{yz}}{E_y}\right)\cos\phi\sin\phi, \quad (A.3k)$$

$$\alpha_1 = \cos^2\phi\alpha_x + \sin^2\phi\alpha_y, \quad (A.3l)$$

$$\alpha_2 = \sin^2\phi\alpha_x + \cos^2\phi\alpha_y, \quad (A.3m)$$

$$\alpha_3 = \alpha_z, \quad (A.3n)$$

$$\alpha_6 = \cos\phi\sin\phi\left(\alpha_y - \alpha_x\right), \quad (A.3o)$$

$$\beta_1 = \cos^2\phi\beta_x + \sin^2\phi\beta_y, \quad (A.3p)$$

$$\beta_2 = \sin^2\phi\beta_x + \cos^2\phi\beta_y, \quad (A.3q)$$

$$\beta_3 = \beta_z, \quad (A.3r)$$

$$\beta_6 = \cos\phi\sin\phi\left(\beta_y - \beta_x\right). \quad (A.3s)$$

Nomenclature

A:	Area of the region around the crack tip
A_r:	Ratio of the relative displacements of the crack faces
a:	Crack length
a_{ij}:	Elements of the compliance matrix in the crack tip coordinate system
c:	Specific moisture concentration
c_{ij}:	Elements of the compliance matrix in the principal coordinate system
D_x, D_y:	Mass diffusivities
E_x, E_y, G_{xy}:	Elastic moduli and shear modulus
h:	Height of the orthotropic functionally graded layer
h_c:	Height of the crack mouth
J_k:	J_k-integral vector
K_{I}:	Mode I stress intensity factor
K_{II}:	Mode II stress intensity factor
k_x, k_y:	Thermal conductivities
L:	Length of the orthotropic functionally graded layer
R:	Radius of the area around the crack tip
r_a:	Radial location at which relative displacements of crack faces are calculated
T:	Temperature
u_i:	Displacement vector
W:	Mechanical strain energy density function
$\alpha_x, \alpha_y, \alpha_z$:	Thermal expansion coefficients
$\beta_x, \beta_y, \beta_z$:	Moisture expansion coefficients
δ:	Length of the region over which the line integral is evaluated analytically
$\varepsilon_{xx}, \varepsilon_{yy}, \varepsilon_{xy}$:	Total strains in the principal coordinate system
$\varepsilon_{11}, \varepsilon_{22}, \varepsilon_{12}$:	Total strains in the crack tip coordinate system
ϕ:	Crack inclination angle
$\nu_{xy}, \nu_{xz}, \nu_{zx}, \nu_{zy}$:	Poisson's ratios
$\sigma_{xx}, \sigma_{yy}, \sigma_{xy}$:	Stress components in the principal coordinate system
$\sigma_{11}, \sigma_{22}, \sigma_{12}$:	Stress components in the crack tip coordinate system.

Conflict of Interests

The authors declare that there is no conflict of interests in this study.

Acknowledgment

This work was supported by the Scientific and Technological Research Council of Turkey (TUBITAK) through Grant MAG-109M511.

References

[1] N. Noda, "Thermal stresses in functionally graded materials," *Journal of Thermal Stresses*, vol. 22, no. 4, pp. 477–512, 1999.

[2] F. Watari, A. Yokoyama, M. Omori et al., "Biocompatibility of materials and development to functionally graded implant for bio-medical application," *Composites Science and Technology*, vol. 64, no. 6, pp. 893–908, 2004.

[3] T. Nomura, H. Moriguchi, K. Tsuda, K. Isobe, A. Ikegaya, and K. Moriyama, "Material design method for the functionally graded cemented carbide tool," *International Journal of Refractory Metals and Hard Materials*, vol. 17, no. 6, pp. 397–404, 1999.

[4] D. C. Pender, N. P. Padture, A. E. Giannakopoulos, and S. Suresh, "Gradients in elastic modulus for improved contact-damage resistance—part I: The silicon nitride-oxynitride glass system," *Acta Materialia*, vol. 49, no. 16, pp. 3255–3262, 2001.

[5] Y. Liu, C. Compson, and M. Liu, "Nanostructured and functionally graded cathodes for intermediate temperature solid oxide fuel cells," *Journal of Power Sources*, vol. 138, no. 1-2, pp. 194–198, 2004.

[6] S. Sampath, H. Herman, N. Shimoda, and T. Saito, "Thermal spray processing of FGMs," *MRS Bulletin*, vol. 20, no. 1, pp. 27–31, 1995.

[7] W. A. Kaysser and B. Ilschner, "FGM research activities in Europe," *MRS Bulletin*, vol. 20, no. 1, pp. 22–26, 1995.

[8] M. A. Benatta, I. Mechab, A. Tounsi, and E. A. Adda Bedia, "Static analysis of functionally graded short beams including warping and shear deformation effects," *Computational Materials Science*, vol. 44, no. 2, pp. 765–773, 2008.

[9] S. Dag, B. Yildirim, and F. Erdogan, "Interface crack problems in graded orthotropic media: Analytical and computational approaches," *International Journal of Fracture*, vol. 130, no. 1, pp. 471–496, 2004.

[10] S. Dag, B. Yildirim, and D. Sarikaya, "Mixed-mode fracture analysis of orthotropic functionally graded materials under mechanical and thermal loads," *International Journal of Solids and Structures*, vol. 44, no. 24, pp. 7816–7840, 2007.

[11] S. Dag and A. A. Ilhan, "Mixed-mode fracture analysis of orthotropic functionally graded material coatings using analytical and computational methods," *Journal of Applied Mechanics, Transactions ASME*, vol. 75, no. 5, Article ID 051104, 2008.

[12] J.-H. Kim and G. H. Paulino, "Mixed-mode fracture of orthotropic functionally graded materials using finite elements and the modified crack closure method," *Engineering Fracture Mechanics*, vol. 69, no. 14–16, pp. 1557–1586, 2002.

[13] J.-H. Kim and G. H. Paulino, "The interaction integral for fracture of orthotropic functionally graded materials: Evaluation of stress intensity factors," *International Journal of Solids and Structures*, vol. 40, no. 15, pp. 3967–4001, 2003.

[14] B. N. Rao and S. Rahman, "A continuum shape sensitivity method for fracture analysis of orthotropic functionally graded materials," *Mechanics of Materials*, vol. 37, no. 10, pp. 1007–1025, 2005.

[15] S. Dag, E. Erhan Arman, and B. Yildirim, "Computation of thermal fracture parameters for orthotropic functionally graded materials using Jk-integral," *International Journal of Solids and Structures*, vol. 47, no. 25-26, pp. 3480–3488, 2010.

[16] ANSYS, *ANSYS Basic Analysis Procedures Guide*, Release 5.4, ANSYS Inc., Canonsburg, Pa, USA, 1997.

[17] J.-H. Kim and G. H. Paulino, "Mixed-mode J-integral formulation and implementation using graded elements for fracture analysis of nonhomogeneous orthotropic materials," *Mechanics of Materials*, vol. 35, pp. 107–128, 2003.

[18] P. Sollero and M. H. Aliabadi, "Fracture mechanics analysis of anisotropic plates by the boundary element method," *International Journal of Fracture*, vol. 64, no. 4, pp. 269–284, 1993.

[19] B. Yildirim, S. Dag, and F. Erdogan, "Three dimensional fracture analysis of FGM coatings under thermomechanical loading," *International Journal of Fracture*, vol. 132, no. 4, pp. 369–395, 2005.

Hindawi Publishing Corporation
Mathematical Problems in Engineering
Volume 2013, Article ID 250567, 11 pages
http://dx.doi.org/10.1155/2013/250567

Research Article

On Free Vibrations of Elastodynamic Problem in Rotating Non-Homogeneous Orthotropic Hollow Sphere

S. R. Mahmoud,[1,2] M. Marin,[3] S. I. Ali,[4,5] and K. S. Al-Basyouni[1]

[1] *Department of Mathematics, Science Faculty, King Abdulaziz University, P.O. Box 80203, Jeddah 21589, Saudi Arabia*
[2] *Mathematics Department, Science Faculty, Sohag University, Sohag 82524, Egypt*
[3] *Mathematics Department, Faculty of Mathematics, Brasov University, Brasov, Romania*
[4] *Department of Mathematics, Science Faculty, Hail University, Saudi Arabia*
[5] *Department of Mathematics, Science Faculty, Al-Azhar University, Nassr City, Egypt*

Correspondence should be addressed to K. S. Al-Basyouni; kalbasyouni@kau.edu.sa

Received 30 April 2013; Accepted 23 June 2013

Academic Editor: Abdelouahed Tounsi

Copyright © 2013 S. R. Mahmoud et al. This is an open access article distributed under the Creative Commons Attribution License, which permits unrestricted use, distribution, and reproduction in any medium, provided the original work is properly cited.

The effect of non-homogenity and rotation on the free vibrations for elastodynamic problem of orthotropic hollow sphere is discussed. The free vibrations are studied on the basis of the linear elasticity. The determination is concerned with the eigenvalues of the natural frequency for mixed boundary conditions. The numerical results of the frequency equations are discussed in the presence and absence of non-homogenity and rotation. The computer simulated results indicate that the influence of non-homogenity and rotation in orthotropic material is pronounced.

1. Introduction

Hollow spheres are frequently encountered in engineering industries and the corresponding free vibration problem has become one of the basic problems in elastodynamics. The analyses for transient problems of spherical structures are important and interesting research fields for engineers and scientists. The applications for non-homogeneous orthotropic hollow sphere have continuously increased in some engineering areas, including aerospace, offshore, infrared detectors, frequency control filters, chemical vessels, information storage devices, and signal processing devices. Accidental failures of rotating sphere due to flexural vibrations have frequently occurred in rotodynamic machinery such as steam turbines and gas turbines. Free vibrations of elastodynamic have many applications in a micropolar porous cubic crystal, poroelastic material [1–3]. Many applications dealing with the elastic bodies and materials, we can only mention a few recent interesting investigations [4–8], the analysis of the dynamic problems of elastic bodies is an important and interesting research field for engineers and scientists. The hollow spheres are frequently used as structural components and their vibration characteristics are obviously important for practical design. Mahmoud et al. [1, 2] discussed the effect of the rotation on plane vibrations in a transversely isotropic infinite hollow cylinder and the effect of the rotation on wave motion through cylindrical bore in a micropolar porous cubic crystal. Mahmoud [3] studied wave propagation in cylindrical poroelastic dry bones. Abd-Alla and Mahmoud [8, 9] solved magnetothermoelastic problem in rotating non-homogeneous orthotropic hollow cylindrical under the hyperbolic heat conduction model and investigated problem of radial vibrations in non-homogeneity isotropic cylinder under influence of initial stress and magnetic field. Influences of rotation, magnetic field, and gravity on Rayleigh waves in a homogeneous orthotropic elastic half space and the solution of electromechanical wave propagation are investigated by Abd-Alla et al. [10–13]. Marin et al. [14, 15] studied porous materials and nonsimple material problems addressed by the Lagrange's identity. Wang [16] studied the elastodynamic solution for an anisotropic hollow sphere. Ding et al. [17, 18] discussed elastodynamic solution of a non-homogeneous orthotropic hollow cylinder, a solution of a non-homogeneous orthotropic cylindrical shell for axisymmetric plane

strain dynamic thermo elastic problems. Inclusion of arbitrary shape in magnetoelectro-elastic composite materials has been investigated by Wang and Shen [19]. Ding et al. [20] obtained the analytical solution for the axisymmetric plane strain electroelastic dynamics of a non-homogeneous piezoelectric hollow cylinder. Hou and Leung [21] further study the corresponding problem of magnetoelectroelastic hollow cylinders. Buchanan and Liu [22] discussed an analysis of the free vibration of thick-walled isotropic toroidal shells. Yu et al. [23] investigated wave propagation in non-homogeneous magnetoelectroelastic hollow cylinders. Recently, Abd-Alla and Mahmoud [24] discussed analytical solution of wave propagation in non-homogeneous orthotropic rotating elastic media. Abd-Alla et al. [25] studied the effect of the rotation, magnetic field, and initial stress on peristaltic motion of micropolar fluid. Mahmoud [26] investigated wave propagation in piezoelectric hollow cylinder and influence of rotation and generalized magnetothermoelastic on Rayleigh waves in a granular medium under effect of initial stress and gravity field. Sharma et al. [27] studied free vibration analysis of a viscothermoelastic solid sphere. Abd-Alla et al. [28–33] investigated problem of radial and free vibrations in non-homogeneity cylinder under influence of initial stress rotation and magnetic field. Ozsahin and Taskner [34] investigated contact problem for an elastic layer on an elastic half plane. Daouadji et al. [35] studied the Free transverse vibration of the fluid-conveying single-walled carbon nanotube using nonlocal elastic theory. The present paper deals with the problem of free vibrationsof elastodynamic equations of rotating non-homogeneous and orthotropic hollow sphere. The effect of non-homogeneous and rotation in the equations of motion has been taken into account and the numerical results of the fundamental frequency equations are discussed. Comparisons are made with the result in the present and absence of non-homogeneous and rotation in cases of orthotropic hollow sphere.

2. Formulation of the Problem

Take the spherical coordinates (r, θ, φ) and consider elastodynamic problem of non-homogeneous rotating hollow sphere of inner radius a and outer radius b, as Figure 1. The stresses-strain relations for non-homogeneous spherically orthotropic material in two dimensions are in the form

$$\begin{aligned}
\sigma_{rr} &= r^{2m}\left(\alpha_{11}e_{rr} + \alpha_{12}e_{\theta\theta} + \alpha_{13}e_{\varphi\varphi}\right),\\
\sigma_{\theta\theta} &= r^{2m}\left(\alpha_{12}e_{rr} + \alpha_{22}e_{\theta\theta} + \alpha_{23}e_{\varphi\varphi}\right),\\
\sigma_{\varphi\varphi} &= r^{2m}\left(\alpha_{13}e_{rr} + \alpha_{23}e_{\theta\theta} + \alpha_{33}e_{\varphi\varphi}\right),\\
\tau_{r\theta} &= r^{2m}\alpha_{44}e_{r\theta}, \qquad \tau_{r\theta} = 0, \qquad \tau_{\theta\varphi} = 0.
\end{aligned} \tag{1a}$$

The strain-displacements relations in two dimensions are in the form

$$\begin{aligned}
e_{rr} &= \frac{\partial u_r}{\partial r}, \qquad e_{\theta\theta} = \frac{1}{r}\left(\frac{\partial u_\theta}{\partial \theta} + u_r\right),\\
e_{\varphi\varphi} &= \frac{1}{r\sin\theta}\left(u_r\sin\theta + u_\theta\cos\theta\right),
\end{aligned}$$

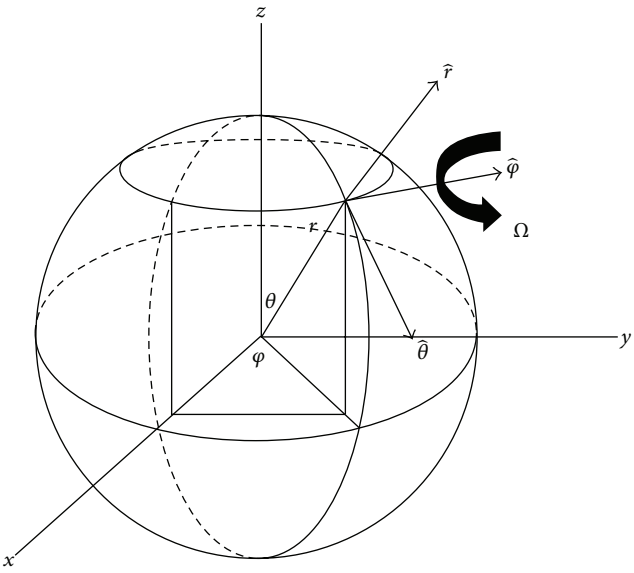

Figure 1: Problem geometry of non-homogeneous orthotropic material.

$$e_{r\theta} = \frac{1}{2}\left(\frac{1}{r}\frac{\partial u_r}{\partial \theta} + \frac{\partial u_\theta}{\partial r} - \frac{u_\theta}{r}\right), \qquad e_{r\varphi} = 0, \qquad e_{\theta\varphi} = 0. \tag{1b}$$

Substituting from (1b) into (1a) we obtain the stresses-displacements relations in two dimensions in the form

$$\begin{aligned}
\sigma_{rr} &= r^{1+2m}\left(\left(\alpha_{11} + \alpha_{13}\right)u_r + \alpha_{13}u_\theta\cot\theta + \alpha_{12}\frac{\partial u_\theta}{\partial \theta} + r\alpha_{11}\frac{\partial u_r}{\partial r}\right),\\
\sigma_{\theta\theta} &= r^{1+2m}\left(\left(\alpha_{22} + \alpha_{22}\right)u_r + \alpha_{23}u_\theta\cot\theta + \alpha_{22}\frac{\partial u_\theta}{\partial \theta} + r\alpha_{12}\frac{\partial u_r}{\partial r}\right),\\
\sigma_{\varphi\varphi} &= r^{1+2m}\left(\left(\alpha_{23} + \alpha_{33}\right)u_r + \alpha_{33}u_\theta\cot\theta + \alpha_{23}\frac{\partial u_\theta}{\partial \theta} + r\alpha_{13}\frac{\partial u_r}{\partial \theta}\right),\\
\tau_{r\theta} &= \frac{1}{2}r^{1+2m}\alpha_{44}\left(-u_\theta + \frac{\partial u_r}{\partial \theta} + r\frac{\partial u_\theta}{\partial r}\right),\\
\tau_{r\theta} &= 0, \qquad \tau_{\theta\varphi} = 0,
\end{aligned} \tag{2}$$

where u_r and u_θ are, respectively, the components of displacement in the radial and tangential directions, e_{ij} are the strain components, and σ_{ij} are the stress components. Where we have characterized the elastic constants c_{ij} and the density ρ of non-homogeneous material in the form

$$c_{ij} = \alpha_{ij}r^{2m}, \quad \rho = \rho_0 r^{2m}, \quad i, j = 1, 2, 3, \tag{3}$$

where α_{ij} and ρ_0 are the values of c_{ij} and ρ in the homogeneous case, respectively, and m is the non-homogeneous parameter. The displacement equations of motion in the rotating frame have two additional terms centripetal acceleration $\overrightarrow{\Omega} \times (\overrightarrow{\Omega} \times \overrightarrow{u}) = (-\Omega^2 u_r, -\Omega^2 u_\theta, 0)$, due to time varying motion only, where $\overrightarrow{\Omega} = (0, 0, \Omega)$, and $\overrightarrow{u} = (u_r, u_\theta, 0)$.

The elastodynamic equations of rotating non-homogeneous medium in two dimensions in the direction r, θ are given by:

$$\begin{aligned}&\frac{\partial \sigma_{rr}}{\partial r} + \frac{1}{r}\frac{\partial \tau_{r\theta}}{\partial \theta} + \frac{1}{r}\left(2\sigma_{rr} - \sigma_{\theta\theta} - \sigma_{\varphi\varphi} + \tau_{r\theta}\cot\theta\right) \\ &\quad + \rho_0 r^{2m}\Omega^2 u_r = \rho_0 r^{2m}\frac{\partial^2 u_r}{\partial t^2},\end{aligned} \tag{4}$$

$$\begin{aligned}&\frac{\partial \tau_{r\theta}}{\partial \theta} + \frac{1}{r}\frac{\partial \sigma_{\theta\theta}}{\partial \theta} + \frac{1}{r}\left(\left(\sigma_{\theta\theta} - \sigma_{\varphi\varphi}\right)\cot\theta + 3\tau_{r\theta}\right) \\ &\quad + \rho_0 r^{2m}\Omega^2 u_\theta = \rho_0 r^{2m}\frac{\partial^2 u_\theta}{\partial t^2}.\end{aligned} \tag{5}$$

Substituting from (1a), (1b), and (2) into (4) and (5), we obtain:

$$\begin{aligned}r^{-1+m}\Bigg[&2\left(a_0 + r^2\rho_0\Omega^2\right)u_r + a_1 u_\theta \cot\theta + a_2\frac{\partial u_\theta}{\partial \theta} \\ &+ \alpha_{44}\cot\theta\frac{\partial u_r}{\partial \theta} - \frac{\partial u_\theta}{\partial \theta} + \frac{\partial^2 u_r}{\partial \theta^2} + r - 2r\rho_0\frac{\partial^2 u_\theta}{\partial t^2} \\ &+ 4(1+m)\alpha_{11}\frac{\partial u_r}{\partial r} + \left(2\alpha_{13} + \alpha_{44}\right)\cot\theta\frac{\partial u_\theta}{\partial r} \\ &+ \left(2\alpha_{12} + \alpha_{44}\right)\frac{\partial^2 u_\theta}{\partial r \partial \theta} + 2\alpha_{11} r\frac{\partial^2 u_r}{\partial r^2}\Bigg] = 0,\end{aligned} \tag{6}$$

where $a_0 = \alpha_{12} + 2m\alpha_{12} + \alpha_{13} + 2m\alpha_{13} - \alpha_{22} - 2\alpha_{23} - \alpha_{33}$, $a_1 = ((2+4m)\alpha_{13} - 2(\alpha_{23} + \alpha_{33}) - \alpha_{44})$, and $a_2 = 2(\alpha_{12} + 2m\alpha_{12} - \alpha_{22} - \alpha_{23})$.

One has

$$\begin{aligned}r^{-1+m}\Bigg[&2\left(\alpha_{22} - \alpha_{33}\right)u_r\cot\theta \\ &- 2\left(a_3 - r^2\rho_0\Omega^2 + \alpha_{33}\csc^2\theta\right)u_\theta \\ &+ a_4\frac{\partial u_r}{\partial \theta} + 2\alpha_{22}\cot\theta\frac{\partial u_\theta}{\partial \theta} + \frac{\partial^2 u_\theta}{\partial \theta^2} \\ &+ r\Bigg(-2r\rho_0\frac{\partial^2 u_\theta}{\partial t^2} + 2\left(\alpha_{12} - \alpha_{13}\right)\cot\theta\frac{\partial u_r}{\partial r} \\ &\quad + 2(1+m)\alpha_{44}\frac{\partial u_\theta}{\partial r}\Bigg) \\ &+ r\left(a_5\frac{\partial^2 u_r}{\partial r \partial \theta} + r\alpha_{44}\frac{\partial^2 u_\theta}{\partial \theta^2}\right)\Bigg] = 0,\end{aligned} \tag{7}$$

where $a_3 = \alpha_{23} - \alpha_{33} + \alpha_{44} + m\alpha_{44}$, $a_4 = 2(\alpha_{22} + \alpha_{23} + \alpha_{44} + m\alpha_{44})$, and $a_5 = 2\alpha_{12} + \alpha_{44}$.

3. Solution of the Problem

By Helmohltz's theorem, the displacement vector $\overleftarrow{u}$ can be written as

$$\overleftarrow{u} = \underline{\nabla}\Phi_1 + \underline{\nabla} \wedge \overleftarrow{\Psi}, \tag{8}$$

where the two functions Φ_1 and $\overleftarrow{\Psi}$ are known in the theory of elasticity, by Lame' potentials irrotational and rotatoinal parts of the displacement vector $\overleftarrow{u}$, respectively. The displacement potentials are introduced for facilitating the solution of the field equations (5) and (6). It is possible to take only one components of the vector $\overleftarrow{\Psi}$ to be nonzero $\overleftarrow{\Psi} = (0, 0, \psi_1)$. From (8), we obtain

$$\begin{aligned}u_r &= \frac{\cot\theta\ \Psi_1 + (\partial/\partial\theta)\Psi_1}{r} + \frac{\partial \Phi_1}{\partial r}, \\ u_\theta &= -\frac{\Psi_1 - \partial\Phi_1/\partial\theta + r(\partial/\partial r)\Psi_1}{r}.\end{aligned} \tag{9}$$

Substituting from (9) into (6) and (7) and regrouping them lead to the following equations for Φ_1 and Ψ_1:

$$\begin{aligned}r^{-2+m}\Bigg[&2\left(a_1 + r^2\rho_0\Omega^2\right)h_1 - a_2\cot\theta\left(\psi_1 - \frac{\partial \phi_1}{\partial \theta} + r\frac{\partial \psi_1}{\partial r}\right) \\ &- a_3\left(\frac{\partial \psi_1}{\partial \theta} - \frac{\partial^2 \phi_1}{\partial \theta^2} + r\frac{\partial^2 \psi_1}{\partial r\,\partial \theta}\right) \\ &+ \alpha_{44}\Bigg(\cot\theta\csc^2\theta\psi_1 - \csc^2\theta\frac{\partial \psi_1}{\partial \theta} - \frac{\partial^2 \phi_1}{\partial \theta^2} \\ &\quad + 2\cot\theta\frac{\partial^2 \psi_1}{\partial \theta^2} + \frac{\partial^3 \psi_1}{\partial \theta^3} + rh_2\Bigg) \\ &- 2\rho_0 r^2\left(\cot\theta\frac{\partial^2 \psi_1}{\partial t^2} + \frac{\partial^3 \psi_1}{\partial \theta \partial t^2} + r\frac{\partial^3 \phi_1}{\partial r \partial t^2}\right) \\ &+ 4(1+m)\alpha_{11} r^2 h_3 + \left(2\alpha_{13} + \alpha_{44}\right) \\ &\times \cot\theta h_3 + \left(2\alpha_{12} + \alpha_{44}\right)h_4 \\ &+ 2\alpha_{11}\left(2\cot\theta\psi_1 + 2\frac{\partial \psi_1}{\partial \theta} + rh_5\right)\Bigg] = 0,\end{aligned} \tag{10}$$

where

$$h_1 = \left(\cot\theta\psi_1 + \frac{\partial \psi_1}{\partial \theta} + r\frac{\partial \phi_1}{\partial r}\right),$$

$$h_2 = \left(\cot\theta\frac{\partial^2 \phi_1}{\partial r \partial \theta} + \frac{\partial^2 \psi_1}{\partial r \partial \theta} + \frac{\partial^3 \phi_1}{\partial r \partial \theta^2}\right),$$

$$
\begin{aligned}
h_3 &= \left(-\left(\cot\theta\psi_1 + \left(\frac{\partial\psi_1}{\partial\theta} \right) \right.\right. \\
&\qquad \left. -r\left(\cot\theta\left(\frac{\partial\psi_1}{\partial r} \right) + \frac{\partial^2\psi_1}{\partial r\partial\theta} \right)\right) \\
&\qquad \times r^{-2} + \frac{\partial^2\phi_1}{\partial r^2} \Bigg), \\
h_3 &= \left(\psi_1 - \frac{\partial\phi_1}{\partial\theta} - r\left(\frac{\partial\psi_1}{\partial r} - \frac{\partial^2\phi_1}{\partial r\partial\theta} + r\frac{\partial^2\psi_1}{\partial r^2} \right)\right), \\
h_4 &= \left(\frac{\partial\psi_1}{\partial\theta} - \frac{\partial^2\phi_1}{\partial\theta^2} - r\left(\frac{\partial^2\psi_1}{\partial r\partial\theta} - \frac{\partial^3\phi_1}{\partial r\partial\theta^2} + r\frac{\partial^3\psi_1}{\partial r^2\partial\theta} \right)\right), \\
h_5 &= \left(-2\cot\theta\frac{\partial\psi_1}{\partial r} - 2\frac{\partial^2\psi_1}{\partial r\partial\theta} \right. \\
&\qquad \left. + r\left(\cot\theta\frac{\partial^2\psi_1}{\partial r^2} + \frac{\partial^3\psi_1}{\partial r^2\partial\theta} + r\frac{\partial^3\phi_1}{\partial r^3} \right)\right).
\end{aligned} \tag{11}
$$

One has

$$
\begin{aligned}
& r^{-2+m}\left(2\left(\alpha_{22}-\alpha_{33}\right)\cot\theta\left(\cot\theta\psi_1 + \frac{\partial\psi_1}{\partial\theta} + r\frac{\partial\phi_1}{\partial r} \right)\right. \\
&\quad + 2\left(a_3 - r^2\rho_0\Omega^2 + \alpha_{33}\csc^2\theta \right)\left(\psi_1 - \frac{\partial\phi_1}{\partial\theta} + r\frac{\partial\psi_1}{\partial r} \right) \\
&\quad + 2\left(a_6\left(-\csc^2\theta\psi_1 + \cot\theta\frac{\partial\psi_1}{\partial\theta} + \frac{\partial^2\psi_1}{\partial\theta^2} + r\frac{\partial^2\phi_1}{\partial r\partial\theta} \right)\right. \\
&\qquad - \alpha_{22}\left(\frac{\partial^2\psi_1}{\partial\theta^2} - \frac{\partial^3\phi_1}{\partial\theta^3} \right. \\
&\qquad\quad \left. + \cot\theta\left(\frac{\partial\psi_1}{\partial\theta} - \frac{\partial^2\phi_1}{\partial\theta^2} + r\frac{\partial^2\psi_1}{\partial r\partial\theta} \right)\right. \\
&\qquad\quad \left. + r\frac{\partial^3\psi_1}{\partial r\partial\theta^2} \right)\Bigg) \\
&\quad + r^2\left(2\rho_0\left(\frac{\partial^2\psi_1}{\partial t^2} - \frac{\partial^3\phi_1}{\partial\theta\partial t^2} + r\frac{\partial^3\psi_1}{\partial r\partial t^2} \right)\right. \\
&\qquad - \alpha_{44}\left(\frac{\partial^2\psi_1}{\partial\theta^2} - \frac{\partial^3\phi_1}{\partial\theta^3} + r\frac{\partial^3\psi_1}{\partial r\partial\theta^2} \right) \\
&\qquad + 2\left(\alpha_{12}-\alpha_{13}\right) \\
&\qquad \times\cot\theta\left(-\frac{h_8}{r^2} + \frac{\partial^2\phi_1}{\partial r^2} \right) - \frac{2\left(1+m\right)\alpha_{44}h_7}{r^2} \\
&\qquad \left. + \frac{\left(2\alpha_{12}+\alpha_{44}\right)h_6}{r^2} \right)\Bigg) = 0,
\end{aligned} \tag{12}
$$

where

$$
\begin{aligned}
a_6 &= \left(\alpha_{22}+\alpha_{23}+\alpha_{44}+m\alpha_{44}\right), \\
h_6 &= \left(-\cot\theta\frac{\partial\psi_1}{\partial\theta} - \frac{\partial^2\psi_1}{\partial\theta^2} + \csc^2\theta\left(\psi_1 - r\frac{\partial\psi_1}{\partial r} \right)\right. \\
&\qquad \left. + r\cot\theta\frac{\partial^2\psi_1}{\partial r\partial\theta} + r\frac{\partial^3\psi_1}{\partial r\partial\theta^2}\left(r\frac{\partial^3\phi_1}{\partial r^2\partial\theta} \right)\right), \\
h_7 &= \left(-\psi_1 + \frac{\partial\phi_1}{\partial\theta} + r\left(\frac{\partial\psi_1}{\partial r} - \frac{\partial^2\phi_1}{\partial r\partial\theta} + r\frac{\partial^2\psi_1}{\partial r^2} \right)\right), \\
h_8 &= \cot\theta\psi_1 + \frac{\partial\psi_1}{\partial\theta} - r\left(\cot\theta\frac{\partial\psi_1}{\partial r} + \frac{\partial^2\psi_1}{\partial r\partial\theta} \right).
\end{aligned} \tag{13}
$$

To study the propagation of harmonic waves, we assume a solution in the form

$$
\begin{aligned}
\Phi_1\left(r,\theta,t\right) &= \Phi_2\left(r\right)e^{i\left(\gamma\theta-\omega t\right)}, \\
\Psi_1\left(r,\theta,t\right) &= \Psi_2\left(r\right)e^{i\left(\gamma\theta-\omega t\right)}.
\end{aligned} \tag{14}
$$

Substituting from (14) into (10) and (12) and regrouping them lead to the following equations for Φ_2 and Ψ_2:

$$
\begin{aligned}
& e^{i(\gamma\theta-t\omega)}r^{-1+m}\left[2\gamma\left(a_7 - a_8\cot\theta\right)\phi_2 \right. \\
&\quad + \left(-i\gamma\left(a_9 - 2r^2\rho_0\left(\omega^2+\Omega^2\right)\right.\right. \\
&\qquad \left. + \alpha_{44}\csc^2\theta\right) \\
&\qquad + \cot\theta\left(2\left(a_{10} + r^2\rho_0\left(\omega^2+\Omega^2\right)\right)\right. \\
&\qquad\quad \left. \left. + \alpha_{44}\csc^2\theta\right)\right)\Psi_2 \\
&\quad + r\left(2\left(a_{11} + r^2\rho_0\left(\omega^2+\Omega^2\right)\right.\right. \\
&\qquad \left. \left. + i\left(a_{13}+\alpha_{44}\right)\gamma\cot\theta\right)\frac{d\Phi_2}{dr}\right. \\
&\qquad + 2\left(a_{12} + a_{13}\cot\theta\right)\frac{d\Psi_2}{dr} \\
&\qquad + r\left(4\left(1+m\right)a_{11}\frac{d^2\Phi_2}{dr^2}\right. \\
&\qquad\quad + \left(a_{14} + a_{15}\cot\theta\right)\frac{d^2\Psi_2}{dr^2} \\
&\qquad\quad \left. \left. \left. + 2r\alpha_{11}\frac{d^3\Phi_2}{dr^3} \right)\right)\right] = 0,
\end{aligned} \tag{15}
$$

where

$$\begin{aligned}
a_7 &= \left(-2m\alpha_{12} + \alpha_{22} + \alpha_{23} + \alpha_{44}\right)\gamma,\\
a_8 &= i\left(-2m\alpha_{13} + \alpha_{23} + \alpha_{33} + \alpha_{44}\right),\\
a_9 &= -2\alpha_{12} + 4m\left(\alpha_{11} - \alpha_{13}\right) - 2\alpha_{13} + 2\alpha_{23}\\
&\quad + 2\alpha_{33} + \alpha_{44}\left(-1 + \gamma^2\right),\\
a_{10} &= \alpha_{12} + 2m\left(-\alpha_{11} + \alpha_{12}\right) + \alpha_{13} - \alpha_{22}\\
&\quad - \alpha_{23} + \alpha_{44} - \alpha_{44}\gamma^2,\\
a_{11} &= \alpha_{12} + 2m\alpha_{12} + \alpha_{13} + 2m\alpha 13 - \alpha_{22}\\
&\quad - 2\alpha_{23} - \alpha_{33} - \left(\alpha_{12} + \alpha_{44}\right)\gamma^2,\\
a_{12} &= i\left(2m\alpha_{11} - 2\alpha_{12} - 2m\alpha_{12} + \alpha_{22} + \alpha_{23}\right)\gamma,\\
a_{13} &= 2\left(2m\alpha_{11} - 2\alpha_{13} - 2m\alpha_{13} + \alpha_{23} + \alpha_{33}\right),\\
a_{14} &= i\left(2\alpha_{11} - 2m\alpha_{12} - \alpha_{44}\right)\gamma + \left(2\alpha_{11} - 2\alpha_{13} - \alpha_{44}\right),\\
a_{15} &= \left(2m\alpha_{11} - 2\alpha_{13} - \alpha_{44}\right).
\end{aligned} \tag{16}$$

One has

$$\begin{aligned}
e^{i(\gamma\theta - t\omega)} r^{-1+m} \Bigg[& -i\gamma\left(a_{16} + \alpha_{44}\left(4 + 4m + r^2\gamma^2\right)\right.\\
&\quad - 2r^2\rho_0\left(\omega^2 + \Omega^2\right) - 2i\alpha_{22}\gamma\cot\theta\\
&\quad \left. + 2\alpha 33\csc^2\theta\right)\Phi_2 + 2\left(\alpha_{12} - \alpha_{13}\right)\Psi_2\\
&+ \left(a_{17} + \left(-1 - 2m + r^2\right)\alpha_{44}\gamma^2\right.\\
&\quad - 2\alpha_{23}\left(-1 + \gamma^2\right) - 2r^2\rho_0\left(\omega^2 + \Omega^2\right)\\
&\quad \left. -a_{18}\cot\theta + a_{19}\csc^2\theta\right)\Psi_2\\
&+ r\left(2i\left(a_{20} - i\left(\alpha_{22} - \alpha_{23}\right)\cot\theta\right)\frac{d\Phi_2}{dr}\right.\\
&\quad - \left(a_{21} + 2r^2\rho_0\omega^2 + 2r^2\rho_0\Omega^2\right.\\
&\quad \left. -a_{22}\cot\theta + a_{23}\csc^2\theta\right)\frac{d\Psi_2}{dr}\\
&+ r\left(i\left(2\alpha_{12} + \alpha_{44}\right)\gamma\right.\\
&\quad \left. +2\left(\alpha_{12} - \alpha_{13}\right)\cot\theta\right)\frac{d^2\Phi_2}{dr^2}\\
&\left. -2\left(1 + m\right)\alpha_{44} r\frac{d^2\Psi_2}{dr^2}\right)\Bigg] = 0,
\end{aligned} \tag{17}$$

where

$$\begin{aligned}
a_{16} &= 2\alpha_{23} - 2\alpha_{33} + 2\alpha_{22}\gamma^2,\\
a_{17} &= -2\alpha_{22} + 4\left(1 + m\right)\alpha_{44} + 2\alpha_{12}\gamma^2,\\
a_{18} &= i\left(4\alpha_{12} - 2\left(\alpha_{13} + \alpha_{22} + \alpha_{23} - \alpha_{33}\right)\right.\\
&\quad \left. - \left(1 + 2m\right)\alpha_{44}\right)\gamma,\\
a_{19} &= \left(2\alpha_{13} - 2\alpha_{23} - \alpha_{44} - 2m\alpha_{44}\right),\\
a_{20} &= \left(\alpha_{22} + \alpha_{23} + 2\left(1 + m\right)\alpha_{44}\right)\gamma,\\
a_{21} &= -2\left(\alpha_{13} + \alpha_{23} - \alpha_{33}\right) - 2\alpha_{22}\gamma^2\\
&\quad + \alpha_{44}\gamma^2 - r^2\alpha_{44}\gamma^2 + 2\alpha_{12}\left(1 + \gamma^2\right),\\
a_{22} &= i\left(4\alpha_{12} - 2\left(\alpha_{13} + \alpha_{22}\right) + \alpha_{44}\right)\gamma,\\
a_{23} &= \left(2\alpha_{13} - 2\alpha_{33} + \alpha_{44}\right),
\end{aligned} \tag{18}$$

where γ is the wave number, ω is the angular frequency, $\gamma = 2\pi/\lambda$, and λ is the wavelength. Substituting from (14) into (15) and (17) and after regrouping them leads to two independent equations for Φ_2 and Ψ_2; these equations are called spherical Bessel's equations whose general solution is in the form

$$\begin{aligned}
\Phi_2\left(r\right) &= A_1 j_n\left(kr\right) + A_2 y_n\left(kr\right),\\
\Psi_2\left(r\right) &= A_3 j_n\left(k_1 r\right) + A_4 y_n\left(k_1 r\right),
\end{aligned} \tag{19}$$

where

$$\begin{aligned}
n\left(n+1\right) &= \frac{\left(\alpha_{22} + \alpha_{33} + 2\alpha_{23}\right) - \left(2m + 1\right)\left(\alpha_{12} + \alpha_{13}\right)}{\alpha_{11}}\\
&\quad + m\left(m + 1\right),\\
k^2 &= \frac{\alpha_{44} + \rho_0\omega^2}{\alpha_{11}} + L_1 - \gamma^2\left(\alpha_{11} - 2\alpha_{43}\right) + \frac{\rho_0}{\alpha_{11}}\left(\Omega^2 + \omega^2\right),\\
k_1^2 &= \frac{\rho_0}{\alpha_{11}}\left(\Omega^2 + \omega^2\right) + \frac{\left(L_2 + \rho_0\omega^2\right)}{\alpha_{11}}\\
&\quad + 2\gamma^2\left(\alpha_{12} + 2m\alpha_{12} - \alpha_{22} - \alpha_{23}\right),\\
L_1 &= \left(\left(2 + 4m\right)\alpha_{13} - 2\left(\alpha_{23} + \alpha_{33}\right) - m\alpha_{44}\right),\\
L_2 &= 2\alpha_{12} + 2m\alpha_{13} - \alpha_{22} - 2\alpha m_{23} - \alpha_{33},
\end{aligned} \tag{20}$$

where A_1, A_2, A_3, and A_4 are arbitrary constants and $j_n(kr)$ and $y_n(kr)$ denote spherical Bessel's functions of the first and second kind of order n, respectively, which are defined in terms of Bessel's function as follows: $j_n(kr) = \sqrt{\pi/2kr}J_{n+1/2}(kr)$, $y_n(kr) = \sqrt{\pi/2kr}Y_{n+1/2}(kr)$. From (19) and (14) we get the following solutions for Φ_1 and Ψ_1 as follows:

$$\begin{aligned}
\Phi_1\left(r,\theta,t\right) &= e^{i\left(\gamma\theta - wt\right)}\left[A_1 j_n\left(kr\right) + A_2 y_n\left(kr\right)\right],\\
\Psi_1\left(r,\theta,t\right) &= e^{i\left(\gamma\theta - wt\right)}\left[A_3 j_n\left(k_1 r\right) + A_4 y_n\left(k_1 r\right)\right].
\end{aligned} \tag{21}$$

Substituting from (21) into (9), we obtain the final solution of the displacement components in the following form:

$$u_r = \frac{1}{r}e^{i(\gamma\theta - wt)}\left[A_1\left\{nj_n(kr) - rkj_{n+1}(kr)\right\}\right.$$
$$+ A_2\left\{ny_{n+1}(kr) + y_{n+1}(kr)\right\}$$
$$\left.+A_3\left(i\gamma + \cot\theta\right)j_n(k_1r) + A_4y_{n+1}(k_1r)\right],$$
$$u_\theta = \frac{1}{r}e^{i(\gamma\theta - wt)}\left[A_1i\gamma j_n(kr) + A_2y_n(kr)\right.$$
$$- A_3\left\{(1+n)\,j_n(k_1r) + k_1rj_{n+1}(k_1r)\right\}$$
$$\left.-A_4\left\{(1+n)\,y_n(k_1r) + rk_1y_{n+1}(k_1r)\right\}\right]. \tag{22}$$

Substituting from (22) into (2), we obtain the final solution of the stress components in the following form:

$$\sigma_{rr} = r^{-2+2m}e^{i(\gamma\theta - t\omega)}$$
$$\times\left[A_1\left\{\left((\alpha_{12}+\alpha_{13})\,n\right.\right.\right.$$
$$+\alpha_{11}\left((-1+n)\,n - k^2r^2\right) - \alpha_{12}\gamma^2$$
$$\left.+i\alpha_{13}\gamma\cot\theta\right)j_n(kr)$$
$$\left.+\left(2\alpha_{11} - \alpha_{12} - \alpha_{13}\right)krj_{n+1}(kr)\right\}$$
$$+A_3\left\{\left(i\left(\alpha_{13} + \alpha_{11}(-1+n) - \alpha_{12}n\right)\gamma\right.\right.$$
$$+\left(\alpha_{12} + \alpha_{11}(-1+n)\right.$$
$$\left.-\alpha_{13}n\right)\cot\theta\Big)\,j_n(k_1r)$$
$$+k_1r\left(-i\left(\alpha_{11} - \alpha_{12}\right)\gamma + \left(-\alpha_{11} + \alpha_{13}\right)\right.$$
$$\left.\left.\times\cot\theta\right)j_{n+1}(k_1r)\right\}$$
$$+A_2\left\{\left(\left(\alpha_{12}+\alpha_{13}\right)n + \alpha_{11}\left((-1+n)\,n - k^2r^2\right)\right.\right.$$
$$\left.-\alpha_{12}\gamma^2 + i\alpha_{13}\gamma\cot\theta\right)y_n(kr)$$
$$\left.+\left(2\alpha_{11} - \alpha_{12} - \alpha_{13}\right)kry_{n+1}(kr)\right\}$$
$$+A_4\left\{\left(i\left(\alpha_{13} + \alpha_{11}(-1+n) - \alpha_{12}n\right)\gamma\right.\right.$$
$$+\left(\alpha_{12} + \alpha_{11}(-1+n)\right.$$
$$\left.-\alpha_{13}n\right)\cot\theta\Big)\,y_n(k_1r)$$
$$+k_1r\left(-i\left(\alpha_{11} - \alpha_{12}\right)\gamma\right.$$
$$\left.\left.+\left(-\alpha_{11} + \alpha_{13}\right)\cot\theta\right)y_{n+1}(k_1r)\right\}\Big], \tag{23a}$$

$$\sigma_{\theta\theta} = r^{-2+2m}e^{i(\gamma\theta - t\omega)}$$
$$\times\left[A_1\left\{\left(\left(\alpha_{22}+\alpha_{23}\right)n\right.\right.\right.$$
$$+\alpha_{12}\left((-1+n)\,n - k^2r^2\right) - \alpha_{22}\gamma^2$$
$$\left.+i\alpha_{23}\gamma\cot\theta\right)j_n(kr)$$
$$+\left(2\alpha_{12} - \alpha_{22} - \alpha_{23}\right)krj_{n+1}(kr)\Big\}$$
$$+A_3\left\{\left(i\left(\alpha_{23} + \alpha_{12}(-1+n) - \alpha_{22}n\right)\gamma\right.\right.$$
$$+\left(\alpha_{22} + \alpha_{12}(-1+n)\right.$$
$$\left.-\alpha_{23}n\right)\cot\theta\Big)\,j_n(k_1r)$$
$$\left.+k_1r\left(-i\left(\alpha_{12} - \alpha_{22}\right)\gamma + \left(-\alpha_{12} + \alpha_{23}\right)\right.\right.$$
$$\left.\left.\times\cot\theta\right)j_{n+1}(k_1r)\right\}$$
$$+A_2\left\{\left(\left(\alpha_{22}+\alpha_{23}\right)n + \alpha_{12}\left((-1+n)\,n - k^2r^2\right)\right.\right.$$
$$\left.-\alpha_{22}\gamma^2 + i\alpha_{23}\gamma\cot\theta\right)y_n(kr)$$
$$\left.+\left(2\alpha_{12} - \alpha_{22} - \alpha_{23}\right)kry_{n+1}(kr)\right\}$$
$$+A_4\left\{\left(i\left(\alpha_{23} + \alpha_{12}(-1+n) - \alpha_{22}n\right)\gamma\right.\right.$$
$$+\left(\alpha_{22} + \alpha_{12}(-1+n)\right.$$
$$\left.-\alpha_{23}n\right)\cot\theta\Big)\,y_{n+1}(k_1r)$$
$$+k_1r\left(-i\left(\alpha_{12} - \alpha_{22}\right)\gamma\right.$$
$$\left.\left.+\left(-\alpha_{12} + \alpha_{23}\right)\cot\theta\right)y_{n+1}(k_1r)\right\}\Big], \tag{23b}$$

$$\sigma_{\varphi\varphi} = r^{-2+2m}e^{i(\gamma\theta - t\omega)}$$
$$\times\left[A_1\left\{\left(\left(\alpha_{23}+\alpha_{33}\right)n\right.\right.\right.$$
$$+\alpha_{13}\left((-1+n)\,n - k^2r^2\right) - \alpha_{23}\gamma^2$$
$$\left.+i\alpha_{33}\gamma\cot\theta\right)j_n(kr)$$
$$+\left(2\alpha_{13} - \alpha_{23} - \alpha_{33}\right)krj_{n+1}(kr)\Big\}$$
$$+A_3\left\{\left(i\left(\alpha_{33} + \alpha_{13}(-1+n) - \alpha_{23}n\right)\gamma\right.\right.$$
$$+\left(\alpha_{23} + \alpha_{13}(-1+n)\right.$$
$$\left.-\alpha_{33}n\right)\cot\theta\Big)\,j_n(k_1r)$$
$$\left.+k_1r\left(-i\left(\alpha_{13} - \alpha_{23}\right)\gamma + \left(-\alpha_{13} + \alpha_{33}\right)\right.\right.$$
$$\left.\left.\times\cot\theta\right)j_{n+1}(k_1r)\right\}$$
$$+A_2\left\{\left(\left(\alpha_{23}+\alpha_{33}\right)n + \alpha_{13}\left((-1+n)\,n - k^2r^2\right)\right.\right.$$
$$\left.-\alpha_{23}\gamma^2 + i\alpha_{33}\gamma\cot\theta\right)y_n(kr)$$
$$\left.+\left(2\alpha_{13} - \alpha_{23} - \alpha_{33}\right)kry_{n+1}(kr)\right\}$$
$$+A_4\left\{\left(i\left(\alpha_{33} + \alpha_{13}(-1+n) - \alpha_{23}n\right)\gamma\right.\right.$$
$$+\left(\alpha_{23} + \alpha_{13}(-1+n)\right.$$
$$\left.-\alpha_{33}n\right)\cot\theta\Big)\,y_n(k_1r)$$
$$+k_1r\left(-i\left(\alpha_{13} - \alpha_{23}\right)\gamma\right.$$
$$\left.\left.+\left(-\alpha_{13} + \alpha_{33}\right)\cot\theta\right)y_{n+1}(k_1r)\right\}\Big], \tag{23c}$$

$$\tau_{r\theta} = -\frac{r^{-2+2m}}{2}\alpha_{44}e^{i(\gamma\theta - t\omega)} \times \left[A_1\left\{-2i\left(-1+n\right)\gamma j_n\left(kr\right) + 2ikr\gamma j_{n+1}\left(kr\right)\right\} + A_3\left\{\left(-2+\left(-1+n\right)n - k_1^2r^2 + \gamma^2 - i\gamma\cot\theta + \csc^2\theta\right) j_n\left(k_1r\right) + 2k_1rj_{n+1}\left(k_1r\right)\right\} - A_2\left\{2i\left(-1+n\right)\gamma y_n\left(kr\right) + 2ikr\gamma y_{n+1}\left(kr\right)\right\} + A_4\left\{\left(-2+\left(-1+n\right)n - k_1^2r^2 + \gamma^2 - i\gamma\cot\theta + \csc^2\theta\right) y_n\left(k_1r\right) + 2k_1ry_{n+1}\left(k_1r\right)\right\}\right]. \tag{23d}$$

From the solutions of elastic wave equations, the systems of equations depend on non-homogenity, rotation and the frequency.

4. Boundary Conditions and Frequency Equation

The solutions of the hollow sphere with different boundary conditions are performed, the mixed boundary conditions which consist of two kinds of boundary conditions, the inner surface fixed and the outer surface free, that is,

$$u_r = u_\theta = 0, \quad r = a, \qquad \sigma_{rr} = \tau_{r\theta} = 0, \quad r = b. \tag{24}$$

In this case, from (22), (23a), (23b), (23c), (23d), and (24) we have

$$A_1\left\{nj_n\left(ka\right) - akj_{n+1}\left(ka\right)\right\} + A_2\left\{ny_{n+1}\left(ka\right) + y_{n+1}\left(ka\right)\right\} + A_3\left(i\gamma + \cot\theta\right) j_n\left(k_1a\right) + A_4y_{n+1}\left(k_1a\right) = 0, \tag{25a}$$

$$A_1i\gamma j_n\left(ka\right) + A_2y_n\left(ka\right) - A_3\left\{\left(1+n\right) j_n\left(k_1a\right) + k_1aj_{n+1}\left(k_1a\right)\right\} - A_4\left\{\left(1+n\right) y_n\left(k_1a\right) + ak_1y_{n+1}\left(k_1a\right)\right\} = 0, \tag{25b}$$

$$A_1\left\{\left(\left(\alpha_{12}+\alpha_{13}\right)n + \alpha_{11}\left(\left(-1+n\right)n - k^2b^2\right) - \alpha_{12}\gamma^2 + i\alpha_{13}\gamma\cot\theta\right) j_n\left(kb\right) + \left(2\alpha_{11} - \alpha_{12} - \alpha_{13}\right)kbj_{n+1}\left(kb\right)\right\} + A_2\left\{\left(\left(\alpha_{12}+\alpha_{13}\right)n + \alpha_{11}\left(\left(-1+n\right)n - k^2b^2\right) - \alpha_{12}\gamma^2 + i\alpha_{13}\gamma\cot\theta\right) y_n\left(kb\right) + \left(2\alpha_{11} - \alpha_{12} - \alpha_{13}\right)k\ by_{n+1}\left(kb\right)\right\} + A_3\left\{\left(i\left(\alpha_{13} + \alpha_{11}\left(-1+n\right) - \alpha_{12}n\right)\gamma + \left(\alpha_{12} + \alpha_{11}\left(-1+n\right) - \alpha_{13}n\right) \times \cot\theta\right) j_n\left(k_1b\right) + k_1b\left(-i\left(\alpha_{11} - \alpha_{12}\right)\gamma + \left(-\alpha_{11} + \alpha_{13}\right) \times\cot\theta\right) j_{n+1}\left(k_1b\right)\right\} + A_4\left\{\left(i\left(\alpha_{13} + \alpha_{11}\left(-1+n\right) - \alpha_{12}n\right)\gamma + \left(\alpha_{12} + \alpha_{11}\left(-1+n\right) - \alpha_{13}n\right) \times \cot\theta\right) y_n\left(k_1b\right) + k_1b\left(-i\left(\alpha_{11} - \alpha_{12}\right)\gamma + \left(-\alpha_{11} + \alpha_{13}\right) \times \cot\theta\right) y_{n+1}\left(k_1b\right)\right\} = 0, \tag{25c}$$

$$A_1\left\{-2i\left(-1+n\right)\gamma j_n\left(kb\right) + 2ikb\gamma j_{n+1}\left(kb\right)\right\} - A_2\left\{2i\left(-1+n\right)\gamma y_n\left(kb\right) + 2ikb\gamma y_{n+1}\left(kb\right)\right\} + A_3\left\{\left(-2+\left(-1+n\right)n - k_1^2b^2 + \gamma^2 - i\gamma\cot\theta + \csc^2\theta\right) j_n\left(k_1b\right) + 2k_1bj_{n+1}\left(k_1b\right)\right\} + A_4\left\{\left(-2+\left(-1+n\right)n - k_1^2b^2 + \gamma^2 - i\gamma\cot\theta + \csc^2\theta\right) y_n\left(k_1b\right) + 2k_1by_{n+1}\left(k_1b\right)\right\}. \tag{25d}$$

From (25a), (25b), (25c), and (25d) we get the following frequency equation:

$$\left|a_{ij}\right| = 0, \quad i, j = 1, 2, 3, 4, \tag{26}$$

where the coefficients a_{ij} are functions of rotation, non-homogenity, frequency, the radius r. Finally, we confined our attention to make these quantities dimensionless to simplify the calculation of the eigenvalues of equations. The coefficients a_{ij} are

$$a_{11} = nj_n\left(ka\right) - rkj_{n+1}\left(ka\right),$$
$$a_{12} = ny_{n+1}\left(ka\right) + y_{n+1}\left(ka\right),$$
$$a_{13} = \left(i\gamma + \cot\theta\right) j_n\left(k_1a\right),$$
$$a_{14} = y_{n+1}\left(k_1a\right), \qquad a_{21} = i\gamma j_n\left(ka\right),$$
$$a_{22} = y_n\left(ka\right),$$
$$a_{23} = -\left(1+n\right) j_n\left(k_1a\right) - k_1aj_{n+1}\left(k_1a\right),$$
$$a_{24} = \left(1+n\right) y_n\left(k_1a\right) + ak_1y_{n+1}\left(k_1a\right),$$
$$a_{31} = \left(\left(\alpha_{12}+\alpha_{13}\right)n + \alpha_{11}\left(\left(-1+n\right)n - k^2b^2\right) - \alpha_{12}\gamma^2 + i\alpha_{13}\gamma\cot\theta\right) j_n\left(kb\right) + \left(2\alpha_{11} - \alpha_{12} - \alpha_{13}\right)kbj_{n+1}\left(kb\right),$$

$$
\begin{aligned}
a_{32} &= \left(\left(\alpha_{12}+\alpha_{13}\right) n + \alpha_{11}\left((-1+n)\, n - k^2 b^2\right) \right. \\
&\quad \left. - \alpha_{12}\gamma^2 + i\alpha_{13}\gamma\cot\theta \right) y_n\left(kb\right) \\
&\quad + \left(2\alpha_{11} - \alpha_{12} - \alpha_{13}\right) k\, b y_{n+1}\left(kb\right), \\
a_{33} &= \{ \left(i\left(\alpha_{13} + \alpha_{11}\left(-1+n\right) - \alpha_{12} n\right)\gamma \right. \\
&\quad + \left(\alpha_{12} + \alpha_{11}\left(-1+n\right) - \alpha_{13} n\right) \\
&\quad \left. \times\cot\theta \right) j_n\left(k_1 b\right) \\
&\quad + k_1 b \left(-i\left(\alpha_{11} - \alpha_{12}\right)\gamma + \left(-\alpha_{11} + \alpha_{13}\right)\right. \\
&\quad \left. \times\ \cot\theta \right) j_{n+1}\left(k_1 b\right) \}, \\
a_{34} &= \left(i\left(\alpha_{13} + \alpha_{11}\left(-1+n\right) - \alpha_{12} n\right)\gamma \right. \\
&\quad + \left(\alpha_{12} + \alpha_{11}\left(-1+n\right) - \alpha_{13} n\right) \\
&\quad \left. \times\ \cot\theta \right) y_n\left(k_1 b\right) \\
&\quad + k_1 b \left(-i\left(\alpha_{11} - \alpha_{12}\right)\gamma \right. \\
&\quad \left. + \left(-\alpha_{11} + \alpha_{13}\right)\cot\theta \right) y_{n1+1}\left(k_1 b\right), \\
a_{41} &= -\,2i\left(-1+n\right)\gamma j_n\left(kb\right) + 2ikb\gamma j_{n+1}\left(kb\right), \\
a_{42} &= -\,2i\left(-1+n\right)\gamma y_n\left(kb\right) - 2ikb\gamma y_{n+1}\left(kb\right), \\
a_{43} &= \left(-2 + \left(-1+n\right) n - k_1^2 b^2 + \gamma^2 \right. \\
&\quad \left. - i\gamma\cot\theta + \csc^2\theta \right) j_n\left(k_1 b\right) \\
&\quad + 2k_1 b j_{n+1}\left(k_1 b\right), \\
a_{44} &= \left(-\,2 + \left(-1+n\right) n - k_1^2 b^2 + \gamma^2 \right. \\
&\quad \left. -i\gamma\cot\theta + \csc^2\theta \right) y_n\left(k_1 b\right) \\
&\quad + 2k_1 b y_{n+1}\left(k_1 b\right).
\end{aligned}
\tag{27}
$$

5. Numerical Results and Discussion

To examine the influence of non-homogenity, rotation and variation of the non-dimensional frequency in hollow sphere with the radius r have been shown graphically. Free vibrations have been studied using a half-interval method. The frequency equations have been obtained under the effects of non-homogenity and rotation. It is found that the non-dimensional frequency increases with the increases of radius r for all cases. As an illustrative example, the elastic constants for an orthotropic non-homogeneous material from Hearmon [36, 37] are $\alpha_{23} = 3.945$, $\alpha_{11} = 3.198$, $\alpha_{33} = 2.7951$, $\alpha_{13} = 2.310$, $\alpha_{12} = 0.713$, $\alpha_{22} = 4.560$, and $\rho = 2.680$. Numerical calculations are carried out for the displacement and the stress components along the r-direction at different values of the rotation $\Omega = 0.0, 1.3, 2.6$ in the case of non-homogeneous material and orthotropic material. Figure 2 shows the response histories of the non-dimensional frequencies with the radius r for rotating hollow sphere $\Omega = 2.5$. With the effect of various values of non-homogeneous $m = 0.0, 0.5, 0.9$ in the case of orthotropic material, it can be found that the distribution of the non-dimensional frequencies is increasing as the increase in the radius r and the non-dimensional frequencies are increasing with the increase in the non-homogenity. Figure 3 shows the variation of the non-dimensional frequencies with the radius r for hollow sphere with the effect of various values of rotation $\Omega = 0.0, 1.3, 2.6$ in the case of non-homogeneous $m = 0.65$ orthotropic

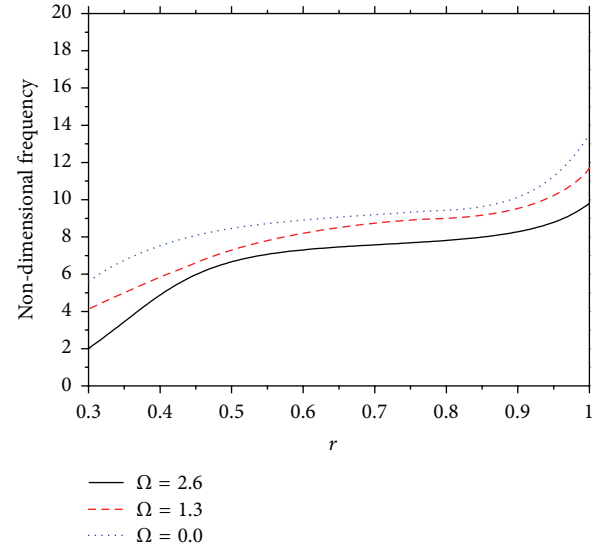

Figure 2: Variation of non-dimensional frequency versus the radius r, for the various values of rotation Ω and non-homogeneous $m = 0.65$ (inner fixed surfaces and outer free surfaces) and $n = 0$.

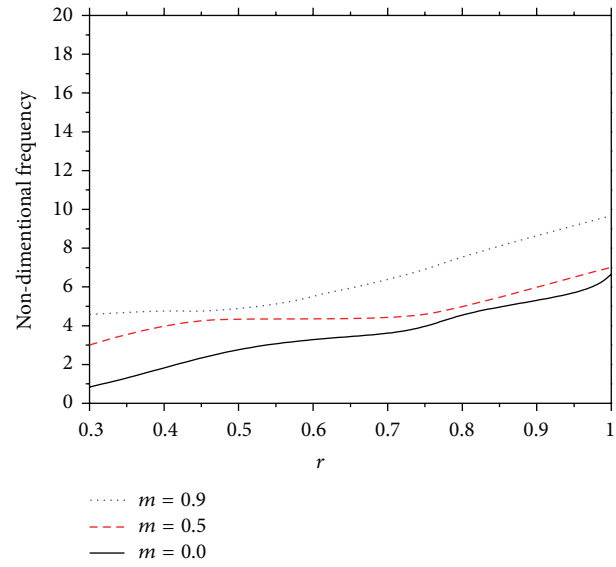

Figure 3: Variation of non-dimensional frequency versus the radius r, for the various values of non-homogeneous m and rotation $\Omega = 2.5$ (inner fixed surfaces and outer free surfaces) and $n = 0$.

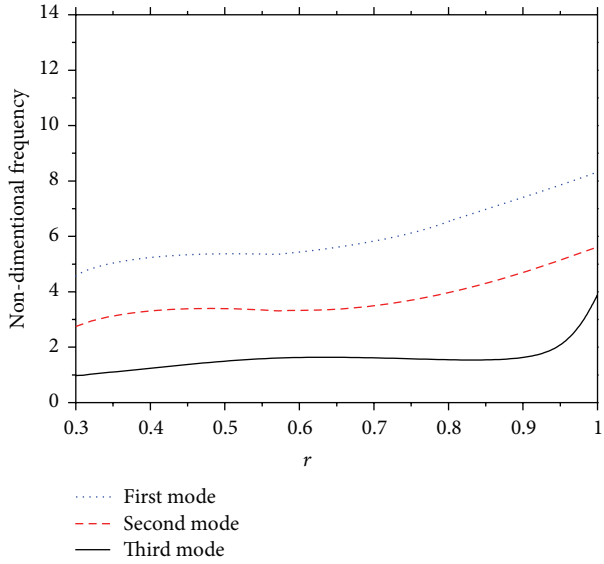

Figure 4: Variation of non-dimensional frequency (three modes) versus the radius r of the hollow sphere at rotation $\Omega = 2.5$ and non-homogeneous $m = 0.65$ (inner fixed surfaces and outer free surfaces) and $n = 0$.

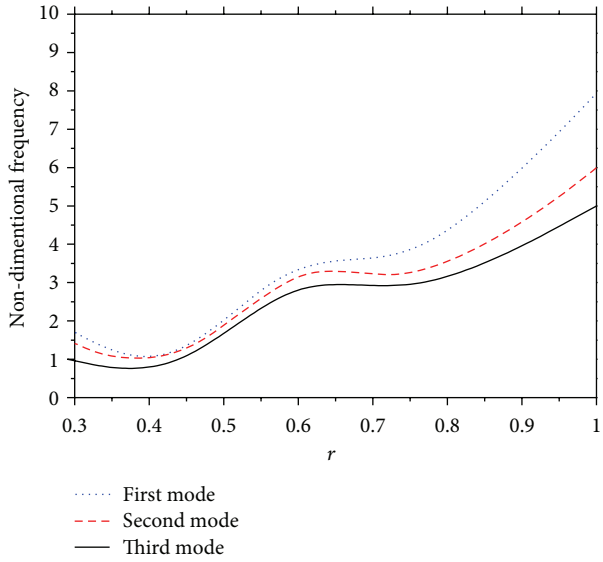

Figure 5: Variation of non-dimensional frequency (three modes) versus the radius r of the hollow sphere at absent of rotation $\Omega = 0.0$ and non-homogeneous $m = 0.5$ (inner fixed surfaces and outer free surfaces) and $n = 0$.

material. It can be found that the distribution of the non-dimensional frequencies is increasing with the increase in the radius r, but the non-dimensional frequencies are increasing with the decrease in the rotation. Figure 4 shows the response histories of the non-dimensional frequencies (the first mode, the second mode, and the third mode) with the radius r at value of non-homogeneous $m = 0.65$ and the rotation $\Omega = 2.5$. It can be found that the distribution of the non-dimensional frequencies is increasing with the increase in the

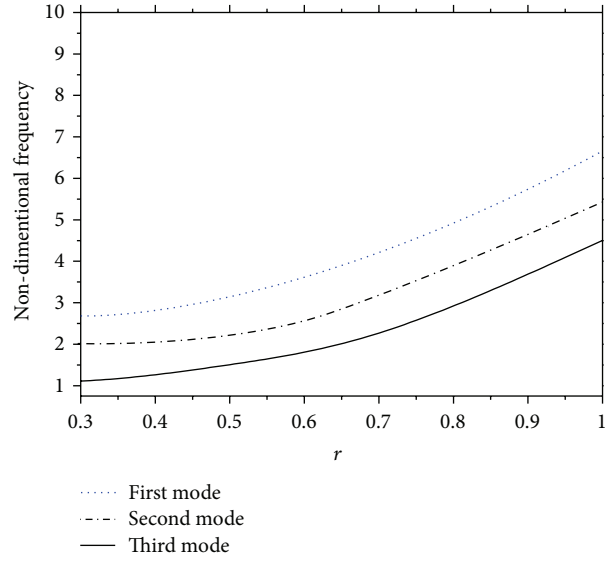

Figure 6: Variation of non-dimensional frequency (three modes) versus the radius r of the hollow sphere at rotation $\Omega = 2.5$ and non-homogeneous $m = 0.0$ (inner fixed surfaces and outer free surfaces) and $n = 0$.

radius r, for various boundary conditions, inner fixed surface, and outer free surface. Figure 5 shows the variation of the non-dimensional frequencies (three modes) with the radius r for orthotropic sphere in the absence of rotation $\Omega = 0.0$ in the case of non-homogeneous material $m = 0.65$. We observed that the frequency is increasing with the increase of the radius r in the case of free traction surfaces, $n = 0$. Figure 6 shows the first three modes of non-dimensional frequency for homogeneous $m = 0.0$ orthotropic material in presence of the rotation $\Omega = 2.5$. We observed that the frequency is increasing with the increase in the radius r in the case of orthotropic homogeneous hollow sphere more than in the case non-homogeneous hollow sphere. It is evident; non-homogenity, rotation, and orthotropic have a significant influence on non-dimensional frequencies.

6. Conclusion

The effect of non-homogenity and rotation on surface wave dispersion in elastodynamic problem in orthotropic hollow sphere is studied. The vibration of sphere with the mixed surfaces boundary conditions is evaluated. The natural frequencies (eigenvalues) are calculated and compared with those reported in the absence and presence of non-homogenity and rotation. The effects of non-homogenity and rotation on the natural frequencies are shown graphically.

Acknowledgment

This work was funded by the Deanship of Scientific Research (DSR), King Abdulaziz University, Jeddah, under grant. The authors, therefore, acknowledge with thanks the DSR technical and financial support.

References

[1] S. R. Mahmoud, A. M. Abd-Alla, and N. A. Al-Shehri, "Effect of the rotation on plane vibrations in a transversely isotropic infinite hollow cylinder," *International Journal of Modern Physics B*, vol. 25, no. 26, pp. 3513–3528, 2011.

[2] S. R. Mahmoud, A. M. Abd-Alla, and M. A. El-Sheikh, "Effect of the rotation on wave motion through cylindrical bore in a micropolar porous medium," *International Journal of Modern Physics B*, vol. 25, no. 20, pp. 2713–2728, 2011.

[3] S. R. Mahmoud, "Wave propagation in cylindrical poroelastic dry bones," *Applied Mathematics & Information Sciences*, vol. 4, no. 2, pp. 209–226, 2010.

[4] M. A. Sumbatyan, V. Tibullo, and V. Zampoli, "Reconstruction of round voids in the elastic half-space: antiplane problem," *Mathematical Problems in Engineering*, vol. 2006, Article ID 49797, 12 pages, 2006.

[5] V. Seremet, G. Bonnet, and T. Speianu, "New poisson's type integral formula for thermoelastic half-Space," *Mathematical Problems in Engineering*, vol. 2009, Article ID 284380, 18 pages, 2009.

[6] S. R. Mahmoud, "Effect of rotation and magnetic field through porous medium on peristaltic transport of a Jeffrey fluid in tube," *Mathematical Problems in Engineering*, vol. 2011, Article ID 971456, 13 pages, 2011.

[7] J. Rungamornrat and P. Tangnovarad, "Analysis of linearly elastic inextensible frames undergoing large displacement and rotation," *Mathematical Problems in Engineering*, vol. 2011, Article ID 592958, 37 pages, 2011.

[8] A. M. Abd-Alla and S. R. Mahmoud, "Magneto-thermoelastic problem in rotating non-homogeneous orthotropic hollow cylinder under the hyperbolic heat conduction model," *Meccanica*, vol. 45, no. 4, pp. 451–462, 2010.

[9] A. M. Abd-Alla and S. R. Mahmoud, "On problem of radial vibrations in non-homogeneity isotropic cylinder under influence of initial stress and magnetic field," *Journal of Vibration and Control*, vol. 19, no. 9, pp. 1283–1293, 2013.

[10] A. M. Abd-Alla, S. R. Mahmoud, S. M. Abo-Dahab, and M. I. Helmy, "Influences of rotation, magnetic field, initial stress, and gravity on Rayleigh waves in a homogeneous orthotropic elastic half-space," *Applied Mathematical Sciences*, vol. 4, no. 1–4, pp. 91–108, 2010.

[11] A. M. Abd-Alla, S. M. Abo-Dahab, H. A. Hammad, and S. R. Mahmoud, "On generalized magneto-thermoelastic Rayleigh waves in a granular medium under the influence of a gravity field and initial stress," *Journal of Vibration and Control*, vol. 17, no. 1, pp. 115–128, 2011.

[12] A. M. Abd-Alla, S. R. Mahmoud, and N. A. Al-Shehri, "Effect of the rotation on a non-homogeneous infinite cylinder of orthotropic material," *Applied Mathematics and Computation*, vol. 217, no. 22, pp. 8914–8922, 2011.

[13] A. M. El-Naggar, A. M. Abd-Alla, and S. R. Mahmoud, "Analytical solution of electro-mechanical wave propagation in long bones," *Applied Mathematics and Computation*, vol. 119, no. 1, pp. 77–98, 2001.

[14] M. Marin, R. P. Agarwal, and S. R. Mahmoud, "Nonsimple material problems addressed by the Lagrange's identity," *Boundary Value Problems*, vol. 2013, article 135, 2013.

[15] M. Marin, "Weak solutions in elasticity of dipolar porous materials," *Mathematical Problems in Engineering*, vol. 2008, Article ID 158908, 8 pages, 2008.

[16] X. Wang, "An elastodynamic solution for an anisotropic hollow sphere," *International Journal of Solids and Structures*, vol. 31, no. 7, pp. 903–911, 1994.

[17] H. Ding, H. Wang, and W. Chen, "Elastodynamic solution of a non-homogeneous orthotropic hollow cylinder," *Acta Mechanica Sinica*, vol. 18, no. 6, pp. 621–628, 2002.

[18] H. J. Ding, H. M. Wang, and W. Q. Chen, "A solution of a non-homogeneous orthotropic cylindrical shell for axisymmetric plane strain dynamic thermoelastic problems," *Journal of Sound and Vibration*, vol. 263, no. 4, pp. 815–829, 2003.

[19] X. Wang and Y. P. Shen, "Inclusions of arbitrary shape in magnetoelectroelastic composite materials," *International Journal of Engineering Science*, vol. 41, no. 1, pp. 85–102, 2003.

[20] H. J. Ding, H. M. Wang, and P. F. Hou, "The transient responses of piezoelectric hollow cylinders for axisymmetric plane strain problems," *International Journal of Solids and Structures*, vol. 40, no. 1, pp. 105–123, 2003.

[21] P. F. Hou and A. Y. T. Leung, "The transient responses of magneto-electro-elastic hollow cylinders," *Smart Materials and Structures*, vol. 13, no. 4, pp. 762–776, 2004.

[22] G. R. Buchanan and Y. J. Liu, "An analysis of the free vibration of thick-walled isotropic toroidal shells," *International Journal of Mechanical Sciences*, vol. 47, no. 2, pp. 277–292, 2005.

[23] J. Yu, Q. Ma, and S. Su, "Wave propagation in non-homogeneous magneto-electro-elastic hollow cylinders," *Ultrasonics*, vol. 48, no. 8, pp. 664–677, 2008.

[24] A. M. Abd-Alla and S. R. Mahmoud, "Analytical solution of wave propagation in a non-homogeneous orthotropic rotating elastic media," *Journal of Mechanical Science and Technology*, vol. 26, no. 3, pp. 917–926, 2012.

[25] A. M. Abd-Alla, G. A. Yahya, S. R. Mahmoud, and H. S. Alosaimi, "Effect of the rotation, magnetic field and initial stress on peristaltic motion of micropolar fluid," *Meccanica*, vol. 47, no. 6, pp. 1455–1465, 2012.

[26] S. R. Mahmoud, "Influence of rotation and generalized magneto-thermoelastic on Rayleigh waves in a granular medium under effect of initial stress and gravity field," *Meccanica*, vol. 47, no. 7, pp. 1561–1579, 2012.

[27] J. N. Sharma, D. K. Sharma, and S. S. Dhaliwal, "Free vibration analysis of a viscothermoelastic solid sphere," *International Journal of Applied Mathematics and Mechanics*, vol. 8, no. 11, pp. 45–68, 2012.

[28] A. M. Abd-Alla, S. R. Mahmoud, and S. M. Abo-Dahab, "On problem of transient coupled thermoelasticity of an annular fin," *Meccanica*, vol. 47, no. 5, pp. 1295–1306, 2012.

[29] A. M. Abd-Alla, G. A. Yahya, and S. R. Mahmoud, "Effect of magnetic field and non-homogeneity on the radial vibrations in hollow rotating elastic cylinder," *Meccanica*, vol. 48, no. 3, pp. 555–566, 2013.

[30] A. M. Abd-Alla, G. A. Yahya, and S. R. Mahmoud, "Radial vibrations in a non-homogeneous orthotropic elastic hollow sphere subjected to rotation," *Journal of Computational and Theoretical Nanoscience*, vol. 10, no. 2, pp. 455–463, 2013.

[31] A. M. Abd-Alla, S. M. Abo-Dahab, S. R. Mahmoud, and T. A. Al-Thamalia, "Influence of the rotation and gravity field on stonely waves in a non-homogeneous orthotropic elastic medium," *Journal of Computational and Theoretical Nanoscience*, vol. 10, no. 2, pp. 297–305, 2013.

[32] A. M. Abd-Alla, S. R. Mahmoud, S. M. Abo-Dahab, and M. I. Helmy, "Propagation of S-wave in a non-homogeneous anisotropic incompressible and initially stressed medium under

influence of gravity field," *Applied Mathematics and Computation*, vol. 217, no. 9, pp. 4321–4332, 2011.

[33] A. M. Abd-Alla, S. R. Mahmoud, and S. M. Abo-Dahab, "Wave propagation modeling in cylindrical human long wet bones with cavity," *Meccanica*, vol. 46, no. 6, pp. 1413–1428, 2011.

[34] T. S. Ozsahin and O. Taskner, "Contact problem for an elastic layer on an elastic half plane loaded by means of three rigid flat punches," *Mathematical Problems in Engineering*, vol. 2013, Article ID 137427, 14 pages, 2013.

[35] T. H. Daouadji, A. H. Henni, A. Tounsi, and A. B. El Abbes, "A new hyperbolic shear deformation theory for bending analysis of functionally graded plates," *Modelling and Simulation in Engineering*, vol. 2012, Article ID 159806, 10 pages, 2012.

[36] F. R. Hearmon, *An Introduction to Applied Anisotropic Elasticity*, Oxford University Press, Oxford, UK, 1961.

[37] R. F. S. Hearmon, "The elastic constants of anisotropic materials," *Reviews of Modern Physics*, vol. 18, no. 3, pp. 409–440, 1946.

Hindawi Publishing Corporation
Mathematical Problems in Engineering
Volume 2013, Article ID 816385, 8 pages
http://dx.doi.org/10.1155/2013/816385

Research Article

Analytic Solutions for Heat Conduction in Functionally Graded Circular Hollow Cylinders with Time-Dependent Boundary Conditions

Sen-Yung Lee and Chih-Cheng Huang

Department of Mechanical Engineering, National Cheng Kung University, Tainan 701, Taiwan

Correspondence should be addressed to Sen-Yung Lee; sylee@mail.ncku.edu.tw

Received 16 May 2013; Revised 27 June 2013; Accepted 1 July 2013

Academic Editor: Abdelouahed Tounsi

Copyright © 2013 S.-Y. Lee and C.-C. Huang. This is an open access article distributed under the Creative Commons Attribution License, which permits unrestricted use, distribution, and reproduction in any medium, provided the original work is properly cited.

An analytic solution method, without integral transformation, is developed to find the exact solutions for transient heat conduction in functionally graded (FG) circular hollow cylinders with time-dependent boundary conditions. By introducing suitable shifting functions, the governing second-order regular singular differential equation with variable coefficients and time-dependent boundary conditions is transformed into a differential equation with homogenous boundary conditions. The exact solution of the system with thermal conductivity and specific heat in power functions with different orders is developed. Finally, limiting studies and numerical analyses are given to illustrate the efficiency and the accuracy of the analysis.

1. Introduction

The applications of heat conduction in functionally graded (FG) circular hollow cylinders with time-dependent boundary conditions can be widely found in many engineering fields, such as cannon barrels, heat exchanger tubes, time varied heating on walls of circular structure, and heat treatment on hollow cylinders. As such, an accurate solution method is very helpful for relevant developments.

The problem of heat conduction with time-dependent boundary conditions cannot be solved directly by the method of separation of variables. In most of the analyses, an integral transform has been used to remove the time-dependent term. For the problem of heat conduction in circular hollow uniform cylinders with time-dependent boundary conditions, the associated governing differential equation is a second-order Bessel differential equation with constant coefficients. After conducting a Laplace transformation, the analytical solution can be obtained and found in the book by Őzisik [1].

When the structure is an FG circular hollow cylinder, the associated governing differential equation is a second-order regular singular differential equation with variable coefficients. For problems with time-independent boundary conditions, various numerical methods have been developed, such as the perturbation method [2], the finite difference method [3], and the finite element method [4]. Jabbari et al. [5, 6] derived analytical solutions for thermal stresses of FG hollow cylinders whose material properties vary with power law distribution through the thickness due to radially symmetric loads and nonaxisymmetric loads. By using the Laplace transformation and a series expansion of Bessel functions, Ootao and Tanigawa [7] analyzed one-dimensional transient thermoelastic problem with the material properties varying with the powerlaw form of the radial coordinate variable. Zhao et al. [8] analyzed the temperature change when the thermal and thermoelastic properties are assumed to vary exponentially in the radial direction. Hosseini et al. [9] considered the material properties to be nonlinear with a power law distribution through the thickness, while the temperature distribution was derived analytically using the Bessel functions.

In the study of heat conduction in FG circular hollow cylinders with time-dependent boundary conditions, only limited studies can be found. Ootao et al. [10] studied the transient temperature and thermal stress distribution in an infinitely long nonhomogeneous hollow cylinder due to

a moving heat source in the axial direction from the inner and/or outer surfaces using the layerwise theory in conjunction with the method of Fourier cosine and the Laplace transformations. Shao and Ma [11] employed the Laplace transform techniques and the series solving method to study thermomechanical stresses in FG circular hollow cylinders with linearly increasing boundary temperature. Jabbari et al. [12] developed an analytical solution for the one-dimensional temperature distribution, mechanical and thermal stresses in an infinitely long FG hollow cylinder under a moving heat source, which moves across the thickness of the cylinder. Asgari and Akhlaghi [13] employed the finite element method to study the transient thermal stresses in a thick hollow cylinder with finite length mad of 2D-FGM that its material properties are varied in the radial and axial directions with a power law function. The thermal boundary conditions at the inner and outer radiuses are time dependent. Singh et al. [14] applied the finite integral transform method and the separation of variables method to solve time-dependent heat conduction problem in a multilayer annulus. Malekzadeh and Heydarpour [15] used the differential quadrature method (DQM) in conjunction with the finite element method (FEM) to study the response of FG cylindrical shells under moving thermomechanical loads. Recently, Wang and Liu [16] have employed the method of separation of variables to develop the analytical solution of transient temperature fields for two-dimensional transient heat conduction in a fiber-reinforced multilayer cylindrical composite.

In the study of thermal elastic response of FG cylinders without mechanical loading, the heat conduction problem is not incorporated with the elastic field and can be studied independently. However, the thermal field will be coupled with the temperature field. In this paper, one considers the heat conduction problem of FG cylinders only. A new solution method, which is a modification on the method developed by Lee and Lin [17] and Chen et al. [18], is used to develop the analytical solution for transient heat conduction in FG circular hollow cylinders with time-dependent boundary conditions. By introducing suitable shifting functions, the governing second-order differential equation with variable coefficients and time-dependent boundary conditions is transformed into a differential equation with homogenous boundary conditions. The analytic solution of the system with thermal conductivity and specific heat in power functions with different orders is developed. Finally, limiting studies and numerical analysis are given to illustrate the efficiency and accuracy of the solution method.

2. Mathematical Modeling

Consider the transient heat conduction in an FG circular hollow cylinder with time-dependent boundary condition at the inner and outer surfaces, as shown in Figure 1. The governing differential equation of the system is

$$\frac{1}{r}\frac{1}{\partial r}\left[rk\left(r\right)\frac{\partial T\left(r,t\right)}{\partial r}\right]+\dot{g}\left(r,t\right)=\rho c\left(r\right)\frac{\partial T\left(r,t\right)}{\partial t}. \quad a<r<b,\ t>0. \tag{1}$$

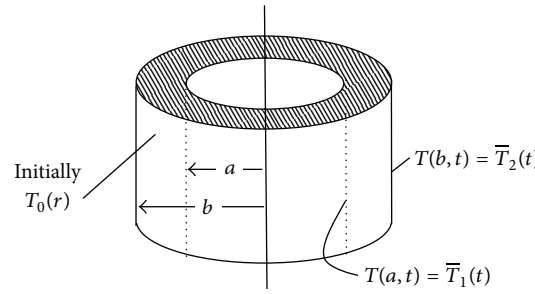

Figure 1: FG circular hollow cylinder with time-dependent boundary conditions.

The boundary conditions are

$$T\left(a,t\right)=\overline{T}_1\left(t\right),$$
$$T\left(b,t\right)=\overline{T}_2\left(t\right), \tag{2}$$

and the initial condition is

$$T\left(r,0\right)=T_0\left(r\right). \tag{3}$$

Here, r is the space variable and t is the time variable, $c(r)$ is the specific heat, $k(r)$ is the thermal conductivity, $T(r,t)$ is the temperature, ρ is the mass density, and $\dot{g}(r,t)$ is the heat source inside the circular hollow cylinder. $\overline{T}_1(t)$ and $\overline{T}_2(t)$ are the time-dependent temperatures at the inner and outer surfaces, respectively.

In terms of the following dimensionless parameters

$$K\left(\xi\right)=\frac{k\left(r\right)}{k\left(a\right)},\qquad C\left(\xi\right)=\frac{c\left(r\right)}{c\left(a\right)},\qquad G\left(\xi,\tau\right)=\frac{\dot{g}\left(r,t\right)b^2}{k\left(a\right)T_r},$$
$$\xi=\frac{r}{b},\qquad \overline{r}=\frac{a}{b},\qquad \theta=\frac{T}{T_r},\qquad \theta_0=\frac{T_0}{T_r},$$
$$\overline{\theta}_i=\frac{\overline{T}_i}{T_r},\qquad \tau=\frac{k\left(a\right)t}{c\left(a\right)\rho b^2}, \tag{4}$$

where T_r is the reference temperature, the boundary value problem of heat conduction becomes

$$\frac{1}{\xi}\frac{1}{\partial\xi}\left[\xi K\left(\xi\right)\frac{\partial\theta\left(\xi,\tau\right)}{\partial\xi}\right]+G\left(\xi,\tau\right)=C\left(\xi\right)\frac{\partial\theta\left(\xi,\tau\right)}{\partial\tau},\quad \overline{r}<\xi<1,\ \tau>0,$$
$$\theta\left(\overline{r},\tau\right)-\overline{\theta}_1=0,$$
$$\theta\left(1,\tau\right)-\overline{\theta}_2=0, \tag{5}$$
$$\theta\left(\xi,0\right)=\theta_0\left(\xi\right).$$

3. Solution Method

3.1. Change of Variables. To find the solution for the second-order differential equation with nonhomogeneous boundary conditions, the shifting variable method developed by Lee and Lin [17] and Chen et al. [18] was extended by taking

$$\theta(\xi,\tau) = \nu(\xi,\tau) + f_1(\tau)\, g_1(\xi) + f_2(\tau)\, g_2(\xi), \quad (6)$$

where $g_i(\xi)$, $i = 1, 2$ are shifting functions to be specified and $\nu(\xi,\tau)$ is the transformed function. Substituting (6) into (5) yields the following partial differential equation:

$$\frac{1}{\xi}\frac{\partial}{\partial\xi}\left[\xi K(\xi)\frac{\partial\nu(\xi,\tau)}{\partial\xi}\right] - C(\xi)\frac{\partial\nu(\xi,\tau)}{\partial\tau} = -G(\xi,\tau) + \sum_{i=1}^{2}\left\{\begin{array}{c} C(\xi)\, g_i(\xi)\dfrac{df_i(\tau)}{d\tau} \\ -f_i(\tau)\dfrac{1}{\xi}\dfrac{d}{d\xi}\left[\xi K(\xi)\dfrac{dg_i(\xi)}{d\xi}\right]\end{array}\right\}, \quad (7)$$

the associated boundary conditions:

$$\begin{aligned}\nu(\overline{r},\tau) + f_1(\tau)\, g_1(\overline{r}) + f_2(\tau)\, g_2(\overline{r}) &= f_1(\tau),\\ \nu(1,\tau) + f_1(\tau)\, g_1(1) + f_2(\tau)\, g_2(1) &= f_2(\tau),\end{aligned} \quad (8)$$

and the associated initial condition

$$\nu(\xi,0) = \theta(\xi,0) - f_1(0)\, g_1(\xi) - f_2(0)\, g_2(\xi). \quad (9)$$

3.2. Shifting Functions. To simplify the analysis, the shifting functions are specifically chosen such that they satisfy the following differential equations and the boundary conditions

$$\begin{aligned}\frac{d^2 g_i(\xi)}{d\xi^2} &= 0, \quad i = 1, 2,\\ g_1(\overline{r}) &= 1,\\ g_1(1) &= 0,\\ g_2(\overline{r}) &= 0,\\ g_2(1) &= 1.\end{aligned} \quad (10)$$

These two shifting functions can be easily determined as

$$\begin{aligned} g_1(\xi) &= \frac{1}{1-\overline{r}}(1-\xi),\\ g_2(\xi) &= \frac{1}{1-\overline{r}}(-\overline{r}+\xi).\end{aligned} \quad (11)$$

3.3. Reduced Homogenous Problem. With these two shifting functions, (11), the governing differential equation (7) becomes

$$\frac{1}{\xi}\frac{\partial}{\partial\xi}\left[\xi K(\xi)\frac{\partial\nu(\xi,\tau)}{\partial\xi}\right] - C(\xi)\frac{\partial\nu(\xi,\tau)}{\partial\tau} = F(\xi,\tau), \quad (12)$$

where

$$F(\xi,\tau) = -G(\xi,\tau) + \sum_{i=1}^{2}\left\{C(\xi)\, g_i(\xi)\frac{df_i(\tau)}{d\tau} - \frac{f_i(\tau)}{\xi}\frac{d}{d\xi}\left[\xi K(\xi)\right]\frac{dg_i(\xi)}{d\xi}\right\}. \quad (13)$$

The two nonhomogenous boundary conditions, (8), for the transformed function $\nu(\xi,\tau)$ are reduced to homogenous ones:

$$\begin{aligned}\nu(\overline{r},\tau) &= 0,\\ \nu(1,\tau) &= 0.\end{aligned} \quad (14)$$

The transformed initial condition is

$$\nu(\xi,0) = \theta_0(\xi) - f_1(0)\, g_1(\xi) - f_2(0)\, g_2(\xi) = \nu_0(\xi). \quad (15)$$

3.4. Solution of Transformed Variable

3.4.1. Characteristic Solution. To find the solution $\nu(\xi,\tau)$, we use the eigenfunction expansion method and assume the solution to be in the form

$$\nu(\xi,\tau) = \phi(\xi)\, B(\tau). \quad (16)$$

The separation equation for the dimensionless time variable $B(\tau)$ is

$$\frac{dB(\tau)}{d\tau} = -\lambda^2 B(\tau), \quad (17)$$

and the dimensionless space variable $\phi(\xi)$ satisfies the following self-adjoin operator:

$$\frac{1}{\xi}\frac{\mathrm{d}}{d\xi}\left[\xi K(\xi)\frac{d\phi(\xi)}{d\xi}\right] + \lambda^2 C(\xi)\,\phi(\xi) = 0, \quad \xi \in (\overline{r}, 1), \quad (18)$$

$$\phi(\overline{r}) = 0, \quad (19)$$

$$\phi(1) = 0. \quad (20)$$

Let $X_j(\xi)$, $j = 1, 2$, be the two linearly independent fundamental solutions of the system; then, the solution of the differential equation (18) can be expressed as

$$\phi(\xi) = C_1 X_1(\xi) - C_2 X_2(\xi), \quad (21)$$

where C_1 and C_2 are constants to be determined from the boundary conditions, (19)-(20).

After substituting solutions, (21), into the boundary conditions, (19)-(20), we obtain the following characteristic equation

$$X_1(1)\, X_2(\overline{r}) - X_1(\overline{r})\, X_2(1) = 0. \quad (22)$$

Consequently, the eigenvalues $\lambda_n, n = 1, 2, 3, \ldots$ can be determined. The associated nth eigenfunction $\phi_n(\xi)$ is determined as

$$\phi_n(\xi) = X_2(1) X_{n,1}(\xi) - X_1(1) X_{n,2}(\xi), \tag{23}$$

where $X_{n,1}(\xi)$ and $X_{n,2}(\xi)$ are, respectively, the fundamental solutions $X_1(\lambda_n, \xi)$ and $X_2(\lambda_n, \xi)$ associated with eigenvalues λ_n, $n = 1, 2, 3, \ldots$. They are defined as $X_{n,1}(\xi) = X_1(\lambda_n, \xi)$ and $X_{n,2}(\xi) = X_2(\lambda_n, \xi)$. The eigenfunctions $\phi_n(\xi)$ constitute an orthogonal set in the interval $\bar{r} \le \xi \le 1$, with respect to a weighting function $\xi C(\xi)$:

$$\int_{\bar{r}}^{1} \xi C(\xi) \phi_m(\xi) \phi_n(\xi) d\xi = \begin{cases} 0, & \text{for } m \neq n \\ \delta_n, & \text{for } m = n, \end{cases} \tag{24}$$

where

$$\delta_n = \int_{\bar{r}}^{1} \xi C(\xi) \phi_n^2(\xi) d\xi. \tag{25}$$

In terms of eigenfunctions, the transformed variable $\nu(\xi, \tau)$ can be expressed as

$$\nu(\xi, \tau) = \sum_{n=1}^{\infty} \phi_n(\xi) B_n(\tau). \tag{26}$$

Substituting (26) into (12), multiplying it by $\xi\phi_m$, and integrating from $\bar{r}$ to 1, we obtain

$$\frac{dB_n(\tau)}{d\tau} + \lambda_n^2 B_n(\tau) = -\gamma_n(\tau), \tag{27}$$

where

$$\gamma_n(\tau) = \frac{1}{\delta_n} \int_{\bar{r}}^{1} \xi \phi_n(\xi) F(\xi, \tau) d\xi. \tag{28}$$

The general solution of (27) is

$$B_n(\tau) = e^{-\lambda_n^2 \tau} \left[\alpha_n - \int_0^{\tau} e^{\lambda_n^2 \chi} \gamma_n(\chi) d\chi \right], \tag{29}$$

α_n is determined from the initial condition (15), and

$$\alpha_n = B_n(0) = \frac{1}{\delta_n} \int_{\bar{r}}^{1} \xi C(\xi) \phi_n(\xi) \nu_0(\xi) d\xi. \tag{30}$$

After substituting the solution of the transformed variable (26) and the shifting functions (11) back to (6), the exact solution for the general system is obtained.

4. Verification and Examples

To illustrate the previous analysis, the following examples and limiting cases are given.

Example 1. Consider the heat conduction in an uniform circular hollow cylinder with time-dependent boundary conditions. The boundary value problem of the heat conduction in dimension-less form is

$$\begin{gathered} \frac{1}{\xi} \frac{1}{\partial \xi} \left[\xi \frac{\partial \theta(\xi, \tau)}{\partial \xi} \right] = \frac{\partial \theta(\xi, \tau)}{\partial \tau}, \quad \bar{r} < \xi < 1, \ \tau > 0, \\ \theta(\bar{r}, \tau) = \frac{\psi_1(\tau)}{T_r}, \\ \theta(1, \tau) = \frac{\psi_2(\tau)}{T_r}, \\ \theta(\xi, 0) = \frac{\bar{\theta}_0(\xi)}{T_r}. \end{gathered} \tag{31}$$

In this case, $K(\xi) = 1$, $C(\xi) = 1$. The two shifting functions are

$$\begin{aligned} g_1(\xi) &= \frac{1}{1 - \bar{r}} (1 - \xi), \\ g_2(\xi) &= \frac{1}{1 - \bar{r}} (\xi - \bar{r}). \end{aligned} \tag{32}$$

The two linearly independent fundamental solutions are

$$\begin{aligned} X_1(\lambda_n, \xi) &= J_0(\lambda_n \xi), \\ X_2(\lambda_n, \xi) &= Y_0(\lambda_n \xi). \end{aligned} \tag{33}$$

This leads to

$$\begin{aligned} F(\xi, \tau) = \frac{1}{(1 - \bar{r}) T_r} \Big[& (1 - \xi) \psi_1'(\tau) + (-\bar{r} + \xi) \psi_2'(\tau) \\ & + \frac{\psi_1(\tau)}{\xi} - \frac{\psi_2(\tau)}{\xi} \Big], \end{aligned} \tag{34}$$

where the characteristic equation is

$$X_1(1) X_2(\bar{r}) - X_1(\bar{r}) X_2(1) = 0. \tag{35}$$

The associated nth eigenfunction $\phi_n(\xi)$ is determined as

$$\phi_n(\xi) = \frac{J_0(\lambda_n \xi)}{J_0(\lambda_n)} - \frac{Y_0(\lambda_n \xi)}{Y_0(\lambda_n)}. \tag{36}$$

The eigenvalues λ_n and the associated eigenfunctions $\phi_n(\xi)$ are obtained from (35) and (36). The two coefficients in (28)-(29) are derived as

$$\begin{aligned} \gamma_n(\tau) = & \frac{1}{\delta_n} \frac{1}{(1 - \bar{r}) T_r} \\ & \times \int_{\bar{r}}^{1} \Big\{ \phi_n(\xi) \Big[\left(\xi - \xi^2 \right) \psi_1'(\tau) + \left(-\bar{r}\xi + \xi^2 \right) \psi_2'(\tau) \\ & + \psi_1(\tau) - \psi_2(\tau) \Big] \Big\} d\xi \\ B_n(\tau) = & e^{-\lambda_n^2 \tau} \left[\alpha_n - \int_0^{\tau} e^{\lambda_n^2 \chi} \gamma_n(\chi) d\chi \right], \end{aligned} \tag{37}$$

where

$$\delta_n = \left[\int_{\bar{r}}^{1} \xi \phi_n^2(\xi)\, d\xi\right],$$
$$\alpha_n = \frac{1}{\delta_n T_r}\int_{\bar{r}}^{1} \xi \phi_n(\xi)\,\bar{\theta}_0(\xi)\, d\xi. \tag{38}$$

As a result, the analytic closed solution of the system in dimensionless form is

$$\theta(\xi,\tau) = \sum_{n=1}^{\infty}\left[\phi_n(\xi) B_n(\tau)\right] + \left(\frac{1-\xi}{1-\bar{r}}\right)\frac{\psi_1(\tau)}{T_r} + \left(\frac{-\bar{r}+\xi}{1-\bar{r}}\right)\frac{\psi_2(\tau)}{T_r}, \tag{39}$$

when

$$\psi_1(\tau) = \psi_2(\tau) = 0. \tag{40}$$

The analytic closed solution, in dimensionless form, is reduced to

$$\theta(\xi,\tau) = \sum_{n=1}^{\infty}\left[e^{-\lambda_n^2\tau}\phi_n(\xi)\,\alpha_n\right]. \tag{41}$$

The solution is exactly the same as the one given by Özisik [1].

Example 2. Consider the heat conduction in an FG circular hollow cylinder with time-dependent boundary conditions. The coefficients of thermal conductivity and the specific heat are $K(\xi) = k_m\xi^{\beta_1}$ and $C(\xi) = c_m\xi^{\beta_2}$, respectively. The boundary value problem of the heat conduction in dimensionless form is

$$\frac{1}{\xi}\frac{\partial}{\partial\xi}\left[\xi K(\xi)\frac{\partial\theta(\xi,\tau)}{\partial\xi}\right] - C(\xi)\frac{\partial\theta(\xi,\tau)}{\partial\tau} = 0, \quad \bar{r} < \xi < 1,\ \tau > 0, \tag{42}$$

$$\theta(\bar{r},\tau) = 0, \tag{43}$$

$$\theta(1,\tau) = \left(1 - e^{-C_0\tau}\right)\bar{\theta}_2, \tag{44}$$

$$\theta(\xi,0) = 0. \tag{45}$$

In this case, two shifting functions are

$$g_1(\xi) = \frac{1}{1-\bar{r}}(1-\xi),$$
$$g_2(\xi) = \frac{1}{1-\bar{r}}(\xi-\bar{r}). \tag{46}$$

The route to two independent fundamental solutions of of (42) lies in the use of the Frobenius method which can be represented in terms of the Bessel functions:

$$X_1(\lambda_n,\xi) = \xi^{-\beta_1/2}J_\nu\left(\eta_n\xi^{(2+\beta_2-\beta_1)/2}\right),$$
$$X_2(\lambda_n,\xi) = \xi^{-\beta_1/2}Y_\nu\left(\eta_n\xi^{(2+\beta_2-\beta_1)/2}\right), \tag{47}$$

where

$$\eta_n = \sqrt{\frac{c_m}{k_m}}\left(\frac{2\lambda_n}{\beta_1-\beta_2-2}\right),$$
$$\nu = \frac{\beta_1}{\beta_1-\beta_2-2}. \tag{48}$$

Now,

$$F(\xi,\tau) = e^{-C_0\tau}\bar{\theta}_2\left[c_m\xi^{\beta_2}C_0\left(a^* + b^*\xi\right) + b^*\left(\beta_1+1\right)k_m\xi^{\beta_1-1}\right] - b^*\left[\bar{\theta}_2\left(\beta_1+1\right)k_m\xi^{\beta_1-1}\right], \tag{49}$$

where

$$a^* = \frac{-\bar{r}}{1-\bar{r}},$$
$$b^* = \frac{1}{1-\bar{r}}. \tag{50}$$

The characteristic equation is

$$X_1(1)X_2(\bar{r}) - X_1(\bar{r})X_2(1) = 0. \tag{51}$$

The associated nth eigenfunction $\phi_n(\xi)$ is determined as

$$\phi_n(\xi) = X_2(1)X_{n,1}(\xi) - X_1(1)X_{n,2}(\xi). \tag{52}$$

The eigenvalues λ_n and the associated eigenfunctions $\phi_n(\xi)$ are obtained from (51) and (52) by numerical analysis. Two coefficients in (28)–(30) are derived as

$$\gamma_n(\tau) = \bar{\gamma}_{n1}(\xi)e^{-C_0\tau} + \bar{\gamma}_{n2}(\xi),$$
$$B_n(\tau) = \left[\alpha_n + \frac{\bar{\gamma}_{n1}(\xi)}{\lambda_n^2 - C_0} + \frac{\bar{\gamma}_{n2}(\xi)}{\lambda_n^2}\right]e^{-\lambda_n^2\tau} - \frac{\bar{\gamma}_{n1}(\xi)}{\lambda_n^2 - C_0}e^{-C_0\tau} - \frac{\bar{\gamma}_{n2}(\xi)}{\lambda_n^2}, \tag{53}$$

where

$$\delta_n = \left[\int_{\bar{r}}^{1} c_m\xi^{\beta_2+1}\phi_n^2(\xi)\, d\xi\right],$$
$$\bar{\gamma}_{n1}(\xi) = \frac{\bar{\theta}_2}{\delta_n}\left\{\int_{\bar{r}}^{1}\phi_n(\xi)\left[c_m\xi^{\beta_2}C_0\left(a^* + b^*\xi\right) + b^*\left(\beta_1+1\right)k_m\xi^{\beta_1-1}\right]d\xi\right\}, \tag{54}$$
$$\bar{\gamma}_{n2}(\xi) = \frac{-b^*\bar{\theta}_2}{\delta_n}\left[\int_{\bar{r}}^{1}\phi_n(\xi)\left(\beta_1+1\right)k_m\xi^{\beta_1-1}d\xi\right],$$
$$\alpha_n = 0.$$

Table 1: Temperature distribution of FG circular hollow cylinders with constant value of β_2 and various parameters of β_1 and C_0 at $\tau = 0.5$, $[k_m = 1, c_m = 1, \theta(1,\tau) = (C_0 \sin\omega\tau)\overline{\theta}_2 : \overline{\theta}_2 = 4 \text{ and } \omega = 2.5]$.

C_0	β_1	β_2	ξ					
			0.5	0.6	0.7	0.8	0.9	1.0
0.1	0.75	1	0	4.595	2.259	1.845	1.632	0.380
	1		0	4.592	2.285	1.990	1.820	0.380
	1.25		0	4.486	2.279	2.133	1.975	0.380
1	0.75	1	0	45.952	22.589	18.453	16.320	3.796
	1		0	45.920	22.848	19.895	18.202	3.796
	1.25		0	44.865	22.788	21.329	19.752	3.796
10	0.75	1	0	459.520	225.888	184.526	163.201	37.959
	1		0	459.196	228.480	198.950	182.017	37.959
	1.25		0	448.647	227.881	213.290	197.520	37.959

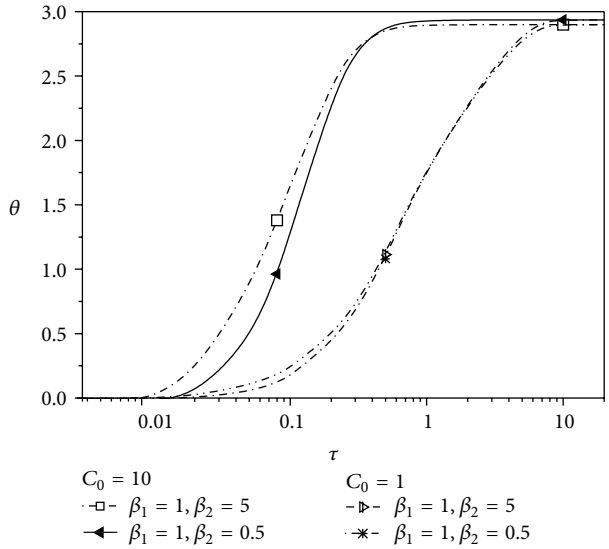

Figure 2: Temperature variation of FG circular hollow cylinders with constant value of β_1 and various values of β_2 and C_0 at $\xi = 0.75$, $[k_m = 1, c_m = 1, \theta(1,\tau) = (1 - e^{-C_0\tau})\overline{\theta}_2 : \overline{\theta}_2 = 4]$.

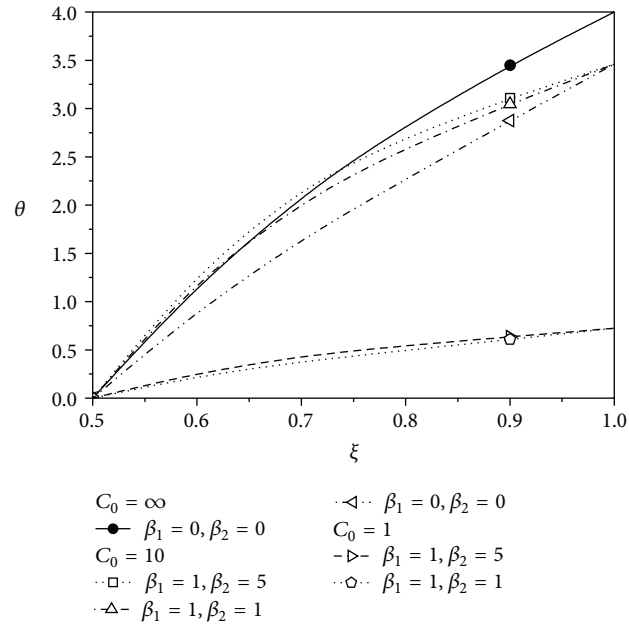

Figure 3: Temperature distribution of FG circular hollow cylinders with constant value of β_1 and various values of β_2 and C_0 at $\tau = 0.2$, $[k_m = 1, c_m = 1, \theta(1,\tau) = (1 - e^{-C_0\tau})\overline{\theta}_2 : \overline{\theta}_2 = 4]$.

Consequently, the analytic closed solution for the system can be derived as

$$\begin{aligned}\theta(\xi,\tau) &= \frac{\left(1 - e^{-C_0\tau}\right)\overline{\theta}_2}{1-\overline{r}}(\xi - \overline{r}) \\ &+ \sum_{n=1}^{\infty}\left\{X_2(1)X_{n,1}(\xi) - X_1(1)X_{n,2}(\xi)\right\} \\ &\times \left\{\begin{array}{l}\left[\dfrac{\overline{\gamma}_{n1}(\xi)}{\lambda_n^2 - C_0} + \dfrac{\overline{\gamma}_{n2}(\xi)}{\lambda_n^2}\right]e^{-\lambda_n^2\tau} \\ -\dfrac{\overline{\gamma}_{n1}(\xi)}{\lambda_n^2 - C_0}e^{-c_0\tau} - \dfrac{\overline{\gamma}_{n2}(\xi)}{\lambda_n^2}\end{array}\right\}.\end{aligned} \tag{55}$$

In Figure 2, the temperature variation of FG circular hollow cylinders with various parameters of β_1, β_2, and C_0 at $\xi = 0.75$ is shown. It can be found that when C_0 is a positive constant, the temperature parameter of the mediums at $\xi = 0.75$ increases then reaches the associated constant temperatures over time. The temperature increase rate for the system with a higher value of C_0 is greater than that of one with a lower value of C_0. Figures 3 and 4 show the temperature distribution of FG circular hollow cylinders with various parameters of β_1, β_2, and C_0 at $\tau = 0.2$. From these figures, it can be observed that with constant parameter β_1, the temperature of the mediums increases as parameter β_2

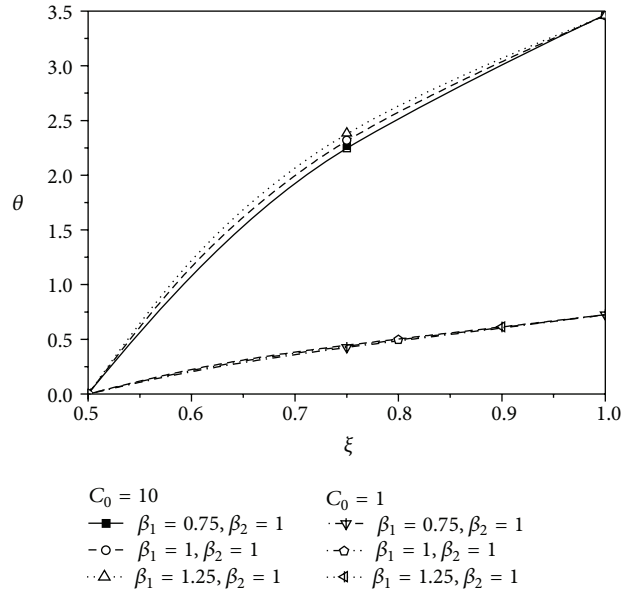

Figure 4: Temperature distribution of FG circular hollow cylinders with constant value of β_2 and various values of β_1 and C_0 at $\tau = 0.2$, $[k_m = 1, c_m = 1, \theta(1,\tau) = (1 - e^{-C_0\tau})\overline{\theta}_2 : \overline{\theta}_2 = 4]$.

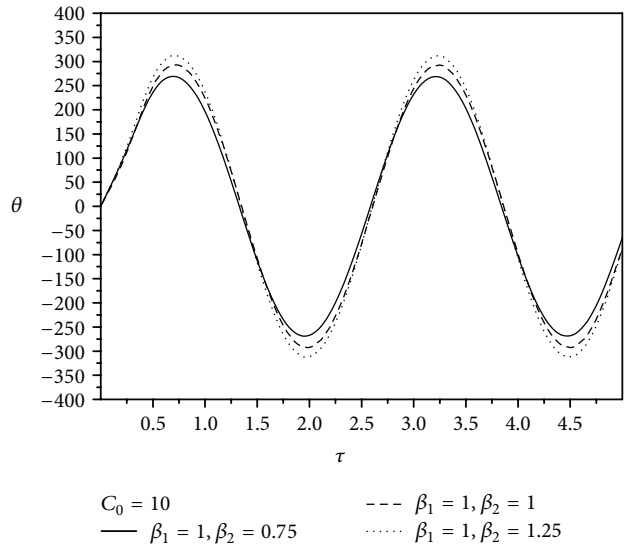

Figure 5: Temperature variation of FG circular hollow cylinders with constant value of β_1 and various values of β_2 at $\xi = 0.75$, $[k_m = 1, c_m = 1, \theta(1,\tau) = (C_0 \sin\omega\tau)\overline{\theta}_2 : \overline{\theta}_2 = 4, C_0 = 10$ and $\omega = 2.5]$.

is increased. With constant parameter β_2, the temperature of the mediums increases as parameter β_1 is increased.

Example 3. Consider the same physical system as discussed in Example 2. In this case, the time dependent boundary condition at $\xi = 1$, (44), is changed to the form

$$\theta(1,\tau) = \left(C_0 \sin\omega\tau\right)\overline{\theta}_2. \tag{56}$$

In this case, the eigenvalues and eigenfunctions are the same as those given in Example 2.

Now,

$$F(\xi,\tau) = \frac{-\overline{\theta}_2 C_0}{1-\overline{r}}\left[\left(\beta_1+1\right)k_m\xi^{\beta_1}\sin\omega\tau - \left(\xi-\overline{r}\right)\omega c_m\xi^{\beta_2}\cos\omega\tau\right]. \tag{57}$$

Following the same solution procedures as shown, the exact solution for the general system can be derived as

$$\theta(\xi,\tau) = \frac{C_0\sin\omega\tau}{1-\overline{r}}\overline{\theta}_2\left(\xi-\overline{r}\right) + \sum_{n=1}^{\infty}\left[X_2(1)X_{n,1}(\xi) - X_1(1)X_{n,2}(\xi)\right]B_n(\tau), \tag{58}$$

where

$$B_n(\tau) = \frac{1}{\omega\left[\left(\lambda_n^2/\omega\right)^2+1\right]} \times \left\{\begin{array}{l}\left(\dfrac{\lambda_n^2}{\omega}\cos\omega\tau + \sin\omega\tau - \dfrac{\lambda_n^2}{\omega}e^{-\lambda_n^2\tau}\right)\overline{\gamma}_{n1}(\xi) \\ -\left(\dfrac{\lambda_n^2}{\omega}\sin\omega\tau - \cos\omega\tau - e^{-\lambda_n^2\tau}\right)\overline{\gamma}_{n2}(\xi)\end{array}\right\},$$

$$\delta_n = \left[\int_{\overline{r}}^{1} c_m\xi^{\beta_2+1}\phi_n^2(\xi)\,d\xi\right],$$

$$\overline{\gamma}_{n1}(\xi) = \frac{-\overline{\theta}_2 C_0}{(1-\overline{r})\delta_n}\left[\int_0^1 \phi_n(\xi)\left(\xi-\overline{r}\right)\omega c_m\xi^{\beta_2+1}d\xi\right],$$

$$\overline{\gamma}_{n2}(\xi) = \frac{-\overline{\theta}_2 C_0}{(1-\overline{r})\delta_n}\left[\int_0^1 \phi_n(\xi)\left(\beta_1+1\right)k_m\xi^{\beta_1+1}d\xi\right],$$

$$\alpha_n = 0. \tag{59}$$

Figure 5 shows the harmonic temperature variation of FG circular hollow cylinders with constant value of β_1, various parameters of β_2 at $\xi = 0.75$, $C_0 = 10$, and $\omega = 2.5$. It can be observed that with constant value of β_1, the amplitude of temperature oscillation for the system with a higher value of β_2 will be more than that of one with a lower value of β_2.

In Table 1, the temperature variations of FG circular hollow cylinders with constant value of β_2 and various values of β_1 and C_0 at $\tau = 0.5$ are given. It can be observed that with constant parameter β_2, the temperature of the mediums will decrease as parameter β_1 is decreased.

5. Conclusions

The problem of heat conduction with general time-dependent boundary conditions cannot be solved directly by the method of separation of variables. In most of the analyses, an integral transform was used to remove the time-dependent term.

In this paper, a new analytic solution method is developed to find the analytic closed solutions for the transient heat conduction in FG circular hollow cylinders with general time-dependent boundary conditions. The developed solution method is free of any kind of integral transformation.

By introducing suitable shifting functions, the governing second-order regular singular differential equation with variable coefficients and time-dependent boundary conditions is transformed into a differential equation with homogenous boundary conditions. The analytic solution of the system with thermal conductivity and specific heat in power functions with different orders is developed. Finally, limiting studies and numerical analyses are given to illustrate the efficiency and the accuracy of the analysis. The proposed solution method can also be extended to the problems with various kinds of FG materials and time-dependent boundary conditions.

Acknowledgment

It is gratefully acknowledged that this research was supported by the National Science Council of Taiwan, Taiwan, under Grant NSC 99-2221-E-006-021.

References

[1] M. N. Őzisik, *Boundary Value Problems of Heat Conduction*, International Textbook Company, Scranton, Pa, USA, 1st edition, 1968.

[2] Y. Obata and N. Noda, "Steady thermal stresses in a hollow circular cylinder and a hollow sphere of a functionally gradient material," *Journal of Thermal Stresses*, vol. 17, no. 3, pp. 471–487, 1994.

[3] H. Awaji and R. Sivakumar, "Temperature and stress distributions in a hollow cylinder of functionally graded material: the case of temperature-independent material properties," *Journal of the American Ceramic Society*, vol. 84, no. 5, pp. 1059–1065, 2001.

[4] G. N. Praveen and J. N. Reddy, "Nonlinear transient thermoelastic analysis of functionally graded ceramic-metal plates," *International Journal of Solids and Structures*, vol. 35, no. 33, pp. 4457–4476, 1998.

[5] M. Jabbari, S. Sohrabpour, and M. R. Eslami, "Mechanical and thermal stresses in a functionally graded hollow cylinder due to radially symmetric loads," *International Journal of Pressure Vessels and Piping*, vol. 79, no. 7, pp. 493–497, 2002.

[6] M. Jabbari, S. Sohrabpour, and M. R. Eslami, "General solution for mechanical and thermal stresses in a functionally graded hollow cylinder due to nonaxisymmetric steady-state loads," *ASME Transactions Journal of Applied Mechanics*, vol. 70, no. 1, pp. 111–118, 2003.

[7] Y. Ootao and Y. Tanigawa, "Transient thermoelastic analysis for a functionally graded hollow cylinder," *Journal of Thermal Stresses*, vol. 29, no. 11, pp. 1031–1046, 2006.

[8] J. Zhao, X. Ai, Y. Li, and Y. Zhou, "Thermal shock resistance of functionally gradient solid cylinders," *Materials Science and Engineering A*, vol. 418, no. 1-2, pp. 99–110, 2006.

[9] S. M. Hosseini, M. Akhlaghi, and M. Shakeri, "Transient heat conduction in functionally graded thick hollow cylinders by analytical method," *Heat and Mass Transfer*, vol. 43, no. 7, pp. 669–675, 2007.

[10] Y. Ootao, T. Akai, and Y. Tanigawa, "Three-dimensional transient thermal stress analysis of a nonhomogeneous hollow circular cylinder due to a moving heat source in the axial direction," *Journal of Thermal Stresses*, vol. 18, no. 5, pp. 497–512, 1995.

[11] Z. S. Shao and G. W. Ma, "Thermo-mechanical stresses in functionally graded circular hollow cylinder with linearly increasing boundary temperature," *Composite Structures*, vol. 83, no. 3, pp. 259–265, 2008.

[12] M. Jabbari, A. H. Mohazzab, and A. Bahtui, "One-dimensional moving heat source in a hollow FGM cylinder," *ASME Transactions Journal of Pressure Vessel Technology*, vol. 131, no. 2, article 021202, 7 pages, 2009.

[13] M. Asgari and M. Akhlaghi, "Transient thermal stresses in two-dimensional functionally graded thick hollow cylinder with finite length," *Archive of Applied Mechanics*, vol. 80, no. 4, pp. 353–376, 2010.

[14] S. Singh, P. K. Jain, and R.-U. Rizwan-Uddin, "Finite integral transform method to solve asymmetric heat conduction in a multilayer annulus with time-dependent boundary conditions," *Nuclear Engineering and Design*, vol. 241, no. 1, pp. 144–154, 2011.

[15] P. Malekzadeh and Y. Heydarpour, "Response of functionally graded cylindrical shells under moving thermo-mechanical loads," *Thin-Walled Structures*, vol. 58, pp. 51–66, 2012.

[16] H. M. Wang and C. B. Liu, "Analytical solution of two-dimensional transient heat conduction in fiber-reinforced cylindrical composites," *International Journal of Thermal Sciences*, vol. 69, pp. 43–52, 2013.

[17] S. Y. Lee and S. M. Lin, "Dynamic analysis of nonuniform beams with time-dependent elastic boundary conditions," *ASME Transactions Journal of Applied Mechanics*, vol. 63, no. 2, pp. 474–478, 1996.

[18] H. T. Chen, S. L. Sun, H. C. Huang, and S. Y. Lee, "Analytic closed solution for the heat conduction with time dependent heat convection coefficient at one boundary," *Computer Modeling in Engineering and Sciences*, vol. 59, no. 2, pp. 107–126, 2010.

Hindawi Publishing Corporation
Mathematical Problems in Engineering
Volume 2013, Article ID 793062, 12 pages
http://dx.doi.org/10.1155/2013/793062

Research Article

Buckling Analyses of Axially Functionally Graded Nonuniform Columns with Elastic Restraint Using a Localized Differential Quadrature Method

Yasin Yilmaz, Zekeriya Girgin, and Savas Evran

Mechanical Engineering Department, Faculty of Engineering, Pamukkale University, Kinikli Campus, 20070 Denizli, Turkey

Correspondence should be addressed to Yasin Yilmaz; yyilmaz@pau.edu.tr

Received 24 April 2013; Accepted 7 July 2013

Academic Editor: Abdelouahed Tounsi

Copyright © 2013 Yasin Yilmaz et al. This is an open access article distributed under the Creative Commons Attribution License, which permits unrestricted use, distribution, and reproduction in any medium, provided the original work is properly cited.

A localized differential quadrature method (LDQM) is introduced for buckling analysis of axially functionally graded nonuniform columns with elastic restraints. Weighting coefficients of differential quadrature discretization are obtained making use of neighboring points in forward and backward type schemes for the reference grids near the beginning and end boundaries of the physical domain, respectively, and central type scheme for the reference grids inside the physical domain. Boundary conditions are directly implemented into weighting coefficient matrices, and there is no need to use fictitious points near the boundaries. Compatibility equations are not required because the governing differential equation is discretized only once for each reference grid using neighboring points and variation of flexural rigidity is taken to be continuous in the axial direction. A large case of columns having different variations of cross-sectional profile and modulus of elasticity in the axial direction are considered. The results for nondimensional critical buckling loads are compared to the analytical and numerical results available in the literature. Some new results are also given. Comparison of the results shows the potential of the LDQM for solving such generalized eigenvalue problems governed by fourth-order variable coefficient differential equations with high accuracy and less computational effort.

1. Introduction

Beams and columns with variable flexural rigidities are commonly used in complex structures to achieve a better distribution of strength and weight and sometimes to satisfy architectural and functional requirements. The accurate prediction of dynamic behavior of beams and columns, particularly when the properties of the material and cross-section are variable, is of crucial importance in many areas of science and engineering such as civil, mechanical, biomedical, and aerospace engineering. Moreover, elastic restraints may also become an important issue for determination of critical buckling loads. The continuous change of the material properties can be achieved by gradually varying the volume fraction of the individual constituent materials from one point to another through any of the spatial coordinates. These types of materials are specifically called as functionally graded materials (FGMs). Continuity in FGM properties allows the elimination of interlayer delamination due to high stress and crack initiation and propagation in intermediate faces caused by high plastic deformation, frequently seen in laminated composites. The property variation of FGMs can be tailored to obtain the desired mechanical properties for different applications. With the advent of more advanced techniques, FGMs are now used in production of beam, plate, and shell structures that are emerging as promising structural elements in today's industry (automotive and aircraft industry, space vehicles, machine elements, etc.) [1].

There are many analytical and numerical studies for buckling analysis of beams and columns in the literature, but most of them are limited to the case of uniform case and a few studies take into account variation of both material properties and cross-section through the axial direction for columns with elastic restraints. Closed form solutions for these types of columns are only available for some special cases [2–8], and to obtain a general solution, numerical methods should be employed. As far as numerical methods are concerned, differential quadrature method (DQM) is

claimed to be an efficient and powerful numerical technique with minimum computational effort and also an alternative to the finite difference and finite element methods. DQM, introduced firstly by Bellmann and his coworkers [9, 10], discretizes any derivative at a point in the solution domain by a weighted linear sum of function values along the direction of its respective coordinate. Since its advance, DQM has been successfully applied to a variety of problems in engineering science and a review can be found in [11]. The DQM and its modified versions are applied to buckling analyses of nonuniform and functionally graded columns in [12–15]. Other numerical methods such as differential transform method [15], semi-inverse method [16–18], functional perturbation method [19], variational iteration method [20, 21], homotopy perturbation method [22, 23], finite difference method [24], finite element method [25], integral-equation approach [26], dynamic stiffness method [27], Newton's eigenvalue iteration method [28], and Fredholm integral technique [29] are also successfully applied to buckling analyses of nonuniform and axially functionally graded columns. Recently, Huang and Luo [30] proposed a method that uses power series and integral technique to obtain a polynomial characteristic equation in terms of critical buckling loads for axially inhomogeneous beams with elastic restraint. Then they solved this equation for smallest positive root using a commercial software.

The key procedure in DQM lies in the determination of the weighting coefficients. Also, implementation of boundary conditions is another important issue. With this respect, many studies are conducted to overcome deficiencies of the DQM. Detailed information about the DQM and its development stages can be found in [31]. Even though, DQM has been regarded as an efficient numerical technique with high accuracy at the beginning, large number of grid numbers cannot be used, that is, more than 21, due to the stability problems. To overcome these deficiencies, more advanced version of DQM, localized differential quadrature method (LDQM) is proposed and applied to some engineering and physical problems such as 2D wave equation [32], 2D stream function formulation of Navier–Stokes equations [33], and mild slope equation [34]. The basic idea in the LDQ method is to apply DQ approximation to a small neighborhood of the grid point of interest rather than to the whole domain. The derivatives at each grid point are then approximated by a weighted sum of function values on its neighboring points, rather than on all of the grid points. Thus, a very accurate solution without losing stability can be obtained. The discussion and basic ideas beyond the LDQM are given in detail in [35].

In this study, LQDM is applied to the buckling analyses of nonuniform axially functionally graded columns with elastic restraints for different boundary conditions. To the best of the authors' knowledge, in the open literature, LDQM is not applied before to solutions of generalized eigenvalue problems governed by fourth-order variable coefficient differential equations. Fictitious points are not used for implementation of boundary conditions at the tip nodes and boundary conditions are directly implemented into weighting coefficient matrices. It is seen that problems encountered in original DQ method for implementation of clamped boundary conditions into weighting coefficient matrices are eliminated using LDQM. There is no restriction in the continuous variation of cross-section and elastic modulus in the axial direction. In the following at first, mathematical formulation of the problem is provided and an introduction is given for classical DQM and LDQM. Then numerical results for critical buckling loads are given for a large case of columns using LDQM.

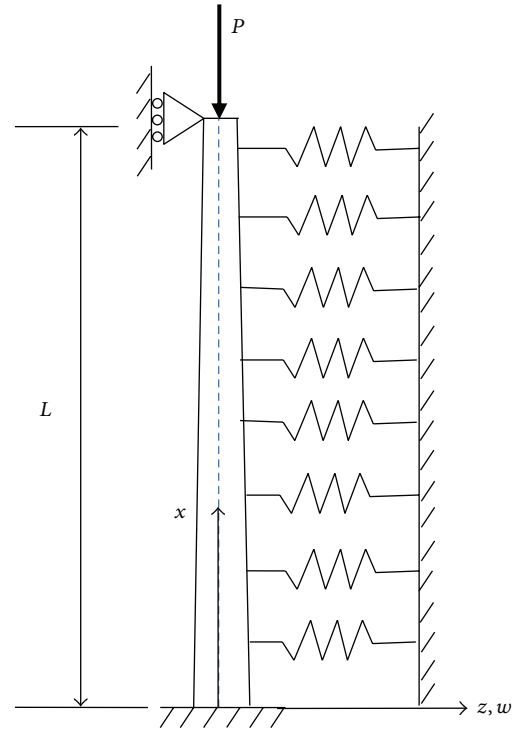

Figure 1: Column with continuous elastic restraint.

2. Mathematical Formulation

2.1. Governing Differential Equation. A nonuniform axially functionally graded column of length L subjected to an axial compressive load P at the centroid axis with a continuous elastic restraint is considered (see Figure 1). The material properties and cross-section of the beam are assumed to vary continuously along the axial direction, x. According to Euler-Bernoulli beam theory, the effects of shear deformation and rotary inertia are neglected; thus the governing differential equation for buckling of an axially FG nonuniform beam on elastic foundation can be written as follows [8]:

$$\frac{d^2}{dx^2}\left[E(x)\,I(x)\,\frac{d^2w}{dx^2}\right] + P\frac{d^2w}{dx^2} + kw = 0, \quad 0 < x < L, \tag{1}$$

where $w(x)$ is the lateral displacement, $E(x)$ and $I(x)$ are axially varying modulus of elasticity and moment of inertia

of the column, respectively, and k is the stiffness of the uniformly distributed lateral springs per unit length. Introducing nondimensional coordinate and deflection as

$$\xi = \frac{x}{L}, \qquad W(\xi) = \frac{w(x)}{L}, \tag{2}$$

(1) can be written as [30]

$$\frac{d^2}{d\xi^2}\left[E(\xi) I(\xi) \frac{d^2W}{d\xi^2}\right] + \alpha^* \frac{d^2W}{d\xi^2} + \beta^* W = 0, \quad 0 < \xi < 1, \tag{3}$$

where $\alpha^* = PL^2$ is the normalized critical load and $\beta^* = kL^4$ is the normalized restrained stiffness parameter.

2.2. Boundary Conditions. End supports of the beam directly affect the critical buckling load of the column. In the present study, four types of boundary conditions shown in Figure 2 are considered [8]. The explicit expressions for the boundary conditions can be given in terms of $W(\xi)$ as follows.

Clamped support (C):

$$W = 0, \quad \frac{dW}{d\xi} = 0. \tag{4a}$$

Pin support (P):

$$W = 0, \quad \frac{d^2W}{d\xi^2} = 0. \tag{4b}$$

Free end (F):

$$\frac{d^2W}{d\xi^2} = 0, \quad \frac{d}{d\xi}\left[E(\xi) I(\xi) \frac{d^2W}{d\xi^2}\right] + \alpha^* \frac{dW}{d\xi} = 0. \tag{4c}$$

Guided end (G):

$$\frac{dW}{d\xi} = 0, \quad \frac{d}{d\xi}\left[E(\xi) I(\xi) \frac{d^2W}{d\xi^2}\right] + \alpha^* \frac{dW}{d\xi} = 0. \tag{4d}$$

The problem is to find the critical buckling load of the column using the fourth-order variable coefficient ordinary differential equation (3) subject to corresponding boundary conditions given in (4a), (4b), (4c), and (4d). A closed-form solution of the problem is not generally possible for arbitrarily varying coefficients except for some special cases [3–7] and it is of crucial importance to find the smallest root of the equations for general case in engineering applications. In Section 3, LDQM discretization of the governing differential equation and boundary conditions will be shown for general case of axial variation of material properties and cross-section and, in Section 4, various types of nonuniform axially FG beams will be considered and corresponding numerical solutions will be obtained for the critical buckling loads.

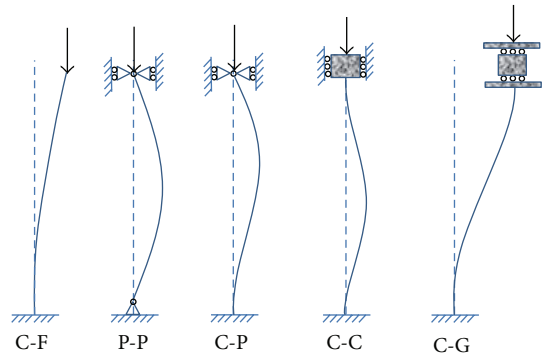

Figure 2: Boundary conditions.

3. Numerical Discretization and Method of Solution

3.1. Classical Differential Quadrature Method (DQM). The method of differential quadrature (DQ) is based on an assumption that the derivative of a function with respect to a space variable at a given discrete point can be expressed as a weighted linear sum of the function values at all discrete points in the solution domain. Weighting coefficients of DQM can be calculated in several ways. In order to find simple algebraic expressions for the weighting coefficients without restricting the choice of grid points, the generalized DQM was developed by Shu and Richards [36]. Consider a function $f(x)$ prescribed in a field domain $a \le x \le b$. Let $f(x_i)$ be the function values specified in a finite set of N discrete points x_i $(i = 1, 2, \ldots, N)$ of the field domain. The rth-order derivative of $f(x)$ at any discrete point x_i can be written in DQ analog form as

$$\frac{d^r f(x_i)}{dx^r} = \sum_{j=1}^{N} a_{ij}^{(r)} f\left(x_j\right), \quad i = 1, 2, \ldots, N, \tag{5}$$

where $a_{ij}^{(r)}$ are the weighting coefficients of the rth-order derivative of the function $f(x)$ associated with points x_i.

In the generalized DQM, the test functions are assumed to be the Lagrange interpolation test functions such as

$$\ell_j(x) = \frac{M(x)}{\left(x - x_j\right) M^{(1)}\left(x_j\right)}, \quad j = 1, 2, \ldots, N, \tag{6}$$

where

$$M(x) = \prod_{m=1}^{N} \left(x - x_m\right),$$
$$M^{(1)}\left(x_j\right) = \frac{dM\left(x_j\right)}{dx} = \prod_{m=1, m\neq j}^{N} \left(x_j - x_m\right). \tag{7}$$

The weighting coefficients for the first-order derivative can be obtained using Lagrange interpolation polynomial as follows:

$$a_{ij}^{(1)} = \frac{d\ell_j(x_i)}{dx} = \frac{M^{(1)}(x_i)}{(x_i - x_j)\,M^{(1)}(x_j)}, \quad i, j = 1, 2, \ldots, N, \quad i \neq j, \tag{8a}$$

$$a_{ii}^{(1)} = \frac{d\ell_i(x_i)}{dx} = -\sum_{j=1, j\neq i}^{N} a_{ij}^{(1)}, \quad i = 1, 2, \ldots, N, \tag{8b}$$

and these coefficients give the $[A^{(1)}]$ matrix as

$$\left[A^{(1)}\right] = \begin{bmatrix} a_{11}^{(1)} & a_{12}^{(1)} & \cdots & a_{1N}^{(1)} \\ a_{21}^{(1)} & a_{22}^{(1)} & \cdots & a_{2N}^{(1)} \\ \vdots & \vdots & \ddots & \vdots \\ a_{N1}^{(1)} & a_{N2}^{(1)} & \cdots & a_{NN}^{(1)} \end{bmatrix}. \tag{9}$$

Similarly, the weighting coefficients for the rth-order derivative can be evaluated using the following equations:

$$a_{ij}^{(r)} = \frac{d^r\ell_j(x_i)}{dx^r} = r\left(a_{ii}^{(r-1)}a_{ij}^{(1)} - \frac{a_{ij}^{(r-1)}}{(x_i - x_j)}\right), \quad i, j = 1, 2, \ldots, N, \quad i \neq j, \quad r \geq 2, \tag{10a}$$

$$a_{ii}^{(r)} = \frac{d^r\ell_i(x_i)}{dx^r} = -\sum_{j=1, j\neq i}^{N} a_{ij}^{(r)}, \quad i = 1, 2, \ldots, N, \ r \geq 2. \tag{10b}$$

The weighting coefficients for second- and higher-order derivatives can also be evaluated using the following expression:

$$a_{ij}^{(r)} = \sum_{k=1}^{N} a_{ik}^{(r-1)}a_{kj}^{(1)}, \quad i, j = 1, 2, \ldots, N, \ r \geq 2. \tag{11}$$

These coefficients give the matrix $A^{(r)}$ which can be interpreted as follows:

$$\left[A^{(r)}\right] = \begin{bmatrix} a_{11}^{(r)} & a_{12}^{(r)} & \cdots & a_{1N}^{(r)} \\ a_{21}^{(r)} & a_{22}^{(r)} & \cdots & a_{2N}^{(r)} \\ \vdots & \vdots & \ddots & \vdots \\ a_{N1}^{(r)} & a_{N2}^{(r)} & \cdots & a_{NN}^{(r)} \end{bmatrix}. \tag{12}$$

When x is taken in the interval $x \in [0, L]$ instead of $x \in [0, 1]$, the right-hand side of (14) must be divided by L^r which can be smaller or greater than 1. Then, the weighting coefficient matrix takes the following form:

$$\left[A^{(r)}\right] = \left(\frac{d}{dx}\right)^r = \frac{d^r}{dx^r} = \frac{1}{L^r}\begin{bmatrix} a_{11}^{(r)} & a_{12}^{(r)} & \cdots & a_{1N}^{(r)} \\ a_{21}^{(r)} & a_{22}^{(r)} & \cdots & a_{2N}^{(r)} \\ \vdots & \vdots & \ddots & \vdots \\ a_{N1}^{(r)} & a_{N2}^{(r)} & \cdots & a_{NN}^{(r)} \end{bmatrix}. \tag{13}$$

Figure 3: Discretization of boundary and near boundary reference points for $N_x = 7$ and $N = 21$.

Figure 4: Discretization of an interior reference point for $N_x = 7$ and $N = 21$.

After calculating the matrix $A^{(1)}$, weighting coefficient matrices for second- and higher-order derivatives can also be calculated using the following formulae:

$$\left[A^{(r)}\right] = \left[A^{(1)}\right]\left[A^{(r-1)}\right] = \left[A^{(r-1)}\right]\left[A^{(1)}\right]. \tag{14}$$

3.2. Localized Differential Quadrature Method (LDQM) and Sampling Points. In LDQM, firstly neighboring grids of any discrete point x_i in the computational domain should be determined according to the position of the point of interest and order of the first derivative approximation. For example if the function is discretized at the beginning boundary of the physical domain with respect to space variable x (at $x = 0$) or nearby it and a sixth-order first derivative approximation is used that means 7 neighboring points are needed ($N_x = 7$), the selection of the neighboring grid points should be forward type in the direction of the space variable, and if the function is discretized at the end boundary of the physical domain with respect to space variable x (at $x = L$) or nearby it, the selection of the neighboring grid points should be backward type. At the other interior reference points central type scheme is used. Figures 3 and 4 show the selection of neighboring points of a discrete point x_i in the solution domain for the previously mentioned cases. Then, the discretization of the first-order derivative of a function $f(x)$ with respect to space variable, x, at any discrete point x_i can be approximated using a weighted linear combination of the function values at some of the neighboring reference points within the computational domain as [32]

$$\frac{df(x_i)}{dx} = \sum_{j\in S_i} a_{ij}^{(1)} f(x_j), \quad i = 1, 2, \ldots, N, \tag{15}$$

where S_i represents the corresponding set of the neighboring nodes for the discrete grid point x_i in the domain or at the boundaries, N is the total amount of grid points in the direction of x. Weighting coefficients of the first-order derivative with respect to spatial coordinate x can be evaluated using the following equations:

$$a_{ij}^{(1)} = \frac{\prod_{m\in S_i, m\neq i}(x_i - x_m)}{(x_i - x_j)\cdot\prod_{m\in S_i, m\neq j}(x_j - x_m)}, \quad i = 1, 2, \ldots, N, \quad j \in S_i, \quad i \neq j, \tag{16a}$$

$$a_{ii}^{(1)} = -\sum_{j\in S_i, j\neq i} a_{ij}^{(1)}, \quad i = 1, 2, \ldots, N. \tag{16b}$$

Similarly, the discretization of the higher-order derivatives of $f(x)$ with respect to space variable, x, at any discrete point x_i can be expressed as

$$\frac{d^r f(x_i)}{dx^r} = \sum_{j\in S_i} a_{ij}^{(r)} f\left(x_j\right), \quad i = 1, 2, \ldots, N, \ r \geq 2. \tag{17}$$

The weighting coefficients for the rth-order derivative at any discrete point x_i can be evaluated using the following equations:

$$a_{ij}^{(r)} = r \cdot \left(a_{ij} a_{ii}^{(r-1)} - \frac{a_{ij}^{(r-1)}}{\left(x_i - x_j\right)} \right), \tag{18a}$$

$$i = 1, 2, \ldots, N, \quad j \in S_i, \quad i \neq j, \quad r \geq 2,$$

$$a_{ii}^{(r)} = - \sum_{j\in S_i, j\neq i} a_{ij}^{(r)}, \quad i = 1, 2, \ldots, N, \ r \geq 2. \tag{18b}$$

It is instructive to note that (18a) and (18b) are rewritten forms of (10a) and (10b) in the neighborhood of the reference point x_i.

A frequently used and convenient choice for the sampling points is that of the equally spaced sampling points which can be given in normalized coordinate of the space variable x_i by

$$\xi_i = \frac{i-1}{N-1}, \quad i = 1, 2, \ldots, N. \tag{19}$$

In the present study, equally spaced sampling points are used.

3.3. LDQM Formulation of the Governing Differential Equation and Boundary Conditions. Introducing $D(\xi) = E(\xi)I(\xi)$ for flexural rigidity, (3) can be expanded into following form:

$$D(\xi)\frac{d^4W}{d\xi^4} + 2\frac{dD(\xi)}{d\xi}\frac{d^3W}{d\xi^3} + \frac{d^2D(\xi)}{d\xi^2}\frac{d^2W}{d\xi^2} + \alpha^*\frac{d^2W}{d\xi^2} + \beta^* W = 0. \tag{20}$$

For the numerical computation equation (20) can be discretized using LDQM as follows:

$$D(\xi_i)\sum_{j\in S_i} a_{ij}^{(4)} W\left(\xi_j\right) + 2\left.\frac{dD(\xi)}{d\xi}\right|_{\xi=\xi_i}\sum_{j\in S_i} a_{ij}^{(3)} W\left(\xi_j\right) + \left.\frac{d^2D(\xi)}{d\xi^2}\right|_{\xi=\xi_i}\sum_{j\in S_i} a_{ij}^{(2)} W\left(\xi_j\right) + \alpha^*\sum_{j\in S_i} a_{ij}^{(2)} W\left(\xi_j\right) + \beta^* W\left(\xi_i\right) = 0, \quad i = 1, 2, \ldots, N. \tag{21}$$

Boundary conditions given in (4a), (4b), (4c), and (4d) can be discretized at $\xi = 0$ using LDQM as follows.

Clamped support (C):

$$W(\xi_1) = 0, \qquad \sum_{j\in S_i} a_{1j}^{(1)} W\left(x_j\right) = 0. \tag{22a}$$

Pin support (P):

$$W(\xi_1) = 0, \qquad \sum_{j\in S_i} a_{1j}^{(2)} W\left(x_j\right) = 0. \tag{22b}$$

Free end (F):

$$\sum_{j\in S_i} a_{1j}^{(2)} W\left(x_j\right) = 0,$$

$$\left.\frac{dD(\xi)}{d\xi}\right|_{\xi=0}\sum_{j\in S_i} a_{1j}^{(2)} W\left(x_j\right) + D(\xi_1)\sum_{j\in S_i} a_{1j}^{(3)} W\left(x_j\right) + \alpha^*\sum_{j\in S_i} a_{1j}^{(1)} W\left(x_j\right) = 0. \tag{22c}$$

Guided end (G):

$$\sum_{j\in S_i} a_{1j}^{(1)} W\left(x_j\right) = 0,$$

$$\left.\frac{dD(\xi)}{d\xi}\right|_{\xi=0}\sum_{j\in S_i} a_{1j}^{(2)} W\left(x_j\right) + D(\xi_1)\sum_{j\in S_i} a_{1j}^{(3)} W\left(x_j\right) + \alpha^*\sum_{j\in S_i} a_{1j}^{(1)} W\left(x_j\right) = 0. \tag{22d}$$

Boundary conditions at $\xi = 1$ can also be discretized in a similar manner. Boundary conditions given in (22a), (22b), (22c), and (22d) can directly be substituted into weighting coefficient matrices as described by Shu [31]. It will be shown in the next section that the disadvantages of substituting boundary conditions into weighting coefficient matrices, encountered in classical DQM for clamped boundary condition, disappeared in LDQM. It is also worth mentioning that no compatibility equations are needed in LDQM because the governing differential equation is discretized only once for each reference grid using neighboring points and variation of flexural rigidity is continuous in the axial direction.

Resulting set of algebraic equations can be put into matrix form to solve the generalized eigenvalue problem for critical buckling loads. Required matrix dimension is $(N-2)\times(N-2)$ for combination of clamped and simply supported end conditions since the function values at $\xi = 0$ and $\xi = 1$ are known. For combination of clamped and other boundary conditions (free and guided), the resulting matrix dimension is $(N-1)\times(N-1)$ since function value is only known at the clamped end.

4. Numerical Results and Discussions

In this section, LDQM is used to investigate the buckling behavior of axially FG nonuniform beams with a continuous elastic restraint. Firstly buckling behavior of homogeneous uniform columns with elastic restraints that has analytical solution is investigated to show the effectiveness of the method. Then the effects of variable cross-section and variable elastic modulus are investigated individually and both together.

4.1. Uniform Homogeneous Column with Elastic Restraints. For this case, (3) has an analytic solution and Wang et al. [8] have derived the stability criteria in nondimensional critical buckling load $\alpha = PL^2/EI$ and normalized restrained stiffness parameter $\beta = kL^4/EI$ for the columns with different end conditions. Stability criteria are as follows:

P-P Column:

$$\sin T = 0. \tag{23}$$

C-P Column:

$$T \cos T \sin S - S \sin T \cos S = 0. \tag{24}$$

C-G Column:

$$T \sin T \cos S - S \cos T \sin S = 0. \tag{25}$$

C-C Column:

$$2ST\left[\cos T \cos S - 1\right] + \left(T^2 + S^2\right) \sin T \sin S = 0. \tag{26}$$

C-F Column:

$$\left[\alpha\left(S^2 + T^2\right) - 2S^2T^2\right] \cos T \cos S - \alpha\left(S^2 + T^2\right) + \left(S^4 + T^4\right) + ST\left[2\alpha - \left(S^2 + T^2\right)\right] \sin T \sin S = 0, \tag{27}$$

where

$$S = \sqrt{\frac{\alpha}{2} - \sqrt{\left(\frac{\alpha}{2}\right)^2 - \beta}}, \qquad T = \sqrt{\frac{\alpha}{2} + \sqrt{\left(\frac{\alpha}{2}\right)^2 - \beta}}. \tag{28}$$

The stability criteria given in (23)–(27) are extremely nonlinear and finding the smallest root of the equation which is the critical buckling load is not easy for any assumed stiffness parameter. To show the effectiveness of the LDQM, nondimensional critical buckling loads, $\alpha = PL^2/EI$, are calculated for clamped-clamped beams with different normalized restrained stiffness parameters $\beta = kL^4/EI$ and compared to the exact results. In calculations the number of neighboring grids N_x is taken to be 11 and total number of grid points N is changed from 21 to 41. As can be seen from Table 1, critical buckling load converges to exact results as N increases from 11 to 41. In the following, neighboring grids N_x is taken to be 11 and total number of grid points N is taken to be 41 unless otherwise specified.

The critical buckling loads of the aforementioned columns have also been calculated by Atay and Coşkun [21] using a variation iteration approach and Huang and Luo [30] using power series and the integral technic. Nondimensional critical buckling loads for other boundary conditions are also obtained using LDQM and compared with the exact results [8], and with [21, 30]. The LDQM results given in Table 2 are in good agreement with the exact and other numerical results. It is also seen from Tables 1 and 2 that although the critical buckling load increases as the normalized restrained stiffness parameter increases for all of the boundary conditions, the column with C-G end condition is more sensitive to normalized restrained stiffness parameter change than the others.

4.2. Effect of Variable Cross-Section. Euler-Bernoulli columns with nonuniform cross-section along the axial direction are considered to see the effect of variable cross-section on critical buckling load. For this case elastic modulus E is taken to be constant and moment of inertia term changes according to a power law:

$$I(\xi) = I_0(1 + a\xi)^p, \quad a > -1, \tag{29}$$

where a is a geometric parameter and $p = 1$, 2, and 3.

First let us consider the case $p = 1$ which corresponds to the columns of linearly varying width and constant height. Nondimensional critical buckling loads, $\alpha = PL^2/EI_0$, are calculated using LDQM for different geometric parameter values, a, and normalized restrained stiffness parameters $\beta = kL^4/EI_0$. The results are compared to available results in the literature and given in Tables 3 and 4. It is seen from Tables 3 and 4 that with a changes from negative to positive values, nondimensional critical buckling load increases since negative values of a correspond to decreasing width and positive values of a correspond to increasing width as ξ changes from 0 to 1. As normalized restrained stiffness parameter increases, critical buckling loads also increase for all of the boundary conditions as in the case of uniform columns.

$p = 2$ case corresponds to the columns of parabolic varying width and constant height. For this case nondimensional critical buckling loads, $\alpha = PL^2/EI_0$, are calculated using LDQM for different geometric parameter values, a, and normalized restrained stiffness parameters $\beta = kL^4/EI_0$. The results are compared to available results in the literature and given in Tables 5 and 6. Comparison of results given in Tables 3 and 4 with the results given in Tables 5 and 6 shows that critical buckling loads for $p = 2$ case are higher than $p = 1$ case for $a > 0$ and critical buckling loads for $p = 2$ case are lower than $p = 1$ case for $a < 0$ for all of the boundary conditions since decrease and increase in column width are influenced by a factor of 2 for the case of $p = 2$. It is also seen from Tables 5 and 6 that although C-P and P-C columns have the same critical buckling loads for $\beta = 0$, they have somewhat different critical buckling loads for $\beta = 25$, 50, and 100.

For the case of $p = 3$, column has constant width and linearly varying height. The numerical results for nondimensional critical buckling loads, $\alpha = PL^2/EI_0$, are given in Table 7 for different geometric parameter values, a, and normalized restrained stiffness parameters $\beta = kL^4/EI_0$. Looking at Table 7, it is seen that the increase in critical

Table 1: Non dimensional critical buckling loads ($\alpha = PL^2/EI$) for clamped-clamped uniform homogeneous columns with continuous elastic restraint ($\beta = kL^4/EI$).

β	Exact [8]	DQM $N = 21$	DQM $N = 31$	DQM $N = 41$	LDQM $N_x = 11$, $N = 21$	LDQM $N_x = 11$, $N = 31$	LDQM $N_x = 11$, $N = 41$
0	39.47841760	39.47841735	39.46144027	—	39.47841219	39.47841756	39.47841760
50	43.26056590	43.26107726	38.55373074	—	43.26023292	43.26056213	43.26056583
100	47.00660086	47.00980042	37.89095672	—	47.00612534	47.00659571	47.00660072

Table 2: Non dimensional critical buckling loads ($\alpha = PL^2/EI$) for uniform homogeneous columns with continuous elastic restraint ($\beta = kL^4/EI$).

BC	$\beta = 0$				$\beta = 50$				$\beta = 100$			
	Exact [8]	Reference [21]	Reference [30]	LDQM	Exact [8]	Reference [21]	Reference [30]	LDQM	Exact [8]	Reference [21]	Reference [30]	LDQM
C-P	20.1907	20.1908	20.190729	20.190729	24.2852	24.2855	24.285198	24.285198	28.3066	28.3080	28.306631	28.306631
P-P	9.8696	9.8696	9.869604	9.869604	14.9357	14.9357	14.935664	14.935664	20.0017	20.0017	20.001723	20.001723
C-G	9.8696	9.8696	9.869604	9.869604	23.5717	23.5722	23.571661	23.571659	32.6690	32.6482	32.668976	32.668976
C-F	2.4674	2.4674	2.467401	2.467401	8.8614	8.8614	8.861396	8.861396	11.9964	11.9964	11.996413	11.996413

Table 3: Non dimensional critical buckling loads ($\alpha = PL^2/EI_0$) for the columns of linearly varying width and constant height ($I(\xi) = I_0(1 + a\xi)$) for $\beta = 0$.

BC	a	Reference [28]	Reference [3]	Reference [30]	LDQM
C-F	−0.5	—	—	—	2.06209226
	0.5	—	—	—	2.81006133
	1.0	3.12277257	3.11769623	3.11769623	3.11769628
F-C	−0.5	—	—	—	1.55884812
	0.5	—	—	—	3.31117993
	1.0	—	4.12418445	4.12418445	4.12418442
P-P	−0.5	—	—	—	7.25562477
	0.5	—	—	—	12.25041131
	1.0	14.50520092	14.51124954	14.51124954	14.51124954
C-P	−0.5	—	—	—	14.73942213
	0.5	—	—	—	24.99361144
	1.0	29.49596465	29.44896281	29.44896281	29.44896281
P-C	−0.5	—	—	—	14.72448141
	0.5	—	—	—	24.99874044
	1.0	—	29.47884426	29.47884426	29.47884426
C-C	−0.5	—	—	—	28.69697807
	0.5	—	—	—	48.81145815
	1.0	57.44524609	57.39395614	57.39395614	57.39395614
C-G	−0.5	—	—	—	7.16883539
	0.5	—	—	—	12.19969805
	1.0	—	—	—	14.33767077

buckling loads for $a > 0$ and the decrease in critical buckling loads for $a < 0$ are more pronounced as compared to $p = 2$ case because this time moment of inertia term is affected by a factor of 3. In Section 4.4, a column that has linearly varying width and height is also considered with varying elastic modulus.

4.3. Effect of Material Nonhomogeneity in the Axial Direction. Euler-Bernoulli columns with material nonhomogeneity along the axial direction are considered to see the effect of variable elastic modulus on critical buckling loads. For this case moment of inertia term, I, is taken to be constant and elastic modulus varies according to a power law or an exponential low gradient assumption.

4.3.1. Power Law Gradient Assumption. For power law gradient assumption, the variation of elastic modulus along the axial direction is taken as

$$E(\xi) = E_0 + (E_1 - E_0)\xi^m, \quad m > 0, \tag{30}$$

where m is a material gradient index and takes the values of 0.25, 0.5, 1, 2, and 4 in the present study. Specifically, two constituent materials are taken to be Aluminum and Alumina. The elastic moduli of these constituents are 70 GPa (E_0) and 380 Gpa (E_1), respectively [37]. Poisson's ratio is taken to be constant. The LDQM results for nondimensional critical buckling loads, $\alpha = PL^2/E_0I$, are given in Table 8 for different material gradient index values, m, and normalized restrained stiffness parameters $\beta = kL^4/E_0I$. It is seen that although the constituent materials are not changed, the critical buckling loads change drastically as material gradient index value changes, that is, increase as m gets smaller values because as m goes to zero, the volume fraction of Alumina becomes dominant.

4.3.2. Exponential Law Gradient Assumption. For exponential law gradient assumption, the variation of elastic modulus along the axial direction is taken to be

$$E(\xi) = E_0 e^{\mu\xi}, \tag{31}$$

where μ is a material gradient index and takes the values of −1, −0.5, 0.5, and 1 in the present study. Negative values

Table 4: Non dimensional critical buckling loads ($\alpha = PL^2/EI_0$) for the columns of linearly varying width and constant height ($I(\xi) = I_0(1 + a\xi)$) with continuous elastic restraint ($\beta = kL^4/EI_0$).

BC	$a = -0.5$			$a = 0.5$			$a = 1$		
	$\beta = 25$	$\beta = 50$	$\beta = 100$	$\beta = 25$	$\beta = 50$	$\beta = 100$	$\beta = 25$	$\beta = 50$	$\beta = 100$
C-F	5.320851	7.249834	9.496180	7.002455	10.034833	13.926981	7.575957	10.969773	15.525985
F-C	5.484886	7.762992	10.365666	7.065179	9.787644	13.328385	7.822199	10.641702	14.499668
P-P	9.774589	12.290572	17.308835	14.778728	17.306502	22.359993	17.030858	19.549179	24.581143
C-P	16.663069	18.556531	22.240823	27.120454	29.236109	33.430687	31.622334	33.787588	38.091765
P-C	16.893794	19.045882	23.289167	26.982108	28.949869	32.834737	31.409689	33.326139	37.113062
C-C	30.583452	32.457228	36.164501	50.705246	52.591875	56.342983	59.283541	61.166905	64.914456
C-G	13.693532	18.852382	24.928160	19.887489	26.982550	38.296345	22.292684	29.808724	42.676370

Table 5: Non dimensional critical buckling loads ($\alpha = PL^2/EI_0$) for the columns of parabolic varying width and constant height ($I(\xi) = I_0(1 + a\xi)^2$) for $\beta = 0$.

BC	a	Reference [28]	Reference [3]	Reference [30]	LDQM
C-F	−0.5	—	—	—	1.68296637
	0.5	—	—	—	3.17193009
	1.0	3.85763006	3.83637692	3.83637692	3.83637679
F-C	−0.5	—	—	—	0.95909423
	0.5	—	—	—	4.40655924
	1.0	—	6.73186541	6.73186541	6.73186555
P-P	−0.5	—	—	—	5.19807211
	0.5	—	—	—	15.07084413
	1.0	20.79163330	20.79228846	20.79228846	20.79228846
C-P	−0.5	—	—	—	10.52729403
	0.5	—	—	—	30.72425899
	1.0	42.31345100	42.10917612	42.10917612	42.10917612
P-C	−0.5	—	—	—	10.52729403
	0.5	—	—	—	30.72425899
	1.0	—	42.10917612	42.10917612	42.10917612
C-C	−0.5	—	—	—	20.48084102
	0.5	—	—	—	59.97123859
	1.0	82.22844561	81.92336388	81.92336364	81.92336379
C-G	−0.5	—	—	—	5.19807212
	0.5	—	—	—	15.07084413
	1.0	—	—	—	20.79228847

of μ correspond to the case; the column is ceramic rich at $\xi = 0$ and metal rich at $\xi = 1$ whereas positive values of μ corresponds to the case; the column is metal rich at $\xi = 0$ and ceramic rich at $\xi = 1$. The LDQM results for nondimensional critical buckling loads, $\alpha = PL^2/E_0I$, are given in Table 9 for different material gradient index values, μ, and normalized restrained stiffness parameters $\beta = kL^4/E_0I$. As can be seen from Table 9, critical buckling load increases for all of the boundary conditions with an increase in material gradient index as expected and it is also seen that restrained stiffness parameter has an important influence on critical buckling loads.

4.4. Effects of Both Material Nonhomogeneity and Variable Cross-Section. To investigate the effects of varying elastic modulus and cross-section along the axial direction together, a column that has linearly varying width and height and linearly varying elastic modulus is considered.

Width of the column:

$$b(\xi) = b_0(1 - c_b\xi), \quad 0 < c_b < 1. \tag{32a}$$

Height of the column:

$$h(\xi) = h_0(1 - c_h\xi), \quad 0 < c_h < 1. \tag{32b}$$

Moment of inertia of the column:

$$I(\xi) = I_0(1 - c_b\xi)(1 - c_h\xi)^3. \tag{32c}$$

Elastic modulus of the column:

$$E(\xi) = E_0(1 + \xi), \tag{32d}$$

where b_0, h_0, I_0, and E_0 are width, height, moment of inertia, and elastic modulus of the column at $\xi = 0$, respectively, c_b and c_h are geometric parameters that correspond to width and height taper ratios, respectively.

The case of $E(\xi) = E_0(1 + \xi)$ with linearly varying width and height is investigated by Shahba and Rajasekaran [15] using differential quadrature element method of lowest order (DQEL) for $\beta = 0$ case, that is, there are no elastic restraints. In [15], 12 elements each consisting of 11 nodes were chosen; thus total number of reference grids were taken to be 121. In DQEL, four compatibility equations should be written at the connection points of the elements and required matrix dimension to solve the problem is 576 × 576. To be consistent with [15], in LDQM solution of the problem total number of reference grids and neighboring nodes are also taken to be 121 and 11, respectively, but now required matrix dimension to solve the problem is 121 × 121. The nondimensional critical buckling loads, $\alpha = PL^2/E_0I_0$, of the columns for C-F, C-C, P-P, and C-P end conditions are given in Tables 10, 11, 12, and 13, respectively. For $\beta = 0$

Table 6: Non dimensional critical buckling loads ($\alpha = PL^2/EI_0$) for the columns of parabolic varying width and constant height ($I(\xi) = I_0(1 + a\xi)^2$) with continuous elastic restraint ($\beta = kL^4/EI_0$).

BC	$a = -0.5$			$a = 0.5$			$a = 1$		
	$\beta = 25$	$\beta = 50$	$\beta = 100$	$\beta = 25$	$\beta = 50$	$\beta = 100$	$\beta = 25$	$\beta = 50$	$\beta = 100$
C-F	4.341228	5.715021	7.305691	7.704323	11.199778	15.954946	8.844363	13.022270	19.259820
F-C	4.814955	6.692851	8.861021	8.038782	10.842500	14.737209	10.168566	13.021924	17.364909
P-P	7.672218	10.127971	14.937938	17.585157	20.097766	25.116851	23.271880	25.748067	30.688871
C-P	12.293759	14.009160	17.265144	32.912173	35.092823	39.430646	44.369842	46.626819	51.129119
P-C	12.782280	15.020605	19.433707	32.627483	34.516476	38.249232	43.893645	45.666325	49.175037
C-C	22.316590	24.131698	27.694119	61.849231	63.721127	67.446145	83.766543	85.604838	89.266360
C-G	10.832136	14.608627	18.532817	23.114885	30.762149	44.091245	29.276062	37.551999	53.151712

Table 7: Non dimensional critical buckling loads ($\alpha = PL^2/EI_0$) for the columns of constant width and linearly varying height ($I(\xi) = I_0(1 + a\xi)^3$) with continuous elastic restraint ($\beta = kL^4/EI_0$).

	$a = -0.5$				$a = 0.5$				$a = 1$			
	$\beta = 0$	$\beta = 25$	$\beta = 50$	$\beta = 100$	$\beta = 0$	$\beta = 25$	$\beta = 50$	$\beta = 100$	$\beta = 0$	$\beta = 25$	$\beta = 50$	$\beta = 100$
C-F	1.336426	3.406304	4.350010	5.487807	3.551010	8.394751	12.332922	18.020661	4.612119	10.082221	14.934526	22.864147
F-C	0.576515	4.175688	5.657646	7.558428	5.811363	9.281395	12.095892	16.252824	10.691414	13.774455	16.483421	20.954255
P-P	3.627812	6.022524	8.352143	12.576225	18.375617	20.866994	23.355361	28.321680	29.022499	31.437359	33.847167	38.650332
C-P	7.362241	8.951802	10.460281	13.205198	37.498111	39.736262	41.969764	46.421968	58.957688	61.272201	63.584952	68.205009
P-C	7.369711	9.677768	11.969157	16.483968	37.490417	39.306827	41.110477	44.677867	58.897925	60.520678	62.134215	65.333104
C-C	14.348488	16.093293	17.802510	21.098101	73.217187	75.065707	76.908867	80.578722	114.787912	116.546905	118.302355	121.800784
C-G	3.757964	8.394621	10.934803	13.536789	18.603820	26.955608	35.048357	49.998675	30.063711	38.940072	47.723673	64.917551

Table 8: Non-dimensional critical buckling loads ($\alpha = PL^2/E_0I$) for the axially functionally graded uniform columns with continuous elastic restraint ($\beta = kL^4/E_0I$) for power law gradient assumption ($E(\xi) = E_0 + (E_1 - E_0)\xi^m$).

BC	β	$m = 0.25$	$m = 0.5$	$m = 1$	$m = 2$	$m = 4$
C-F	0	10.246957	7.735606	4.817137	3.371243	2.744415
	50	19.568013	17.538824	14.864166	12.616815	10.701577
	100	27.169221	25.136738	22.408392	18.876263	15.432611
P-P	0	45.748909	38.940772	28.774564	18.792973	13.011352
	50	50.803306	43.960898	33.699710	23.651864	17.958863
	100	55.857000	48.977666	38.610936	28.483003	22.886075
C-P	0	88.219496	73.141853	56.085968	40.610932	29.196866
	50	92.644745	77.725784	60.691265	45.136468	33.591204
	100	97.057453	82.298033	65.2873438	49.648452	37.960864
C-C	0	171.978825	141.782221	108.012834	79.801395	61.973263
	50	194.878114	164.325089	111.724718	83.269291	65.289531
	100	198.515086	167.927968	115.422272	86.713451	68.575996
C-G	0	43.162442	36.512699	26.886961	21.480866	17.319545
	50	66.091837	59.354530	44.201739	38.490118	33.745313
	100	79.619024	73.035781	60.849096	54.508426	48.551928

Table 9: Non dimensional critical buckling loads ($\alpha = PL^2/E_0I$) for the axially functionally graded uniform columns with continuous elastic restraint ($\beta = kL^4/E_0I$) for exponential law gradient assumption ($E(\xi) = E_0e^{\mu\xi}$).

BC	β	$\mu = -1$	$\mu = -0.5$	$\mu = 0.5$	$\mu = 1$
C-F	0	1.782102	2.112127	2.844778	3.241181
	50	6.272146	7.534741	10.200538	11.507320
	100	8.112043	9.940415	14.224745	16.544646
P-P	0	5.826546	7.634493	12.587151	15.838195
	50	10.824282	12.684208	17.638042	20.845819
	100	15.772528	17.725908	22.685148	25.842687
C-P	0	11.988386	15.639912	25.782548	32.554915
	50	15.640533	19.528086	30.050913	36.962919
	100	19.113129	23.299501	34.275138	41.344887
C-C	0	23.490038	30.598353	50.448156	63.852545
	50	27.172950	34.353512	54.212593	67.556554
	100	30.785108	38.059830	57.948273	71.236233
C-G	0	5.972525	7.682708	12.666644	16.235007
	50	16.438031	19.863476	27.642188	32.240813
	100	21.152920	26.511574	39.345458	46.225436

case, the results are compared to results of [15] for available boundary conditions and found to be perfectly consistent. The results show the potential of LDQM for solution of generalized eigenvalue problems governed by fourth order varying coefficient ordinary differential equations with high accuracy and less computational effort.

5. Conclusions

In this study an LDQM is proposed and applied to the critical buckling load analyses of axially functionally graded nonuniform columns with elastic restraint. The method can be applied for any type of nonhomogeneity in the axial

Table 10: Non dimensional critical buckling loads ($\alpha = PL^2/E_0I_0$) for the axially functionally graded non-uniform columns with continuous elastic restraint ($\beta = kL^4/E_0I_0$) for C-F boundary condition.

β	c_h		c_b 0	0.2	0.4	0.6	0.8
0	0	Reference [15]	3.1177	2.9497	2.7676	2.5652	2.3285
		LDQM	3.117663	2.949668	2.767637	2.565141	2.328495
	0.2	Reference [15]	2.6225	2.4638	2.2915	2.0992	1.8725
		LDQM	2.622455	2.463779	2.291515	2.099165	1.872518
	0.4	Reference [15]	2.1054	1.9585	1.7988	1.6200	1.4074
		LDQM	2.105415	1.958547	1.798693	1.619887	1.407356
	0.6	Reference [15]	1.5522	1.4217	1.2798	1.1208	0.9309
		LDQM	1.552205	1.421546	1.279989	1.120782	0.930901
	0.8	Reference [15]	0.9245	0.8217	0.7109	0.5883	0.4441
		LDQM	0.924469	0.821641	0.710897	0.588251	0.444050
50	0	LDQM	10.969897	10.399534	9.730454	8.911626	7.828378
	0.2	LDQM	9.235948	8.649698	7.968922	7.148865	6.086033
	0.4	LDQM	7.195173	6.631250	5.989832	5.235064	4.284203
	0.6	LDQM	4.857766	4.387832	3.866699	3.271051	2.544323
	0.8	LDQM	2.344717	2.062718	1.758631	1.421514	1.024155
100	0	LDQM	15.525762	14.520910	13.367622	11.997451	10.254518
	0.2	LDQM	12.557084	11.612707	10.545695	9.300364	7.742857
	0.4	LDQM	9.374096	8.560820	7.656126	6.617654	5.337232
	0.6	LDQM	6.093411	5.484473	4.816329	4.058816	3.136808
	0.8	LDQM	2.854117	2.516107	2.150262	1.741823	1.254405

Table 11: Non dimensional critical buckling loads ($\alpha = PL^2/E_0I_0$) for the axially functionally graded non-uniform columns with continuous elastic restraint ($\beta = kL^4/E_0I_0$) for C-C boundary condition.

β	c_h		c_b 0	0.2	0.4	0.6	0.8
0	0	Reference [15]	57.3940	51.7856	45.7356	38.9917	30.8922
		LDQM	57.393956	51.785589	45.735646	38.991689	30.892202
	0.2	Reference [15]	41.9169	37.6023	32.9638	27.8171	21.6802
		LDQM	41.916891	37.602328	32.963838	27.817083	21.680218
	0.4	Reference [15]	28.1794	25.0890	21.7813	18.1332	13.8242
		LDQM	28.179398	25.089039	21.781290	18.133162	13.824196
	0.6	Reference [15]	16.3412	14.3958	12.3266	10.0639	7.4275
		LDQM	16.341179	14.395830	12.326582	10.063919	7.427477
	0.8	Reference [15]	6.6801	5.7836	4.8399	3.8228	2.6649
		LDQM	6.680051	5.783574	4.839860	3.822760	2.664885
50	0	LDQM	61.166910	55.582013	49.557537	42.839820	34.759070
	0.2	LDQM	45.734227	41.416605	36.768958	31.599542	25.400286
	0.4	LDQM	31.958849	28.829688	25.466443	21.730794	17.253425
	0.6	LDQM	19.880964	17.847607	15.659665	13.222303	10.279687
	0.8	LDQM	9.367432	8.320721	7.182753	5.897801	4.324708
100	0	LDQM	64.914455	59.351070	53.349176	46.652798	38.579025
	0.2	LDQM	49.518379	45.193527	40.530226	35.326471	29.036478
	0.4	LDQM	35.683768	32.505243	29.069896	25.216920	20.502165
	0.6	LDQM	23.285078	21.132662	18.778906	16.088335	12.689894
	0.8	LDQM	11.549700	10.288383	8.886242	7.271719	5.279100

Table 12: Non dimensional critical buckling loads ($\alpha = PL^2/E_0I_0$) for the axially functionally graded non-uniform columns with continuous elastic restraint ($\beta = kL^4/E_0I_0$) for P-P boundary condition.

β	c_h		c_b 0	0.2	0.4	0.6	0.8
0	0	Reference [15]	14.5112	13.1398	11.6969	10.1451	8.3957
		LDQM	14.511250	13.139786	11.696914	10.145084	8.395671
	0.2	Reference [15]	10.6860	9.5971	8.4543	7.2284	5.8498
		LDQM	10.686041	9.597121	8.454289	7.228449	5.849840
	0.4	Reference [15]	7.2831	6.4715	5.6228	4.7164	3.7019
		LDQM	7.283103	6.471476	5.622776	4.716370	3.701880
	0.6	Reference [15]	4.3287	3.7892	3.2283	2.6338	1.9748
		LDQM	4.328693	3.789166	3.228315	2.633792	1.974761
	0.8	Reference [15]	1.8667	1.5950	1.3157	1.0239	0.7075
		LDQM	1.866691	1.595022	1.315685	1.023937	0.707517
50	0	LDQM	19.549179	18.192929	16.760939	15.207995	13.417864
	0.2	LDQM	15.752005	14.659979	13.503215	12.238938	10.750059
	0.4	LDQM	12.298411	11.454703	10.551443	9.542443	8.289481
	0.6	LDQM	9.058173	8.426077	7.721329	6.876642	5.694553
	0.8	LDQM	5.246198	4.728938	4.126561	3.402176	2.479665
100	0	LDQM	24.581143	23.242950	21.824406	20.269884	18.419554
	0.2	LDQM	20.817957	19.721682	18.544637	17.218652	15.521898
	0.4	LDQM	17.286073	16.384686	15.372020	14.125521	12.234643
	0.6	LDQM	13.406960	12.499393	11.357450	9.833780	7.688312
	0.8	LDQM	6.909430	6.121287	5.250381	4.263196	3.070432

Table 13: Non dimensional critical buckling loads ($\alpha = PL^2/E_0I_0$) for the axially functionally graded non-uniform columns with continuous elastic restraint ($\beta = kL^4/E_0I_0$) for C-P boundary condition.

β	c_h	c_b 0	0.2	0.4	0.6	0.8
0	0	29.448963	26.600568	23.560586	20.230563	16.374540
	0.2	21.553772	19.335410	16.972868	14.391143	11.408619
	0.4	14.537718	12.927659	11.218322	9.357427	7.216955
	0.6	8.475484	7.447400	6.361291	5.186232	3.845576
	0.8	3.499195	3.018030	2.514197	1.975492	1.371273
50	0	33.787588	30.872734	27.742199	24.278066	20.188428
	0.2	25.672288	23.367048	20.888218	18.137705	14.868142
	0.4	18.300248	16.579568	14.724334	12.655490	10.170102
	0.6	11.626112	10.462193	9.200015	7.780077	6.049347
	0.8	5.487561	4.864484	4.184411	3.415437	2.479706
100	0	38.091765	35.101502	31.866729	28.245336	23.874818
	0.2	29.723039	27.314852	24.695929	21.738031	18.107927
	0.4	21.920220	20.060135	18.018363	15.680300	12.748168
	0.6	14.463191	13.118252	11.623244	9.887789	7.688601
	0.8	6.910808	6.130247	5.269028	4.287546	3.090197

direction either in cross-section or in material properties. No fictitious points are used and boundary conditions are directly substituted into weighting coefficient matrices. The matrix dimension in the solution procedure reduces drastically compared to other DQ methods since there is no need to write any compatibility equations. The introduced method can easily be extended to 2Dimensional problems.

Acknowledgment

The authors would like to thank Pamukkale University Scientific Research Council for supporting this study under project contract no. 2011BSP013.

References

[1] V. Birman and L. W. Byrd, "Modeling and analysis of functionally graded materials and structures," *Applied Mechanics Reviews*, vol. 60, no. 1–6, pp. 195–216, 2007.

[2] A. Dinnik, "Design of columns of varying cross-section," *Journal of Applied Mechanics*, vol. 54, pp. 165–171, 1932.

[3] M. Eisenberger, "Buckling loads for variable cross-section members with variable axial forces," *International Journal of Solids and Structures*, vol. 27, no. 2, pp. 135–143, 1991.

[4] I. Elishakoff and F. Pellegrini, "Exact solutions for buckling of some divergence-type nonconservative systems in terms of bessel and lommel functions," *Computer Methods in Applied Mechanics and Engineering*, vol. 66, no. 1, pp. 107–119, 1988.

[5] I. Elishakoff and O. Rollot, "New closed-form solutions for buckling of a variable stiffness column by mathematica," *Journal of Sound and Vibration*, vol. 224, no. 1, pp. 172–182, 1999.

[6] I. Caliò and I. Elishakoff, "Closed-form trigonometric solutions for inhomogeneous beam-columns on elastic foundation," *International Journal of Structural Stability and Dynamics*, vol. 4, no. 1, pp. 139–146, 2004.

[7] I. Calio and I. Elishakoff, "Closed-form solutions for axially graded beam-columns," *Journal of Sound and Vibration*, vol. 280, no. 3–5, pp. 1083–1094, 2005.

[8] C. M. Wang, C. Y. Wang, and J. N. Reddy, *Exact Solutions for Buckling of Structural Members*, CRC Press, 2005.

[9] R. Bellman and J. Casti, "Differential quadrature and long-term integration," *Journal of Mathematical Analysis and Applications*, vol. 34, no. 2, pp. 235–238, 1971.

[10] R. Bellman, B. G. Kashef, and J. Casti, "Differential quadrature: a technique for the rapid solution of nonlinear partial differential equations," *Journal of Computational Physics*, vol. 10, no. 1, pp. 40–52, 1972.

[11] C. W. Bert and M. Malik, "Differential quadrature method in computational mechanics: a review," *Applied Mechanics Reviews*, vol. 49, no. 1, pp. 1–27, 1996.

[12] G. Karami and P. Malekzadeh, "A new differential quadrature methodology for beam analysis and the associated differential quadrature element method," *Computer Methods in Applied Mechanics and Engineering*, vol. 191, no. 32, pp. 3509–3526, 2002.

[13] S. Rajasekaran, "Buckling of fully and partially embedded nonprismatic columns using differential quadrature and differential transformation methods," *Structural Engineering and Mechanics*, vol. 28, no. 2, pp. 221–238, 2008.

[14] S. Rajasekaran, L. Gimena, P. Gonzaga, and F. N. Gimena, "Solution method for the classical beam theory using differential quadrature," *Structural Engineering and Mechanics*, vol. 33, no. 6, pp. 675–696, 2009.

[15] A. Shahba and S. Rajasekaran, "Free vibration and stability of tapered Euler-Bernoulli beams made of axially functionally graded materials," *Applied Mathematical Modelling*, vol. 36, no. 7, pp. 3094–3111, 2012.

[16] I. Elishakoff, "Inverse buckling problem for inhomogeneous columns," *International Journal of Solids and Structures*, vol. 38, no. 3, pp. 457–464, 2001.

[17] L. Wu, Q.-S. Wang, and I. Elishakoff, "Semi-inverse method for axially functionally graded beams with an anti-symmetric vibration mode," *Journal of Sound and Vibration*, vol. 284, no. 3–5, pp. 1190–1202, 2005.

[18] M. Aydogdu, "Semi-inverse method for vibration and buckling of axially functionally graded beams," *Journal of Reinforced Plastics and Composites*, vol. 27, no. 7, pp. 683–691, 2008.

[19] E. M. Totry, E. Altus, and A. Proskura, "Buckling of nonuniform beams by a direct functional perturbation method," *Probabilistic Engineering Mechanics*, vol. 22, no. 1, pp. 88–99, 2007.

[20] S. B. Coşkun and M. T. Atay, "Determination of critical buckling load for elastic columns of constant and variable cross-sections using variational iteration method," *Computers and Mathematics with Applications*, vol. 58, no. 11-12, pp. 2260–2266, 2009.

[21] M. T. Atay and S. B. Coşkun, "Elastic stability of Euler columns with a continuous elastic restraint using variational iteration method," *Computers and Mathematics with Applications*, vol. 58, no. 11-12, pp. 2528–2534, 2009.

[22] S. B. Coçkun, "Determination of critical buckling loads for euler columns of variable flexural stiffness with a continuous elastic restraint using homotopy perturbation method," *International Journal of Nonlinear Sciences and Numerical Simulation*, vol. 10, no. 2, pp. 191–197, 2009.

[23] M. T. Atay, "Determination of critical buckling loads for variable stiffness euler columns using homotopy perturbation method," *International Journal of Nonlinear Sciences and Numerical Simulation*, vol. 10, no. 2, pp. 199–206, 2009.

[24] M. O'Rourke and T. Zebrowski, "Buckling load for nonuniform columns," *Computers and Structures*, vol. 7, no. 6, pp. 717–720, 1977.

[25] A. Shahba, R. Attarnejad, and S. Hajilar, "Free vibration and stability of axially functionally graded tapered Euler-Bernoulli beams," *Shock and Vibration*, vol. 18, no. 5, pp. 683–696, 2011.

[26] F. Arbabi and F. Li, "Buckling of variable cross-section columns. Integral-equation approach," *Journal of Structural Engineering*, vol. 117, no. 8, pp. 2426–2441, 1991.

[27] S. Yuan, K. Ye, C. Xiao, F. W. Williams, and D. Kennedy, "Exact dynamic stiffness method for non-uniform Timoshenko beam vibrations and Bernoulli-Euler column buckling," *Journal of Sound and Vibration*, vol. 303, no. 3–5, pp. 526–537, 2007.

[28] K. V. Singh and G. Li, "Buckling of functionally graded and elastically restrained non-uniform columns," *Composites B*, vol. 40, no. 5, pp. 393–403, 2009.

[29] Y. Huang and X.-F. Li, "Buckling analysis of nonuniform and axially graded columns with varying flexural rigidity," *Journal of Engineering Mechanics*, vol. 137, no. 1, pp. 73–81, 2010.

[30] Y. Huang and Q.-Z. Luo, "A simple method to determine the critical buckling loads for axially inhomogeneous beams with elastic restraint," *Computers and Mathematics with Applications*, vol. 61, no. 9, pp. 2510–2517, 2011.

[31] C. Shu, *Differential Quadrature and Its Application in Engineering*, Springer, London, UK, 2000.

[32] Z. Zong and K. Y. Lam, "A localized differential quadrature (LDQ) method and its application to the 2D wave equation," *Computational Mechanics*, vol. 29, no. 4-5, pp. 382–391, 2002.

[33] C. H. Tsai, D. L. Young, and C. C. Hsiang, "The localized differential quadrature method for two-dimensional stream function formulation of Navier-Stokes equations," *Engineering Analysis with Boundary Elements*, vol. 35, no. 11, pp. 1190–1203, 2011.

[34] M. E. Hamidi, M. R. Hashemi, N. Talebbeydokhti, and S. P. Neill, "Numerical modeling of the mild slope equation using localised differential quadrature method," *Ocean Engineering*, vol. 47, pp. 88–103, 2012.

[35] Z. Zong and Y. Zhang, *Advanced Differential Quadrature Methods*, Chapman & Hall/CRC Applied Mathematics and Nonlinear Science Series, CRC Press, Boca Raton, Fla, USA, 2009.

[36] C. Shu and B. E. Richards, "Application of generalized differential quadrature to solve two-dimensional incompressible Navier-Stokes equations," *International Journal for Numerical Methods in Fluids*, vol. 15, no. 7, pp. 791–798, 1992.

[37] M. Shariyat and M. M. Alipour, "Differential transform vibration and modal stress analyses of circular plates made of two-directional functionally graded materials resting on elastic foundations," *Archive of Applied Mechanics*, vol. 81, no. 9, pp. 1289–1306, 2011.

Hindawi Publishing Corporation
Mathematical Problems in Engineering
Volume 2013, Article ID 476131, 10 pages
http://dx.doi.org/10.1155/2013/476131

Research Article

Analysis of Sigmoid Functionally Graded Material (S-FGM) Nanoscale Plates Using the Nonlocal Elasticity Theory

Woo-Young Jung[1] and Sung-Cheon Han[2]

[1] *Department of Civil Engineering, Gangneung-Wonju National University, 7 Jukheon, Gangneung 210-702, Republic of Korea*
[2] *Department of Civil & Railroad Engineering, Daewon University College, 599 Shinwol, Jecheon 390-702, Republic of Korea*

Correspondence should be addressed to Sung-Cheon Han; hasc1203@daum.net

Received 13 April 2013; Accepted 16 May 2013

Academic Editor: Abdelouahed Tounsi

Copyright © 2013 W.-Y. Jung and S.-C. Han. This is an open access article distributed under the Creative Commons Attribution License, which permits unrestricted use, distribution, and reproduction in any medium, provided the original work is properly cited.

Based on a nonlocal elasticity theory, a model for sigmoid functionally graded material (S-FGM) nanoscale plate with first-order shear deformation is studied. The material properties of S-FGM nanoscale plate are assumed to vary according to sigmoid function (two power law distribution) of the volume fraction of the constituents. Elastic theory of the sigmoid FGM (S-FGM) nanoscale plate is reformulated using the nonlocal differential constitutive relations of Eringen and first-order shear deformation theory. The equations of motion of the nonlocal theories are derived using Hamilton's principle. The nonlocal elasticity of Eringen has the ability to capture the small scale effect. The solutions of S-FGM nanoscale plate are presented to illustrate the effect of nonlocal theory on bending and vibration response of the S-FGM nanoscale plates. The effects of nonlocal parameters, power law index, aspect ratio, elastic modulus ratio, side-to-thickness ratio, and loading type on bending and vibration response are investigated. Results of the present theory show a good agreement with the reference solutions. These results can be used for evaluating the reliability of size-dependent S-FGM nanoscale plate models developed in the future.

1. Introduction

The nanoscale plates have attracted attention of scientific community in solid-state physics, materials science, and nanoelectronics due to their superior mechanical, chemical, and electronic properties. Conducting experiments with nanoscale size specimens is both expensive and difficult. Hence, development of appropriate mathematical models for nanostructures is an important issue concerning the application of nanostructures. The nanostructures are modeled into three main categories using atomistic [1, 2], hybrid atomistic-continuum mechanics [3–5] and continuum mechanics [6, 7]. Continuum mechanics approach is less computationally expensive than the former two approaches. Further, it has been found that continuum mechanics results are in good agreement with those obtained from atomistic and hybrid approaches. Due to the presence of small scale effects at the nanoscale structures, size-dependent continuum mechanics models such as the strain gradient theory (Nix and Gao [8]), couple stress theory (Hadjesfandiari and Dargush [9]), modified couple stress theory (Asghari et al. [10]; Ma et al. [11]; Reddy [12]), and nonlocal elasticity theory (Eringen [13]) are used.

The small size analysis using local theory overpredicts the results. Thus the consideration of small effects is necessary for correct prediction of micro/nano-structures. Peddieson et al. [14] applied nonlocal elasticity to formulate a nonlocal version of the Euler-Bernoulli beam model and concluded that nonlocal continuum mechanics could potentially play a useful role in nanotechnology applications. One of the well-known continuum mechanics theory that includes small scale effects with good accuracy is the nonlocal theory of Eringen [6, 7, 13]. Unlike the local theories which assume that the stress at a point is a function of strain at that point, the nonlocal elasticity theory assumes that the stress at a point is a function of strains at all points in the continuum. Compared to classical continuum mechanics theories, nonlocal theory of Eringen has capability to predict behavior of the large nano-sized structures, while it avoids solving the large number of equations.

Functionally graded material (FGM) is a class of composites in which the material properties vary smoothly and continuously from one surface to the other and thus eliminates the stress concentration found in laminated composites. The other advantage of FGM is that it mitigates singularities at intersections between interfaces usually presented in laminate composites due to their abrupt transitions in material compositions and properties. A generally FGM is made from a mixture of ceramic and metal. The FGM is a composite material whose composition varies according to the required performance. The increase in FGM applications requires accurate models to predict their responses. A critical review of recent works on the bending analysis of functionally graded (FG) plates can be found in Jha et al. [15]. Since the shear deformation has significant effects on the responses of FG plates, shear deformation theories such as first-order shear deformation theory (FSDT) should be used to analyze FG plates. If a high external pressure is applied to the composite plate and shell structures, the high stresses occurred in the structure will affect its integrity, and the structure, as the result, susceptible to failure. For these reasons, understanding the mechanical behavior of FGM plates and shells is very important to assess the safety of the shell and plate structure. Chung and Chi [16] proposed a sigmoid FGM (S-FGM), which is composed of two power-law functions to define a new volume fraction. The effect of loading conditions, the aspect ratio, and the change of elastic modulus on the mechanical behavior of S-FGM plates was investigated in Chi and Chung [17]. Recent work on the vibration, buckling, and geometrically nonlinear analysis of S-FGM plates and shells can be founded in Han et al. [18] and Han et al. [19].

In the literature a great deal of attention has been focused on studying the bending, vibration, and buckling behavior of one-dimensional nanostructures using nonlocal elasticity theory (Aydogdu [20]; Civalek and Demir [21]; Reddy [22]; Reddy and Pang [23]; Reddy [24]; Roque et al. [25]; Wang and Liew [26]; Wang et al. [27]). These nanostructures include nanobeams, nanorods, and carbon nanotubes. In recent years, the application of FGMs has broadly been spread in micro- and nanoscale devices and systems such as thin films [28, 29], atomic force microscopes [30], micro- and nanoelectromechanical systems (MEMS and NEMS) [31, 32]. In such applications, size effects have been experimentally observed [33–36]. On the contrary a few works appear related to the bending analysis of functionally graded material (FGM) nanoscale plate based on first-order shear deformation theory. The present study deals with the use of the nonlocal first-order plate theory in bending response of S-FGM nanoscale plates. Based on the nonlocal constitutive relations of Eringen, equations of motion of nanoscale plates are derived using Hamilton's principle. Closed-form solutions of deflection are obtained for simply supported S-FGM nanoscale plates. The effects of (i) nonlocal parameters, (ii) power law indexes, (iii) E_1/E_2 ratios, (iv) aspect ratios, (v) side-to-thickness ratios, and (vi) loading types on nondimensional bending responses are investigated. To illustrate the accuracy of the present theory, the numerical examples are investigated and compared with those solutions from the previous literatures. The present work would be helpful while designing nano-electro-mechanical system and micro-electro-mechanical systems devices using the S-FGM nanoscale plates.

2. Review of Nonlocal Elasticity

According to Eringen [6, 7, 13], the stress field at a point x in an elastic continuum not only depends on the strain field at the point (hyperelastic case) but also on strains at all other points of the body. Eringen attributed this fact to the atomic theory of lattice dynamics and experimental observations on phonon dispersion. Thus, the nonlocal stress tensor components σ_{ij} at point $\mathbf{x}$ are expressed as

$$\sigma_{ij}(\mathbf{x}) = \int_V K(|\overline{\mathbf{x}} - \mathbf{x}|, \tau)\, t_{ij}(\overline{\mathbf{x}})\, d\overline{\mathbf{x}}, \tag{1}$$

where $t_{ij}(\mathbf{x})$ are the components of the classical macroscopic stress tensor at point $\mathbf{x}$ and the kernel function $K(|\overline{\mathbf{x}} - \mathbf{x}|, \tau)$ represents the nonlocal modulus, $|\overline{\mathbf{x}} - \mathbf{x}|$ being the distance (in Euclidean norm) and τ is a material constant that depends on internal and external characteristic lengths (such as the lattice spacing and wavelength, resp.). The macroscopic stress $\mathbf{t}$ at point $\mathbf{x}$ in a Hookean solid is related to the strain at the point by the generalized Hooke's law

$$t(\mathbf{x}) = \mathbf{C}(\mathbf{x}) : \varepsilon(\mathbf{x}) \quad \text{or} \quad t_{ij} = C_{ijkl}\varepsilon_{kl}, \tag{2}$$

where $\mathbf{C}$ is the fourth-order elasticity tensor and: denotes the "double-dot product" (see Reddy [22]).

In the nonlocal linear elasticity, equations of motion can be obtained from nonlocal balance law

$$\sigma_{ij,j} + f_i = \rho \ddot{u}_i, \tag{3}$$

where i, j take the symbols x, y, z and f_i, ρ, and u_i are the components of the body force, mass density and displacement vector [13]. By substituting (1) into (3), the integral form of nonlocal constitutive equation is obtained. Because solving an integral equation is more difficult than a differential equation, Eringen [6, 7, 13] proposed a differential form of the nonlocal constitutive equation as

$$t_{ij,j} + \mathscr{L}\left(f_i - \rho \ddot{u}_i\right) = 0, \tag{4}$$

in which the linear differential operator $\mathscr{L}$ was defined by

$$\mathscr{L} = 1 - \mu\nabla^2, \qquad \mu = e_0^2 \overline{a}^2, \tag{5}$$

where μ is the nonlocal parameter, e_0 is material constant which is defined by the experiment, and $\overline{a}$ is the internal characteristic length.

By applying this operator on (1), the constitutive equation can be simplified to

$$\mathscr{L}\left(\sigma_{ij}\right) = C_{ijkl}\varepsilon_{kl}. \tag{6}$$

Equation (6) is simpler and more convenient than the integral relation (1) to apply to various linear elasticity problems.

3. Plate Equations of Nonlocal Elasticity

Using (2) and (6), stress resultants introduced in plate and shell theories can be reformulated in terms of strain for the nonlocal theory. In plate theories based on plane-stress assumption, we take $\sigma_{zz} = 0$ and the resulting theory becomes two-dimensional.

Consider a (x, y, z) coordinate system with the xy-plane coinciding with the mid-plane of the plate. So the stress-strain relations of plane-stress can be expressed as

$$t_{\alpha\beta} = \overline{C}_{\alpha\beta\gamma\delta}\varepsilon_{\gamma\delta}, \tag{7}$$

where $\overline{C}_{\alpha\beta\gamma\delta} = C_{\alpha\beta\gamma\delta} - C_{\alpha\beta zz}C_{zz\gamma\delta}/C_{zzzz}$, and transverse shear stress-strain relation is expressed as

$$t_{\alpha z} = 2\overline{C}_{\alpha z\gamma z}\varepsilon_{\gamma z}, \tag{8}$$

where α, β, γ, s the shear correction factoand δ take the symbols x, y.

The relations between stress resultants in local theory and nonlocal theory are defined by integrating (6) through the plate thickness:

$$\mathscr{L}\left(N_{ij}\right) = N_{ij}^{L}, \qquad \mathscr{L}\left(M_{ij}\right) = M_{ij}^{L}, \tag{9}$$

where

$$\begin{Bmatrix} N_{\alpha\beta}, N_{\alpha\beta}^{L} \\ M_{\alpha\beta}, M_{\alpha\beta}^{L} \end{Bmatrix} = \int_{-h/2}^{h/2} \left\{\sigma_{\alpha\beta}, t_{\alpha\beta}\right\} \begin{Bmatrix} 1 \\ z \end{Bmatrix} dz, \tag{10}$$

$$\left\{N_{\alpha z}, N_{\alpha z}^{L}\right\} = \int_{-h/2}^{h/2} \left\{\sigma_{\alpha z}, t_{\alpha z}\right\} dz. \tag{11}$$

The superscript L denoted the quantities in local first-order shear deformation theory and h is the thickness of the plate. The governing equation of the plate in nonlocal theory can be determined by integrating (3) through the plate thickness and noting (10)

$$N_{\alpha i,\alpha} + F_i = \int_{-h/2}^{h/2} \rho\ddot{u}_i \, dz, \tag{12}$$

where $F_i = \int_{-h/2}^{h/2} f_i dz$. By multiplying (3) by z and then integrating from it through plate thickness and using integration-by-parts, we obtain

$$M_{\alpha\beta,\beta} - N_{\alpha z} = \int_{-h/2}^{h/2} \rho\ddot{u}_\alpha z \; dz. \tag{13}$$

In general, differential operator ∇ in (6) is the 3D Laplace operator. For 2D problems, the operator ∇ may be reduced to 2D one. Thus, the linear differential operator $\mathscr{L}$ becomes

$$\overline{\mathscr{L}} = 1 - \left(\frac{\partial^2}{\partial x^2} + \frac{\partial^2}{\partial y^2}\right). \tag{14}$$

It is clear that the operator $\overline{\mathscr{L}}$ is independent of the z direction.

4. Nonlocal First-Order Shear Deformation Theory

The classical plate theory is based on the Kirchhof assumptions, in which transverse normal and shear stresses are neglected. In the first-order shear deformation theory (FSDT), a constant state of transverse shear stresses is accounted for, and often the transverse normal stress is neglected. The displacement field of the first-order theory of plates is given by

$$u_\alpha = u_\alpha^0 + z\phi_\alpha, \qquad u_z = w^0, \tag{15}$$

where u_α are the inplane displacements of point on the mid-plane (i.e., $z = 0$) at $t = 0$, u_z is the transverse displacement of the mid-plane of the plate, and ϕ_α denotes the slope of the transverse normal on mid-plane.

By substituting the displacement field into (12)-(13), we obtain

$$N_{\alpha i,\alpha} + F_i = I_0\ddot{u}_i^0, \tag{16}$$

$$M_{\alpha\beta,\beta} - N_{\alpha z} = I_2\ddot{\phi}_\alpha. \tag{17}$$

Then (16) for $i = z$ and (17) can be combined to drive the following governing equations for flexural response of the nonlocal first-order plate theory:

$$N_{\alpha z,\alpha} + q_z = I_0\ddot{w}^0, \tag{18}$$

$$M_{\alpha\beta,\beta} - N_{\alpha z} = I_2\ddot{\phi}_\alpha, \tag{19}$$

where $I_k = \int_{-h/2}^{h/2} \rho(z)^k dz \ (k = 0, 2)$.

5. Variational Statements

The variational statements facilitate the direct derivation of the equations of motion in terms of the displacements. Hence, we also present the variational form of governing equations which is useful in integral formulations and displacement finite element formulations. The governing equations of the first-order nonlocal plate theory can be derived using dynamic version of the principle of virtual displacement (Hamilton's principle)

$$0 = \int_0^T (\delta U + \delta V - \delta K) \; dt. \tag{20}$$

By substituting nonlocal stress resultants in terms of the displacements into the principle of virtual displacements and integrate by part, the equations of motion can be obtained as follows:

$$\delta u_x^0 : N_{xx,x} + N_{xy,y} - \overline{\mathscr{L}}\left(I_0\ddot{u}_x^0\right) = 0, \tag{21}$$

$$\delta u_y^0 : N_{xy,x} + N_{yy,y} - \overline{\mathscr{L}}\left(I_0\ddot{u}_y^0\right) = 0, \tag{22}$$

$$\delta w^0 : N_{xz,x} + N_{yz,y} - \overline{\mathscr{L}}\left[q_z - I_0\ddot{w}^0\right] = 0, \tag{23}$$

$$\delta\phi_x : M_{xx,x} + M_{xy,y} - N_{xz} - \overline{\mathscr{L}}\left[I_2\ddot{\phi}_x\right] = 0, \tag{24}$$

$$\delta\phi_y : M_{xy,x} + M_{yy,y} - N_{yz} - \overline{\mathscr{L}}\left[I_2\ddot{\phi}_y\right] = 0. \tag{25}$$

6. Constitutive Relations of S-FGM Structures

The functionally graded material (FGM) can be produced by continuously varying the constituents of multiphase materials in a predetermined profile. The most distinct features of an FGM are the nonuniform microstructures with continuously graded properties. An FGM can be defined by the variation in the volume fractions. Most researchers use the power-law function, exponential function, or sigmoid function to describe the volume fractions. This paper uses FGM plates and shells with sigmoid function.

The volume fraction using two power-law functions which ensure smooth distribution of stresses is defined as

$$V_f^1(t) = 1 - \frac{1}{2}\left(\frac{h/2 - t}{h/2}\right)^p \quad \text{for } 0 \le t \le \frac{h}{2}, \tag{26a}$$

$$V_f^2(t) = \frac{1}{2}\left(\frac{h/2 + t}{h/2}\right)^p \quad \text{for } -\frac{h}{2} \le t \le 0. \tag{26b}$$

By using the rule of mixture, the material properties of the S-FGM can be calculated by

$$H(t) = V_f^1(t)\,H_1 + \left(1 - V_f^1(t)\right)H_2 \quad \text{for } 0 \le t \le \frac{h}{2}, \tag{27a}$$

$$H(t) = V_f^2(t)\,H_1 + \left(1 - V_f^2(t)\right)H_2 \quad \text{for } -\frac{h}{2} \le t \le 0. \tag{27b}$$

Figure 1 shows that the variation of Young's modulus in (27a) and (27b) represents sigmoid distributions, and this FGM structure is thus called a sigmoid FGM structure (S-FGM structures). In this paper, the volume fraction using two power-law functions by Chung and Chi [16] is used to ensure smooth distribution of stresses among all the interfaces.

Consider an elastic rectangular plate and shell. The local coordinates r and s define the mid-plane of the plate and shell, whereas the t-axis originated at the middle surface of the plate and shell is in the thickness direction. The material properties, both of Young's modulus and the Poisson's ratio, the upper and lower surfaces are different but are preassigned according to the performance demands. However, the Young's modulus and Poisson's ratio of the plates and shells vary continuously only in the thickness direction (t-axis); that is, $E = E(t)$, $\nu = \nu(t)$. It is called functionally graded material (FGM) plate and shell.

The constitutive relations of the FGM structures are as follows:

$$\begin{Bmatrix} N_{\alpha\beta} \\ M_{\alpha\beta} \end{Bmatrix} = \begin{bmatrix} A_{\mathrm{FGM}}^{\alpha\beta\gamma\delta} & B_{\mathrm{FGM}}^{\alpha\beta\gamma\delta} \\ B_{\mathrm{FGM}}^{\alpha\beta\gamma\delta} & D_{\mathrm{FGM}}^{\alpha\beta\gamma\delta} \end{bmatrix} \begin{Bmatrix} \varepsilon_{\gamma\delta}^m \\ \varepsilon_{\gamma\delta}^b \end{Bmatrix}, \tag{28}$$

$$\{N_{\alpha z}\} = \left[A_{\mathrm{FGM}}^{\alpha z\beta z}\right]\left\{\varepsilon_{\beta z}^s\right\}. \tag{29}$$

The coefficients of (28) and (29) for FGM structures are defined as follows:

$$A_{\mathrm{FGM}}^{\alpha\beta\gamma\delta},\ B_{\mathrm{FGM}}^{\alpha\beta\gamma\delta},\ D_{\mathrm{FGM}}^{\alpha\beta\gamma\delta} = \int_{-h/2}^{h/2} C_{\mathrm{FGM}}^{\alpha\beta\gamma\delta}\left(1, z, z^2\right)dz,$$
$$A_{\mathrm{FGM}}^{\alpha z\beta z} = k_s \int_{-h/2}^{h/2} C_{\mathrm{FGM}}^{\alpha z\beta z}\,dz, \tag{30}$$

where k_s is the shear correction factor ($k_s = 5/6$). For details see Han et al. [18].

7. The Navier Solutions of S-FGM Nanoscale Plates

Here, analytical solutions for bending of simply supported S-FGM nanoscale plates are presented using the nonlocal first-order plate theory to illustrate the small scale effects on deflections of the nan-scale plates. For the static case, all time derivative terms are set to zero. For the set of simply supported boundary conditions, the analytical solution can be obtained [37]. According to the Navier solution theory, the generalized displacements at middle of the plane ($z = 0$) are expanded in double Fourier series as follows:

$$\begin{aligned}
u_x^0(x,y,t) &= \sum_{m=1}^{\infty}\sum_{n=1}^{\infty} U_{mn}\Lambda_1, \\
u_y^0(x,y,t) &= \sum_{m=1}^{\infty}\sum_{n=1}^{\infty} V_{mn}\Lambda_2, \\
w^0(x,y,t) &= \sum_{m=1}^{\infty}\sum_{n=1}^{\infty} W_{mn}\Lambda_3, \\
\phi_x(x,y,t) &= \sum_{m=1}^{\infty}\sum_{n=1}^{\infty} X_{mn}\Lambda_1, \\
\phi_y(x,y,t) &= \sum_{m=1}^{\infty}\sum_{n=1}^{\infty} Y_{mn}\Lambda_2, \\
q_z(x,y,t) &= \sum_{m=1}^{\infty}\sum_{n=1}^{\infty} Q_{mn}\Lambda_3,
\end{aligned} \tag{31}$$

where $\Lambda_1 = \cos\xi x \sin\eta y \cdot e^{i\bar{\omega}_{mn}t}$, $\Lambda_2 = \sin\xi x \cos\eta y \cdot e^{i\bar{\omega}_{mn}t}$, and $\Lambda_3 = \sin\xi x \sin\eta y \cdot e^{i\bar{\omega}_{mn}t}$ in which $\xi = m\pi/a$, $\eta = n\pi/b$, and $\bar{\omega}_{mn}$ is the natural frequency.

By substituting (31) into (21)–(25), matrix form is as follows:

$$[\mathbf{K}]\{\Delta\} + [\mathbf{M}]\left\{\ddot{\Delta}\right\} = \{Q\}, \tag{32}$$

where $\{\Delta\} = \{U_{mn}, V_{mn}, W_{mn}, X_{mn}, Y_{mn}\}$, the superposed dots denote differentiation with respect to time, $[\mathbf{K}]$ is the stiffness matrix, $[\mathbf{M}]$ is the mass matrix, and $\{Q\}$ is the force vector.

8. Numerical Results and Discussion

In order to validate, several numerical examples are solved to test the performance in bending analysis. Examples include

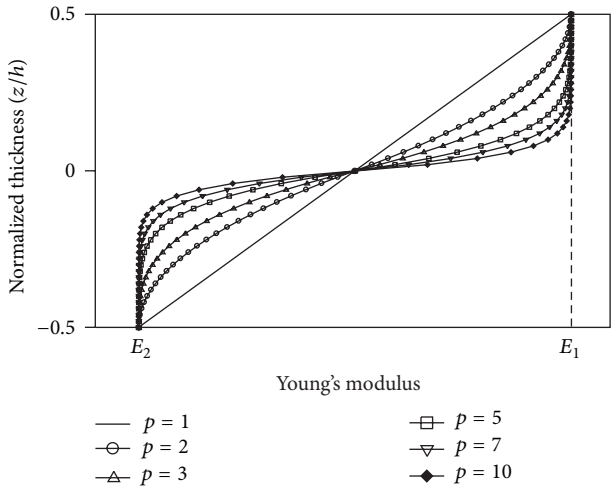

Figure 1: The variation of Young's modulus of S-FGM plate and shell.

P-FGM to check some crucial features and to make comparison with previous published analysis results.

8.1. Validation. Firstly, since the results of nanoscale plate made of S-FGM are not available in the open literature, homogeneous and P-FGM ($p = 1$) plates are used herein for the verification.

Table 1 shows the nondimensional displacements of simply supported plates with various values of side-to-thickness ratio a/h in homogeneous and functionally graded ($p = 1$) plates. The nanoscale plate is made of epoxy with the following material properties:

$$E_1 = 14.4 \text{ GPa}, \quad E_2 = 1.44 \text{ GPa}, \quad \nu = 0.38,$$
$$h = 17.6 \times 10^{-6} \text{ m}, \quad q_0 = 1.0 \text{ N/m}, \tag{33}$$
$$\rho_1 = 12.2 \times 10^3 \text{ kg/m}^3, \quad \rho_2 = 1.22 \times 10^3 \text{ kg/m}^3.$$

The nondimensional displacement and frequency are defined as

$$\overline{w} = w \frac{E_2 h^3}{q_0 a^4} \times 10^2, \quad \overline{\omega} = \omega \frac{a^2}{h} \sqrt{\frac{\rho_2}{E_2}}. \tag{34}$$

A shear correction factor of 5/6 is used for FSDT plate theory. The calculated displacements based on FSDT plate theory with S-FGM power law index ($p = 1$) are compared with those reported by Thai and Choi [38] based on Mindlin plate theory (MPT) with P-FGM index (Table 2). It can be observed that the present results are identical with those given by Thai and Choi [38] based on MPT. There is no difference between the present S-FGM results and those P-FGM results given by Thai and Choi [38]. This is due to the fact that the S-FGM material properties are identical with P-FGM, when the power law index is 1.

Secondly, the analytical bending solutions are numerically evaluated here for an isotropic plate to discuss the effects of nonlocal parameter μ on the plate bending response.

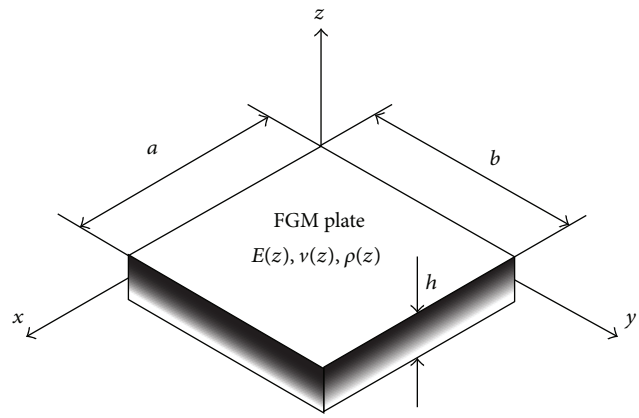

Figure 2: Geometry of S-FGM plate.

Table 3 shows the non-dimensional displacements of simply supported plates with various values of nonlocal parameter μ in homogeneous plates. The nanoscale plate is made of the following material properties:

$$E = 30 \times 10^6, \quad \nu = 0.3, \quad q_0 = 1.0. \tag{35}$$

The results based on FSDT plate theory with various values of nonlocal parameter μ are compared with those reported by Lee et al. [39] based on HSDT. It can be observed that the present results are identical with those given by Lee et al. [39] when the side-to-thickness ratio is 100. For the case of the $a/h = 10$, there is small difference between the present results and those given by Lee et al. [39]. This is due to the fact that Lee et al. [39] used HSDT to calculate the displacement, whereas the present results are based on the FSDT.

Thirdly, in Tables 4 and 5, the calculated frequency based on FSDT plate theory with S-FGM power law index ($p = 1$) is compared with those reported by Thai and Choi [38] with P-FGM index. The present results are identical with those given by Thai and Choi [38]. As we expected, there is no difference between the present S-FGM results and those P-FGM results given by Thai and Choi [38].

Fourthly, the results of S-FGM plates (see Figure 2) using the classical plate theory [17] are compared with present solutions using the FSDT for validation. The material properties are

$$E_1 = 2.1 \times 10^6 \text{ kg/cm}^2, \quad E_2 = \text{varied}, \quad \nu = 0.3,$$
$$a = 100 \text{ cm}, \quad h = 2 \text{ cm}, \quad q_0 = 1.0 \text{ kg/cm}^2. \tag{36}$$

The results of classical plate theory by Chi and Chung [17] and the results of first-order shear deformation theory are plotted in Figure 3. It shows that the more of E_1/E_2 brings the larger deflection, because lager E_1/E_2 decreases the stiffness of the FGM plate. The present and reference results agree very well.

In order to investigate the effects of the aspect ratio a/b, the center deflection of the FGM plate is shown in Figure 4. The center deflection increases upon raising the aspect ratio

Table 1: Nondimensional displacement of simply supported FGM plate.

a/h	A homogeneous plate		$p = 1$	
	P-FGM (Thai and Choi [38])	Present (S-FGM)	P-FGM (Thai and Choi [38])	Present (S-FGM)
5	0.5147	0.5147	1.1536	1.1536
10	0.4415	0.4415	1.0205	1.0205
20	0.4232	0.4232	0.9873	0.9873
100	—	0.4173	—	0.9766

Table 2: Nondimensional displacement of simply supported nano-scale FGM plate.

μ	A homogeneous plate		$p = 1$	
	P-FGM (Thai and Choi [38])	Present (S-FGM)	P-FGM (Thai and Choi [38])	Present (S-FGM)
0	0.4415	0.4415	1.0205	1.0205
1.0	—	0.6969	—	1.6123
2.25	—	1.0160	—	2.3521
4.0	—	1.4629	—	3.3878

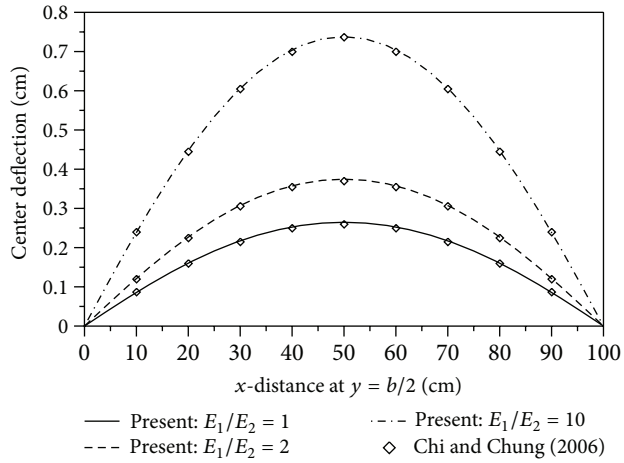

Figure 3: The deflection of S-FGM plate along the x direction for different E_1/E_2.

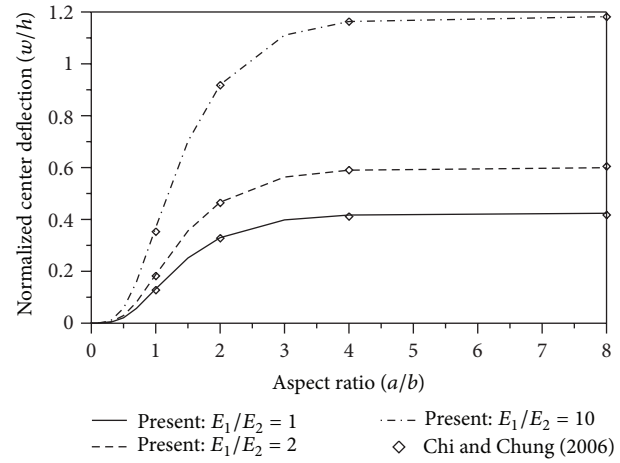

Figure 4: Normalized center deflection of S-FGM plate versus the aspect ratio for different E_1/E_2.

Table 3: Nondimensional displacement of simply supported nano-scale plate (100 term series).

μ	$a/h = 10$		$a/h = 100$	
	Lee et al. [39]	Present	Lee et al. [39]	Present
0	4.6658	4.6658	4.4384	4.4384
0.5	5.0836	5.0836	4.8408	4.8408
1	5.5014	5.5012	5.2432	5.2432
1.5	5.9192	5.9189	5.6456	5.6456
2	6.3370	6.3365	6.0480	6.0480
2.5	6.7548	6.7542	6.4504	6.4504
3	7.1726	7.1718	6.8528	6.8528
3.5	—	7.5895	—	7.2552
4	—	8.0071	—	7.6576

for a/b is less than 3. In Figures 3 and 4, it is clear that the results show very good agreement, because of the large side-to-thickness ratio. As expected, the less side-to-thickness ratio is, the error is larger. In this study, all discussions are based on the first-order shear deformation theory.

8.2. Parameter Studies. Consider a simply supported square plate with the material properties of (33). Parameter studies are presented to investigate the influences of transverse shear deformation, nonlocal parameter ($NT = \mu$), and power law index p on bending responses of S-FGM nanoscale plate.

To illustrate the effect of nonlocal parameter on responses of S-FGM nanoscale plate, Figure 5 plots the deflection with respect to dimensionless nonlocal parameter μ for a simply supported S-FGM plate with $p = 1.0$ and $a/h = 10$. The nonlocal parameters are taken as $\mu = 0, 1.0, 2.25$, and 4. These values are taken because $e_0\overline{a}$ in (5) should be smaller than 2.0 nm for carbon nanotubes as described by Q. Wang and C. M. Wang [40]. The inclusion of the nonlocal scale effect

Table 4: Nondimensional frequency of simply supported FGM plate.

a/h	A homogeneous plate		$p = 1$	
	P-FGM (Thai and Choi [38])	Present (S-FGM)	P-FGM (Thai and Choi [38])	Present (S-FGM)
5	5.3871	5.3871	4.8744	4.8744
10	5.9301	5.9301	5.2697	5.2697
20	6.0997	6.0997	5.3880	5.3880
100	—	6.1579	—	5.4280

Table 5: Nondimensional frequency of simply supported nano-scale FGM plate.

μ	A homogeneous plate		$p = 1$	
	P-FGM (Thai and Choi [38])	Present (S-FGM)	P-FGM (Thai and Choi [38])	Present (S-FGM)
0	5.9301	5.9301	5.2697	5.2697
1.0	—	4.6345	—	4.1184
2.25	—	3.8012	—	3.3779
4.0	—	3.1478	—	2.7973

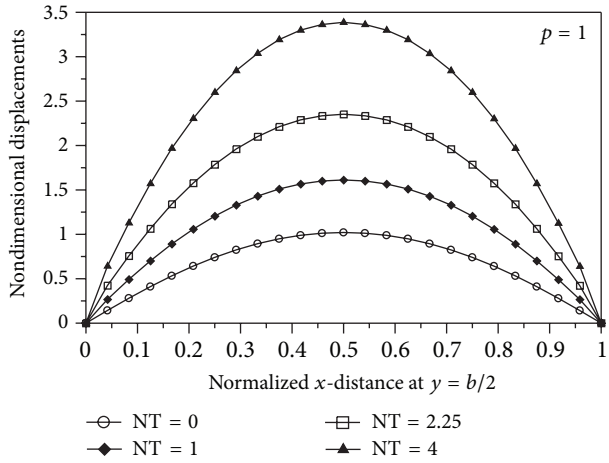

Figure 5: Effect of the nonlocal parameter on the nondimensional displacement of a simply supported S-FGM plate with $a/h = 10$.

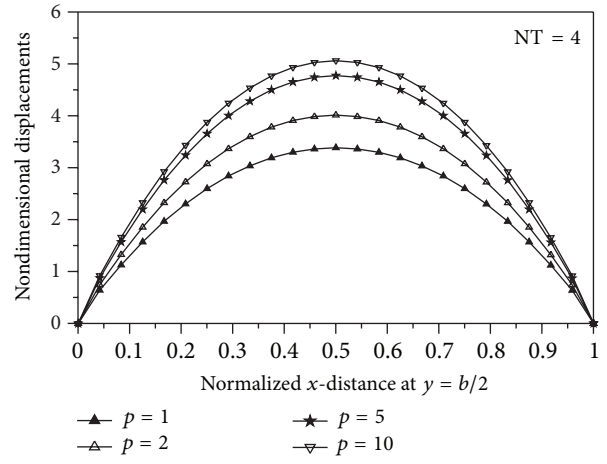

Figure 6: Effect of the power law index on the nondimensional displacement of a simply supported S-FGM plate with $a/h = 10$.

will decrease the stiffness of the S-FGM nanoscale plate, and consequently, leads to an enlargement of deflection.

The effect of the power law index p on the dimensionless deflection is presented in Figure 6 for a simply supported square plate with $\mu = 4.0$ and $a/h = 10$. The increasing value of the power law index decreases the stiffness of the S-FGM nanoscale plates. It can be seen that increasing value of the power law index leads to an increase in the magnitude of deflection. When the nonlocal parameter (NT) is 0, a nonlocal S-FGM nanoscale plate is treated as a local nanoplate.

To show the effect of E_1/E_2 of S-FGM nanoscale plate, Figure 7 plots the nondimensional displacement with $\mu = 4.0$, $p = 1.0$, and $a/h = 10$. In this case, E_1 is varied and E_2 is fixed. It shows that the more of E_1/E_2 brings the smaller deflection, because lager E_1/E_2 increases the stiffness of the S-FGM nanoscale plate.

It is shown that the effects of side-to-thickness ratio on the dimensionless deflection is presented in Figure 8 for a simply supported square plate with $\mu = 4.0$ and $a/h = 10$. Figure 8 clearly shows the diminishing effect of transverse shear deformation on deflections, the effect being negligible for side-to-thickness ratios larger than 30. The increasing value of the power law index leads to an increase in the magnitude of deflection and the increasing value of side-to-thickness ratio leads to a decrease in the deflection. As expected, the effect of transverse shear deformation is to increase deflection. The differences in deflection values predicted by the present model and the classical model are significant when the side-to-thickness ration is small, but they are negligible when the side-to-thickness ratio becomes larger.

Figure 9 shows that the effect of power law index on the dimensionless deflection is presented for a simply supported square plate with various nonlocal parameters. The increasing

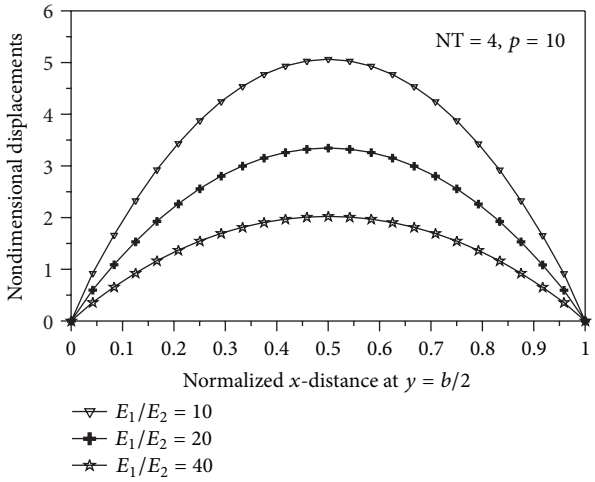

Figure 7: Effect of the E_1/E_2 ratio on the nondimensional displacement of a simply supported S-FGM plate with $a/h = 10$.

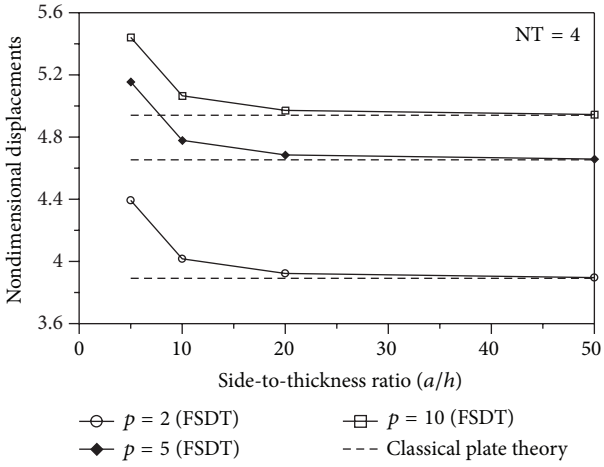

Figure 8: Effect of the side-to-thickness ratio on the nondimensional displacement of a simply supported S-FGM plate with $\mu = 4.0$.

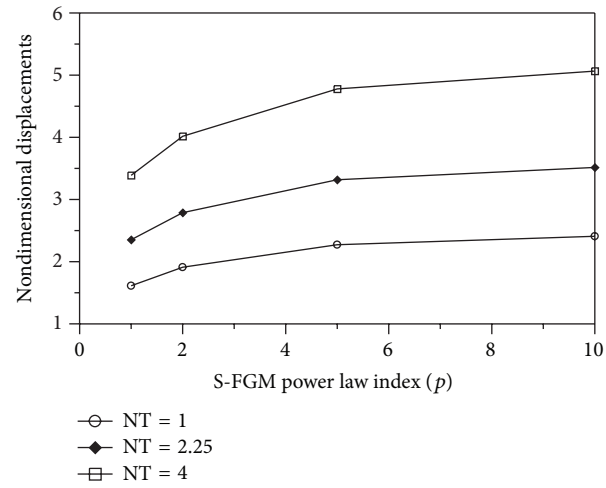

Figure 9: Effect of the power law index on the nondimensional displacement of a simply supported S-FGM plate with various nonlocal parameters.

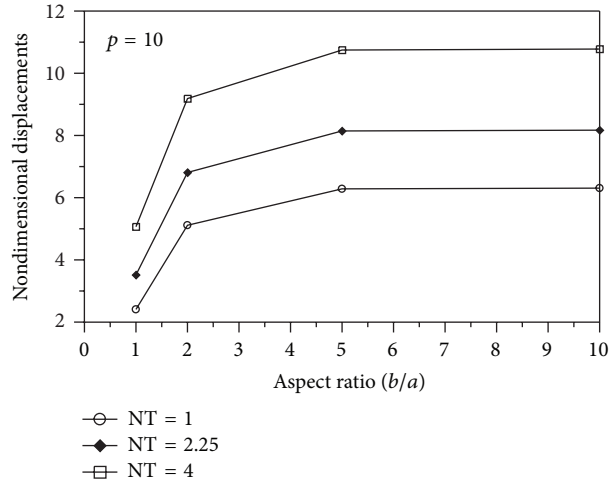

Figure 10: Effect of the aspect ratio on the nondimensional displacement of a simply supported S-FGM plate with various nonlocal parameters.

value of the power law index decreases the stiffness and the increasing value of the nonlocal parameter increases the load vector of the S-FGM nanoscale plates. The increasing value of the power law index leads to an increase in the magnitude of deflection and the increasing value of the nonlocal parameter leads to an increase in the deflection.

It is shown that the effect of the aspect ratio on the dimensionless deflection is presented in Figure 10 for a simply supported square plate with various nonlocal parameters and $p = 10.0$. The increasing values of the aspect ratio (b/a) and nonlocal parameter decrease the stiffness of the S-FGM nanoscale plates. When the width b of a nanoscale plate is very small compared to the length a, it is treated as a nanoscale beam. The increasing value of the aspect ratio leads to an increase in the magnitude of deflection and the increasing value of the nonlocal parameter leads to an increase in the deflection. The nondimensional center deflection increases upon raising the aspect ratio for b/a less than 5.

Figure 11 shows that the aspect ratio on the dimensionless deflection is presented for a simply supported square plate with various power law indexes and $\mu = 4.0$. As we expected, the increasing value of power law index decreases the stiffness of the S-FGM nanoscale plates. For this reason, it increases the deflection. The nondimensional center deflection increases upon raising the aspect ratio for b/a less than 5. When the aspect ratio (b/a) is greater than 5, a S-FGM nanoscale plate is treated as a nanobeam.

To illustrate the effect of the loading type on responses of S-FGM nanoscale plate, Figure 12 plots the deflection with respect to uniform and sinusoidal load for a simply supported S-FGM plate with $\mu = 4.0$, $p = 10.0$, and $a/h = 10$. The sinusoidal load on the S-FGM nanoscale plate is small in

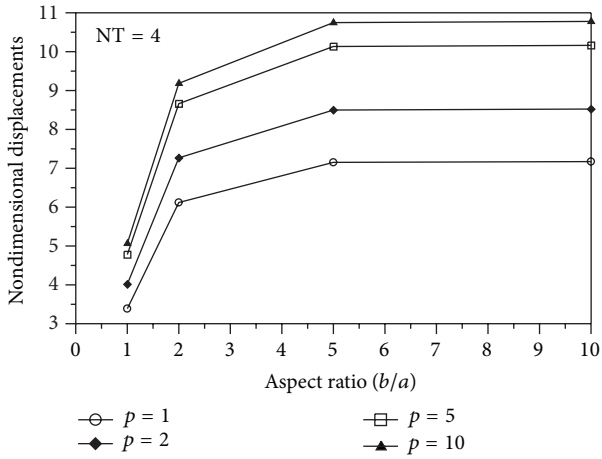

Figure 11: Effect of the aspect ratio on the nondimensional displacement of a simply supported S-FGM plate with various power law indexes.

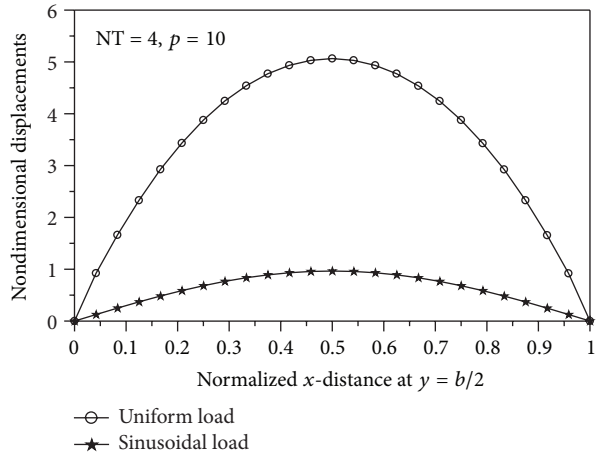

Figure 12: Effect of the loading type on the nondimensional displacement of a simply supported S-FGM plate with $a/h = 10$.

magnitude compared to the uniform load. As we expected, it is observed that the deflections investigated under the uniform load are larger than those investigated under the sinusoidal load. It may be noticed that the load-displacement curve under the sinusoidal load exhibits the value of 20% of the uniform load.

9. Conclusions

Nonlocal elasticity model for bending analysis of sigmoid functionally graded materials (S-FGM) nanoscale plates is presented using a first-order shear deformation theory and Hamilton's principle. The present models contain one nonlocal parameter and can capture the size effect, and two-constituent material variation through the plate thickness. Also, the present model can be reduced to the homogeneous nanoscale plates by setting $E_1 = E_2$ and S-FGM plates of local elasticity theory by setting the nonlocal parameter equal to zero. Analytical solutions for deflection of a simply supported rectangular S-FGM nanoscale plate are presented. The numerical results reveal that the inclusion of the small scale effect and power law index leads to an enlargement of the magnitude of deflection. The differences in deflection values predicted by the present model and the classical model are significant when the side-to-thickness ratio is small, but they are negligible when the side-to-thickness ratio becomes larger.

From the present work the following conclusions are drawn.

(1) The inclusion of the nonlocal scale effect and increasing value of the power law index will decrease stiffness of the S-FGM nanoscale plate, and consequently, leads to an enlargement of deflection.

(2) The increasing value of side-to-thickness ratio leads to a decrease in the deflection. As expected, the effect of transverse shear deformation is to increase deflection.

(3) The increasing value of the aspect ratio leads to an increase in the magnitude of deflection. The nondimensional center deflection increases upon raising the aspect ratio for b/a is less than 5.

(4) As expected, it is observed that the deflections investigated under the uniform load are larger than those investigated under the sinusoidal load.

These predicted trends agree with the size effect at the micron scale observed in experiments. These results can be used for evaluating the reliability of size-dependent plate models developed in the future. Further, in the analysis of S-FGM structures it is necessary to include the nonlocal elasticity theory for nanoscale shell and other boundary conditions.

Acknowledgment

This work was supported by the National Research Foundation of Korea Grant funded (NRF) by the Korea Government (MEST) (no. 2012-0008762).

References

[1] P. Ball, "Roll up for the revolution," *Nature*, vol. 414, pp. 142–144, 2001.

[2] R. H. Baughman, A. A. Zakhidov, and W. A. de Heer, "Carbon nanotubes: the route toward applications," *Science*, vol. 297, no. 5582, pp. 787–792, 2002.

[3] B. H. Bodily and C. T. Sun, "Structural and equivalent continuum properties of single walled carbon nanotubes," *International Journal of Materials and Product Technology*, vol. 18, pp. 381–397, 2003.

[4] C. Li and T. W. Chou, "A structural mechanics approach for the analysis of carbon nanotubes," *International Journal of Solids and Structures*, vol. 40, pp. 2487–2499, 2003.

[5] C. Li and T. Chou, "Single-walled carbon nanotubes as ultrahigh frequency nanomechanical resonators," *Physical Review B*, vol. 68, no. 7, Article ID 073405, pp. 734051–734053, 2003.

[6] A. C. Eringen, "Nonlocal polar elastic continua," *International Journal of Engineering Science*, vol. 10, no. 1, pp. 1–16, 1972.

[7] A. C. Eringen and D. G. B. Edelen, "On nonlocal elasticity," *International Journal of Engineering Science*, vol. 10, no. 3, pp. 233–248, 1972.

[8] W. D. Nix and H. Gao, "Indentation size effects in crystalline materials: a law for strain gradient plasticity," *Journal of the Mechanics and Physics of Solids*, vol. 46, no. 3, pp. 411–425, 1998.

[9] A. R. Hadjesfandiari and G. F. Dargush, "Couple stress theory for solids," *International Journal of Solids and Structures*, vol. 48, no. 18, pp. 2496–2510, 2011.

[10] M. Asghari, M. H. Kahrobaiyan, and M. T. Ahmadian, "A nonlinear Timoshenko beam formulation based on the modified couple stress theory," *International Journal of Engineering Science*, vol. 48, no. 12, pp. 1749–1761, 2010.

[11] H. M. Ma, X. Gao, and J. N. Reddy, "A microstructure-dependent Timoshenko beam model based on a modified couple stress theory," *Journal of the Mechanics and Physics of Solids*, vol. 56, no. 12, pp. 3379–3391, 2008.

[12] J. N. Reddy, "Microstructure-dependent couple stress theories of functionally graded beams," *Journal of the Mechanics and Physics of Solids*, vol. 59, no. 11, pp. 2382–2399, 2011.

[13] A. C. Eringen, "On differential equations of nonlocal elasticity and solutions of screw dislocation and surface waves," *Journal of Applied Physics*, vol. 54, no. 9, pp. 4703–4710, 1983.

[14] J. Peddieson, G. R. Buchanan, and R. P. McNitt, "Application of nonlocal continuum models to nanotechnology," *International Journal of Engineering Science*, vol. 41, no. 3-5, pp. 305–312, 2003.

[15] D. K. Jha, T. Kant, and R. K. Singh, "A critical review of recent research on functionally graded plates," *Composite Structures*, vol. 96, pp. 833–849, 2013.

[16] Y. L. Chung and S. H. Chi, "The residual stress of functionally graded materials," *Journal of the Chinese Institute of Civil and Hydraulic Engineering*, vol. 13, pp. 1–9, 2001.

[17] S. H. Chi and Y. L. Chung, "Mechanical behavior of functionally graded material plates under transverse load-Part II: numerical results," *International Journal of Solids and Structures*, vol. 43, pp. 3675–3691, 2006.

[18] S. Han, G. R. Lomboy, and K. Kim, "Mechanical vibration and buckling analysis of FGM plates and shells using a four-node quasi-conforming shell element," *International Journal of Structural Stability and Dynamics*, vol. 8, no. 2, pp. 203–229, 2008.

[19] S. Han, W. Lee, and W. Park, "Non-linear analysis of laminated composite and sigmoid functionally graded anisotropic structures using a higher-order shear deformable natural Lagrangian shell element," *Composite Structures*, vol. 89, no. 1, pp. 8–19, 2009.

[20] M. Aydogdu, "A general nonlocal beam theory: its application to nanobeam bending, buckling and vibration," *Physica E*, vol. 41, no. 9, pp. 1651–1655, 2009.

[21] Ö. Civalek and Ç. Demir, "Bending analysis of microtubules using nonlocal Euler-Bernoulli beam theory," *Applied Mathematical Modelling*, vol. 35, no. 5, pp. 2053–2067, 2011.

[22] J. N. Reddy, "Nonlocal theories for bending, buckling and vibration of beams," *International Journal of Engineering Science*, vol. 45, no. 2-8, pp. 288–307, 2007.

[23] J. N. Reddy and S. D. Pang, "Nonlocal continuum theories of beams for the analysis of carbon nanotubes," *Journal of Applied Physics*, vol. 103, no. 2, Article ID 023511, 2008.

[24] J. N. Reddy, "Nonlocal nonlinear formulations for bending of classical and shear deformation theories of beams and plates," *International Journal of Engineering Science*, vol. 48, no. 11, pp. 1507–1518, 2010.

[25] C. M. C. Roque, A. J. M. Ferreira, and J. N. Reddy, "Analysis of Timoshenko nanobeams with a nonlocal formulation and meshless method," *International Journal of Engineering Science*, vol. 49, no. 9, pp. 976–984, 2011.

[26] Q. Wang and K. M. Liew, "Application of nonlocal continuum mechanics to static analysis of micro- and nano-structures," *Physics Letters*, vol. 363, no. 3, pp. 236–242, 2007.

[27] C. M. Wang, S. Kitipornchai, C. W. Lim, and M. Eisenberger, "Beam bending solutions based on nonlocal Timoshenko beam theory," *Journal of Engineering Mechanics*, vol. 134, no. 6, pp. 475–481, 2008.

[28] Y. Fu, H. Du, and S. Zhang, "Functionally graded TiN/TiNi shape memory alloy films," *Materials Letters*, vol. 57, no. 20, pp. 2995–2999, 2003.

[29] C. Lu, D. Wu, and W. Chen, "Non-linear responses of nano-scale FGM films including the effects of surface energies," *IEEE Transactions on Nanotechnology*, vol. 10, no. 6, pp. 1321–1327, 2011.

[30] M. Rahaeifard, M. H. Kahrobaiyan, and M. T. Ahmadian, "Sensitivity analysis of atomic force microscope cantilever made of functionally graded materials," in *Proceedings of the 3rd International conference on micro- and nanosystems (DETC '09)*, pp. 539–544, September 2009.

[31] A. Witvrouw and A. Mehta, "The use of functionally graded poly-SiGe layers for MEMS applications," *Materials Science Forum*, vol. 492-493, pp. 255–260, 2005.

[32] Z. Lee, C. Ophus, L. M. Fischer et al., "Metallic NEMS components fabricated from nanocomposite Al-Mo films," *Nanotechnology*, vol. 17, no. 12, article 042, pp. 3063–3070, 2006.

[33] N. A. Fleck, G. M. Muller, M. F. Ashby, and J. W. Hutchinson, "Strain gradient plasticity: theory and experiment," *Acta Metallurgica et Materialia*, vol. 42, no. 2, pp. 475–487, 1994.

[34] J. S. Stolken and A. G. Evans, "A microbend test method for measuring the plasticity length scale," *Acta Materialia*, vol. 46, no. 14, pp. 5109–5115, 1998.

[35] A. C. M. Chong, F. Yang, D. C. C. Lam, and P. Tong, "Torsion and bending of micron-scaled structures," *Journal of Materials Research*, vol. 16, no. 04, pp. 1052–1058, 2001.

[36] D. C. C. Lam, F. Yang, A. C. M. Chong, J. Wang, and P. Tong, "Experiments and theory in strain gradient elasticity," *Journal of the Mechanics and Physics of Solids*, vol. 51, no. 8, pp. 1477–1508, 2003.

[37] J. N. Reddy, *Mechanics of Composite Plates and Shells: Theory and Analysis*, CRC Press, Boca Raton, Fla, USA, 2nd edition, 2004.

[38] H. T. Thai and D. H. Choi, "Size-dependent functionally graded Kirchhoff and Mindlin plate models based on a modified couple stress theory," *Composite Structures*, vol. 96, pp. 376–383, 2013.

[39] W. H. Lee, S. C. Han, and W. T. Park, "Nonlocal elasticity theory for bending and free vibration analysis of nano plates," *Journal of the Korea Academia-Industrial Cooperation Society*, vol. 13, no. 7, pp. 3207–3215, 2012 (Korean).

[40] Q. Wang and C. M. Wang, "The constitutive relation and small scale parameter of nonlocal continuum mechanics for modelling carbon nanotubes," *Nanotechnology*, vol. 18, no. 7, Article ID 075702, 2007.

Hindawi Publishing Corporation
Mathematical Problems in Engineering
Volume 2013, Article ID 867079, 33 pages
http://dx.doi.org/10.1155/2013/867079

Research Article

Mixed Static and Dynamic Optimization of Four-Parameter Functionally Graded Completely Doubly Curved and Degenerate Shells and Panels Using GDQ Method

Francesco Tornabene[1] and Alessandro Ceruti[2]

[1] *DICAM-Department, School of Engineering, University of Bologna, viale del Risorgimento 2, 40136 Bologna, Italy*
[2] *DIN-Department, School of Engineering, University of Bologna, viale del Risorgimento 2, 40136 Bologna, Italy*

Correspondence should be addressed to Francesco Tornabene; francesco.tornabene@unibo.it

Received 14 February 2013; Accepted 2 April 2013

Academic Editor: Abdelouahed Tounsi

Copyright © 2013 F. Tornabene and A. Ceruti. This is an open access article distributed under the Creative Commons Attribution License, which permits unrestricted use, distribution, and reproduction in any medium, provided the original work is properly cited.

This study deals with a mixed static and dynamic optimization of four-parameter functionally graded material (FGM) doubly curved shells and panels. The two constituent functionally graded shell consists of ceramic and metal, and the volume fraction profile of each lamina varies through the thickness of the shell according to a generalized power-law distribution. The Generalized Differential Quadrature (GDQ) method is applied to determine the static and dynamic responses for various FGM shell and panel structures. The mechanical model is based on the so-called First-order Shear Deformation Theory (FSDT). Three different optimization schemes and methodologies are implemented. The Particle Swarm Optimization, Monte Carlo and Genetic Algorithm approaches have been applied to define the optimum volume fraction profile for optimizing the first natural frequency and the maximum static deflection of the considered shell structure. The optimization aim is in fact to reach the frequency and the static deflection targets defined by the designer of the structure: the complete four-dimensional search space is considered for the optimization process. The optimized material profile obtained with the three methodologies is presented as a result of the optimization problem solved for each shell or panel structure.

1. Introduction

Shell structures are widely used in many fields of engineering thanks to their optimum dynamic behavior, strength, and stability guaranteed by the curvature effect. The dynamic and static deflection of these structures, caused by different external forces, can have serious consequences for their strength and safety, like resonance. Therefore, an accurate static deflection and frequency determination are of paramount importance for the technical design of these structural elements. One of the aims of this work is to study the static and dynamic behavior of completely doubly curved shell structures. During the last sixty years, two-dimensional linear theories of thin shells and plates have been developed including important contributions [1–12]. The transverse shear deformation has been incorporated into shell theories by applying the theory of Reissner-Mindlin [13, 14], also named First-order Shear Deformation Theory (FSDT). Abandoning the assumption of the preservation of the normals to the shell middle surface after the deformation, a comprehensive analysis for elastic isotropic shells and plates was made by Kraus [7] and Gould [15, 16]. Indeed, the present work is just based on the FSDT. In order to include the effect of the initial curvature in the evaluation of the stress resultants a generalization of the classical Reissner-Mindlin theory (CRMT) has been proposed in the literature by Kraus [7], by Leissa and Chang [17], by Qatu [18, 19] and by Toorani and Lakis [20]. As a consequence of these contributions

the stress resultants directly depend on the geometry of the structure in terms of the curvature coefficients, and the hypothesis of the symmetry of the in-plane shearing force resultants and the torsional couples declines. A further improvement of the previous theories of shells has been proposed by Toorani and Lakis [21]. In the present work the kinematical model is generalized in order to include the effect of the curvatures from the beginning of the shell formulation. In this way, the strain relationships have been changed, and the equilibrium equations in terms of displacements have to be modified. The General First-order Shear Deformation Theory (GFSDT) is herein considered. It is worth noting that no results are available in the literature about this general theory for doubly curved shells. Thus, the motivation of the present work is based on the lack of results about completely doubly curved shells and panels.

Due to the significant developments that have taken place in composite materials [22], the laminated composite doubly curved shells and panels are considered in this work. As for the static and dynamic analysis of shells, several studies have been presented earlier [23]. Furthermore, some complicated effects in shell structures have been considered in the recent years [24, 25]. Referring to the formulation of the static and dynamic equilibrium in terms of midsurface displacements and rotations, in this paper the system of second-order linear partial differential equations is solved. The static and dynamic solutions are obtained by using the numerical technique named Generalized Differential Quadrature (GDQ) method. The mathematical fundamentals and recent developments of the GDQ method as well as its major applications in engineering are discussed in detail in the book by Shu [26]. In the GDQ method the governing differential equations of equilibrium are directly transformed in one step to obtain the final algebraic form. The interest in researches dealing with this procedure is increasing due to its great simplicity and versatility. As shown in the literature [23, 27], GDQ technique is a global method, which can obtain very accurate numerical results by using a considerably small number of grid points. Therefore, this simple direct procedure has been applied in a large number of cases [28–77] to circumvent the difficulties of programming complex algorithms for the computer, as well as to avoid the excessive use of storage and computing time.

In the last decades, the increased use of functionally graded materials (FGMs) [39, 49–55, 57–62, 64, 65, 70, 75, 78–91] in engineering structures calls for improved analysis and tailored design tools. Thus, in the present paper, functionally graded shells are considered. Typically, FGMs consist of a mixture of ceramic and metal, or a combination of different materials. In this study, ceramic-metal graded shells and panels with two different volume fraction power-law variations of the constituents in the thickness direction are considered. Two different four-parameter power-law distributions, proposed by Tornabene [49], are used for the ceramic volume fraction. Various material profiles through the functionally graded lamina thickness are chosen by varying the four parameters of the power-law distributions.

The need for optimization lies in the mathematical formulation of FGMs, based on the four coefficients [49]: it is in fact quite difficult to handle these materials from the perspective of a designer. Small changes in parameters can lead in fact to strong changes in the distribution of base materials mixing in the thickness. Moreover, the domain of the four parameters is not continuous since some combinations of the parameters lead to distribution in which the mix of ceramics and metal resulting from the mathematical formula is negative or a complex number. From an operative perspective, a typical structural design scenario can include the need for minimizing the weight, the request of avoiding a resonance frequency, the control of the maximum displacement, or other constraints: in this case, there is no way to analytically relate the four parameter values to these important design requirements. As an answer, several authors proposed to apply optimization methods to achieve a feasible solution. For instance, Yas et al. [92] propose to minimize the weight of FGMs by using Imperialist Competitive Algorithm and Artificial Neural Networks. A very similar approach has been followed by Jam et al. [93] to optimize FGM conical shells. According to these examples, heuristic or semi heuristic methods are suitable in such a case since they consider the function to optimize as a "black box", in which only inputs and outputs are considered. A lot of heuristic (or semi heuristic) optimization techniques have been proposed in the literature. A comprehensive but not complete list includes Tabu Search [94], Simulated Annealing [95, 96], Ant Colonies Optimization [97, 98], Genetic Algorithms [99–109], Differential Evolution [110], Particle Swarm Algorithm [111–116], Immune Systems [117, 118], Gravity Optimization [119], Imperialist Competitive Algorithm [120], and Intelligent Water Drop [121, 122]. In this paper, Genetic Algorithm (GA) and Particle Swarm Optimization (PSO) will be used since they are tested, and widespread methods and other techniques could have been applied. Also an optimization with Monte Carlo (MC) technique [115, 123–127] will be presented to check the good performance of GA and PSO and to evaluate how much these methods are efficient and reliable with respect to a completely random approach. From the point of view of the software implementation, the PSO method is more simple than the GA, but it requires more attention to boundary conditions. MC is considered as a support to the GA and PSO techniques: in this paper, it is used to check the functionality of GA and PSO and to confirm that heuristic methods are to be preferred to random approaches. A well-designed algorithm implementing optimization techniques like GA or PSO can be useful to obtain a better solution than MC, requiring a shorter time to solve the optimization problem. MC is in fact a random technique, in which large number of tries is necessary to obtain a good result: moreover, the search is blind and without memory of the past, so that the previous tests of the optimization domain are not exploited by the following computations. The above considerations suggested the application of heuristic methods to the optimization of FGMs; a more detailed description of the implementation of these methods will be provided in the next sections of the present work.

The structure of this article is as follows: after this introduction, the second section describes the mathematical framework necessary to model and study FGM doubly

curved shell structures; the third section shows the GDQ numerical implementation for the static and dynamic analyses; the fourth section describes the implementation of GA, PSO, and MC methods with respect to peculiarities of the case study, while the fifth one presents the results of the FGM optimization procedure applied to a set of six structures. A final section provides some conclusive comments regarding the problem description, the approach followed to solve it, and results obtained. The main novelty of the papers lies in the proposal of a design methodology which can be used by the designer involved in FGM applications to achieve a short time particular performances or characteristics for the FGM doubly curved shell structures.

2. Geometry Description and Shell Fundamental Systems of Equations

A 2D Equivalent Single Layer (ESL) model is proposed to study generic doubly curved shells and panels. The position of an arbitrary point within the shell medium is defined by coordinates $\alpha_1(\alpha_1^0 \le \alpha_1 \le \alpha_1^1)$, $\alpha_2(\alpha_2^0 \le \alpha_2 \le \alpha_2^1)$ upon the middle surface or reference surface $\mathbf{r}(\alpha_1, \alpha_2)$, and ζ directed along the outward normal $\mathbf{n}(\alpha_1, \alpha_2)$ and measured from the reference surface $(-h/2 \le \zeta \le h/2)$, where $h(\alpha_1, \alpha_2)$ is the total thickness of the shell (Figure 1). The differential geometry [7, 11, 12, 23, 74] is used to describe the shell structure, starting with the position vector written in the global reference system:

$$\mathbf{R}(\alpha_1, \alpha_2, \zeta) = \mathbf{r}(\alpha_1, \alpha_2) + \frac{h(\alpha_1, \alpha_2)}{2} z \mathbf{n}(\alpha_1, \alpha_2), \quad (1)$$

where $z = 2\zeta/h(\alpha_1, \alpha_2)$ and $z \in [-1, 1]$. The basic configuration of the problem considered is a laminated composite doubly curved shell, as shown in Figure 1. For a laminated composite shell made of l laminae or plies, the total thickness h is defined as

$$h = \sum_{k=1}^{l} h_k \quad (2)$$

in which $h_k = \zeta_{k+1} - \zeta_k$ is the thickness of the kth lamina or ply. In this study, doubly curved shells and degenerate shells such as plates are considered. It should be noted from (1) that the location of each point of the 3D shell is a function of the location of the point on the reference surface $\mathbf{r}(\alpha_1, \alpha_2)$ and the normal vector $\mathbf{n}(\alpha_1, \alpha_2)$ to the reference surface at the given point (Figure 1). Moreover, the position of the generic point of the shell volume is also a function of the shell thickness $h(\alpha_1, \alpha_2)$. Hence, writing the position vector of the reference surface, it is possible to define the three components along the three global axes $Ox_1x_2x_3$ as

$$\mathbf{r}(\alpha_1, \alpha_2) = r_1(\alpha_1, \alpha_2)\mathbf{e}_1 + r_2(\alpha_1, \alpha_2)\mathbf{e}_2 + r_3(\alpha_1, \alpha_2)\mathbf{e}_3, \quad (3)$$

where $\mathbf{e}_1$, $\mathbf{e}_2$, and $\mathbf{e}_3$ are the unit vector of the global reference system $Ox_1x_2x_3$. From the definition of the first fundamental form [7, 11, 12, 23] of the reference surface $\mathbf{r}(\alpha_1, \alpha_2)$, the Lamé parameters can be expressed as

$$\begin{aligned} A_1(\alpha_1, \alpha_2) &= \sqrt{\mathbf{r}_{,1} \cdot \mathbf{r}_{,1}}, \\ A_2(\alpha_1, \alpha_2) &= \sqrt{\mathbf{r}_{,2} \cdot \mathbf{r}_{,2}}. \end{aligned} \quad (4)$$

The comma in expressions (4) defines the partial derivative with respect to α_1 or α_2, respectively. Moreover, by considering an orthogonal curvilinear coordinate system $O'\alpha_1\alpha_2\zeta$ [7, 11, 12, 23, 74] from the position vector (3) the normal vector $\mathbf{n}(\alpha_1, \alpha_2)$ can be written as

$$\mathbf{n}(\alpha_1, \alpha_2) = \frac{\mathbf{r}_{,1} \times \mathbf{r}_{,2}}{A_1 A_2}. \quad (5)$$

Finally, due to the fact that an orthogonal curvilinear coordinate system $O'\alpha_1\alpha_2\zeta$ is considered and following the definition of the second fundamental form [7, 11, 23, 74] of the reference surface $\mathbf{r}(\alpha_1, \alpha_2)$, the principal radii of curvature can be evaluated as

$$\begin{aligned} R_1(\alpha_1, \alpha_2) &= -\frac{\mathbf{r}_{,1} \cdot \mathbf{r}_{,1}}{\mathbf{r}_{,11} \cdot \mathbf{n}}, \\ R_2(\alpha_1, \alpha_2) &= -\frac{\mathbf{r}_{,2} \cdot \mathbf{r}_{,2}}{\mathbf{r}_{,22} \cdot \mathbf{n}}. \end{aligned} \quad (6)$$

As concerns the shell theory, the present study is based on the following assumptions: (1) the transverse normal is inextensible so that the normal strain is equal to zero: $\varepsilon_n = \varepsilon_n(\alpha_1, \alpha_2, \zeta, t) = 0$; (2) the transverse shear deformation is considered to influence the governing equations so that normal lines to the reference surface of the shell before deformation remain straight but not necessarily normal after deformation (a relaxed Kirchhoff-Love hypothesis is considered); (3) the shell deflections are small and the strains are infinitesimal; (4) the shell is moderately thick, therefore it is possible to assume that the thickness-direction normal stress is negligible so that the plane assumption can be invoked: $\sigma_n = \sigma_n(\alpha_1, \alpha_2, \zeta, t) = 0$; (5) the linear elastic behavior of anisotropic materials is assumed; and (6) the rotary inertias and the initial curvatures are also taken into account. The theory under development is meant to be in the group of moderately thick shells, in which the following ratios of thickness over curvature and curve length are valid:

$$\frac{1}{100} \le \max\left(\frac{h}{R_{\min}}, \frac{h}{L_{\min}}\right) \le \frac{1}{10}. \quad (7)$$

Consistent with the assumptions of a moderately thick shell theory reported above, the displacement field considered in the present study is that of the First-order Shear Deformation Theory (FSDT) and can be put in the following form:

$$\begin{aligned} U_1(\alpha_1, \alpha_2, \zeta, t) &= H_1 u_1(\alpha_1, \alpha_2, t) + \zeta \beta_1(\alpha_1, \alpha_2, t), \\ U_2(\alpha_1, \alpha_2, \zeta, t) &= H_2 u_2(\alpha_1, \alpha_2, t) + \zeta \beta_2(\alpha_1, \alpha_2, t), \\ U_3(\alpha_1, \alpha_2, \zeta, t) &= u_3(\alpha_1, \alpha_2, t), \end{aligned} \quad (8)$$

where

$$H_1 = 1 + \frac{\zeta}{R_1},$$
$$H_2 = 1 + \frac{\zeta}{R_2}, \tag{9}$$

and u_1, u_2, and u_3 are the displacement components of points lying on the middle surface ($\zeta = 0$) of the shell, while t is the time variable. β_1 and β_2 are normal-to-mid-surface rotations, respectively. The kinematic hypothesis expressed by relations (8) should be supplemented by the statement that the shell deflections are small and strains are infinitesimal, that is $u_3 \ll h$. In-plane displacements U_1 and U_2 vary linearly through the thickness, while U_3 remains independent of ζ. Differently from the previous works [43, 44, 47, 49–53, 67, 68, 70], the displacement field has been improved taking into account the effective geometry of the shell and in particular the curvature effect has been directly introduced into the kinematical model, as proposed by Toorani and Lakis [21].

Due to the change of the kinematical model, the relationships between strains and generalized displacements along the shell reference surface ($\zeta = 0$) become the following:

$$\begin{bmatrix} \varepsilon_1^0 \\ \varepsilon_2^0 \\ \gamma_1^0 \\ \gamma_2^0 \\ \chi_1^0 \\ \chi_2^0 \\ \omega_1^0 \\ \omega_2^0 \\ \gamma_{1n}^0 \\ \gamma_{2n}^0 \end{bmatrix} = \begin{bmatrix} \frac{1}{A_1}\frac{\partial}{\partial\alpha_1} & \frac{1}{A_1A_2}\frac{\partial A_1}{\partial\alpha_2} & \frac{1}{R_1} & 0 & 0 \\ \frac{1}{A_1A_2}\frac{\partial A_2}{\partial\alpha_1} & \frac{1}{A_2}\frac{\partial}{\partial\alpha_2} & \frac{1}{R_2} & 0 & 0 \\ -\frac{1}{A_1A_2}\frac{\partial A_1}{\partial\alpha_2} & \frac{1}{A_1}\frac{\partial}{\partial\alpha_1} & 0 & 0 & 0 \\ \frac{1}{A_2}\frac{\partial}{\partial\alpha_2} & -\frac{1}{A_1A_2}\frac{\partial A_2}{\partial\alpha_1} & 0 & 0 & 0 \\ \frac{1}{A_1R_1}\frac{\partial}{\partial\alpha_1} - \frac{1}{A_1R_1^2}\frac{\partial R_1}{\partial\alpha_1} & \frac{1}{A_1A_2R_2}\frac{\partial A_1}{\partial\alpha_2} & 0 & \frac{1}{A_1}\frac{\partial}{\partial\alpha_1} & \frac{1}{A_1A_2}\frac{\partial A_1}{\partial\alpha_2} \\ \frac{1}{A_1A_2R_1}\frac{\partial A_2}{\partial\alpha_1} & \frac{1}{A_2R_2}\frac{\partial}{\partial\alpha_2} - \frac{1}{A_2R_2^2}\frac{\partial R_2}{\partial\alpha_2} & 0 & \frac{1}{A_1A_2}\frac{\partial A_2}{\partial\alpha_1} & \frac{1}{A_2}\frac{\partial}{\partial\alpha_2} \\ -\frac{1}{A_1A_2R_1}\frac{\partial A_1}{\partial\alpha_2} & \frac{1}{A_1R_2}\frac{\partial}{\partial\alpha_1} - \frac{1}{A_1R_2^2}\frac{\partial R_2}{\partial\alpha_1} & 0 & -\frac{1}{A_1A_2}\frac{\partial A_1}{\partial\alpha_2} & \frac{1}{A_1}\frac{\partial}{\partial\alpha_1} \\ \frac{1}{A_2R_1}\frac{\partial}{\partial\alpha_2} - \frac{1}{A_2R_1^2}\frac{\partial R_1}{\partial\alpha_2} & -\frac{1}{A_1A_2R_2}\frac{\partial A_2}{\partial\alpha_1} & 0 & \frac{1}{A_2}\frac{\partial}{\partial\alpha_2} & -\frac{1}{A_1A_2}\frac{\partial A_2}{\partial\alpha_1} \\ 0 & 0 & \frac{1}{A_1}\frac{\partial}{\partial\alpha_1} & 1 & 0 \\ 0 & 0 & \frac{1}{A_2}\frac{\partial}{\partial\alpha_2} & 0 & 1 \end{bmatrix} \begin{bmatrix} u_1 \\ u_2 \\ u_3 \\ \beta_1 \\ \beta_2 \end{bmatrix} \tag{10}$$

that are different from those presented in previous papers [43, 44, 47, 49–53, 67, 68, 70]. In the above (10), the first four strains $\varepsilon_1^0, \varepsilon_2^0, \gamma_1^0$, and γ_2^0 are the in-plane components, and $\chi_1^0, \chi_2^0, \omega_1^0$, and ω_2^0 are the analogous curvature changes. The last two components $\gamma_{1n}^0, \gamma_{2n}^0$ are the transverse shearing strains. The shell is assumed to be made of a linear elastic composite material. Accordingly, the following constitutive equations relate internal stress resultants and internal couples with generalized strain components (10) on the middle surface:

$$\begin{bmatrix} N_1 \\ N_2 \\ N_{12} \\ N_{21} \\ M_1 \\ M_2 \\ M_{12} \\ M_{21} \\ T_1 \\ T_2 \end{bmatrix} = \begin{bmatrix} A^{(0)}_{11(20)} & A^{(0)}_{12(11)} & A^{(0)}_{16(20)} & A^{(0)}_{16(11)} & A^{(1)}_{11(20)} & A^{(1)}_{12(11)} & A^{(1)}_{16(20)} & A^{(1)}_{16(11)} & 0 & 0 \\ A^{(0)}_{12(11)} & A^{(0)}_{22(02)} & A^{(0)}_{26(11)} & A^{(0)}_{26(02)} & A^{(1)}_{12(11)} & A^{(1)}_{22(02)} & A^{(1)}_{26(11)} & A^{(1)}_{26(02)} & 0 & 0 \\ A^{(0)}_{16(20)} & A^{(0)}_{26(11)} & A^{(0)}_{66(20)} & A^{(0)}_{66(11)} & A^{(1)}_{16(20)} & A^{(1)}_{26(11)} & A^{(1)}_{66(20)} & A^{(1)}_{66(11)} & 0 & 0 \\ A^{(0)}_{16(11)} & A^{(0)}_{26(02)} & A^{(0)}_{66(11)} & A^{(0)}_{66(02)} & A^{(1)}_{16(11)} & A^{(1)}_{26(02)} & A^{(1)}_{66(11)} & A^{(1)}_{66(02)} & 0 & 0 \\ A^{(1)}_{11(20)} & A^{(1)}_{12(11)} & A^{(1)}_{16(20)} & A^{(1)}_{16(11)} & A^{(2)}_{11(20)} & A^{(2)}_{12(11)} & A^{(2)}_{16(20)} & A^{(2)}_{16(11)} & 0 & 0 \\ A^{(1)}_{12(11)} & A^{(1)}_{22(02)} & A^{(1)}_{26(11)} & A^{(1)}_{26(02)} & A^{(2)}_{12(11)} & A^{(2)}_{22(02)} & A^{(2)}_{26(11)} & A^{(2)}_{26(02)} & 0 & 0 \\ A^{(1)}_{16(20)} & A^{(1)}_{26(11)} & A^{(1)}_{66(20)} & A^{(1)}_{66(11)} & A^{(2)}_{16(20)} & A^{(2)}_{26(11)} & A^{(2)}_{66(20)} & A^{(2)}_{66(11)} & 0 & 0 \\ A^{(1)}_{16(11)} & A^{(1)}_{26(02)} & A^{(1)}_{66(11)} & A^{(1)}_{66(02)} & A^{(2)}_{16(11)} & A^{(2)}_{26(02)} & A^{(2)}_{66(11)} & A^{(2)}_{66(02)} & 0 & 0 \\ 0 & 0 & 0 & 0 & 0 & 0 & 0 & 0 & \kappa A^{(0)}_{44(20)} & \kappa A^{(0)}_{45(11)} \\ 0 & 0 & 0 & 0 & 0 & 0 & 0 & 0 & \kappa A^{(0)}_{45(11)} & \kappa A^{(0)}_{55(02)} \end{bmatrix} \begin{bmatrix} \varepsilon^0_1 \\ \varepsilon^0_2 \\ \gamma^0_1 \\ \gamma^0_2 \\ \chi^0_1 \\ \chi^0_2 \\ \omega^0_1 \\ \omega^0_2 \\ \gamma^0_{1n} \\ \gamma^0_{2n} \end{bmatrix}, \tag{11}$$

where the elastic engineering stiffnesses $A^{(\tau)}_{ij(pq)}$ are defined as follows:

$$A^{(\tau)}_{ij(pq)} = \sum_{k=1}^{l} \int_{\zeta_k}^{\zeta_{k+1}} \overline{Q}^{(k)}_{ij} \zeta^{\tau} \frac{H_1 H_2}{H_1^p H_2^q} d\zeta, \quad \tau, p, q = 0, 1, 2. \tag{12}$$

Different approaches can be found in the literature to evaluate the engineering elastic constants $A^{(\tau)}_{ij(pq)}$ [7, 17–20, 73, 76]. In the present paper, the relations of the elastic engineering stiffnesses $A^{(\tau)}_{ij(pq)}$ are numerically evaluated using an integral function in order to avoid numerical instabilities. It is worth noting that due to the fact that the elastic engineering stiffnesses $A^{(\tau)}_{ij(pq)}$ depend on curvatures, the corresponding derivatives, with respect to the coordinates along α_1 and α_2 directions of the reference surface, have to be evaluated. In order to perform this operation the Differential Quadrature rule [26] is used. Thus, the derivatives of the elastic engineering stiffnesses $A^{(\tau)}_{ij(pq)}$ are numerically evaluated. The corresponding elastic constants $\overline{Q}^{(k)}_{ij}$ can be found in the article by Tornabene et al. [70, 73], in which all the constants above introduced are explicitly defined for laminated composite and functionally graded shells and panels. κ is the shear correction factor, which is usually taken as $\kappa = 5/6$, such as in the present work. In particular, the determination of shear correction factors for composite laminated structures is still an unresolved issue, since these factors depend on various parameters [20]. In (11), the four components N_1, N_2, N_{12}, and N_{21} are the in-plane force resultants, and M_1, M_2, M_{12}, and M_{21} are the analogous couples, while T_1, T_2 are the transverse shear force resultants. In the above definitions (11) the symmetry of shearing force resultants N_{12}, N_{21} and torsional couples M_{12}, M_{21} is not assumed as a further hypothesis, as done in Reissner-Mindlin theory [7, 12, 22]. This hypothesis is satisfied only in the case of spherical shells and flat plates [7]. The assumption under discussion is derived from the consideration that ratios ζ/R_1, ζ/R_2 cannot be neglected with respect to unity.

Typically, the functionally graded materials are made of a mixture of two constituents. In the present work, it is assumed that the functionally graded material lamina is made of a mixture of ceramic and metal constituents: Silicon Nitride and Stainless Steel. The material properties of the functionally graded shell vary continuously and smoothly in the thickness direction ζ of each lamina and are functions of volume fractions of two constituent materials. The Young's modulus $E^{(k)}(\zeta)$, shear modulus $G^{(k)}(\zeta)$, Poisson's ratio $\nu^{(k)}(\zeta)$, and mass density $\rho^{(k)}(\zeta)$ of the functionally graded shell kth lamina can be expressed as

$$\begin{aligned} \rho^{(k)}(\zeta) &= \left(\rho_C^{(k)} - \rho_M^{(k)}\right) V_C^{(k)}(\zeta) + \rho_M^{(k)}, E^{(k)}(\zeta) \\ &= \left(E_C^{(k)} - E_M^{(k)}\right) V_C^{(k)}(\zeta) + E_M^{(k)}, \nu^{(k)}(\zeta) \\ &= \left(\nu_C^{(k)} - \nu_M^{(k)}\right) V_C^{(k)}(\zeta) + \nu_M^{(k)}, G^{(k)}(\zeta) \\ &= \frac{E^{(k)}(\zeta)}{2\left(1 + \nu^{(k)}(\zeta)\right)}, \quad \text{for } \zeta_k \le \zeta \le \zeta_{k+1}, \end{aligned} \tag{13}$$

where $\rho_C^{(k)}, E_C^{(k)}, \nu_C^{(k)}, V_C^{(k)}$ and $\rho_M^{(k)}, E_M^{(k)}, \nu_M^{(k)}, V_M^{(k)}$ represent mass density, Young's modulus, Poisson's ratio, and volume fraction of the ceramic and metal constituent materials, respectively. In this work, the ceramic volume fraction $V_C^{(k)}(\zeta)$

follows two simple four-parameter power-law distributions [49, 51, 53, 70, 75]:

$$\begin{aligned}
&\mathrm{FGM}_{1(a^{(k)}/b^{(k)}/c^{(k)}/p^{(k)})} : V_C^{(k)}(\zeta) \\
&\quad = \left(1 - a^{(k)}\left(\frac{\zeta}{h_k} - \frac{\zeta_k}{h_k}\right) + b^{(k)}\left(\frac{\zeta}{h_k} - \frac{\zeta_k}{h_k}\right)^{c^{(k)}}\right)^{p^{(k)}}, \\
&\mathrm{FGM}_{2(a^{(k)}/b^{(k)}/c^{(k)}/p^{(k)})} : V_C^{(k)}(\zeta) \\
&\quad = \left(1 - a^{(k)}\left(\frac{\zeta_{k+1}}{h_k} - \frac{\zeta}{h_k}\right) + b^{(k)}\left(\frac{\zeta_{k+1}}{h_k} - \frac{\zeta}{h_k}\right)^{c^{(k)}}\right)^{p^{(k)}},
\end{aligned} \tag{14}$$

where the volume fraction index $p^{(k)}(0 \le p^{(k)} \le \infty)$ and the parameters $a^{(k)}, b^{(k)}$, and $c^{(k)}$ dictate the material variation profile through the functionally graded shell lamina thickness. It is important to remark that the volume fractions of all the constituent materials should add up to unity:

$$V_C^{(k)} + V_M^{(k)} = 1. \tag{15}$$

In order to choose the three parameters $a^{(k)}, b^{(k)}$, and $c^{(k)}$ suitably, the relation (15) must be always satisfied for every volume fraction index $p^{(k)}$ in each lamina. By considering the relations (14), when the power-law exponent is set equal to zero ($p^{(k)} = 0$) or equal to infinity ($p^{(k)} = \infty$), the homogeneous isotropic material is obtained as a special case of functionally graded material. In fact, from (15), (14), and (13) it is possible to obtain

$$\begin{aligned}
p^{(k)} = 0 \longrightarrow V_C^{(k)} = 1, \quad & V_M^{(k)} = 0 \longrightarrow \rho^{(k)}(\zeta) = \rho_C, \\
E^{(k)}(\zeta) = E_C, \quad & \nu^{(k)}(\zeta) = \nu_C, \\
p^{(k)} = \infty \longrightarrow V_C^{(k)} = 0, \quad & V_M^{(k)} = 1 \longrightarrow \rho^{(k)}(\zeta) = \rho_M, \\
E^{(k)}(\zeta) = E_M, \quad & \nu^{(k)}(\zeta) = \nu_M.
\end{aligned} \tag{16}$$

Some material profiles through the functionally graded shell thickness are illustrated in Figures 2 and 3.

Following the Hamilton's principle [7, 12, 19, 22, 23], the five governing equations in terms of internal actions can be written for the shell element:

$$\begin{aligned}
&\frac{1}{A_1A_2}\frac{\partial(N_1A_2)}{\partial\alpha_1} + \frac{1}{A_1A_2}\frac{\partial(N_{21}A_1)}{\partial\alpha_2} \\
&\quad + \frac{N_{12}}{A_1A_2}\frac{\partial A_1}{\partial\alpha_2} - \frac{N_2}{A_1A_2}\frac{\partial A_2}{\partial\alpha_1} \\
&\quad + \frac{1}{R_1}\left(\frac{1}{A_1A_2}\frac{\partial(M_1A_2)}{\partial\alpha_1}\right. \\
&\qquad + \frac{1}{A_1A_2}\frac{\partial(M_{21}A_1)}{\partial\alpha_2} \\
&\qquad \left. + \frac{M_{12}}{A_1A_2}\frac{\partial A_1}{\partial\alpha_2} - \frac{M_2}{A_1A_2}\frac{\partial A_2}{\partial\alpha_1}\right) \\
&\quad + q_1 = \left(I_0 + \frac{2I_1}{R_1} + \frac{I_2}{R_1^2}\right)\ddot{u}_1 + \left(I_1 + \frac{I_2}{R_1}\right)\ddot{\beta}_1, \\
&\frac{1}{A_1A_2}\frac{\partial(N_{12}A_2)}{\partial\alpha_1} + \frac{1}{A_1A_2}\frac{\partial(N_2A_1)}{\partial\alpha_2} \\
&\quad + \frac{N_{21}}{A_1A_2}\frac{\partial A_2}{\partial\alpha_1} - \frac{N_1}{A_1A_2}\frac{\partial A_1}{\partial\alpha_2} \\
&\quad + \frac{1}{R_2}\left(\frac{1}{A_1A_2}\frac{\partial(M_{12}A_2)}{\partial\alpha_1}\right. \\
&\qquad + \frac{1}{A_1A_{\,2}}\frac{\partial(M_2A_1)}{\partial\alpha_2} \\
&\qquad \left. + \frac{M_{21}}{A_1A_2}\frac{\partial A_2}{\partial\alpha_1} - \frac{M_1}{A_1A_2}\frac{\partial A_1}{\partial\alpha_2}\right) \\
&\quad + q_2 = \left(I_0 + \frac{2I_1}{R_2} + \frac{I_2}{R_2^2}\right)\ddot{u}_2 + \left(I_1 + \frac{I_2}{R_2}\right)\ddot{\beta}_2, \\
&\frac{1}{A_1A_2}\frac{\partial(T_1A_2)}{\partial\alpha_1} + \frac{1}{A_1A_2}\frac{\partial(T_2A_1)}{\partial\alpha_2} \\
&\quad - \left(\frac{N_1}{R_1} + \frac{N_2}{R_2}\right) + q_n = I_0\ddot{u}_3, \\
&\frac{1}{A_1A_2}\frac{\partial(M_1A_2)}{\partial\alpha_1} + \frac{1}{A_1A_2}\frac{\partial(M_{21}A_1)}{\partial\alpha_2} + \frac{M_{12}}{A_1A_2}\frac{\partial A_1}{\partial\alpha_2} \\
&\quad - \frac{M_2}{A_1A_2}\frac{\partial A_2}{\partial\alpha_1} - T_1 + m_1 = \left(I_1 + \frac{I_2}{R_1}\right)\ddot{u}_1 + I_2\ddot{\beta}_1, \\
&\frac{1}{A_1A_2}\frac{\partial(M_{12}A_2)}{\partial\alpha_1} + \frac{1}{A_1A_2}\frac{\partial(M_2A_1)}{\partial\alpha_2} + \frac{M_{21}}{A_1A_2}\frac{\partial A_2}{\partial\alpha_1} \\
&\quad - \frac{M_1}{A_1A_2}\frac{\partial A_1}{\partial\alpha_2} - T_2 + m_2 = \left(I_1 + \frac{I_2}{R_2}\right)\ddot{u}_2 + I_2\ddot{\beta}_2,
\end{aligned} \tag{17}$$

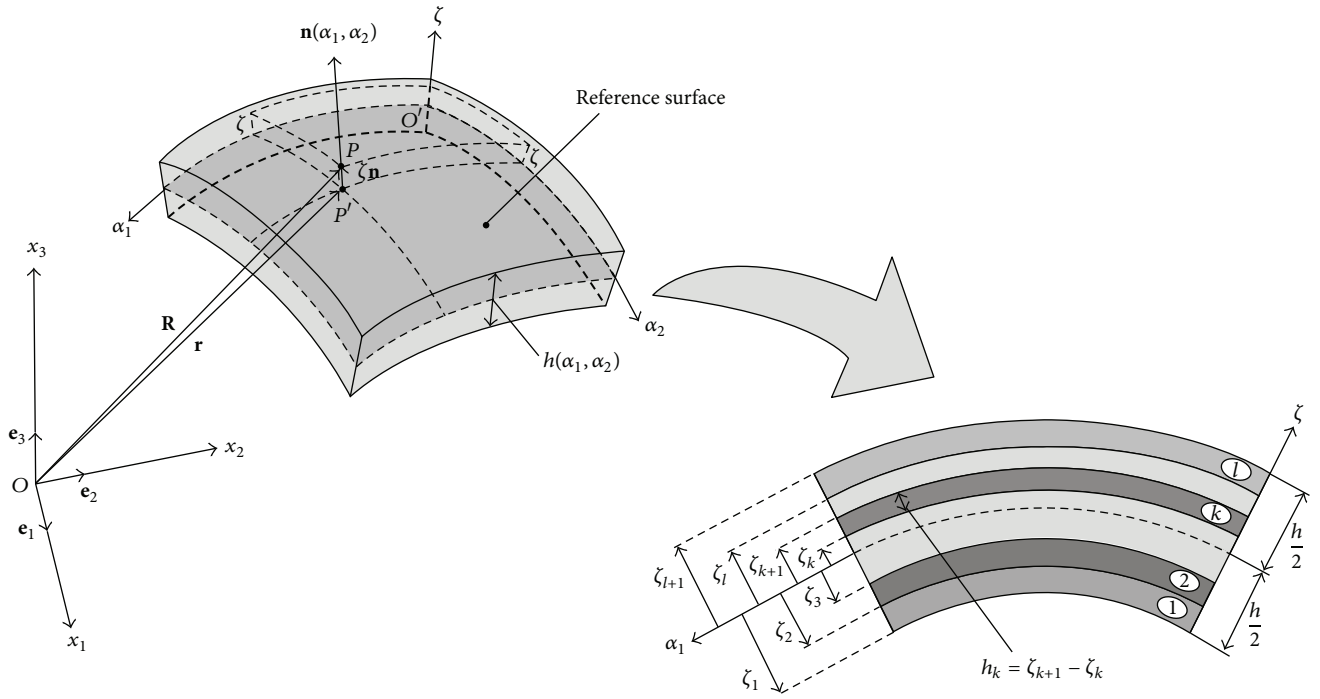

Figure 1: Geometry description and coordinate system of a doubly curved shell.

where

$$I_\tau = \sum_{k=1}^{l} \int_{\zeta_k}^{\zeta_{k+1}} \rho^{(k)} \zeta^\tau H_1 H_2 d\zeta, \quad \tau = 0, 1, 2. \tag{18}$$

Furthermore, the generalized external actions q_1, q_2, q_n, m_1, and m_2 due to the external forces, acting on the top and bottom surfaces of the shell, can be evaluated using the static equivalence principle [7, 23] and can be written on the reference surface of the doubly curved shell as follows:

$$\begin{aligned}
q_1 &= q_1^+ \left(1 + \frac{h}{2R_1}\right)^2 \left(1 + \frac{h}{2R_2}\right) \\
&\quad + q_1^- \left(1 - \frac{h}{2R_1}\right)^2 \left(1 - \frac{h}{2R_2}\right), \\
q_2 &= q_2^+ \left(1 + \frac{h}{2R_1}\right) \left(1 + \frac{h}{2R_2}\right)^2 \\
&\quad + q_2^- \left(1 - \frac{h}{2R_1}\right) \left(1 - \frac{h}{2R_2}\right)^2, \\
q_n &= q_n^+ \left(1 + \frac{h}{2R_1}\right) \left(1 + \frac{h}{2R_2}\right) \\
&\quad + q_n^- \left(1 - \frac{h}{2R_1}\right) \left(1 - \frac{h}{2R_2}\right), \\
m_1 &= q_1^+ \frac{h}{2} \left(1 + \frac{h}{2R_1}\right) \left(1 + \frac{h}{2R_2}\right) \\
&\quad - q_1^- \frac{h}{2} \left(1 - \frac{h}{2R_1}\right) \left(1 - \frac{h}{2R_2}\right), \\
m_2 &= q_2^+ \frac{h}{2} \left(1 + \frac{h}{2R_1}\right) \left(1 + \frac{h}{2R_2}\right) \\
&\quad - q_2^- \frac{h}{2} \left(1 - \frac{h}{2R_1}\right) \left(1 - \frac{h}{2R_2}\right),
\end{aligned} \tag{19}$$

where $q_1^+, q_1^-, q_2^+, q_2^-, q_n^+$, and q_n^- are the external forces in the three principal directions α_1, α_2, and ζ at the top and the bottom surface of the shell, respectively. The three basic sets of equations, namely, the kinematic (10), constitutive (11), and motion (17) equations, may be combined to give the fundamental system of equations, also known as the governing system of equations. By replacing the kinematic equations (10) into the constitutive equations (11) and the result of this substitution into the motion equations (17), the complete equations of motion in terms of displacement and rotational components can be written as

$$\begin{bmatrix} L_{11} & L_{12} & L_{13} & L_{14} & L_{15} \\ L_{21} & L_{22} & L_{23} & L_{24} & L_{25} \\ L_{31} & L_{32} & L_{33} & L_{34} & L_{35} \\ L_{41} & L_{42} & L_{43} & L_{44} & L_{45} \\ L_{51} & L_{52} & L_{53} & L_{54} & L_{55} \end{bmatrix} \begin{bmatrix} u_1 \\ u_2 \\ u_3 \\ \beta_1 \\ \beta_2 \end{bmatrix} + \begin{bmatrix} q_1 \\ q_2 \\ q_n \\ m_1 \\ m_2 \end{bmatrix} = \begin{bmatrix} I_{01} & 0 & 0 & I_{11} & 0 \\ 0 & I_{02} & 0 & 0 & I_{12} \\ 0 & 0 & I_0 & 0 & 0 \\ I_{11} & 0 & 0 & I_2 & 0 \\ 0 & I_{12} & 0 & 0 & I_2 \end{bmatrix} \begin{bmatrix} \ddot{u}_1 \\ \ddot{u}_2 \\ \ddot{u}_3 \\ \ddot{\beta}_1 \\ \ddot{\beta}_2 \end{bmatrix}, \tag{20}$$

where $L_{ij}, i, j = 1, \ldots, 5$ are the equilibrium operators and the new mass inertias are defined as follows:

$$\begin{aligned} I_{01} &= I_0 + \frac{2I_1}{R_1} + \frac{I_2}{R_1^2}, \\ I_{11} &= I_1 + \frac{I_2}{R_1}, \\ I_{02} &= I_0 + \frac{2I_1}{R_2} + \frac{I_2}{R_2^2}, \\ I_{12} &= I_1 + \frac{I_2}{R_2}. \end{aligned} \tag{21}$$

Differently from previous works [43, 44, 47, 49–53, 67, 68, 70], the equilibrium operators L_{ij}, introduced in (20), have been changed due to the choice of using the kinematical model (8).

Three kinds of boundary conditions are considered, namely, the fully clamped edge boundary condition (C), the simply supported edge boundary condition (S), and the free edge boundary condition (F). The equations describing the boundary conditions can be written as follows:

Clamped edge boundary conditions (C):

$$\begin{aligned} &u_1 = u_2 = u_3 = \beta_1 = \beta_2 = 0 \quad \text{at } \alpha_1 = \alpha_1^0 \\ &\qquad \text{or } \alpha_1 = \alpha_1^1, \alpha_2^0 \le \alpha_2 \le \alpha_2^1, \\ &u_1 = u_2 = u_3 = \beta_1 = \beta_2 = 0 \quad \text{at } \alpha_2 = \alpha_2^0 \\ &\qquad \text{or } \alpha_2 = \alpha_2^1, \alpha_1^0 \le \alpha_1 \le \alpha_1^1, \end{aligned} \tag{22}$$

Simply supported edge boundary conditions (S):

$$\begin{aligned} &u_1 = u_2 = u_3 = \beta_2 = 0, \qquad M_1 = 0 \quad \text{at } \alpha_1 = \alpha_1^0 \\ &\qquad \text{or } \alpha_1 = \alpha_1^1, \alpha_2^0 \le \alpha_2 \le \alpha_2^1, \\ &u_1 = u_2 = u_3 = \beta_2 = 0, \qquad M_2 = 0 \quad \text{at } \alpha_2 = \alpha_2^0 \\ &\qquad \text{or } \alpha_2 = \alpha_2^1, \alpha_1^0 \le \alpha_1 \le \alpha_1^1, \end{aligned} \tag{23}$$

Free edge boundary conditions (F):

$$\begin{aligned} &N_1 + \frac{M_1}{R_1} = 0, \qquad N_{12} + \frac{M_{12}}{R_2} = 0, \\ &T_1 = 0, \qquad M_1 = M_{12} = 0 \quad \text{at } \alpha_1 = \alpha_1^0 \\ &\qquad \text{or } \alpha_1 = \alpha_1^1, \alpha_2^0 \le \alpha_2 \le \alpha_2^1, \end{aligned} \tag{24}$$

$$\begin{aligned} &N_2 + \frac{M_2}{R_2} = 0, \qquad N_{21} + \frac{M_{21}}{R_1} = 0, \\ &T_2 = 0, \qquad M_2 = M_{21} = 0 \quad \text{at } \alpha_2 = \alpha_2^0 \\ &\qquad \text{or } \alpha_2 = \alpha_2^1, \alpha_1^0 \le \alpha_1 \le \alpha_1^1. \end{aligned} \tag{25}$$

In addition to the external boundary conditions (22)–(25), the kinematic and physical compatibility conditions should be satisfied at the common closing meridians with $\alpha_2 = 0, 2\pi$, if a complete shell of revolution has to be considered. The kinematic compatibility conditions include the continuity of displacements. The physical compatibility conditions can only be represented by the five continuous conditions for the generalized stress resultants. To consider complete revolute shells characterized by $\alpha_2^1 = 2\pi$, it is necessary to implement the kinematic and physical compatibility conditions between the two computational meridians with $\alpha_2^0 = 0$ and with $\alpha_2^1 = 2\pi$:

Kinematic compatibility conditions along the closing meridian ($\alpha_2 = 0, 2\pi$)

$$\begin{aligned} &u_1(\alpha_1, 0, t) = u_1(\alpha_1, 2\pi, t), \qquad u_2(\alpha_1, 0, t) = u_2(\alpha_1, 2\pi, t), \\ &u_3(\alpha_1, 0, t) = u_3(\alpha_1, 2\pi, t), \\ &\beta_1(\alpha_1, 0, t) = \beta_1(\alpha_1, 2\pi, t), \qquad \beta_2(\alpha_1, 0, t) = \beta_2(\alpha_1, 2\pi, t) \\ &\qquad \alpha_1^0 \le \alpha_1 \le \alpha_1^1, \end{aligned} \tag{26}$$

Physical compatibility conditions along the closing meridian ($\alpha_2 = 0, 2\pi$)

$$\begin{aligned} &N_2(\alpha_1, 0, t) + \frac{M_2(\alpha_1, 0, t)}{R_2} \\ &\qquad = N_2(\alpha_1, 2\pi, t) + \frac{M_2(\alpha_1, 2\pi, t)}{R_2}, \end{aligned}$$

Table 1: First ten frequencies and maximum static deflections for the six shell structures of Figure 4 made of isotropic materials: FGM_C: full ceramic material and FGM_M: full metal material using a 31×31 Chebyshev-Gauss-Lobatto (C-G-L) grid distribution with different boundary conditions.

Mode [Hz]	Square plate CCFF		Cylindrical panel SFSF		Conical shell CF		Toroidal shell panel CF		Catenoidal panel CFCF		Elliptic paraboloid CCCC	
	FGM_C GDQ (31×31)	FGM_M GDQ (31×31)	FGM_C GDQ (31×31)	FGM_M GDQ (31×31)	FGM_C GDQ (31×31)	FGM_M GDQ (31×31)	FGM_C GDQ (31×31)	FGM_M GDQ (31×31)	FGM_C GDQ (31×31)	FGM_M GDQ (31×31)	FGM_C GDQ (31×31)	FGM_M GDQ (31×31)
f_1	375.598	162.089	271.645	115.701	449.402	194.323	28.665	12.452	828.011	359.407	451.863	201.635
f_2	1252.975	536.895	282.473	120.922	449.402	194.323	29.385	12.679	846.255	365.918	485.074	211.268
f_3	1373.081	602.852	546.801	234.445	585.799	247.965	80.330	34.397	1042.714	451.381	487.409	212.299
f_4	2367.239	1019.777	549.102	239.032	585.799	247.965	80.416	34.706	1136.811	486.278	632.857	276.825
f_5	2868.597	1235.869	642.802	276.494	680.296	298.116	113.948	49.115	1147.395	492.825	719.612	314.418
f_6	3084.992	1334.067	648.822	279.014	680.296	298.116	121.533	52.684	1212.360	518.534	747.215	328.314
f_7	3194.352	1399.648	847.611	371.648	860.268	373.956	133.553	57.452	1476.266	632.458	864.072	377.506
f_8	3629.667	1590.719	933.540	404.836	860.268	373.956	160.575	70.062	1566.446	679.318	878.506	383.706
f_9	4018.936	1736.048	973.695	423.554	930.739	411.564	167.115	71.979	1890.222	821.620	1019.096	443.351
f_{10}	4156.483	1800.873	1143.969	483.642	966.531	418.914	197.566	85.108	1941.698	833.159	1034.972	450.206
$u_{3\,\max}$	$1.565687E-05$	$2.456358E-05$	$1.012876E-05$	$1.623087E-05$	$4.773661E-07$	$7.045025E-07$	$3.440893E-05$	$5.244087E-05$	$3.511216E-07$	$5.452771E-07$	$1.819132E-06$	$2.611289E-06$

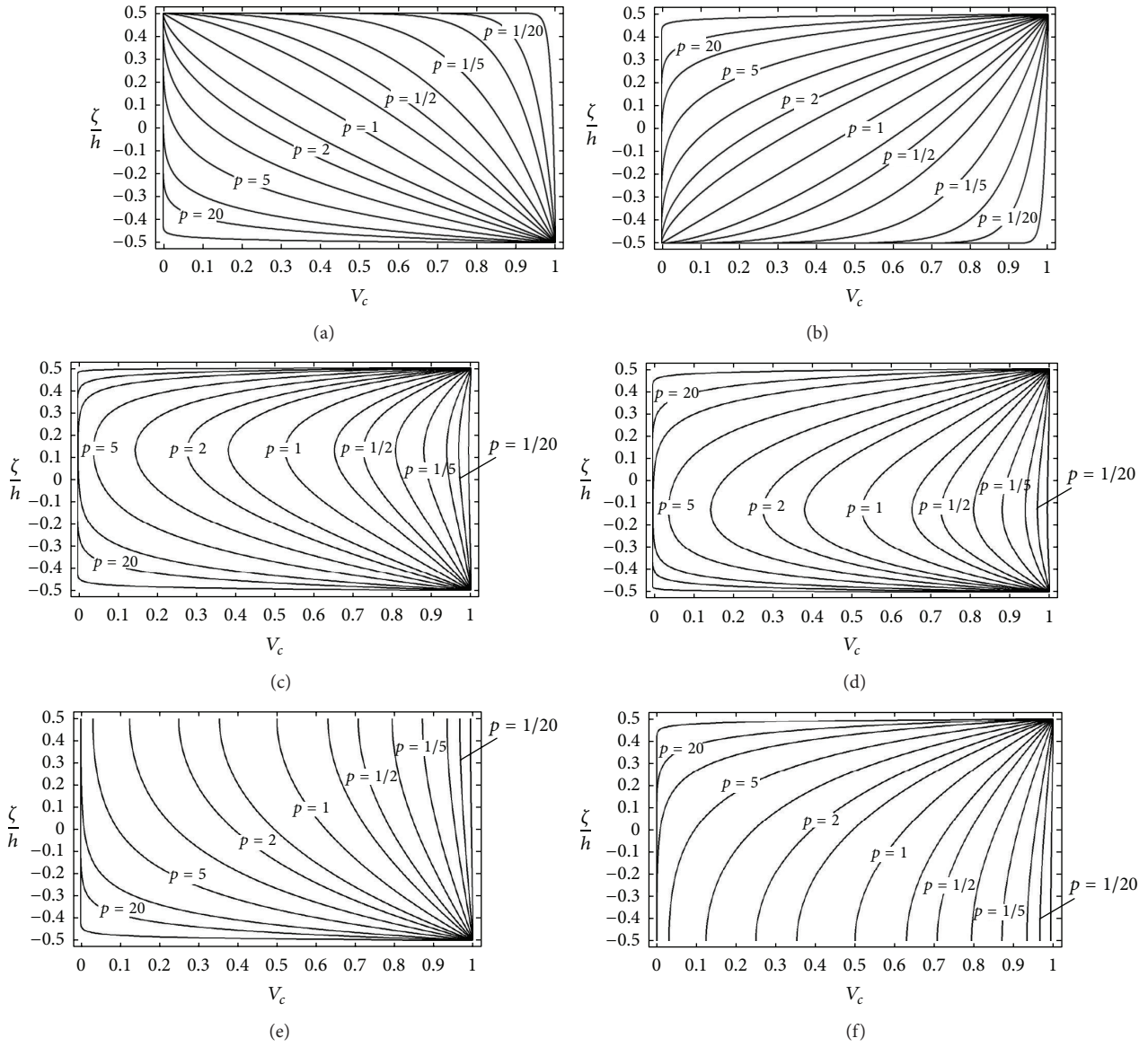

Figure 2: Variations of the ceramic volume fraction V_C through the thickness for different values of the three parameters $a^{(1)}, b^{(1)}$, and $c^{(1)}$ and the power-law index $p^{(1)}$ for a single-layered shell: (a) $\mathrm{FGM}_{1(a^{(1)}=1/b^{(1)}=0/c^{(1)}/p^{(1)})}$, (b) $\mathrm{FGM}_{2(a^{(1)}=1/b^{(1)}=0/c^{(1)}/p^{(1)})}$, (c) $\mathrm{FGM}_{1(a^{(1)}=1/b^{(1)}=1/c^{(1)}=2/p^{(1)})}$, (d) $\mathrm{FGM}_{2(a^{(1)}=1/b^{(1)}=1/c^{(1)}=2/p^{(1)})}$, (e) $\mathrm{FGM}_{1(a=1/b=0.5/c=2/p)}$, and (f) $\mathrm{FGM}_{2(a^{(1)}=1/b^{(1)}=0.5/c^{(1)}=2/p^{(1)})}$.

$$N_{21}(\alpha_1, 0, t) + \frac{M_{21}(\alpha_1, 0, t)}{R_1} = N_{21}(\alpha_1, 2\pi, t) + \frac{M_{21}(\alpha_1, 2\pi, t)}{R_1},$$

$$T_2(\alpha_1, 0, t) = T_2(\alpha_1, 2\pi, t),$$

$$M_2(\alpha_1, 0, t) = M_2(\alpha_1, 2\pi, t),$$

$$M_{21}(\alpha_1, 0, t) = M_{21}(\alpha_1, 2\pi, t),$$

$$\alpha_1^0 \le \alpha_1 \le \alpha_1^1. \tag{27}$$

In analogous way, in order to consider a toroidal shell of revolution it is necessary to implement the kinematic and physical compatibility conditions between the two computational parallels with $\alpha_1^0 = 0$ and with $\alpha_1^1 = 2\pi$:

Kinematic compatibility conditions along the closing parallel $(\alpha_1 = 0, 2\pi)$

$$u_1(0, \alpha_2, t) = u_1(2\pi, \alpha_2, t), \qquad u_2(0, \alpha_2, t) = u_2(2\pi, \alpha_2, t),$$

$$u_3(0, \alpha_2, t) = u_3(2\pi, \alpha_2, t),$$

$$\beta_1(0, \alpha_2, t) = \beta_1(2\pi, \alpha_2, t), \qquad \beta_2(0, \alpha_2, t) = \beta_2(2\pi, \alpha_2, t),$$

$$\alpha_2^0 \le \alpha_2 \le \alpha_2^1, \tag{28}$$

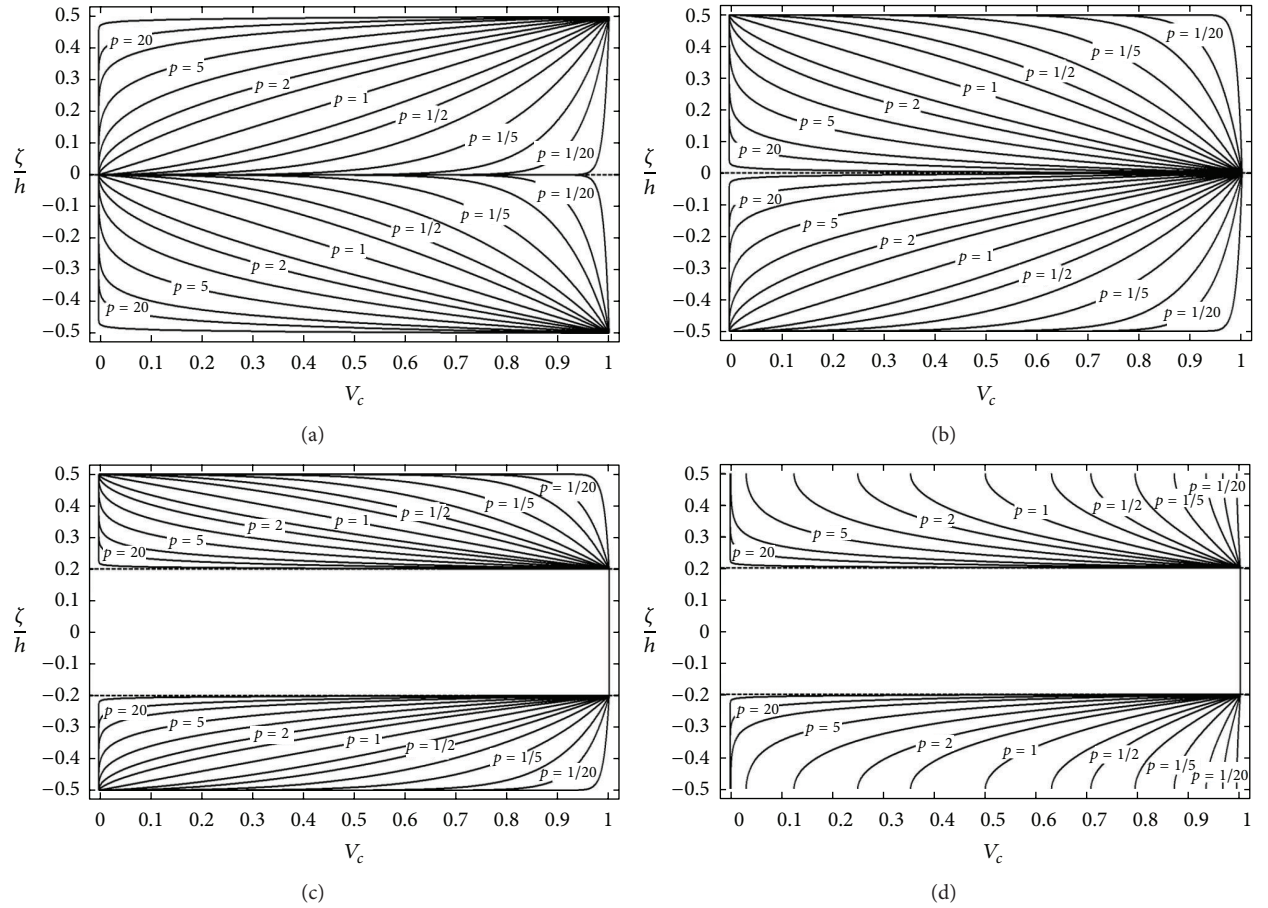

FIGURE 3: Variations of the ceramic volume fraction V_C through the thickness for two-layered and three-layered laminated shells for different values of the power-law index $p = p^{(1)} = p^{(2)}$ and $p = p^{(1)} = p^{(3)}$: (a) $\mathrm{FGM}_{1(a^{(1)}=1/b^{(1)}=0/c^{(1)}/p^{(1)})}/\mathrm{FGM}_{2(a^{(2)}=1/b^{(2)}=0/c^{(2)}/p^{(2)})}$, (b) $\mathrm{FGM}_{2(a^{(1)}=1/b^{(1)}=0/c^{(1)}/p^{(1)})}/\mathrm{FGM}_{1(a^{(2)}=1/b^{(2)}=0/c^{(2)}/p^{(2)})}$, (c) $\mathrm{FGM}_{2(a^{(1)}=1/b^{(1)}=0/c^{(1)}/p^{(1)})}/\mathrm{FGM}_C/\mathrm{FGM}_{1(a^{(3)}=1/b^{(3)}=0/c^{(3)}/p^{(3)})}$, and (d) $\mathrm{FGM}_{2(a^{(1)}=1/b^{(1)}=0.5/c^{(1)}=2/p^{(1)})}/\mathrm{FGM}_C/\mathrm{FGM}_{1(a^{(3)}=1/b^{(3)}=0.5/c^{(3)}=2/p^{(3)})}$.

Physical compatibility conditions along the closing parallel $(\alpha_1 = 0, 2\pi)$

$$
\begin{aligned}
&N_1(0,\alpha_2,t) + \frac{M_1(0,\alpha_2,t)}{R_1} \\
&\quad = N_1(2\pi,\alpha_2,t) + \frac{M_1(2\pi,\alpha_2,t)}{R_1}, \\
&N_{12}(0,\alpha_2,t) + \frac{M_{12}(0,\alpha_2,t)}{R_2} \\
&\quad = N_{12}(2\pi,\alpha_2,t) + \frac{M_{12}(2\pi,\alpha_2,t)}{R_2}, \\
&T_1(0,\alpha_2,t) = T_1(2\pi,\alpha_2,t), \\
&M_1(0,\alpha_2,t) = M_1(2\pi,\alpha_2,t), \\
&M_{12}(0,\alpha_2,t) = M_{12}(2\pi,\alpha_2,t) \\
&\qquad \alpha_2^0 \le \alpha_2 \le \alpha_2^1.
\end{aligned} \tag{29}
$$

3. Discretized Equations and Numerical Implementation

The Generalized Differential Quadrature method is used to discretize the spatial derivatives in the governing equations in terms of generalized displacements, as well as boundary conditions (see Tornabene [49] for a brief review). Throughout the paper, the Chebyshev-Gauss-Lobatto (C-G-L) grid distribution is assumed, for which the coordinates of grid points $(\alpha_{1i}, \alpha_{2j})$ along the reference surface are in the discrete form:

$$
\begin{aligned}
\alpha_{1i} &= \left(1 - \cos\left(\frac{i-1}{N-1}\pi\right)\right)\frac{\left(\alpha_1^1 - \alpha_1^0\right)}{2} + \alpha_1^0, \\
&\qquad i = 1,2,\ldots,N, \quad \text{for } \alpha_1 \in \left[\alpha_1^0, \alpha_1^1\right], \\
\alpha_{2j} &= \left(1 - \cos\left(\frac{j-1}{M-1}\pi\right)\right)\frac{\left(\alpha_2^1 - \alpha_2^0\right)}{2} + \alpha_2^0, \\
&\qquad j = 1,2,\ldots,M, \quad \text{for } \alpha_2 \in \left[\alpha_2^0, \alpha_2^1\right],
\end{aligned} \tag{30}
$$

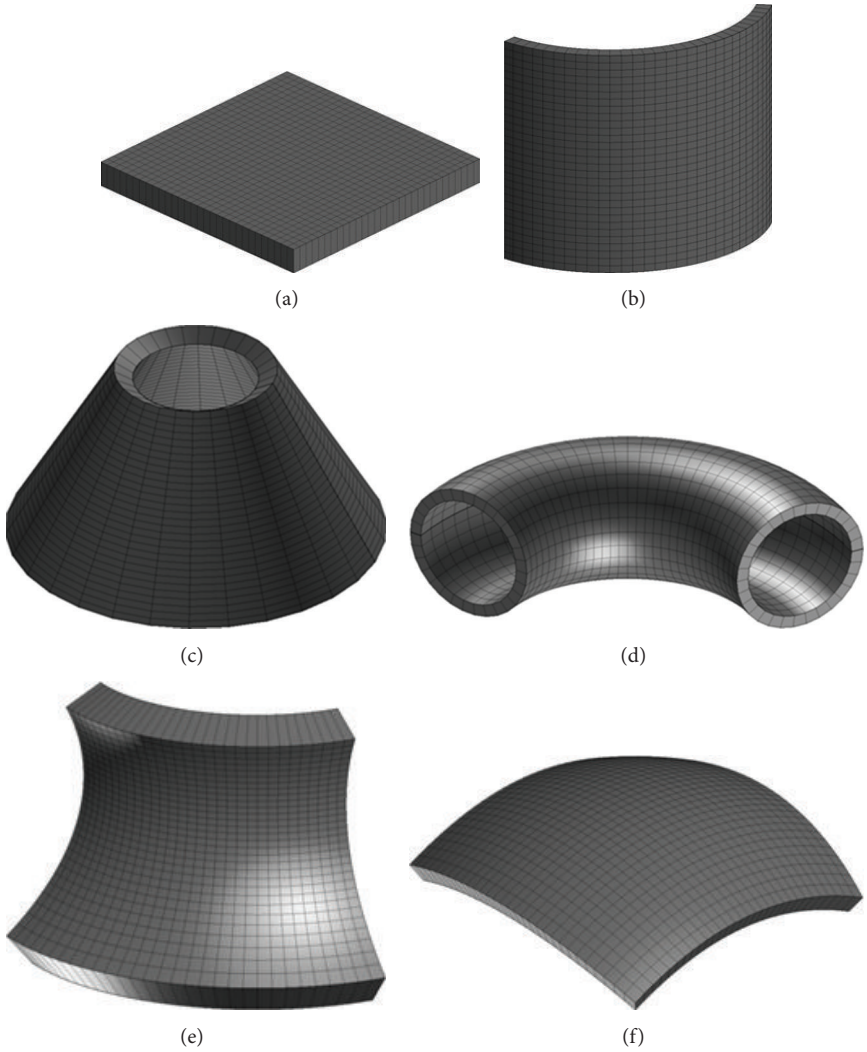

Figure 4: Six different types of FGM shells and panels: (a) rectangular plate (degenerate panel), (b) cylindrical panel (singly curved panel), (c) conical shell (singly curved shell), (d) toroidal shell panel (doubly curved shell panel of revolution), (e) catenoidal panel (doubly curved panel of revolution), and (f) elliptic paraboloid (completely doubly curved panel).

where N, M are the total number of sampling points used to discretize the domain in α_1 and α_2 directions, respectively, of the doubly curved shell. It has been proven that, for the Lagrange interpolating polynomials, the Chebyshev-Gauss-Lobatto sampling points rule guarantees convergence and efficiency to the GDQ technique [23, 43–45, 67, 68]. For the static analysis, when the inertias (21) are set to zero, the GDQ procedure enables to write the governing equations (20) and the boundary and compatibility conditions (22)–(29) in discrete form, transforming each space derivative into a weighted sum of node values of independent variables using the Differential Quadrature rule [26, 49]:

$$\left.\frac{\partial^n f(x)}{\partial x^n}\right|_{x=x_m} = \sum_{k=1}^{T} \varsigma_{mk}^{(n)} f(x_k), \quad m = 1, 2, \ldots, T. \tag{31}$$

Each approximate equation is valid in a single sampling point. Thus, the whole system of differential equations has been discretized and the global assembling leads to the following set of linear algebraic equations:

$$\left[\begin{array}{c|c} \mathbf{K}_{bb} & \mathbf{K}_{bd} \\ \hline \mathbf{K}_{db} & \mathbf{K}_{dd} \end{array}\right] \left[\begin{array}{c} \boldsymbol{\delta}_b \\ \hline \boldsymbol{\delta}_d \end{array}\right] = \left[\begin{array}{c} \mathbf{f}_b \\ \hline \mathbf{f}_d \end{array}\right]. \tag{32}$$

In the above mentioned matrices and vectors, the partitioning is set forth by subscripts b and d, referring to the system degrees of freedom and standing for boundary and domain, respectively. In this sense, b-equations represent the discrete boundary conditions, which are valid only for the points lying on the constrained edges of the shell, while d-equations are the equilibrium equations, assigned on the interior nodes. In order to make the computation more efficient, static condensation of nondomain degrees of freedom is performed:

$$\left(\mathbf{K}_{dd} - \mathbf{K}_{db}\mathbf{K}_{bb}^{-1}\mathbf{K}_{bd}\right)\boldsymbol{\delta}_d = \mathbf{f}_d - \mathbf{K}_{db}\mathbf{K}_{bb}^{-1}\mathbf{f}_b. \tag{33}$$

The deflection of the considered structures can be determined by solving the linear algebraic problem (33). In particular, the

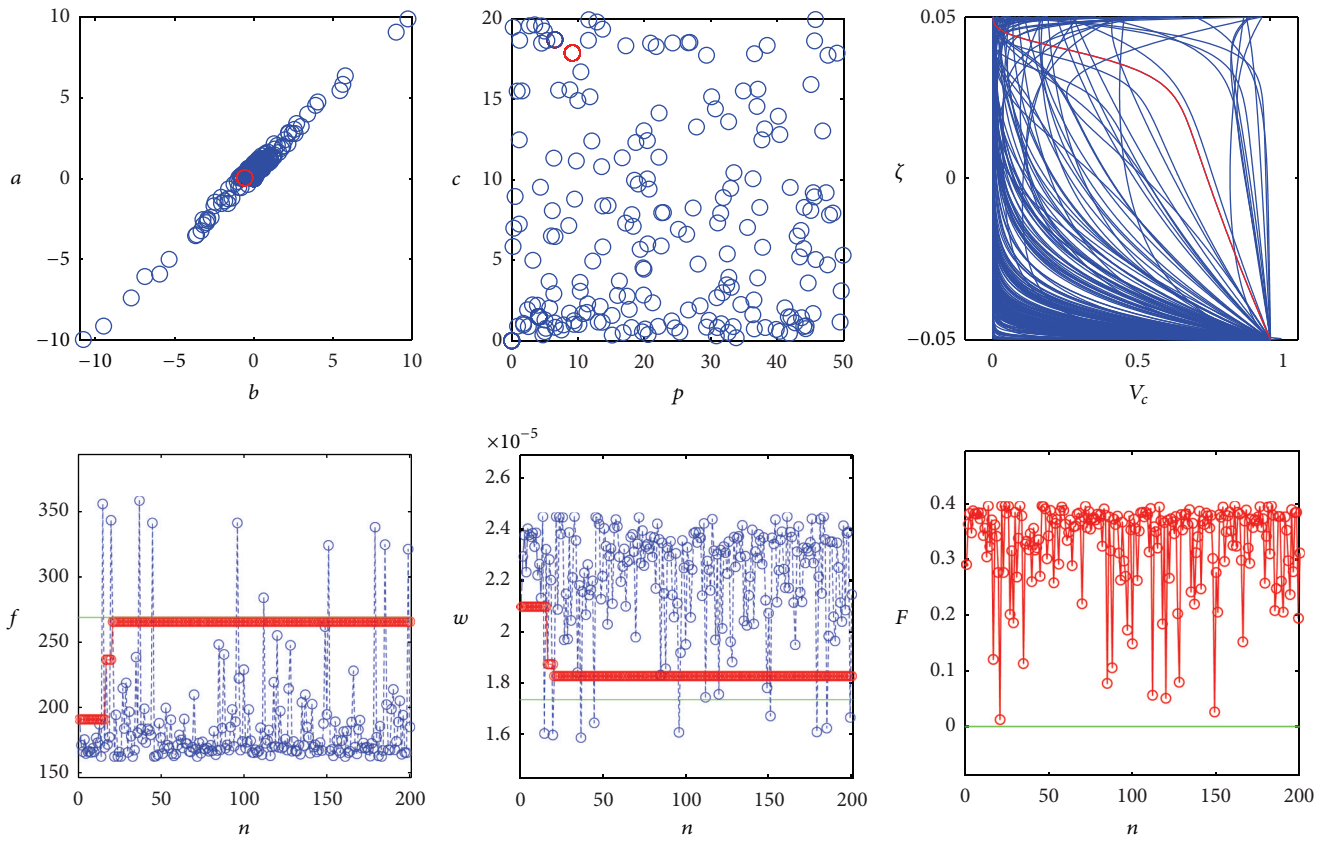

FIGURE 5: Square plate: Monte Carlo optimization with $\eta = 1$; final optimized frequency $f = 265.364$ Hz.

solution procedure by means of the GDQ technique has been implemented in a personal code.

Differently from the static case, when the external forces $q_1^+, q_1^-, q_2^+, q_2^-, q_n^+$, and q_n^- (19) are set to zero, the free vibration of laminated composite doubly curved shells and panels can be studied. Using the method of variable separation, it is possible to seek solutions that are harmonic in time and whose frequency is $f = \omega/2\pi$. The generalized displacements can be written as follows:

$$\begin{aligned} u_1(\alpha_1, \alpha_2, t) &= U^1(\alpha_1, \alpha_2)\, e^{i\omega t}, \\ u_2(\alpha_1, \alpha_2, t) &= U^2(\alpha_1, \alpha_2)\, e^{i\omega t}, \\ u_3(\alpha_1, \alpha_2, t) &= U^3(\alpha_1, \alpha_2)\, e^{i\omega t}, \\ \beta_1(\alpha_1, \alpha_2, t) &= B^1(\alpha_1, \alpha_2)\, e^{i\omega t}, \\ \beta_2(\alpha_1, \alpha_2, t) &= B^2(\alpha_1, \alpha_2)\, e^{i\omega t}, \end{aligned} \tag{34}$$

where the vibration spatial amplitude values U^1, U^2, U^3, B^1, and B^2 fulfil the fundamental differential system (20). Each approximate equation is valid in a single sampling point. Thus, the whole system of differential equations can be discretized and the global assembling leads to a set of linear eigenvalue problem. When kinematic condensation of nondomain degrees of freedom is performed, one gets

$$\left(\mathbf{K}_{dd} - \mathbf{K}_{db}\left(\mathbf{K}_{bb}\right)^{-1}\mathbf{K}_{bd}\right)\boldsymbol{\delta}_d = \omega^2 \mathbf{M}_{dd}\boldsymbol{\delta}_d. \tag{35}$$

The natural frequencies of the structure $f_r = \omega_r/2\pi$, for $r = 1, 2, \ldots, 5(N-2)\times(M-2)$, can be determined by solving the standard eigenvalue problem (35). In particular, the solution procedure by means of the GDQ technique has been implemented in a personal code. The above partitioning (35) is set forth by subscripts b and d, referring to the system degrees of freedom and standing for boundary and domain, respectively. Finally, the results in terms of frequencies are obtained using an eigenvalue function. With the present approach, differing from the finite element method, no integration occurs prior to the global assembly of the linear system, and this represents a further computational cost saving in favour of the Differential Quadrature technique.

4. Optimization Algorithms

4.1. Genetic Algorithm (GA) Optimization Method. The GA approach to optimization was probably introduced at first by Holland [107], while a comprehensive reference including implementation procedures and application notes can be found in later work, like, for instance, the seminal book by Goldberg [99]. GA tries to implement and imitate in

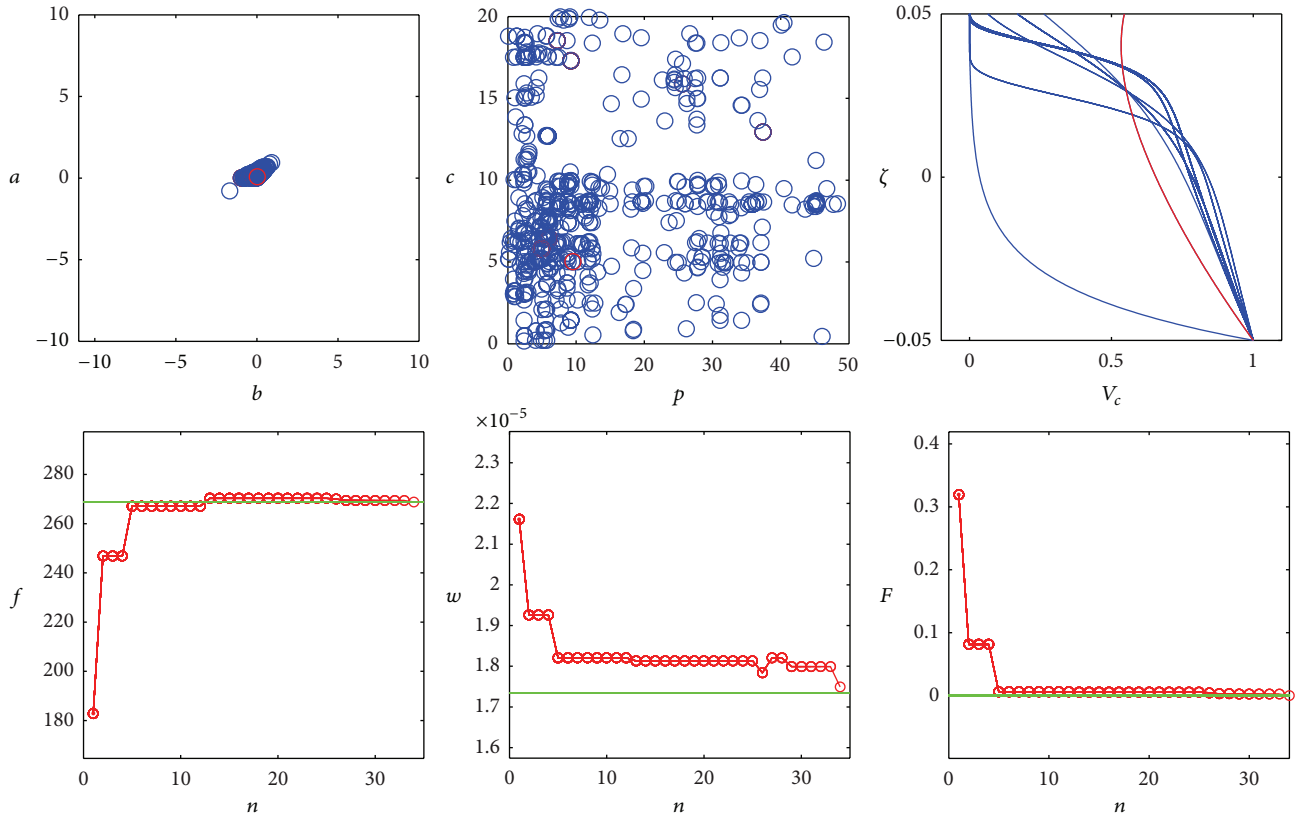

Figure 6: Square plate: Genetic Algorithm optimization with $\eta = 1$; final optimized frequency $f = 268.816$ Hz.

a mathematical framework the law of evolution, which Darwin introduced to explain the changes in nature towards individuals better suited to the environment in which they live: GA can be in fact classified as a typical population-based optimization algorithm. Generation by generation, populations evolve improving the fitness function which represents the ability to survive in a defined environment; the individuals less adapting to the surrounding environment do not mate and their genetic set of chromosomes is lost. A solution is represented by a chromosome, constituted by a set of genes representing the parameters of the solution. The mathematical implementation follows with the coding of a chromosome in binary and with the application of some computational functions like mutations, crossover, and elitarism. When elitarism is set, some of the best individuals are replicated in the following generation without any change in a perfect replication from father to son. The concept of crossover implies a change between genes of two solutions and imitates the reproduction in which the son possesses a part of genes from his mother and the remaining from the father. Aim of mutations, as it happens in nature, is to randomly change some genes of the individual to test new configurations: from an optimization point of view, mutations help in exploring new zones of the space and are useful to avoid the problem of "local minimum" capturing. According to the work by Konak et al. [106], the fitness is the main driver of the capability to survive and to pass genes to the next generation: the chromosome is in fact decoded from binary to decimal and tested in the fitness only after the application of mating functions requiring a binary coding. Modern approaches to the application of GA lie in new formulations and in the introduction of hybridization with other optimization strategies [108]; also Pareto-based analysis for multiobjective optimization [103] has been evaluated, and improvement of GA by the application of fuzzy sets and neural networks [109] has been proposed to solve complex tasks. The algorithm implemented in this work follows the procedure proposed by Goldberg [99], and the fitness has been defined by authors considering the closeness of the solution found to the value set by the designer and the feasibility of the volume fraction distribution in the thickness ($0 < V_C^{(k)} < 1$). The pseudocode of the GA implemented is shown in the following Pseudocode 1.

4.2. Monte Carlo (MC) Optimization Method. The Monte Carlo technique has been developed to support early studies related to the nuclear physics; the idea is to find the best approximation of a constant or to solve a problem through a statistical way, obtaining the results from a very large set

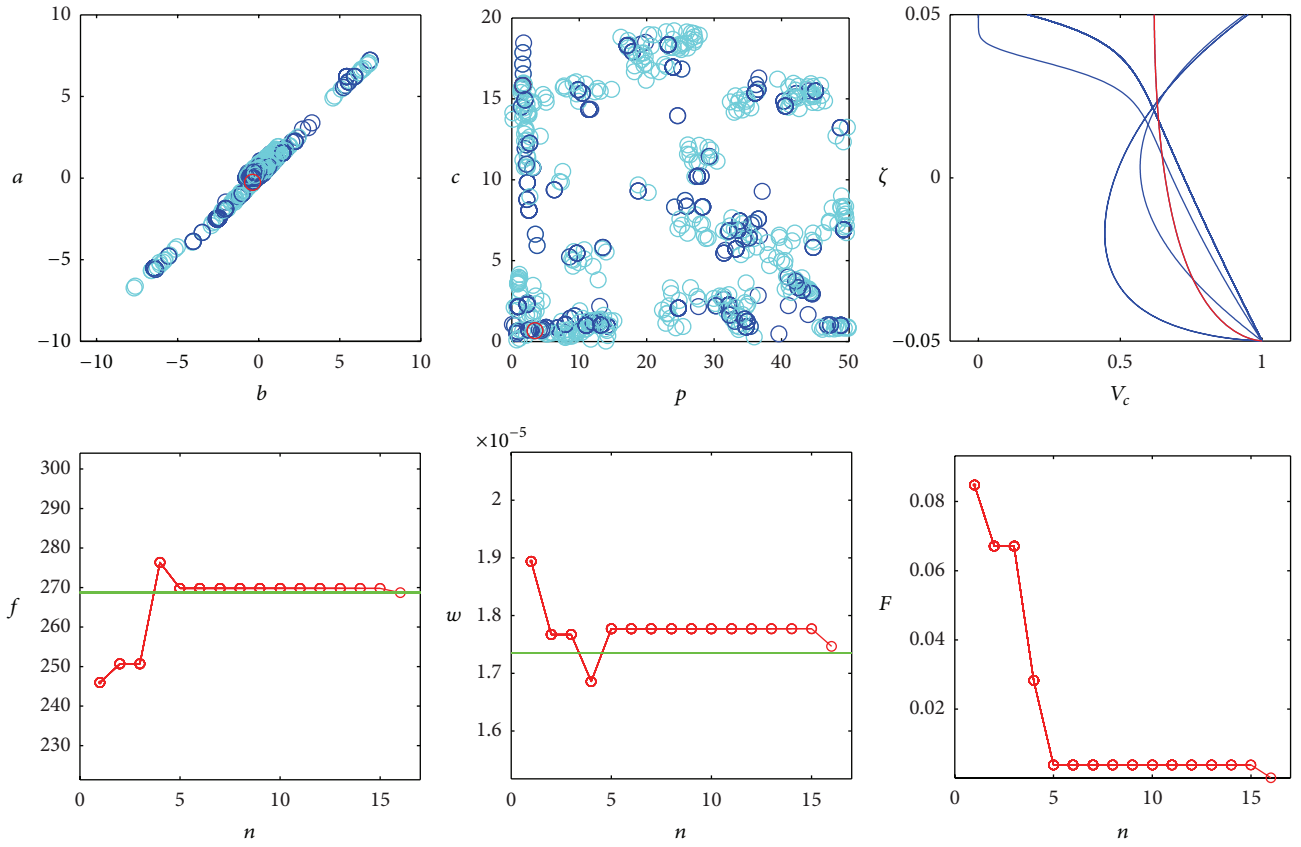

FIGURE 7: Square plate: Particle Swarm Optimization with $\eta = 1$; final optimized frequency $f = 268.710$ Hz.

of random inputs. From a mathematical and formal point of view, for instance, the paper by Mosegaard and Sambridge [123] introduces the way by which an integral in the form

$$I = \int_X g(x) f(x) dx \tag{36}$$

can be evaluated by the generation of random samples $x_1, x_2, x_3, x_4, \ldots, x_S$ of x, when $f(x)$ is an appropriate probability distribution and $g(x)$ is the function of which the integral have to be computed. The integral can be so computed by the expression

$$I \approx \frac{1}{S} \sum_{s=1}^{S} g(x_s). \tag{37}$$

The MC methods are very simple, but studies are focused on the probability distribution shapes providing best results and on the software methods to generate random numbers; this is not a trivial issue, since it can be complex to generate a set of random numbers which are not dependent on the clock of the processor or on other hardware timers. Obviously, considering computational efforts, the MC method is very time expensive; however, due to the increasing computations capabilities of personal computers and the improving of the capabilities which are a constant trend in years, this approach has been recently reconsidered and still applied to a wide range of applications. The continuous improvement in randomizer algorithms helps in the gain of good performances, which are often obtained exploiting the capabilities of clusters of computers. The main critical aspect related to the MC methods application in engineering is that it requires a lot of iteration to obtain a solution; following this approach, in fact, the space is explored in a completely random way and no attention is focused on zones in which solutions are better than the average. The literature presents a lot of interesting applications of MC to engineering problems, like the works [124–126] show; MC is also widely applied to games and strategy since it allows keeping in consideration all the possible scenarios evolving from a situation: some papers dealing with this issue can be found in [127]. A pseudocode of the MC algorithm is included in Pseudocode 2.

4.3. Particle Swarm Optimization (PSO) Method. The PSO algorithm used in this paper is similar to the one proposed by Birge [115], with some variations due to the particular application to the FGM optimization problem. According to the general implementation of PSO, the position of a particle in the n-dimensional solution space can be considered a

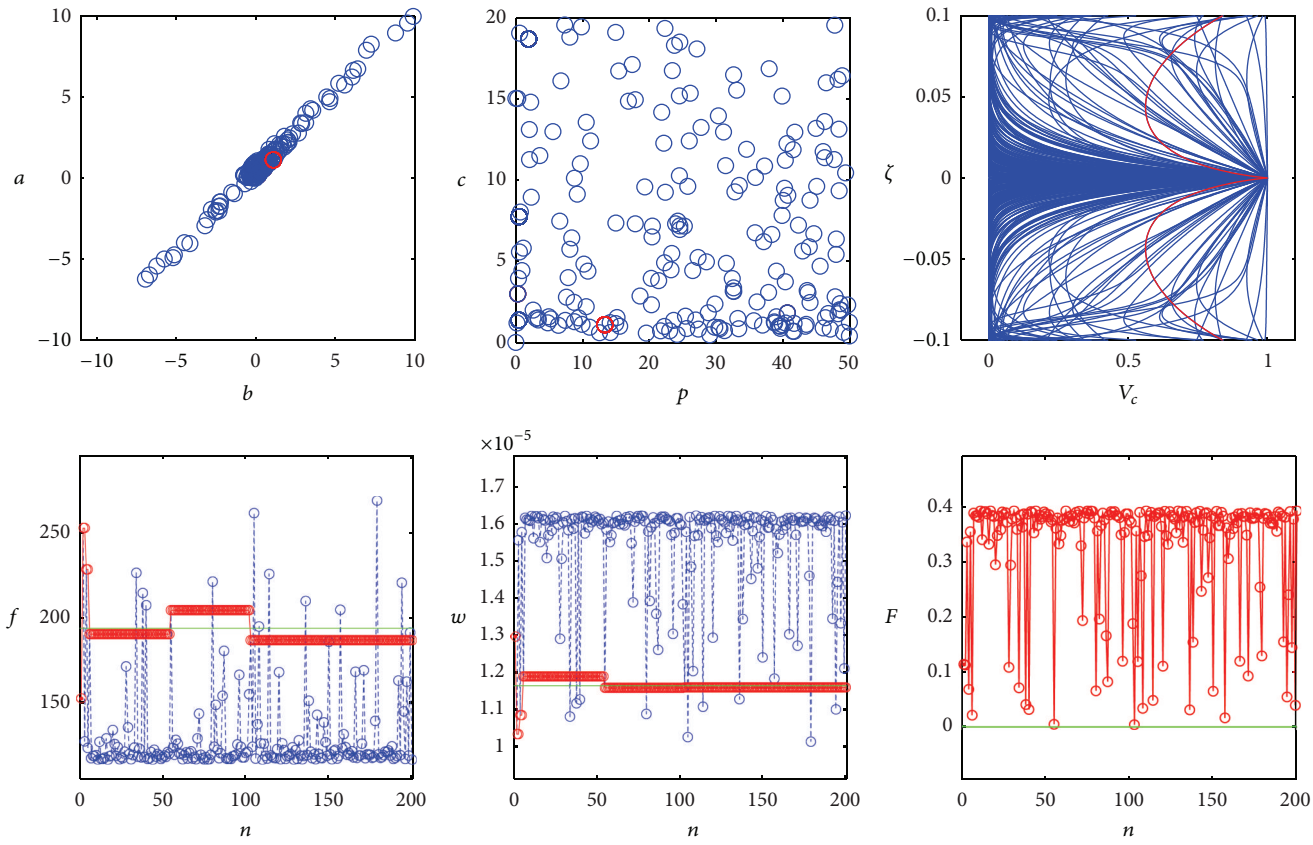

Figure 8: Cylindrical panel: Monte Carlo optimization with $\eta = 1$; final optimized displacement $w = 1.1596 \cdot 10^{-5}$ m.

solution to the problem in the n-dimensional space of the parameters; the n-dimensional speed which is computed in the algorithm represents the direction towards a new position in the n-dimensional space. The velocity can be obtained by

$$v_i^{(m)} = \phi^{(m)} v_i^{(m-1)} + c_1 a_1 \left(P_{bi} - P_i^{(m-1)}\right) + c_2 a_2 \left(P_{bG_b} - P_i^{(m-1)}\right), \tag{38}$$

where m is the algorithm step (n_G generations); i is the index of parameter of the single particle; $\phi^{(m)}$ is the inertia function; $v_i^{(m)}$ is the velocity of the ith particle at the m-step; P_{bi} is the best position found by the ith particle; G_b is the global best position (it is the best position found by the whole swarm); a_1, a_2 are the acceleration constants; c_1, c_2 are random numbers in the interval $[0, 1]$.

The following formulation can be applied to obtain the new position:

$$P_i^{(m)} = P_i^{(m-1)} + v_i^{(m)}, \tag{39}$$

where $P_i^{(m)}$ is the position of the ith particle at the m-step and $v_i^{(m)}$ is the velocity of the ith particle at the m-step. One of the problems of the FGM profile shape in the thickness is that a small variation in $a^{(k)}, b^{(k)}, c^{(k)}$, and $p^{(k)}$ power-law parameters can lead to a solution showing a volume fraction inconsistent ($V_C^{(k)} < 0$ or $V_C^{(k)} > 1$). The PSO algorithm, in fact, belongs to the so-called "trajectory based methods" and sweeps the space following a path in which the new position is equal to the previous one plus a constant segment (the speed). For this reason, sometimes the updated position of a particle lies in a zone in which the volume fraction is out of limit; in this case, the classical implementation of the algorithm stops since the trajectory enters in a trap from which it is impossible to escape. The new position, in fact, can lead to inconsistent volume fractions and the algorithm stalls. In order to solve this problem, a check has been introduced in the algorithm (step 11 and step 12 in Pseudocode 3), so that if an unfeasible position is found by the algorithm, the velocity is rejected and changed until a new valid position is found. By this way, a forecast of the new position is computed and the PSO velocity is accepted if leading to a valid solution, randomized if it does not. The end criterion is due to one of these conditions: the achievement of the maximum number of iterations, or a condition in which after n_ε generations the solution does not improve. The PSO seems to be very attractive for optimization since the studies by Hu et al. [116] and by Ceruti et al. [102] present advantages with respect to GA: easiness of software code implementation, need for the definition of few setting

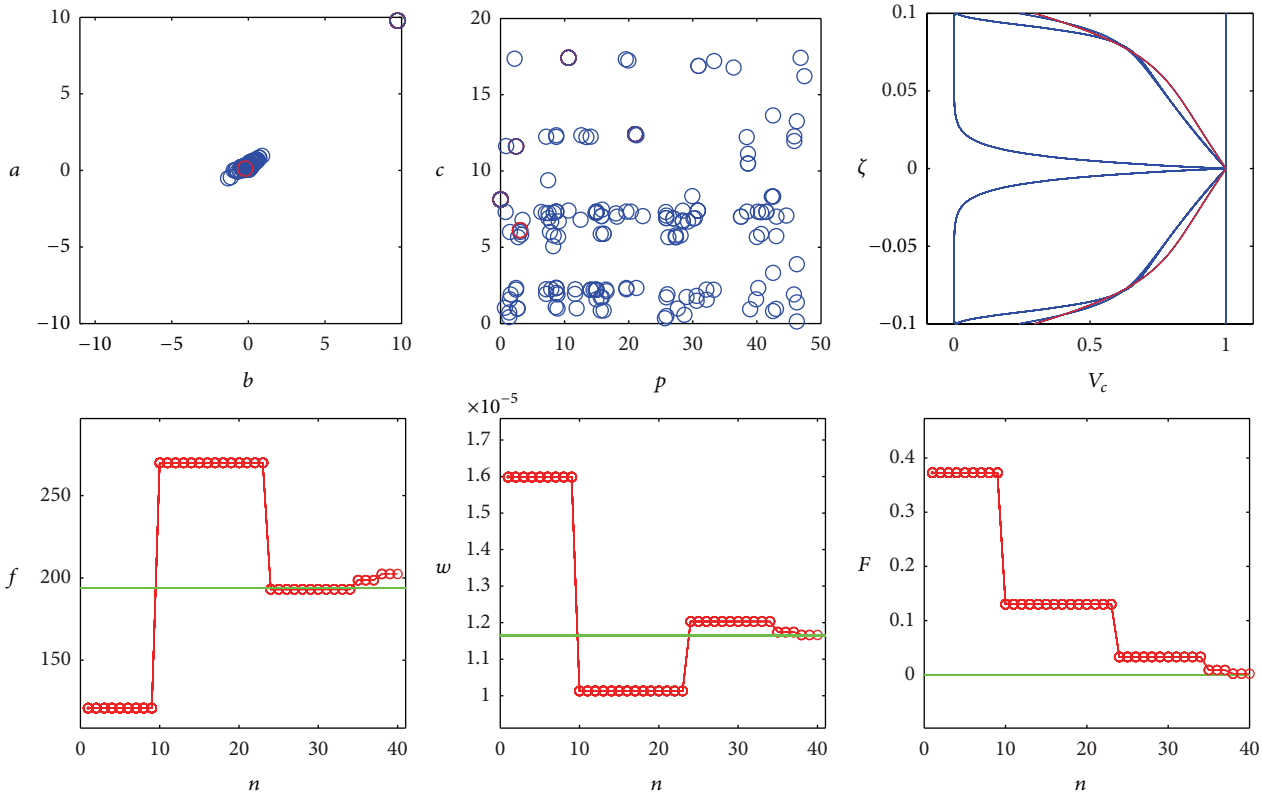

Figure 9: Cylindrical panel: Genetic Algorithm optimization with $\eta = 1$; final optimized displacement $w = 1.1668 \cdot 10^{-5}$ m.

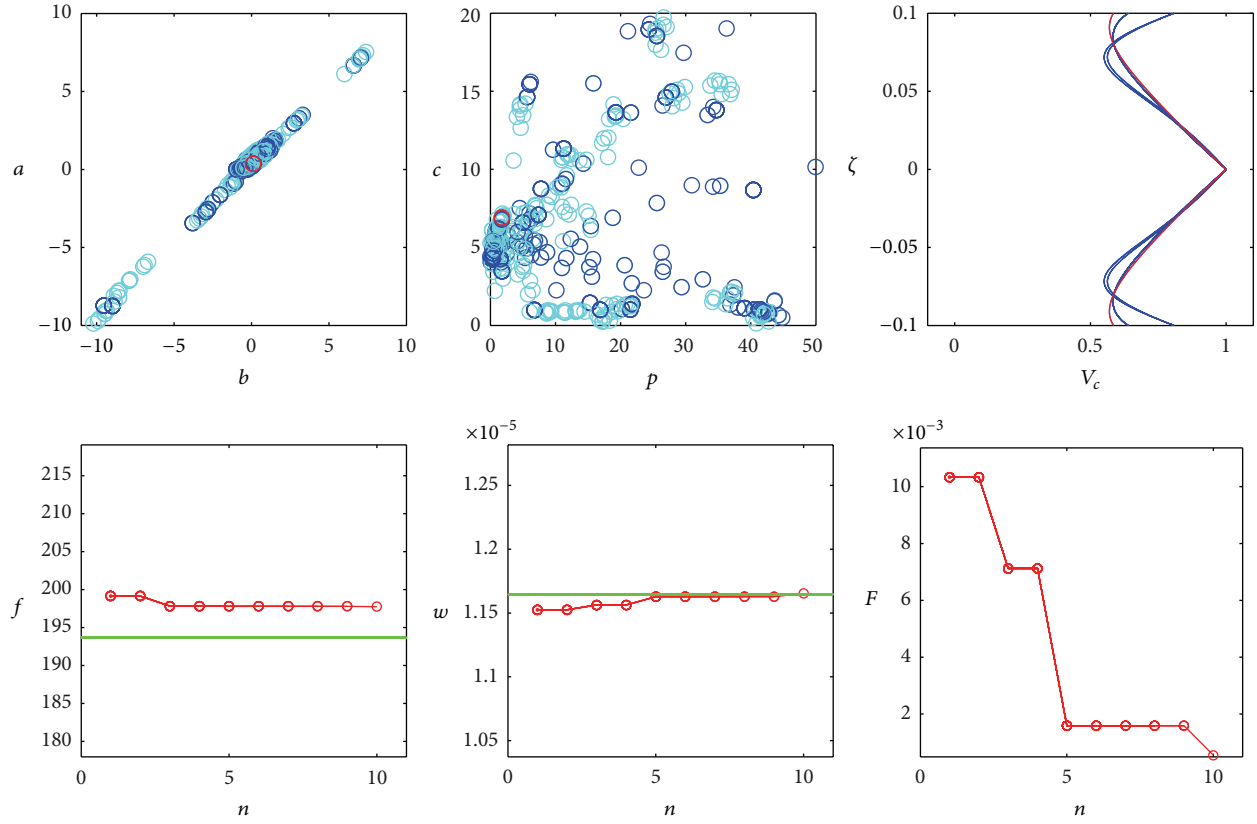

Figure 10: Cylindrical panel: Particle Swarm Optimization with $\eta = 1$; final optimized displacement $w = 1.1653 \cdot 10^{-5}$ m.

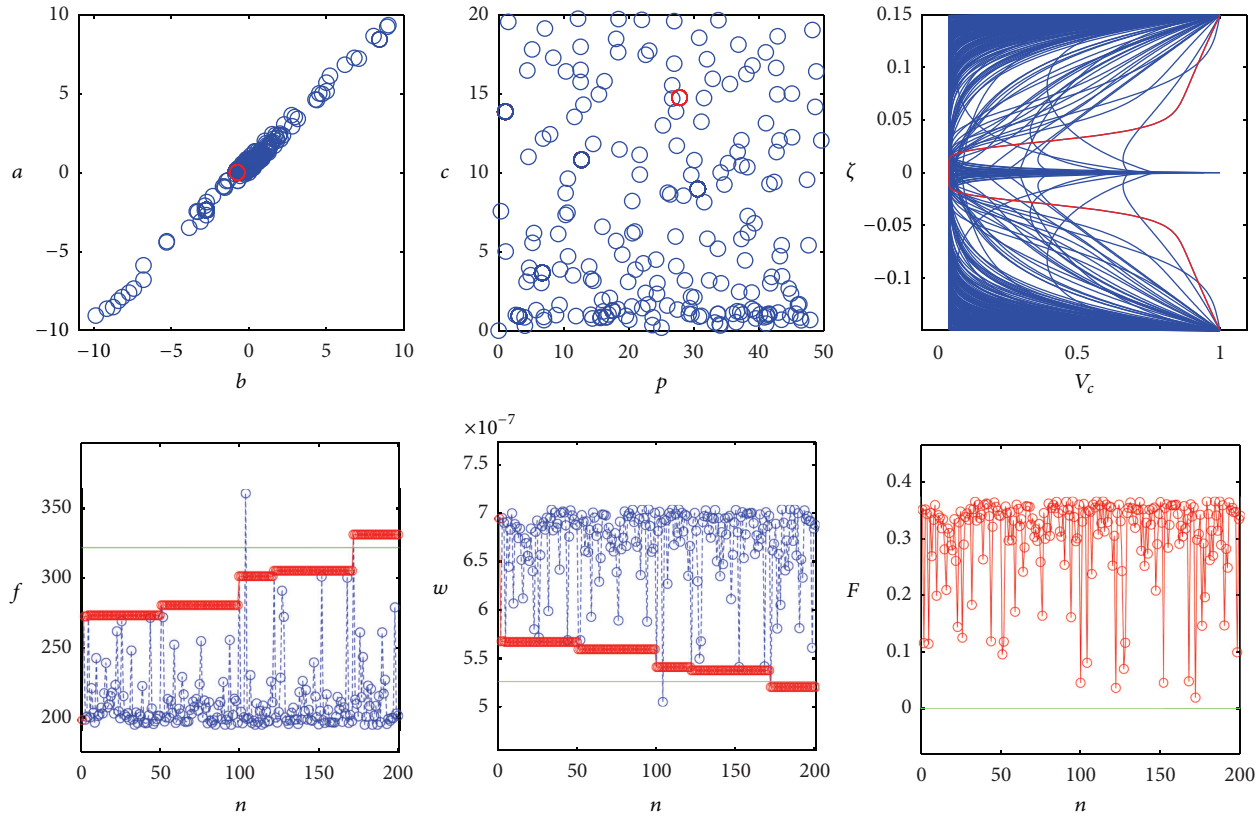

FIGURE 11: Conical shell: Monte Carlo optimization with $\eta = 0.5$; final optimized frequency $f = 330.946$ Hz and final optimized displacement $w = 5.2073 \cdot 10^{-7}$ m.

parameters, and good fitting to engineering application. The PSO implementation and the modifications introduced for this application are described in Pseudocode 3, where an illustrative pseudocode is presented.

5. Numerical Applications and Results

In the present section, some results and considerations about the mixed static and dynamic optimization problem of four-parameter functionally graded doubly curved and degenerate shells and panels are presented. The analysis has been carried out by means of numerical procedures illustrated above. Different types of structures are considered in the present paper. One of the aims of this study is to show some numerical examples about flat plates, singly curved, and doubly curved shells and panels made of FGMs. The six considered structures are depicted in Figure 4. In order to describe the middle surface of the given structures, theoretical formulae of differential geometry [7, 23, 43, 74, 78] are used. The mathematical development of the differential geometry applied to doubly curved shells was deeply explained in [23, 43, 74, 78]. So, in the following, only a few formulae are reported. Furthermore, it is worthwhile noting that the GDQ procedure enables to evaluate the parameters concerning the shell geometry as reported in [74, 78]. For all the GDQ results presented below, the Chebyshev-Gauss-Lobatto grid distributions (30) with $N = M = 31$ along the reference surface have been assumed, and the geometrical parameters with their derivatives are numerically evaluated using the GDQ method [26]. The FGM nomenclature used in the present work is identified by the same convention presented in the previous work by Tornabene et al. [70]. In an analogous way, the geometrical boundary conditions are defined considering similar convention used in the previous works [23, 43, 44, 47, 49–53, 68–76] for shell and panel structures.

For a rectangular flat plate, the position vector [74, 78] can be written as

$$\mathbf{r}(\alpha_1, \alpha_2) = -\alpha_2 \mathbf{e}_2 + \alpha_1 \mathbf{e}_3. \tag{40}$$

In Figure 4(a) the considered square plate has the sides $a = b = 1$ m, thickness $h = 0.1$ m, and it is subjected to a normal load $q_n^+ = -10000$ Pa at the top surface. The plate is free on two adjacent sides and clamped on the other two. The boundary conditions are indicated by the current nomenclature as CCFF. The square plate is a single-layered structure with $\mathrm{FGM}_{1(a^{(1)}/b^{(1)}/c^{(1)}/p^{(1)})}$ four-parameter power-law distribution. In this case, the four parameters $a = a^{(1)}, b = b^{(1)}, c = c^{(1)}$, and $p = p^{(1)}$ have to be determined by the optimization procedure.

The position vector for the cylindrical panel and conical shell of Figures 4(b) and 4(c) can be obtained from the conical shell formula, already presented in [74, 78] and reported here

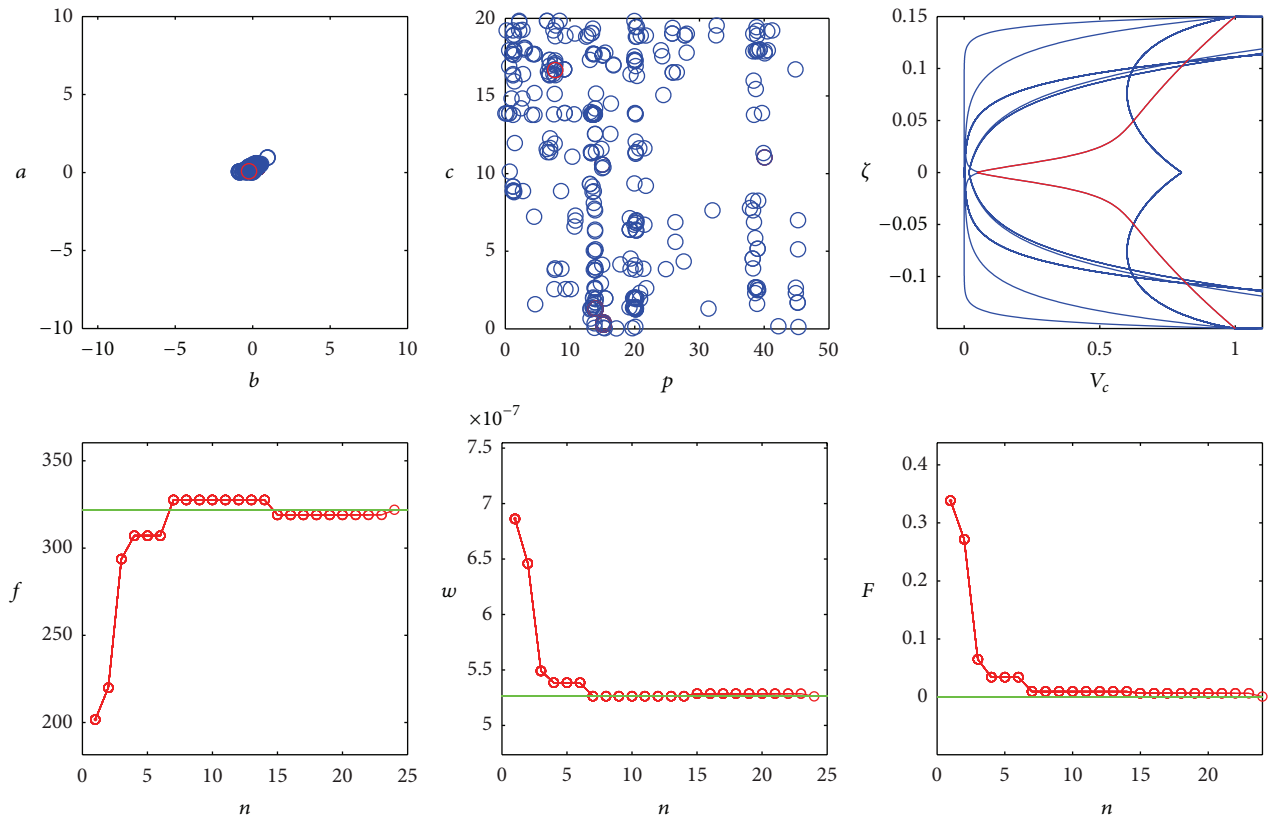

Figure 12: Conical shell: Genetic Algorithm optimization with $\eta = 0.5$; final optimized frequency $f = 321.890$ Hz and final optimized displacement $w = 5.2624 \cdot 10^{-7}$ m.

Step (1) Set a max and min value for each gene
Step (2) Set the max number of generations (T), the convergence tolerance (ε) and the number of consecutive no improvements loops (n_ε) after which algorithm ends, the number of genes (n_g), and the number of population (n_{pop}) members
Step (3) Initialize the first generation of population (P) by randomly set n_{pop} chromosomes, each one made by n_g genes
Step (4) while ($i < T$) or (ε for n_ε loops false)
Step (5) Select $P' \subset P$ (mating pool), initialize $P'' = 0$ (set of children)
Step (6) for $j = 1$ to n
Step (7) Randomly select individuals (chromosomes x_a and x_b) from P'
Step (8) Obtain x_{child} by applying crossover to x_a and x_b (with probability p_{cross})
Step (9) Mutate produced child x_{child} to x_a and x_b (with probability p_{mut})
Step (10) Apply elitarism (if set)
Step (11) Update population $P'' = P' \cup x_{\text{child}}$
Step (12) end for
Step (13) P = survival respect to the fitness* (P', P'')
Step (14) end while
Step (15) best chromosome detection
*In this case the fitness is multiplied by a penalty term if one of the sets $[a^{(k)}, b^{(k)}, c^{(k)}, p^{(k)}]$ leads to volume fractions which are not feasible (e.g. percentage of one constituent in the thickness larger than 1, less than 0, imaginary number).

Pseudocode 1: Genetic Algorithm pseudocode.

Step (1) Set a max and min value for each parameter
Step (2) Set the max number of population (n_g) members, the convergence tolerance (ε) and the number of consecutive no improvements loops (n_ε)
Step (3) while ($i < n_g$) or (ε for n_ε loops false)
Step (4) Randomly generate a member of population P_i, following a probability distribution (normal, exponential, Weibull [113]).
Step (5) Compute volume fraction distribution (V_C) in the thickness for P_i
Step (6) if $0 < V_C < 1$
Step (7) $i = i + 1$
Step (8) Compute Fitness
Step (9) if Fitness (i) > Best Fitness
Step (10) Best Fitness = Fitness (i)
Step (11) Best member = i
Step (12) end if
Step (12) end if
Step (13) end while

Pseudocode 2: Monte Carlo pseudocode.

Step (1) Set number of particles (n_P), number of parameters for each particle (n_{param}), max number of generations (n_G), convergence tolerance (ε) and the number of consecutive no improvements loops (n_ε), δ (ratio between position and speed)
Step (2) Set particles boundary values: $\max\left(1 : n_{\text{param}}\right)$, $\min\left(1 : n_{\text{param}}\right)$
Step (3) Randomly generate particles position $\left(P_i^{(0)}\right) \mid \min(i) < P_i^{(0)} < \max(i)$ and velocity $v_i^{(0)}$
Step (4) Evaluate fitness function $F_i = f\left(P_i^{(0)}\right),\ i = 1, \ldots, n_P$
Step (5) Set $P_b = P^{(0)}$, $F_{\text{best}} = F$, $G_b = \min(F_i)$, g_b = index of the $(\min(F_i))$ value
Step (6) for $m = 1$ to n_G
Step (7) for $i = 1$ to n_P
Step (8) $\Delta v_i = c_1 a_1 \left(P_{bi} - P_i^{(m-1)}\right) + c_2 a_2 (P_{bG_b} - P_i^{(m-1)})$
Step (9) $v_i^{(m)} = \phi^{(m)} v^{(m-1)} + \Delta v_i$
Step (10) $P_i^{(m)} = P_i^{(m-1)} + v_i^{(m)}$
Step (11) Compute Volume fraction distribution (V_C) in the thickness for $P_i^{(m)}$
Step (12) while $\left(P_i^{(m)} > \max(i)\right)$ or $\left(P_i^{(m)} < \min(i)\right)$ or $(V_C < 0)$ or $(V_C > 1)$
Step (13) $v_i^{(m)} = v^{(m-1)} + \delta \cdot (\max(i) - \min(i)) \cdot \text{random}(0 \div 1)$
Step (14) $P_i^{(m)} = P_i^{(m-1)} + v_i^{(m)}$
Step (15) end while
Step (16) Evaluate fitness $F_i = f\left(P_i^{(m)}\right),\ i = 1, \ldots, n_P$
Step (17) for $i = 1, \ldots, n_P$
Step (18) if $F_i < F_{bi}$ then $P_{bi} = P_i^{(m)}$ and $F_{bi} = F_i$
Step (19) if $F_i < G_b$ then $G_b = F_i$ and $g_b = i$
Step (20) end for
Step (21) end for
Step (22) end for

Pseudocode 3: Particle Swarm Optimization pseudocode.

for the sake of completeness. The position vector for the conical shell can be written as follows:

$$\mathbf{r}(\alpha_1, \alpha_2) = (R_b + \alpha_1 \sin\alpha)\cos\alpha_2 \mathbf{e}_1 - (R_b + \alpha_1 \sin\alpha)\sin\alpha_2 \mathbf{e}_2 + \alpha_1 \cos\alpha \mathbf{e}_3. \tag{41}$$

As it is well known [7, 74, 78], a conical shell [23, 42, 43, 49, 52] is a 2D structure having the middle surface generated by the rotation, about a fixed vertical axis, of an inclined straight line. The angle α is the top vertex angle of the cone, where the meridian angle φ can be written as a function of it: $\varphi = \pi/2 - \alpha$. Thus, for cylindrical panel, considering $\alpha = 0$, the position vector (41) takes the form

$$\mathbf{r}(\alpha_1, \alpha_2) = R_b \cos\alpha_2 \mathbf{e}_1 - R_b \sin\alpha_2 \mathbf{e}_2 + \alpha_1 \mathbf{e}_3. \tag{42}$$

The meridian abscissa α_1 is defined as $\alpha_1 \in [0, L]$, where L is the length of the meridian. The presented parameters are graphically shown in the works [23, 42, 43, 49, 52]. The cylindrical panel (Figure 4(b)) is defined by $R = R_b = 2\,\text{m}$,

Table 2: Optimization of the six different structures of Figure 4: (a) square plate, (b) cylindrical panel, (c) conical shell, (d) toroidal shell panel, (e) catenoidal panel, and (f) elliptic paraboloid. $\eta = 1$: optimization of the first frequency f_1; $\eta = 0$: optimization of maximum bending displacement $w_{\max} = u_{3\max}$; $\eta = 0.5$: optimization of the first frequency f_1 and maximum bending displacement $w_{\max} = u_{3\max}$.

Method	a	b	c	p	Final frequency	Final displacement	Final fitness	Computational time (min)
Rectangular plate								
$\eta = 1$: target frequency $f_{1T} = 268.753$ Hz								
MC	0.05582	−0.56831	17.86455	9.14279	265.36499	$1.8270E-05$	$1.2606E-02$	25
GA	0.08800	−0.06160	5.02440	9.53080	268.81630	$1.7493E-05$	$2.3583E-04$	42
PSO	−0.25829	−0.13011	0.67170	3.43176	268.71000	$1.7466E-05$	$1.5970E-04$	31
Cylindrical panel								
$\eta = 0$: target displacement $w_{\max T} = u_{3\max T} = 1.1646 \cdot 10^{-5}$ m								
MC	1.11895	1.10588	1.09493	13.33798	186.78559	$1.1596E-05$	$4.3053E-03$	32
GA	0.12710	−0.33040	6.11930	3.03030	202.41150	$1.1668E-05$	$1.8770E-03$	14
PSO	0.35190	−0.26277	6.90518	1.75727	197.75230	$1.1653E-05$	$5.8904E-04$	20
Conical shell								
$\eta = 0.5$: target frequency $f_{1T} = 268.753$ Hz and target displacement $w_{\max T} = u_{3\max T} = 5.2639 \cdot 10^{-7}$ m								
MC	0.00984	−0.74086	14.77422	27.83370	330.94622	$5.2073E-07$	$1.9799E-02$	35
GA	0.08800	−0.32650	16.65690	7.72240	321.89420	$5.2624E-07$	$4.9477E-04$	25
PSO	0.05769	−0.49331	9.85753	8.35549	322.04900	$5.2615E-07$	$8.2088E-04$	43
Toroidal shell panel								
$\eta = 0$: target displacement $w_{\max T} = u_{3\max T} = 3.9516 \cdot 10^{-5}$ m								
MC	0.05350	−0.54251	17.60320	20.64836	20.21863	$3.9727E-05$	$5.3396E-03$	21
GA	0.02930	−0.78200	12.72730	25.90420	20.56750	$3.9495E-05$	$5.3143E-04$	3
PSO	0.10430	−0.58284	8.53859	8.22430	20.48775	$3.9519E-05$	$7.5919E-05$	6
Catenoidal panel								
$\eta = 1$: target frequency $f_{1T} = 590.557$ Hz								
MC	1.06122	0.90588	2.06831	2.50895	595.86858	$3.9753E-07$	$8.9937E-03$	55
GA	0.08800	−0.48390	13.11830	13.97850	590.77480	$4.0135E-07$	$3.6832E-04$	45
PSO	0.09089	−0.32061	18.33638	14.94431	590.11938	$4.0129E-07$	$7.4152E-04$	43
Elliptic paraboloid								
$\eta = 0.5$: target frequency $f_{1T} = 327.239$ Hz and target displacement $w_{\max T} = u_{3\max T} = 1.9073 \cdot 10^{-6}$ m								
MC	0.29917	0.02997	19.54311	2.65521	332.68799	$1.8923E-06$	$1.2258E-02$	43
GA	0.08800	−0.29910	3.01080	4.93650	327.62800	$1.9075E-06$	$6.4729E-04$	22
PSO	0.25269	−0.65120	13.49764	2.90612	327.39815	$1.9065E-06$	$4.5339E-04$	25

Table 3: Perceptual relative errors in first frequtency $e_f = ((f_1 - f_{1T})/f_{1T}) \cdot 100$ and in maximum bending displacement $e_w = ((w_{\max} - w_{\max T})/w_{\max T}) \cdot 100$ with Monte Carlo, Particle Swarm Optimization, and Genetic Algorithm methods.

Optimization method	Square plate	Cylindrical panel	Conical shell		Toroidal shell panel	Catenoidal panel	Elliptic paraboloid	
	e_f	e_w	e_f	e_w	e_w	e_f	e_f	e_w
MC	−1.261	−0.431	2.884	−1.076	0.534	0.899	1.665	−0.786
GA	0.024	0.188	0.070	−0.029	−0.053	0.037	0.119	0.010
PSO	−0.016	0.059	0.118	−0.046	0.008	−0.074	0.049	−0.042

$L = 3$ m, circumferential angle $\alpha_2 = \vartheta \in [0, 120^\circ]$, and a thickness $h = 0.2$ m. It is subjected to a normal load $q_n^+ = -10000$ Pa at the top surface, and its boundary conditions are SFSF. On the contrary, the conical shell (Figure 4(c)) has $R_b = 1$ m, $L = 3$ m, circumferential angle $\alpha_2 = \vartheta \in [0, 360^\circ]$, $\alpha = 30^\circ$, and a thickness $h = 0.3$ m. Also the conical shell is subjected to a normal load $q_n^+ = -10000$ Pa at the top surface. The conical shell is clamped at the bottom and free at the top, so the boundary conditions are indicated by CF. The cylindrical panel is a two-layered structure with $\mathrm{FGM}_{2(a^{(1)}/b^{(1)}/c^{(1)}/p^{(1)})}/\mathrm{FGM}_{1(a^{(2)}/b^{(2)}/c^{(2)}/p^{(2)})}$ lamination scheme, while the conical shell presents $\mathrm{FGM}_{1(a^{(1)}/b^{(1)}/c^{(1)}/p^{(1)})}/$

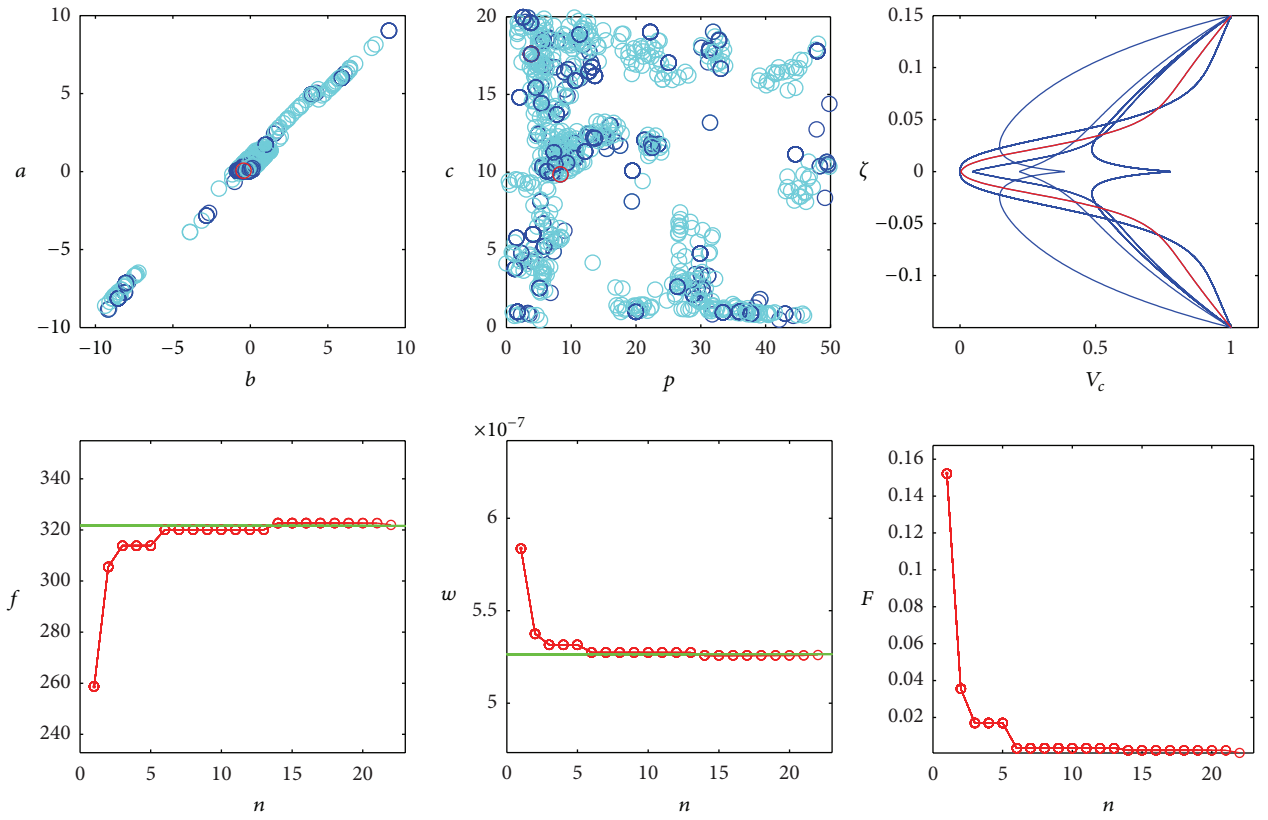

FIGURE 13: Conical shell: optimization by Particle Swarm Algorithm with $\eta = 0.5$; final optimized frequency $f = 322.049$ Hz and final optimized displacement $w = 5.2615 \cdot 10^{-7}$ m.

$\mathrm{FGM}_{2(a^{(2)}/b^{(2)}/c^{(2)}/p^{(2)})}$ lamination scheme. In these two cases the FGM four parameters of the two different power-law distributions are assumed to be equal to the two different laminae of the structure. Thus, only the four parameters $a = a^{(1)} = a^{(2)}, b = b^{(1)} = b^{(2)}, c = c^{(1)} = c^{(2)}$, and $p = p^{(1)} = p^{(2)}$ have to be determined by the optimization procedure.

As already reported in [74, 78], the position vector of a toroidal shell panel (Figure 4(d)) can be written as

$$\begin{aligned}\mathbf{r}(\alpha_1, \alpha_2) = {} & (R_b + R\sin\alpha_1)\cos\alpha_2 \mathbf{e}_1 \\ & - (R_b + R\sin\alpha_1)\sin\alpha_2 \mathbf{e}_2 + R\cos\alpha_1 \mathbf{e}_3,\end{aligned} \tag{43}$$

where R_b is the shift of the circular meridian curve with respect to the axis of revolution [23, 43, 44, 47, 68, 69] and R is the radius of the circular curve section of the toroidal shell panel. The toroidal structure is characterized by $R_b = 9$ m, $R = 3$ m, meridian angle $\alpha_1 = \varphi \in [0, 360^\circ]$, circumferential angle $\alpha_2 = \vartheta \in [0, 120^\circ]$, and a thickness $h = 0.6$ m. Also the toroidal shell has CF boundary conditions, and the normal load $q_n^+ = -10000$ Pa is applied at its top surface. When a catenary curve is considered as a meridian curve of a revolution shell, the position vector of the catenoidal panel (Figure 4(e)) assumes the aspect

$$\begin{aligned}\mathbf{r}(\alpha_1, \alpha_2) = {} & \left(A\cosh\left(\operatorname{arcsinh}\left(\frac{1}{\tan\alpha_1}\right)\right) + R_b\right)\cos\alpha_2 \mathbf{e}_1 \\ & - \left(A\cosh\left(\operatorname{arcsinh}\left(\frac{1}{\tan\alpha_1}\right)\right) + R_b\right)\sin\alpha_2 \mathbf{e}_2 \\ & + A\operatorname{arcsinh}\left(\frac{1}{\tan\alpha_1}\right)\mathbf{e}_3,\end{aligned} \tag{44}$$

where A is the distance of the throat apex of the catenary curve. For further details about the geometry definition of the catenary curve, the reader might refer to [23, 43, 74, 78]. Regarding the catenoidal panel (Figure 4(e)) its geometrical properties are $A = 2$ m, $B = 2$ m, $D = 1$ m, $R_b = 0$ m, circumferential angle $\alpha_2 = \vartheta \in [0, 90^\circ]$, and a thickness $h = 0.5$ m. The catenoidal panel has CFCF boundary conditions, and it is subjected to a normal load $q_n^+ = -10000$ Pa at the top surface. The toroidal shell panel and catenary panel of revolution have the same three-layered lamination scheme $\mathrm{FGM}_{2(a^{(1)}/b^{(1)}/c^{(1)}/p^{(1)})}/\mathrm{FGM}_C/\mathrm{FGM}_{1(a^{(3)}/b^{(3)}/c^{(3)}/p^{(3)})}$. The lamination scheme presents the middle lamina of the structure made of ceramic isotropic material. Also, in these two cases the FGM parameters of the two different power-law distribution are assumed to be equal to the first and the third

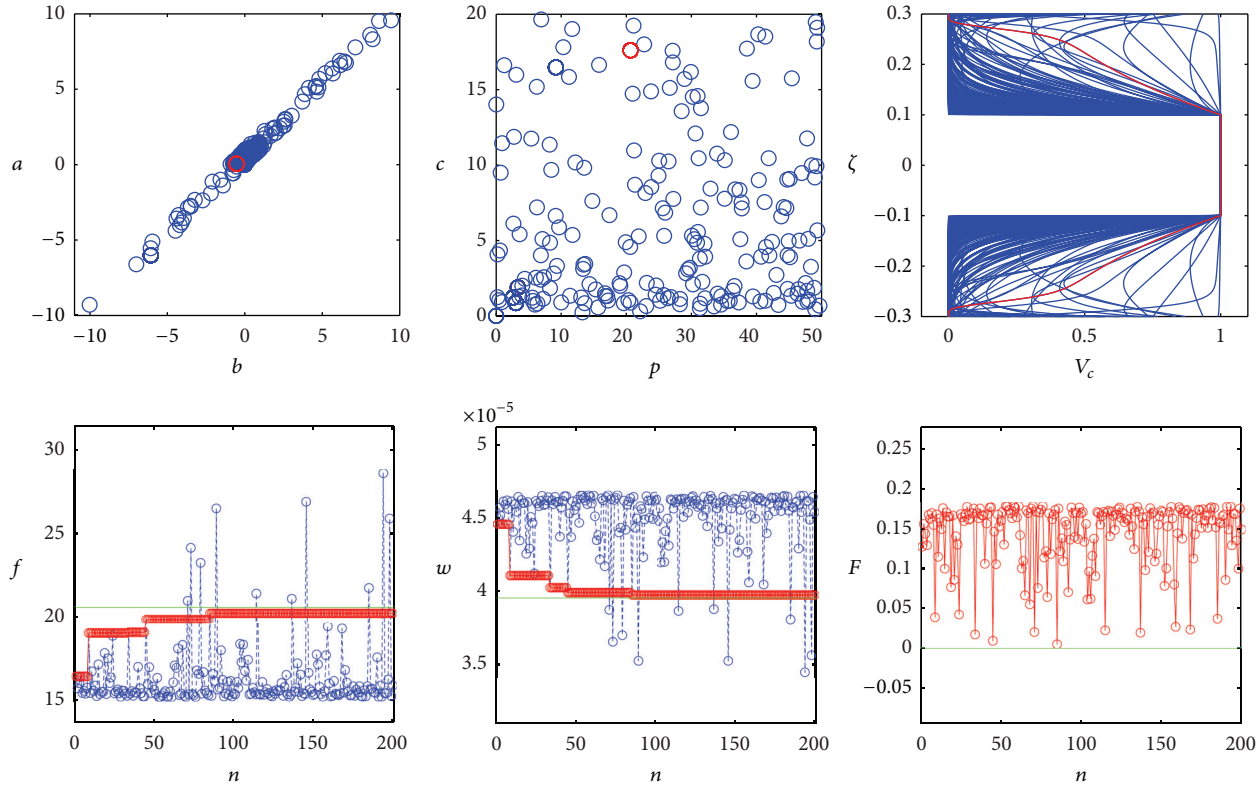

Figure 14: Toroidal shell panel: Monte Carlo optimization with $\eta = 0$; final optimized displacement $w = 3.9727 \cdot 10^{-5}$ m.

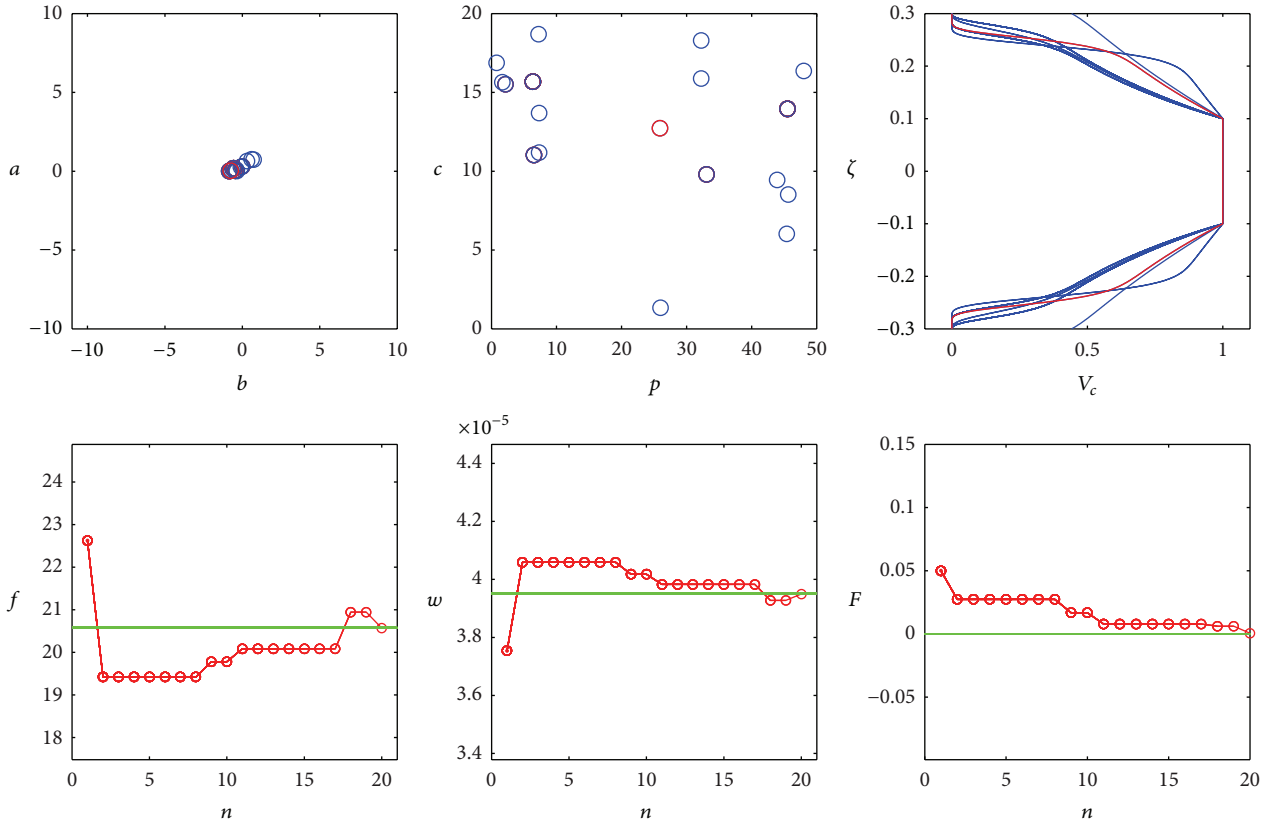

Figure 15: Toroidal shell panel: Genetic Algorithm optimization with $\eta = 0$; final optimized displacement $w = 3.9495 \cdot 10^{-5}$ m.

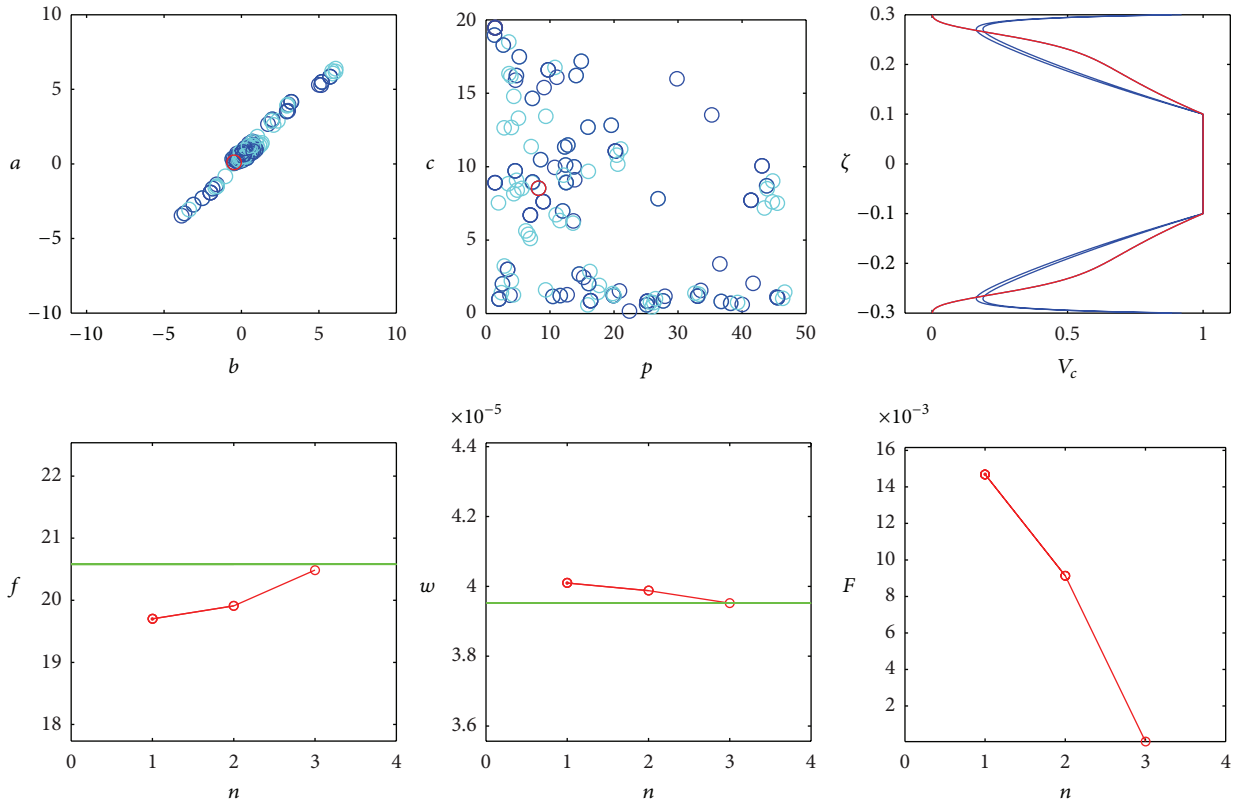

Figure 16: Toroidal shell panel: Particle Swarm Optimization with $\eta = 0$; final optimized displacement $w = 3.9519 \cdot 10^{-5}$ m.

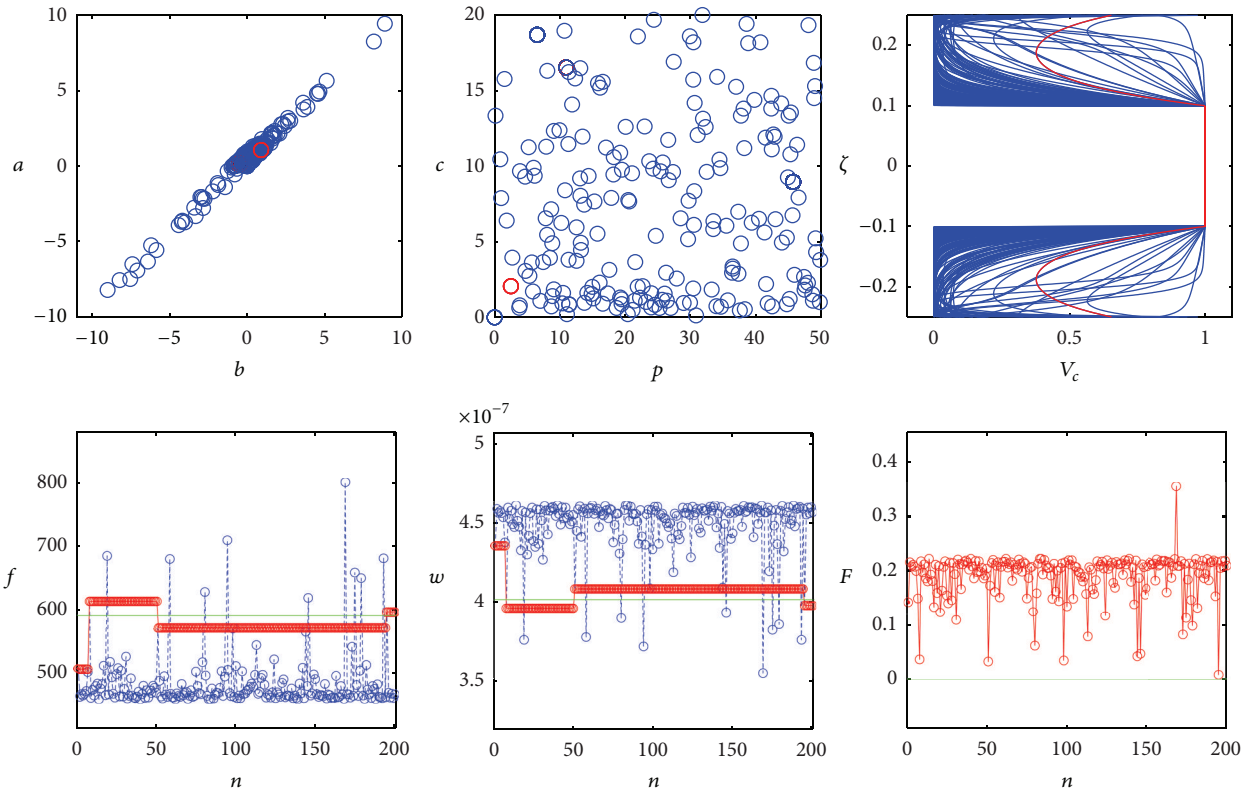

Figure 17: Catenoidal panel: Monte Carlo optimization with $\eta = 1$; final optimized frequency $f = 595.868$ Hz.

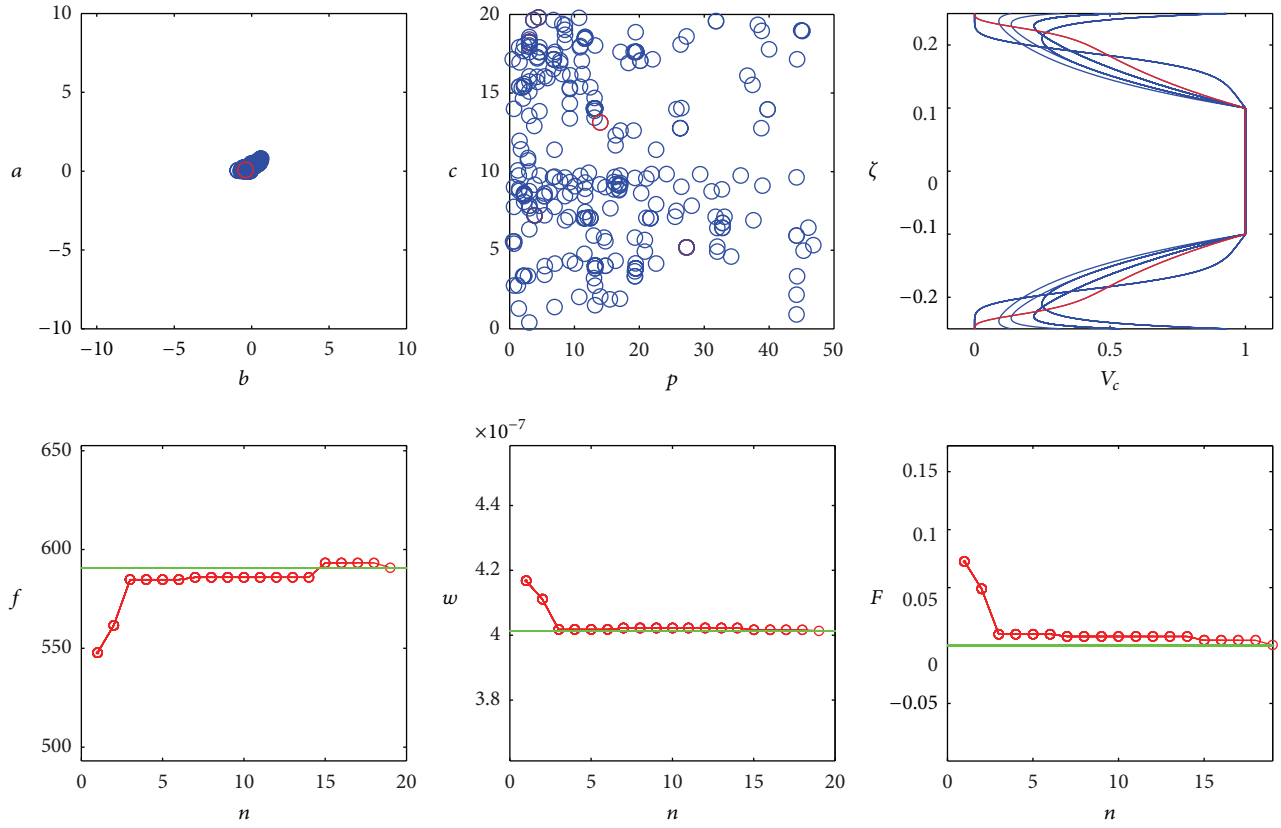

FIGURE 18: Catenoidal panel: Genetic Algorithm optimization with $\eta = 1$; final optimized frequency $f = 590.800$ Hz.

laminae of the structure. In this way, only the four parameters $a = a^{(1)} = a^{(3)}, b = b^{(1)} = b^{(3)}, c = c^{(1)} = c^{(3)}$, and $p = p^{(1)} = p^{(3)}$ have to be determined by the optimization procedure.

Finally, the position vector of the reference surface of the elliptic paraboloid is given in [74, 78]:

$$\mathbf{r}(\alpha_1, \alpha_2) = \left(R_0^{\alpha_1}(\alpha_1) - x_3^{\alpha_2}(\alpha_2)\sin\alpha_1\right)\cos\alpha_2 \mathbf{e}_1 - R_0^{\alpha_2}(\alpha_2)\,\mathbf{e}_2 + \left(x_3^{\alpha_1}(\alpha_1) + x_3^{\alpha_2}(\alpha_2)\cos\alpha_1\right)\mathbf{e}_3. \tag{45}$$

If the generatrix parabola needs to be characterized (the other parabola can be defined analogously), it can be described by the following equation:

$$\left(R_0^{\alpha_1}\right)^2 - \kappa^{\alpha_1} x_3^{\alpha_1} = 0, \tag{46}$$

where $\kappa^{\alpha_1} = (A^2 - D^2)/B$ is a characteristic parameter of the parabolic curve, $R_0^{\alpha_1}$ is the abscissa of a point of the parabola, and $x_3^{\alpha_1}$ is its ordinate in the generatrix plane of the parabolic curve. The abscissa $R_0^{\alpha_1}(\alpha_1)$ of the parabolic curve assumes the form

$$R_0^{\alpha_1}(\alpha_1) = \frac{\kappa^{\alpha_1}\tan\alpha_1}{2}. \tag{47}$$

The parameters describing the two parabolas of the elliptic paraboloid under consideration are $A = 3$ m, $C = -3$ m, $D = 0$ m, and $B = 0.8$ m, and the thickness is $h = 0.4$ m. The elliptic paraboloid is completely clamped at its four edges (CCCC), and it is subjected to a normal load $q_n^+ = -10000$ Pa at the top surface. The elliptic paraboloid is a single-layered structure with $\mathrm{FGM}_{2(a^{(1)}/b^{(1)}/c^{(1)}/p^{(1)})}$ four-parameter power-law distribution. In this case, the four parameters $a = a^{(1)}, b = b^{(1)}, c = c^{(1)}$, and $p = p^{(1)}$ have to be determined by the optimization procedure.

In Table 1 the first ten frequencies and maximum static deflections for the six structures of Figure 4 are presented. In particular, the two limit cases of functionally graded materials are considered. For the first case, named FGM_C, the single-layered structure is made of ceramic isotropic material, while for the second one, named FGM_M, the single-layered structure is made of metal isotropic material. In the present work, it is assumed that the functionally graded material lamina is made of a mixture of ceramic and metal constituents: Silicon Nitride and Stainless Steel. Young's modulus, Poisson's ratio, and mass density for the Silicon Nitride are $E_C = 322.27$ GPa, $\nu_C = 0.24$, and $\rho_C = 2370\,\mathrm{kg/m^3}$, and for the Stainless Steel are $E_M = 207.78$ GPa, $\nu_M = 0.3177$, and $\rho_M = 8166\,\mathrm{kg/m^3}$, respectively.

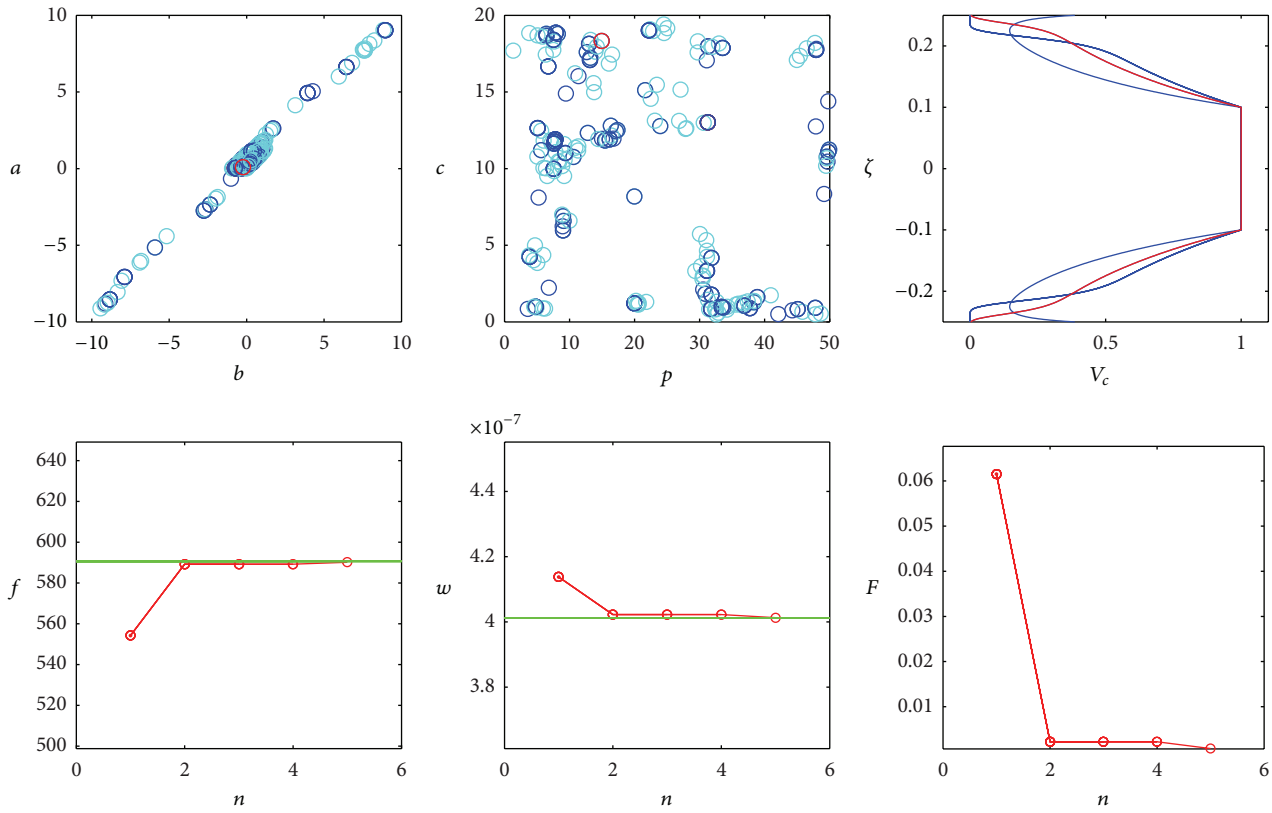

Figure 19: Catenoidal panel: Particle Swarm optimization with $\eta = 1$; final optimized frequency $f = 590.119$ Hz.

As described before, one of the goals of the present paper is to develop and test an operative methodology to support the design of FG materials. Several problems can be faced by the designer; in particular some of the most commonly occurred engineering needs are to avoid resonance frequency, to reduce or control the deformations, to increase the strength to weight ratio, to reduce stresses due to different dilatation properties of two materials, and so on. In this study, frequency and deformation and a combination of the two will be considered. The fitness function F has been modelled to obtain a defined first resonance frequency target (f_{1T}) set by user, a maximum displacement target ($w_{\max T} = u_{3\max T}$) due to bending deformation, or to try to satisfy at the best both the requirements. In this latter case, the designer can decide to stress more the importance on one of the two requirements by using the coefficient η which acts as a weight: in this way the fitness F is still monodimensional but keeps into account two aspects, ranging η from zero to one. According to the above considerations, the fitness expression F can be so represented by the formula

$$F = \eta \sqrt{\left(\frac{f_1 - f_{1T}}{f_{1T}}\right)^2} + (1-\eta)\sqrt{\left(\frac{w_{\max} - w_{\max T}}{w_{\max T}}\right)^2}. \quad (48)$$

It is worth to note that the minimization of the fitness F is equivalent to obtain values of frequency ($f = f_1$) and of displacement ($w = w_{\max} = u_{3\max}$) as close as possible to the desired ones ($f_{1T}, w_{\max T} = u_{3\max T}$), and the ratio between the difference from the obtained value minus the target and the target value itself is used to make dimensionless frequencies and displacements. By this way, parameters with different magnitudes can be compared, allowing to equate items with unit of measurement defined by the experimenter depending on his practice. In the paper, this simple monoobjective fitness has been considered to privilege the simplicity and to suggest the use of this approach also in industrial applications, but more complex multiobjective fitness functions can be implemented depending on the specific case study and on the requirements and needs expressed by the designer.

Figures 5, 6, 7, 8, 9, 10, 11, 12, 13, 14, 15, 16, 17, 18, 19, 20, 21, and 22 present the results of the optimization of the six structures described above. A mix of values of η parameter has been chosen ($\eta = 0, 0.5, 1$), keeping it constant for each structure as to make possible the comparison of the optimization methods. Following formula (48), if $\eta = 1$ only the frequency is optimized, while for $\eta = 0$ only the displacement is considered; an intermediate value $\eta = 0.5$ can be set to find the better compromise between the guess of both frequency and displacement. Each figure presents in the upper left corner the values of a and b parameter for each try; the best solution is represented by a red circle. In the upper centre there are the values of c and p parameters for each try with the best solution in red; in the upper left corner there is the material distribution in the thickness of the structure; an FGM made by one, two, or three layers

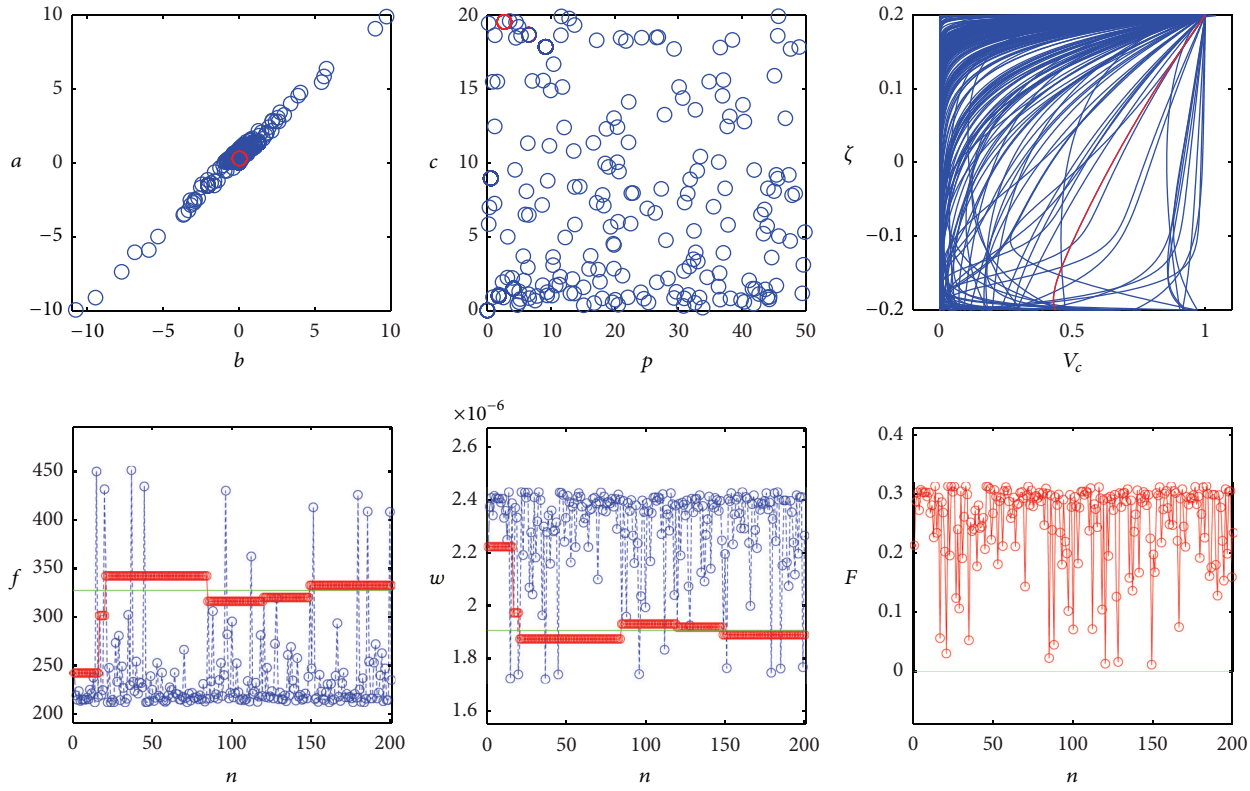

FIGURE 20: Elliptic paraboloid: Monte Carlo optimization with $\eta = 0.5$; final optimized frequency $f = 332.688$ Hz and final optimized displacement $w = 1.8923 \cdot 10^{-6}$ m.

can be visualized, depending on the structure definition (e.g. rectangular plate presents only one layer; cylindrical panel presents two symmetric layers, while, for instance, the conical shell is made by a sandwich between an homogeneous material and two symmetric about the midplane layers of FG materials): the final optimized distribution is in red. The lower part of the figures from left to right presents the trend of frequency, displacement, and fitness in time. In case of Monte Carlo frequency and displacement of the single run are shown (with in blue the trend of the best solution found), while in case of Particle Swarm and Genetic Algorithms the frequency and the displacement referred to the best individual found at the moment are shown. A green line represents the target values for the frequency and the displacement, while in case of the fitness, the ideal value is obviously equal to zero.

Figures 5–7 present the optimization of a rectangular plate when the designer is interested in setting the first resonance frequency of the structure. The plate is made by only one FGM lamina, and a value of $\eta = 1$ is set. Figures 8–10 depict the result of the optimization with MC, PSO, and GA of a cylindrical panel made by two symmetrical FGM distributions about the midplane; in this case $\eta = 0$ is set since the need for a required maximum displacement is simulated. Figures 11–13 refer to a singly curved conical shell made by two FGM laminae, with a distribution symmetric about the midplane of the whole structure; in this case $\eta = 0.5$ is set to consider an interest both in frequency and in maximum displacement. Figures 14–16 present a toroidal shell panel which is a doubly curved shell panel of revolution, made by three laminae: a homogeneous core and two external symmetrical FGM laminae as to simulate a typical sandwich structure. The interest is in maximum displacement, so that η is set equal to zero. Figures 17–19 list the optimization trend of a catenoidal panel structure which can be defined as a doubly curved panel of revolution; the laminate is obtained by three layers also in this case, representing a typical sandwich structure; in this case the attention is focused on frequency optimization, so that $\eta = 1$ is set. Finally, Figures 20–22 present an elliptic paraboloid which is a completely doubly curved panel structure made by only one FGM lamina; considerations will be addressed both on frequency and displacement since $\eta = 0.5$.

As to help the interpretation of the optimization process, the final results are collected in Table 2: the final value of the fitness provides an idea of the goodness of the results found. It is important to note that heuristic methods do not provide the best solution, but a suboptimal solution; in other words, sometimes, similar results of the fitness function can be found with several different set of parameters a, b, c, and p. The Genetic Algorithm has been run with a population of 30 individuals and the Particle Swarm with a number of particles of 30; these algorithms stop when a maximum number of runs are reached or no improvements are found in solution (or alternatively when the percentage error is less

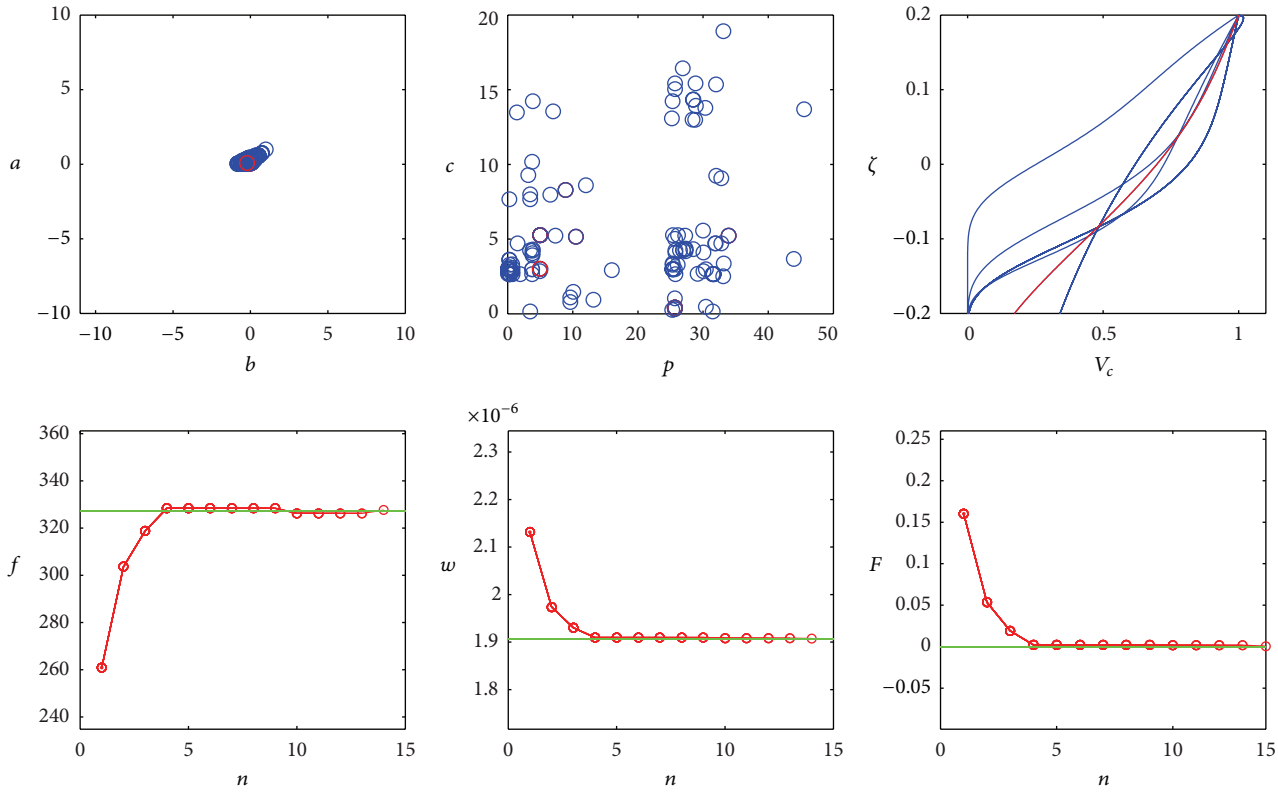

FIGURE 21: Elliptic paraboloid: Genetic Algorithm optimization with $\eta = 0.5$; final optimized frequency $f = 327.600$ Hz and final optimized displacement $w = 1.9075 \cdot 10^{-6}$ m.

than the 0.5%). The Monte Carlo simulation has been run for 200 times for each optimization problem, in order to obtain a comparable number of runs with Genetic Algorithm and Particle Swarm Optimizers. A first comparison between methods can be performed based on Figure 23, in which there is a graph collecting final fitness versus computational time for each optimization performed. Values for Monte Carlo are in red triangles, Particle Swarm in blue squares, while Genetic Algorithm in red circles. As expected GA and PSO results are better than MC ones and provide data with good approximation in a relative short time, which is also compatible with the needs of conceptual design or Multidisciplinary Optimization. Simulations have been carried out on a Notebook equipped with an 8 GB RAM, a 2 GHz core processor, and Windows 7 operating system. Table 3 lists the errors in frequency and in displacement (depending on the case study) for each simulation run; as can be seen by data provided, both GA and PSO present a similar efficiency. The two methods exploit different strategies to solve the optimization problem in this complex task: in this case, in fact, the domain is not continuous and some combinations of the four parameters a, b, c, and p can lead to a distribution of metal and ceramics which is not consistent (percentage represented by a negative or complex or major than one number, which is physically unfeasible). As well described before in the paper, one of the challenges is that slight changes in one of the four parameters can lead to inconsistent solutions. When a particle of the PSO arrives to the border of the domain with a speed pointing to an inconsistent zone of the domain, it is needed to randomly redirect the particle towards an allowed zone, and this reduces the efficiency of the method. On the other hand, GA solves in a better way this problem since mutations and crossover help in exploring new zones of the domain in which the solution is feasible and the distribution percentage of the FGM distributions (ceramics and metal) is always a positive number between zero and one in all the thickness of the structure. Only a small part of the individuals of a generation should mutate because it slows down the convergence. After tests performed it seems that these two effects compensate and both PSO and GA present a very good behavior in optimization. The comparison between random optimization (MC) with heuristic methods (GA, PSO) shows a different relative efficiency of MC when applied to cases in which only frequency or displacement is studied or when both are considered. In the first case the difference in precision obtained by MC with respect to GA and PSO is quite small, while this difference increases dramatically when both frequency and displacement are considered: it can be inferred that when the fitness function deals with only one parameter also the MC alone can be used, while in case of fitness involving more parameters an heuristic or semi heuristic method provides better results.

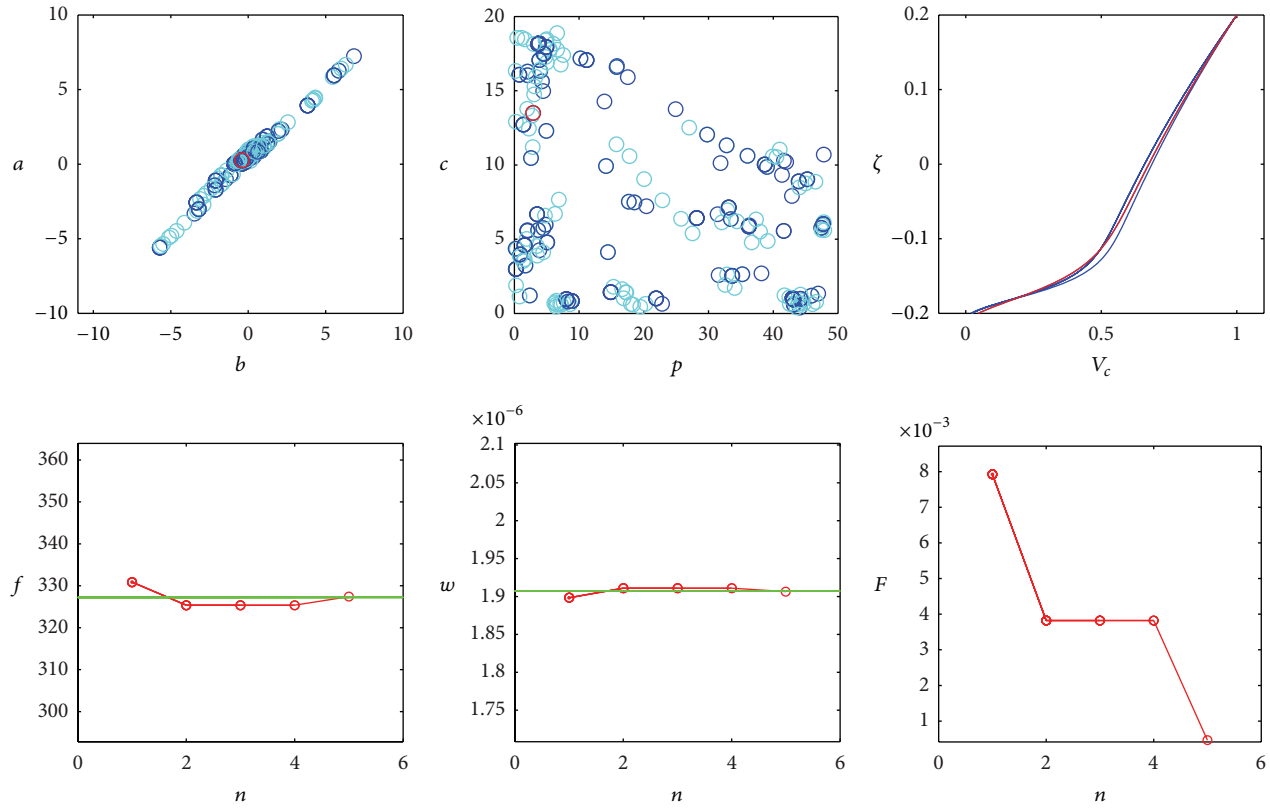

FIGURE 22: Elliptic paraboloid: Particle Swarm Optimization with $\eta = 0.5$; final optimized frequency $f = 327.398$ Hz and final optimized displacement $w = 1.9065 \cdot 10^{-6}$ m.

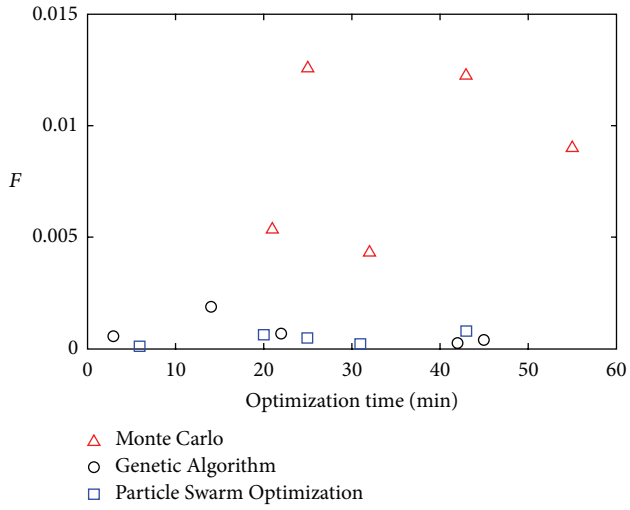

FIGURE 23: Computational optimization time [in minutes] versus fitness for MC (triangle), GA (circle), and PSO (square).

6. Conclusion Remarks and Summary

Functionally graded material applications are increasing due to their potentialities in problems related to aggressive environments, thermal properties, and special structural needs. Theoretical frameworks have been developed to solve the static and dynamic analysis of this type of structures. In the present paper, the Generalized Differential Quadrature method has been presented as a mean to investigate the static and dynamic analysis of functionally graded and laminated composite doubly curved shells and panels. The adopted shell theory is the First-order Shear Deformation Theory. In particular, the Toorani-Lakis theory has been used as a starting point to obtain the governing equations for shells. The 2D equilibrium equations have been discretized with the GDQ method through standard linear algebraic and eigenvalue problems. Thanks to the mathematical approach, the analysis of an FGM shell or panel can be provided. The material distribution can be expressed by a four-parameter power-law. However, the main drawback of this approach from a designer perspective is that it is impossible to analytically relate the set of the four parameters to static or dynamic performances of the structures. An approach based on the application of optimization algorithms to the problem has been carried out to evaluate its suitability to the topic. Due to the domain of the four parameters which includes zones in which no solutions can be found, the optimization algorithms have been modified and tested. Genetic Algorithm, Particle Swarm Optimization, and Monte Carlo algorithms have been selected for tests and applied to six different geometrical structures optimizing the first frequency, maximum bending displacement, or a mix of the two. Results obtained show

the convergence of the optimization for GA and PSO, which provides better results than MC for similar computational effort. In particular, GA and PSO are more precise when both frequency and displacement are considered at the same time. The herein developed methodology can dramatically help the designer in the definition of the mix ceramics/metal which can present the requested properties.

Acknowledgments

This research was supported by the Italian Ministry Education, Universities and Research (MIUR).

References

[1] S. Timoshenko and S. Woinowsky-Krieger, *Theory of Plates and Shells*, McGraw-Hill, New York, NY, USA, 1959.

[2] W. Flügge, *Stresses in Shells*, Springer, Berlin, Germany, 1960.

[3] A. L. Gol'denveizer, *Theory of Elastic Thin Shells*, Pergamon Press, Oxford, UK, 1961.

[4] V. V. Novozhilov, *Thin Shell Theory*, P. Noordhoff, Groningen, The Netherlands, 1964.

[5] V. Z. Vlasov, "General Theory of Shells and Its Application in Engineering, NASA-TT-F-99," 1964.

[6] S. A. Ambartusumyan, "Theory of Anisotropic Shells, NASA-TT-F-118," 1964.

[7] H. Kraus, *Thin Elastic Shells*, John Wiley & Sons, New York, NY, USA, 1967.

[8] A. W. Leissa, "Vibration of Plates, NASA-SP-160," 1969.

[9] A. W. Leissa, "Vibration of Shells, NASA-SP-288," 1973.

[10] S. Markuš, *The Mechanics of Vibrations of Cylindrical Shells*, Elsevier, New York, NY, USA, 1988.

[11] E. Ventsel and T. Krauthammer, *Thin Plates and Shells*, Marcel Dekker, New York, NY, USA, 2001.

[12] W. Soedel, *Vibrations of Shells and Plates*, Marcel Dekker, New York, NY, USA, 2004.

[13] E. Reissner, "The effect of transverse shear deformation on the bending of elastic plates," *Journal of Applied Mechanics*, vol. 12, pp. 66–77, 1945.

[14] R. D. Mindlin, "Influence of rotatory inertia and shear on flexural vibration of isotropic, elastic plates," *Journal of Applied Mechanics*, vol. 18, pp. 31–38, 1951.

[15] P. L. Gould, *Finite Element Analysis of Shells of Revolution*, Pitman Publishing, London, UK, 1984.

[16] P. L. Gould, *Analysis of Plates and Shells*, Prentice-Hall, New York, NY, USA, 1999.

[17] A. W. Leissa and J.-D. Chang, "Elastic deformation of thick, laminated composite shells," *Composite Structures*, vol. 35, no. 2, pp. 153–170, 1996.

[18] M. S. Qatu, "Accurate equations for laminated composite deep thick shells," *International Journal of Solids and Structures*, vol. 36, no. 19, pp. 2917–2941, 1999.

[19] M. S. Qatu, *Vibration of Laminated Shells and Plates*, Elsevier, New York, NY, USA, 2004.

[20] M. H. Toorani and A. A. Lakis, "General equations of anisotropic plates and shells including transverse shear deformations, rotary inertia and initial curvature effects," *Journal of Sound and Vibration*, vol. 237, no. 4, pp. 561–615, 2000.

[21] M. H. Toorani and A. A. Lakis, "Free vibrations of non-uniform composite cylindrical shells," *Nuclear Engineering and Design*, vol. 236, no. 17, pp. 1748–1758, 2006.

[22] J. N. Reddy, *Mechanics of Laminated Composites Plates and Shells*, CRC Press, New York, NY, USA, 2003.

[23] F. Tornabene, *Meccanica delle Strutture a Guscio in Materiale Composito. Il Metodo Generalizzato di Quadratura Differenziale*, Esculapio, Bologna, Italy, 2012.

[24] E. Carrera, S. Brischetto, and P. Nali, *Plates and Shells for Smart Structures: Classical and Advanced Theories for Modeling and Analysis*, John Wiley & Sons, New York, NY, USA, 2011.

[25] E. Carrera, "Historical review of Zig-Zag theories for multilayered plates and shells," *Applied Mechanics Reviews*, vol. 56, no. 3, pp. 287–308, 2003.

[26] C. Shu, *Differential Quadrature and Its Application in Engineering*, Springer, Berlin, Germany, 2000.

[27] C. W. Bert and M. Malik, "Differential quadrature method in computational mechanics: a review," *Applied Mechanics Reviews*, vol. 49, no. 1, pp. 1–27, 1996.

[28] K. M. Liew, J. B. Han, and Z. M. Xiao, "Differential quadrature method for thick symmetric cross-ply laminates with first-order shear flexibility," *International Journal of Solids and Structures*, vol. 33, no. 18, pp. 2647–2658, 1996.

[29] C. Shu and H. Du, "Free vibration analysis of laminated composite cylindrical shells by DQM," *Composites B*, vol. 28, no. 3, pp. 267–273, 1997.

[30] K. M. Liew and T. M. Teo, "Modeling via differential quadrature method: three-dimensional solutions for rectangular plates," *Computer Methods in Applied Mechanics and Engineering*, vol. 159, no. 3-4, pp. 369–381, 1998.

[31] F.-L. Liu and K. M. Liew, "Differential quadrature element method: a new approach for free vibration analysis of polar Mindlin plates having discontinuities," *Computer Methods in Applied Mechanics and Engineering*, vol. 179, no. 3-4, pp. 407–423, 1999.

[32] S. Moradi and F. Taheri, "Delamination buckling analysis of general laminated composite beams by differential quadrature method," *Composites B*, vol. 30, no. 5, pp. 503–511, 1999.

[33] T. Y. Ng, L. Hua, K. Y. Lam, and C. T. Loy, "Parametric instability of conical shells by the generalized differential quadrature method," *International Journal for Numerical Methods in Engineering*, vol. 44, no. 6, pp. 819–837, 1999.

[34] T. C. Fung, "Solving initial value problems by differential quadrature method-part 1: first-order equations," *International Journal for Numerical Methods in Engineering*, vol. 50, no. 6, pp. 1411–1427, 2001.

[35] T. C. Fung, "Solving initial value problems by differential quadrature method. II. Second- and higher-order equations," *International Journal for Numerical Methods in Engineering*, vol. 50, no. 6, pp. 1429–1454, 2001.

[36] K. M. Liew, T. Y. Ng, and J. Z. Zhang, "Differential quadrature-layerwise modeling technique for three-dimensional analysis of cross-ply laminated plates of various edge-supports," *Computer Methods in Applied Mechanics and Engineering*, vol. 191, no. 35, pp. 3811–3832, 2002.

[37] T. Y. Wu, Y. Y. Wang, and G. R. Liu, "Free vibration analysis of circular plates using generalized differential quadrature rule," *Computer Methods in Applied Mechanics and Engineering*, vol. 191, no. 46, pp. 5365–5380, 2002.

[38] G. Karami and P. Malekzadeh, "Static and stability analyses of arbitrary straight-sided quadrilateral thin plates by DQM,"

International Journal of Solids and Structures, vol. 39, no. 19, pp. 4927–4947, 2002.

[39] J. Yang and H.-S. Shen, "Nonlinear bending analysis of shear deformable functionally graded plates subjected to thermo-mechanical loads under various boundary conditions," *Composites B*, vol. 34, no. 2, pp. 103–115, 2003.

[40] K. M. Liew, J. Z. Zhang, C. Li, and S. A. Meguid, "Three-dimensional analysis of the coupled thermo-piezoelectro-mechanical behaviour of multilayered plates using the differential quadrature technique," *International Journal of Solids and Structures*, vol. 42, no. 14, pp. 4239–4257, 2005.

[41] E. Viola and F. Tornabene, "Vibration analysis of damaged circular arches with varying cross-section," *SID Structural Integrity and Durability*, vol. 1, no. 2, pp. 155–169, 2005.

[42] E. Viola and F. Tornabene, "Vibration analysis of conical shell structures using GDQ method," *Far East Journal of Applied Mathematics*, vol. 25, pp. 23–39, 2006.

[43] F. Tornabene, *Modellazione e soluzione di strutture a Guscio in materiale anisotropo [Ph.D. thesis]*, University of Bologna-DISTART Department, Bologna, Italy, 2007.

[44] F. Tornabene and E. Viola, "Vibration analysis of spherical structural elements using the GDQ method," *Computers and Mathematics with Applications*, vol. 53, no. 10, pp. 1538–1560, 2007.

[45] E. Viola, M. Dilena, and F. Tornabene, "Analytical and numerical results for vibration analysis of multi-stepped and multi-damaged circular arches," *Journal of Sound and Vibration*, vol. 299, no. 1-2, pp. 143–163, 2007.

[46] A. Marzani, F. Tornabene, and E. Viola, "Nonconservative stability problems via generalized differential quadrature method," *Journal of Sound and Vibration*, vol. 315, no. 1-2, pp. 176–196, 2008.

[47] F. Tornabene and E. Viola, "2-D solution for free vibrations of parabolic shells using generalized differential quadrature method," *European Journal of Mechanics, A/Solids*, vol. 27, no. 6, pp. 1001–1025, 2008.

[48] A. Alibeigloo and R. Madoliat, "Static analysis of cross-ply laminated plates with integrated surface piezoelectric layers using differential quadrature," *Composite Structures*, vol. 88, no. 3, pp. 342–353, 2009.

[49] F. Tornabene, "Free vibration analysis of functionally graded conical, cylindrical shell and annular plate structures with a four-parameter power-law distribution," *Computer Methods in Applied Mechanics and Engineering*, vol. 198, no. 37–40, pp. 2911–2935, 2009.

[50] F. Tornabene and E. Viola, "Free vibrations of four-parameter functionally graded parabolic panels and shells of revolution," *European Journal of Mechanics*, vol. 28, no. 5, pp. 991–1013, 2009.

[51] F. Tornabene and E. Viola, "Free vibration analysis of functionally graded panels and shells of revolution," *Meccanica*, vol. 44, no. 3, pp. 255–281, 2009.

[52] F. Tornabene, E. Viola, and D. J. Inman, "2-D differential quadrature solution for vibration analysis of functionally graded conical, cylindrical and annular shell structures," *Journal of Sound and Vibration*, vol. 328, no. 3, pp. 259–290, 2009.

[53] E. Viola and F. Tornabene, "Free vibrations of three parameter functionally graded parabolic panels of revolution," *Mechanics Research Communications*, vol. 36, no. 5, pp. 587–594, 2009.

[54] Y. Li and Z. Shi, "Free vibration of a functionally graded piezoelectric beam via state-space based differential quadrature," *Composite Structures*, vol. 87, no. 3, pp. 257–264, 2009.

[55] A. Alibeigloo and V. Nouri, "Static analysis of functionally graded cylindrical shell with piezoelectric layers using differential quadrature method," *Composite Structures*, vol. 92, no. 8, pp. 1775–1785, 2010.

[56] A. Andakhshideh, S. Maleki, and M. M. Aghdam, "Non-linear bending analysis of laminated sector plates using Generalized Differential Quadrature," *Composite Structures*, vol. 92, no. 9, pp. 2258–2264, 2010.

[57] M. Farid, P. Zahedinejad, and P. Malekzadeh, "Three-dimensional temperature dependent free vibration analysis of functionally graded material curved panels resting on two-parameter elastic foundation using a hybrid semi-analytic, differential quadrature method," *Materials and Design*, vol. 31, no. 1, pp. 2–13, 2010.

[58] Sh. Hosseini-Hashemi, H. Akhavan, H. R. D. Taher, N. Daemi, and A. Alibeigloo, "Differential quadrature analysis of functionally graded circular and annular sector plates on elastic foundation," *Materials and Design*, vol. 31, no. 4, pp. 1871–1880, 2010.

[59] Sh. Hosseini-Hashemi, M. Fadaee, and M. Es'Haghi, "A novel approach for in-plane/out-of-plane frequency analysis of functionally graded circular/annular plates," *International Journal of Mechanical Sciences*, vol. 52, no. 8, pp. 1025–1035, 2010.

[60] P. Malekzadeh and A. Alibeygi Beni, "Free vibration of functionally graded arbitrary straight-sided quadrilateral plates in thermal environment," *Composite Structures*, vol. 92, no. 11, pp. 2758–2767, 2010.

[61] O. Sepahi, M. R. Forouzan, and P. Malekzadeh, "Large deflection analysis of thermo-mechanical loaded annular FGM plates on nonlinear elastic foundation via DQM," *Composite Structures*, vol. 92, no. 10, pp. 2369–2378, 2010.

[62] B. Sobhani Aragh and M. H. Yas, "Three-dimensional free vibration of functionally graded fiber orientation and volume fraction cylindrical panels," *Materials and Design*, vol. 31, no. 9, pp. 4543–4552, 2010.

[63] F. Tornabene, A. Marzani, E. Viola, and I. Elishakoff, "Critical flow speeds of pipes conveying fluid by the generalized differential quadrature method," *Advances in Theoretical and Applied Mechanics*, vol. 3, no. 3, pp. 121–138, 2010.

[64] M. H. Yas and B. Sobhani Aragh, "Three-dimensional analysis for thermoelastic response of functionally graded fiber reinforced cylindrical panel," *Composite Structures*, vol. 92, no. 10, pp. 2391–2399, 2010.

[65] O. Sepahi, M. R. Forouzan, and P. Malekzadeh, "Thermal buckling and postbuckling analysis of functionally graded annular plates with temperature-dependent material properties," *Materials and Design*, vol. 32, no. 7, pp. 4030–4041, 2011.

[66] A. H. Sofiyev and N. Kuruoglu, "Natural frequency of laminated orthotropic shells with different boundary conditions and resting on the Pasternak type elastic foundation," *Composites B*, vol. 42, no. 6, pp. 1562–1570, 2011.

[67] F. Tornabene, "Free vibrations of laminated composite doubly-curved shells and panels of revolution via the GDQ method," *Computer Methods in Applied Mechanics and Engineering*, vol. 200, no. 9–12, pp. 931–952, 2011.

[68] F. Tornabene, "2-D GDQ solution for free vibrations of anisotropic doubly-curved shells and panels of revolution," *Composite Structures*, vol. 93, no. 7, pp. 1854–1876, 2011.

[69] F. Tornabene, "Free vibrations of anisotropic doubly-curved shells and panels of revolution with a free-form meridian resting on Winkler-Pasternak elastic foundations," *Composite Structures*, vol. 94, no. 1, pp. 186–206, 2011.

[70] F. Tornabene, A. Liverani, and G. Caligiana, "FGM and laminated doubly curved shells and panels of revolution with a free-form meridian: a 2-D GDQ solution for free vibrations," *International Journal of Mechanical Sciences*, vol. 53, no. 6, pp. 446–470, 2011.

[71] F. Tornabene, A. Liverani, and G. Caligiana, "Laminated composite rectangular and annular plates: a GDQ solution for static analysis with a posteriori shear and normal stress recovery," *Composites B*, vol. 43, no. 4, pp. 1847–1872, 2012.

[72] F. Tornabene, A. Liverani, and G. Caligiana, "Static analysis of laminated composite curved shells and panels of revolution with a posteriori shear and normal stress recovery using generalized differentialquadrature method," *International Journal of Mechanical Sciences*, vol. 61, pp. 71–87, 2012.

[73] F. Tornabene, A. Liverani, and G. Caligiana, "FGM and laminated doubly curved shells and panels of revolution with a free-form meridian: a 2-D GDQ solution for free vibrations," *International Journal of Mechanical Sciences*, vol. 53, no. 6, pp. 446–470, 2011.

[74] E. Viola, F. Tornabene, and N. Fantuzzi, "General higher-order shear deformation theories for the free vibration analysis of completely doubly-curved laminated shells and panels," *Composite Structures*, vol. 95, pp. 639–666, 2013.

[75] F. Tornabene and E. Viola, "Static analysis of functionally graded doubly-curved shells and panels of revolution," *Meccanica*, vol. 48, no. 4, pp. 901–930, 2013.

[76] F. Tornabene and A. Ceruti, "Free-form laminated doubly-curved shells and panels of revolution resting on Winkler-Pasternak elastic foundations: a 2-D GDQ solution for static and free vibration analysis," *World Journal of Mechanics*, vol. 3, pp. 1–25, 2013.

[77] E. Viola, F. Tornabene, and N. Fantuzzi, "Static analysis of completely doubly-curved laminated shells and panels using general higher-order shear deformation theories," *Composite Structures*, vol. 101, pp. 59–93, 2013.

[78] B. Chen and L. Tong, "Sensitivity analysis of heat conduction for functionally graded materials," *Materials and Design*, vol. 25, no. 8, pp. 663–672, 2004.

[79] H.-S. Shen, *Functionally Graded Materials: Nonlinear Analysis of Plates and Shells*, CRC Press, New York, NY, USA, 2009.

[80] P. Malekzadeh, S. A. Shahpari, and H. R. Ziaee, "Three-dimensional free vibration of thick functionally graded annular plates in thermal environment," *Journal of Sound and Vibration*, vol. 329, no. 4, pp. 425–442, 2010.

[81] X. Zhao and K. M. Liew, "Free vibration analysis of functionally graded conical shell panels by a meshless method," *Composite Structures*, vol. 93, no. 2, pp. 649–664, 2011.

[82] P. Malekzadeh, M. R. G. Haghighi, and M. M. Atashi, "Free vibration analysis of elastically supported functionally raded annular plates subjected to thermal environment," *Meccanica*, vol. 46, no. 5, pp. 893–913, 2011.

[83] A. H. Akbarzadeh, M. Abbasi, S. K. Hosseini zad, and M. R. Eslami, "Dynamic analysis of functionally graded plates using the hybrid Fourier-Laplace transform under thermo-mechanical loading," *Meccanica*, vol. 46, no. 6, pp. 1373–1392, 2011.

[84] S. K. Jalali, M. H. Naei, and A. Poorsolhjouy, "Thermal stability analysis of circular functionally graded sandwich plates of variable thickness using pseudo-spectral method," *Materials and Design*, vol. 31, no. 10, pp. 4755–4763, 2010.

[85] E. Jomehzadeh, A. R. Saidi, and S. R. Atashipour, "An analytical approach for stress analysis of functionally graded annular sector plates," *Materials and Design*, vol. 30, no. 9, pp. 3679–3685, 2009.

[86] Y. Fu, P. Zhang, and F. Yang, "Interlaminar stress distribution of composite laminated plates with functionally graded fiber volume fraction," *Materials and Design*, vol. 31, no. 6, pp. 2904–2915, 2010.

[87] N. Wattanasakulpong, B. G. Prusty, D. W. Kelly, and M. Hoffman, "Free vibration analysis of layered functionally graded beams with experimental validation," *Materials & Design*, vol. 36, pp. 182–190, 2012.

[88] W. Montealegre Rubio, G. H. Paulino, and E. C. Nelli Silva, "Analysis, manufacture and characterization of Ni/Cu functionally graded structures," *Materials & Design*, vol. 41, pp. 255–265, 2012.

[89] A. Shaghaghi Moghaddam, M. Alfano, and R. Ghajar, "Determining the mixed mode stress intensity factors of surface cracks in functionally graded hollow cylinders," *Materials & Design*, vol. 43, pp. 475–484, 2013.

[90] R. Moradi-Dastjerdi, M. Foroutan, and A. Pourasghar, "Dynamic analysis of functionally graded material cylinders under an impact load by a mesh-free method," *Acta Mechanica*, vol. 219, no. 3-4, pp. 281–290, 2011.

[91] M. Heshmati and M. H. Yas, "Vibrations of non-uniform functionally graded MWCNTs-polystyrene nanocomposite beams under action of moving load," *Materials & Design*, vol. 46, pp. 206–218, 2013.

[92] M. Yas, S. Kamarian, J. E. Jam, and A. Pourasghar, "Weight minimization of functionally graded structures using ICA and ANN," *International Journal of Advanced Scientific and Technical Research*, vol. 2, pp. 679–696, 2012.

[93] J. E. Jam, S. Kamarian, and A. Pourasghar, "Application of ICA and ANN for optimization of functionally graded conical shells," *International Journal of Engineering Trends in Engineering and Development*, vol. 2, pp. 171–189, 2012.

[94] F. Glover and M. Laguna, *Tabu Search*, Kluwer Academic, Boston, Mass, USA, 1997.

[95] S. Kirkpatrick, C. D. Gelatt Jr., and M. P. Vecchi, "Optimization by simulated annealing," *Science*, vol. 220, no. 4598, pp. 671–680, 1983.

[96] H. H. Hoos and T. Stutzle, *Stochastic Local Search: Foundations and Applications*, Elsevier, Amsterdam, The Netherlands, 2005.

[97] A. Colorni, M. Dorigo, and V. Manniezzo, "An investigation of some properties of an ant algorithm," in *Parallel Problem Solving from Nature 2*, R. Manner and B. Manderick, Eds., pp. 509–520, North-Holland, Amsterdam, The Netherlands, 1992.

[98] M. Dorigo and G. Di Caro, "Ant colony optimization: a new meta-heuristic," in *Proceedings of the 1999 Congress on Evolutionary Computation (CEC '99)*, vol. 2, pp. 1477–1484, 1999.

[99] D. E. Goldberg, *Genetic Algorithms in Search, Optimization and Machine Learning*, Addison-Wesley, Boston, Mass, USA, 1989.

[100] J. Koza, *Genetic Programming: on the Programming of Computers by Means of Natural Selection*, MIT Press, Cambridge, UK, 1992.

[101] R. Beasly, D. Bull, and R. Martin, "An overview on genetic algorithms: part I, fundamentals," *University Computing*, vol. 15, pp. 58–69, 1993.

[102] A. Ceruti, G. Caligiana, and F. Persiani, "Comparative evaluation of different optimization methodologies for the design of UAVs having shape obtained by hot wire cutting techniques," *International Journal on Interactive Design and Manufacturing*, 2012.

[103] H. V. Hultmann Ayala and L. Dos Santos Coelho, "Tuning of PID controller based on a multi-objective genetic algorithm applied to a robotic manipulator," *Expert Systems With Applications*, vol. 39, no. 10, pp. 8968–8974, 2012.

[104] K. S. Tang, K. F. Man, S. Kwong, and Q. He, "Genetic algorithms and their applications," *IEEE Signal Processing Magazine*, vol. 13, no. 6, pp. 22–37, 1996.

[105] M. M. Karim, K. Suzuki, and H. Kai, "Optimal design of hydrofoil and marine propeller using micro-genetic algorithm," *Journal of Naval Architecture and Marine Engineering*, vol. 1, pp. 47–61, 2004.

[106] A. Konak, D. W. Coit, and A. E. Smith, "Multi-objective optimization using genetic algorithms: a tutorial," *Reliability Engineering and System Safety*, vol. 91, no. 9, pp. 992–1007, 2006.

[107] J. H. Holland, *Adaptation in Natural and Artificial Systems*, University of Michigan Press, Ann Arbor, Mich, USA, 1975.

[108] D. Kaur and M. M. Murugappan, "Performance enhancement in solving traveling salesman problem using hybrid genetic algorithm," in *Proceedings of the Annual Conference of the North American Fuzzy Information Processing Society (NAFIPS '08)*, May 2008.

[109] E. Verdú, M. J. Verdú, L. M. Regueras, J. P. De Castro, and R. García, "A genetic fuzzy expert system for automatic question classification in a competitive learning environment," *Expert Systems With Applications*, vol. 39, no. 8, pp. 7471–7478, 2012.

[110] R. Storn and K. Price, "Differential evolution-a simple and efficient heuristic for global optimization over continuous spaces," *Journal of Global Optimization*, vol. 11, no. 4, pp. 341–359, 1997.

[111] J. Kennedy and R. Eberhart, "Particle swarm optimization," in *Proceedings of the 1995 IEEE International Conference on Neural Networks. Part 1 (of 6)*, pp. 1942–1948, December 1995.

[112] R. Poli, "An analysis of publications on particle swarm optimization applications," Technical Report CSM-469, Department of Computer Science, University of Essex, Essex, UK, 2007.

[113] Y. Shi and R. C. Eberhart, "Parameter selection in particle swarm optimization," in *Proceedings of the 7th International Conference on Evolutionary Programming VII (EP '98)*, pp. 591–600, 1998.

[114] L. Zhang, E. Dong, and Y. Xing, "Steering trapezoid mechanism design based on Monte Carlo method," in *Proceedings of the International Conference on Electronic & Mechanical Engineering and Information Technology*, 2011.

[115] B. Birge, "PSOt: a particle swarm optimization toolbox for use with MATLAB," in *Proceedings of the IEEE Swarm Intelligence Symposium (SIS '03)*, pp. 182–186, Indianapolis, Ind, USA, 2003.

[116] X. Hu, L. Wang, and Y. Zhong, "An improved particle swarm optimization algorithm for site index curve model," in *Proceedings 2011 International Conference on Business Management and Electronic Information (BMEI '11)*, vol. 3, pp. 838–842, 2011.

[117] J. Yoo and P. Hajela, "Immune network simulations in multicriterion design," *Structural and Multidisciplinary Optimization*, vol. 18, no. 2-3, pp. 85–94, 1999.

[118] C. A. Coello Coello and N. C. Cortés, "Use of emulations of the immune system to handle constraints in evolutionary algorithms," in *Proceedings of the Intelligent Engineering Systems Through Artificial Neural Networks (ANNIE '01)*, C. H. Dagli, A. L. Buczak, J. Ghosh et al., Eds., vol. 11, pp. 141–146, ASME Press, 2001.

[119] Y. T. Hsiao, C. L. Chuang, J. A. Jiang, and C. C. Chien, "A novel optimization algorithm: space gravitational optimization," in *Proceedings of the International Conference on Systems, Man and Cybernetics*, pp. 2323–2328, Waikoloa, Hawaii, USA, October 2005.

[120] B. Abdi, H. Mozafari, A. Ayob, and R. Kohandel, "Imperialist competitive algorithm and its application in optimization of laminated composite structures," *European Journal of Scientific Research*, vol. 55, no. 2, pp. 174–187, 2011.

[121] H. Shah-Hosseini, "The intelligent water drops algorithm: a nature-inspired swarm-based optimization algorithm," *International Journal of Bio-Inspired Computation*, vol. 1, pp. 71–79, 2008.

[122] H. Duan, S. Liu, and X. Lei, "Air robot path planning based on intelligent water drops optimization," in *Proceedings of the 2008 International Joint Conference on Neural Networks (IJCNN '08)*, pp. 1397–1401, June 2008.

[123] K. Mosegaard and M. Sambridge, "Monte Carlo analysis of inverse problems," *Inverse Problems*, vol. 18, no. 3, pp. R29–R54, 2002.

[124] G. S. Fishman, *Monte Carlo: Concepts, Algorithms, and Applications*, Springer, New York, NY, USA, 1995.

[125] S. Ghahramani, *Fundamentals of Probability Theory*, Prentice Hall, Upper Saddle River, NJ, USA, 2000.

[126] E. M. T. Hendrix and N. J. Olieman, "The smoothed Monte Carlo method in robustness optimization," *Optimization Methods and Software*, vol. 23, no. 5, pp. 717–729, 2008.

[127] K. Madani and J. R. Lund, "A Monte-Carlo game theoretic approach for Multi-Criteria decision making under uncertainty," *Advances in Water Resources*, vol. 34, no. 5, pp. 607–616, 2011.

Hindawi Publishing Corporation
Mathematical Problems in Engineering
Volume 2013, Article ID 569781, 13 pages
http://dx.doi.org/10.1155/2013/569781

Research Article

Finite Element Analysis of the Deformation of Functionally Graded Plates under Thermomechanical Loads

A. E. Alshorbagy, S. S. Alieldin, M. Shaat, and F. F. Mahmoud

Mechanical Engineering Department, Zagazig University, Zagazig 44511, Egypt

Correspondence should be addressed to M. Shaat; shaatscience@yahoo.com

Received 10 December 2012; Accepted 6 March 2013

Academic Editor: Abdelouahed Tounsi

Copyright © 2013 A. E. Alshorbagy et al. This is an open access article distributed under the Creative Commons Attribution License, which permits unrestricted use, distribution, and reproduction in any medium, provided the original work is properly cited.

The first-order shear deformation plate model, accounting for the exact neutral plane position, is exploited to investigate the uncoupled thermomechanical behavior of functionally graded (FG) plates. Functionally graded materials are mainly constructed to operate in high temperature environments. Also, FG plates are used in many applications (such as mechanical, electrical, and magnetic), where an amount of heat may be generated into the FG plate whenever other forms of energy (electrical, magnetic, etc.) are converted into thermal energy. Several simulations are performed to study the behavior of FG plates, subjected to thermomechanical loadings, and focus the attention on the effect of the heat source intensity. Most of the previous studies have considered the midplane neutral one, while the actual position of neutral plane for functionally graded plates is shifted and should be firstly determined. A comparative study is performed to illustrate the effect of considering the neutral plane position. The volume fraction of the two constituent materials of the FG plate is varied smoothly and continuously, as a continuous power function of the material position, along the thickness of the plate.

1. Introduction

Functionally graded materials (FGMs) are microscopically inhomogeneous composite materials, in which the volume fraction of the two or more materials is varied smoothly and continuously as a continuous function of the material position along one or more dimension of the structure. These materials are mainly constructed to operate in high temperature environments.

In conventional laminated composite structures, homogeneous elastic laminae are bonded together to obtain enhanced mechanical and thermal properties. The main inconvenience of such an assembly is the creation of stress concentration sources along the interfaces and specifically when the structure is exposed to elevated temperatures. This can lead to many deficiencies such as delaminations, matrix cracks, and other damage mechanisms which may result from the abrupt change of the mechanical properties at the interface between the layers. One of the ways to overcome this problem is to use functionally graded materials (FGMs) with continuous material properties variations, which can lead to a continuity of the material properties. The concept of functionally graded material (FGM) was proposed in 1984 by the material scientists in Japan [1]. Alieldin et al. [2] suggested three approaches to transform the laminated composite plate, with stepped material properties, to an equivalent functionally graded (FG) plate with a continuous property function across the plate thickness. Such transformations are used to determine the details of a functionally graded plate equivalent to the original laminated one. In addition it may provide an easy and efficient way to investigate the behavior of multilayer composite plates, with direct and less computational efforts. FGMs are usually made of a mixture of ceramic and metals. The ceramic constituent of the material provides a high temperature resistance due to its low thermal conductivity, while the ductile metal constituent, on the other hand, prevents the fracture caused by thermal stress due to high temperature gradient in a very short period of time.

The FGM is suitable for various applications, such as thermal coatings of barrier for ceramic engines, gas turbines, nuclear fusions, optical thin layers, and biomaterial electronics. Cheng and Batra [3] studied thermo-mechanical

deformations of the FG plates. Tanigawa et al. [4] studied the linear thermal bending of FGM plate in steadystate condition. They also studied the stress in transient heat conduction with temperature-dependent material properties. Using the first-order shear deformation theory (FSDT), Praveen and Reddy [5] analyzed nonlinear static and dynamic responses of FG ceramic-metal plates in a steady temperature field. They used finite element method. Lanhe [6] used the FSDT and derived equilibrium and stability equations of a moderately thick rectangular plate made of FGM under thermal loads. He assumed that the material properties varied as a power law of thickness. Alibeigloo [7] derived an exact solution for thermoelastic response of functionally graded rectangular plates subjected to thermo-mechanical loads. A finite element analysis of thermoelastic field in a rotating FGM circular disk is studied by Afsar and Go [8]. This study focuses on the finite element analysis of thermoelastic field in a thin circular functionally graded material disk subjected to a thermal load and an inertia force due to rotation of the disk. Tung and Duc [9] derived a simple analytical approach to investigate the nonlinear stability of functionally graded plates under mechanical and thermal loads. Equilibrium and compatibility equations for FG plates are derived by using the classical plate theory. The nonlinear behaviors of FGM plates under transverse distribution load are investigated by Singha et al. [10] using a high precision plate bending finite element. Material properties of the plate are assumed to be graded in the thickness direction according to the simple power law distribution. The formulation is developed based on the FSDT considering the exact natural surface position. A high-order control volume finite element method is propose by Chareonsuk and Vessakosol [11] to explore thermal stress analysis for functionally graded materials (FGMs) at steady state with unstructured mesh capability for arbitrary-shaped domain. This formulation, also known as cell-vertex finite volume formulation, is useful for material engineers and scientists in determining the thermal response and thermo deformation in FGM that subjected to thermal and mechanical loads. The heat conduction is considered for thermal analysis, whereas the plane elasticity is considered for stress analysis. Wang and Shen performed a nonlinear bending analysis for a FG plate [12] and also performed a nonlinear vibration, a nonlinear bending, and a postbuckling analyses for sandwich plate with FGM face sheets [13]. The two plates are resting on an elastic foundation and subjected to thermal environments.

Functionally graded materials are used in many applications, owing to their stability in high thermal environments. To this aim, many approaches are developed to study the thermoelastic behavior of functionally graded materials. One of these approaches is the finite element analysis of such material type.

In this paper the boundary value problem of the uncoupled thermoelastic behavior of FG plate is formulated and solved. First, the temperature distribution is predicted to be used in the thermoelastic analysis of FG plate. Then, the first-order shear deformation plate theory is proposed, accounting for the exact neutral plane position, for modeling the functionally graded plates. A parametric study is developed to investigate the effects of different distributions of the material properties on the response of the plates. Moreover, some numerical comparisons are performed to show the lack of accuracy while neglecting the effect of neutral plane position for FG plates.

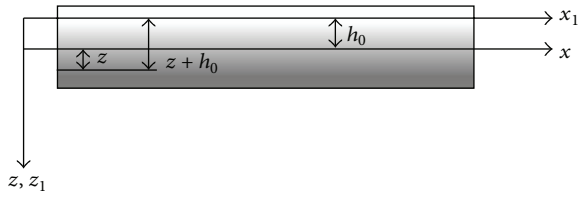

Figure 1: Coordinate system used for a typical FG plate.

2. Mathematical Formulation of the Uncoupled Thermoelasticity System

In this section, a mathematical model is derived for the uncoupled thermoelasticity systems considering the exact neutral plane position. The temperature distribution and the effective material properties of the FGMs are determined firstly and used in the developed model as input data. The effect of neutral plane position is typically neglected in most previous studies, while the position of neutral plane for functionally graded plates must be predetermined. Modifications over the model formulated at [2] are presented to account for the thermal load effects on the finite element model and the neutral plane position effects on the material stiffnesses.

2.1. Governing Equations. Based on the FSDT assumptions, the transverse normals would not remain perpendicular to the midsurface but remain straight after deformation. Thus, the transverse shear strains and consequently the shear stresses are constant throughout the laminate thickness. In practice a convenient shear correction factor, equals to 5/6, is assumed for the analysis of the plates [14, 15]. So, the displacement fields based on FSDT assumptions are

$$\begin{aligned} u(x, y, z) &= u_0(x, y) + (z + h_0)\,\emptyset_x(x, y), \\ v(x, y, z) &= v_0(x, y) + (z + h_0)\,\emptyset_y(x, y), \\ \omega(x, y, z) &= \omega_0(x, y), \end{aligned} \tag{1}$$

where $(u_0, v_0, \omega_0, \emptyset_x, \emptyset_y)$ are unknown functions to be determined. h_0 denotes the position of the neutral plane (see Figure 1) where for isotropic homogenous plates $h_0 = 0$.

The total strain is the variation of the continuum deformation with respect to its volume, so the linear Green-Lagrange strains components for small deformations and moderate rotations ($10^0 - 15^0$) can be determined from (1) as follow:

$$\begin{aligned} e_{xx} &= u_{0,x} + (z + h_0)\,\emptyset_{x,x}, \\ e_{yy} &= v_{0,y} + (z + h_0)\,\emptyset_{y,y}, \end{aligned}$$

$$\gamma_{xy} = u_{0,y} + v_{0,x} + (z + h_0)\left(\emptyset_{x,y} + \emptyset_{y,x}\right),$$
$$\gamma_{xz} = w_{0,x} + \emptyset_x,$$
$$\gamma_{yz} = w_{0,y} + \emptyset_y, \tag{2}$$

where e_{ij} are the total strain components. The total strain components are the sum of the elastic strains ε_{ij}, resulting from the applied mechanical loads and the thermal strains ε_{Ti} produced due to temperature change. So, the total strains are given by

$$e_{ij} = \varepsilon_{ij} + \varepsilon_{Ti}. \tag{3}$$

The total strain components could be divided into $\{e_b\}$ bending strain and $\{e_s\}$ shear strain components as follows:

$$\begin{Bmatrix} e_{xx}(x,y,z) \\ e_{yy}(x,y,z) \\ \gamma_{xy}(x,y,z) \end{Bmatrix} = \begin{bmatrix} 1 & 0 & 0 & (z+h_0) & 0 & 0 \\ 0 & 1 & 0 & 0 & (z+h_0) & 0 \\ 0 & 0 & 1 & 0 & 0 & (z+h_0) \end{bmatrix} \times \begin{bmatrix} u_{0,x}(x,y) \\ v_{0,y}(x,y) \\ u_{0,y}(x,y) + v_{0,x}(x,y) \\ \emptyset_{x,x}(x,y) \\ \emptyset_{y,y}(x,y) \\ \emptyset_{x,y}(x,y) + \emptyset_{y,x}(x,y) \end{bmatrix} \quad \text{or} \quad \{e_b\} = [Z_b]\left\{e_b^0\right\}, \tag{4}$$

$$\begin{Bmatrix} \gamma_{xz}(x,y,z) \\ \gamma_{yz}(x,y,z) \end{Bmatrix} = \begin{bmatrix} 1 & 0 \\ 0 & 1 \end{bmatrix} \begin{bmatrix} \omega_{0,x}(x,y) + \emptyset_x(x,y) \\ \omega_{0,y}(x,y) + \emptyset_y(x,y) \end{bmatrix} \quad \text{or} \quad \{e_s\} = [Z_s]\left\{e_s^0\right\}, \tag{5}$$

where $\{e_b^0\}$ are the nodal bending strains and $\{e_s^0\}$ are the nodal shear strains. The nodal strain components will be determined in the coming sections.

The governing equations for the plate equilibrium are derived based on the principle of minimum total potential energy. So, the total potential energy takes the form

$$\Pi = \left(0.5\int_A \left\{e_b^0\right\}^T [DE_b]\left\{e_b^0\right\} dA - \int_A \left\{e_b^0\right\}^T \{DT_b\}\, dA\right) + \left(0.5\int_A \left\{e_s^0\right\}^T [DE_s]\left\{e_s^0\right\} dA - \int_A \left\{e_s^0\right\}^T \{DT_s\}\, dA\right) - \sum \{P\}\{u^o\}, \tag{6}$$

where $\{DT_b\}$ and $\{DT_s\}$ are given by

$$\{DT_b\} = \int_z [Z_b]^T [D_b]\{\varepsilon_{Tb}\}\, dz,$$
$$\{DT_s\} = \int_z [Z_s]^T [D_s]\{\varepsilon_{Ts}\}\, dz,$$
$$\text{where } \{\varepsilon_{Tb}\} = \begin{Bmatrix} \alpha(z)\,\delta T(z) \\ \alpha(z)\,\delta T(z) \\ 0 \end{Bmatrix}, \ \{\varepsilon_{Ts}\} = \begin{Bmatrix} 0 \\ 0 \end{Bmatrix}, \tag{7}$$

where $\alpha(z)$ is the thermal coefficient of expansion and $\delta T(z)$ is the continuum temperature change through the plate thickness.

Based on the concept that the equivalent single-layer theories are built up, that a heterogeneous plate is treated as a statically equivalent, single layer having a complex constitutive behavior, reducing the 3D continuum problem to 2D problem, the equivalent layer of the FG plate can be obtained. By integrating for the plate material properties through the plate thickness the equivalent single-layer material matrix can be determined to be

$$[DE_b] = \int_{-h/2}^{h/2} [Z_b]^T [D_b]^T [Z_b]\, dz,$$
$$[DE_s] = \int_{-h/2}^{h/2} [Z_s]^T [D_s]^T [Z_s]\, dz, \tag{8}$$

where $[D_b]$ and $[D_s]$ are the bending and shear material matrices, respectively. These material matrices provide the stress-strain relations for FG plates as follows:

$$[D_b] = \begin{bmatrix} \overline{Q}_{11} & \overline{Q}_{12} & \overline{Q}_{16} \\ \overline{Q}_{12} & \overline{Q}_{22} & \overline{Q}_{26} \\ \overline{Q}_{16} & \overline{Q}_{26} & \overline{Q}_{66} \end{bmatrix}, \qquad [D_s] = \begin{bmatrix} \overline{Q}_{44} & \overline{Q}_{45} \\ \overline{Q}_{45} & \overline{Q}_{55} \end{bmatrix}. \tag{9}$$

For FG plates, the two equivalent material matrices can be written in the form

$$[DE_b] = \begin{bmatrix} A_{ij} & B_{ij} \\ B_{ij} & D_{ij} \end{bmatrix}, \qquad [DE_s] = \begin{bmatrix} 0 & 0 \\ 0 & S_{ij} \end{bmatrix}, \tag{10}$$

where A_{ij} are the extensional stiffness components, B_{ij} are the bending-extensional coupling stiffness components, and D_{ij} are the bending stiffness components.

Prior to the determination of the material stiffnesses, the location of the neutral plane must be given. Clearly, due to varying young's modulus of the plate, the neutral plane is no longer at the midplane but shifted from the midplane unless for a plate with symmetrical young's modulus [16].

The material stiffnesses can be determined considering the exact neutral plane position to be in the form

$$\begin{aligned} A_{ij} &= \int_{-h/2}^{h/2} \overline{Q}_{ij}(z)\,dz \quad i,j = 1,2,6,\\ B_{ij} &= \int_{-h/2}^{h/2} (z+h_0)\,\overline{Q}_{ij}(z)\,dz \quad i,j = 1,2,6,\\ D_{ij} &= \int_{-h/2}^{h/2} (z+h_0)^2 \overline{Q}_{ij}(z)\,dz \quad i,j = 1,2,6,\\ S_{ij} &= A_{ij} = \int_{-h/2}^{h/2} \overline{Q}_{ij}(z)\,dz \quad i,j = 4,5. \end{aligned} \tag{11}$$

Note that $\overline{Q}_{ij}(z)$ are the equivalent material property stiffnesses as a function of the material thickness direction z, where in FG plate, its material properties vary smoothly and continuously over the thickness of the structure (plate).

The equivalent material stiffnesses of isotropic FG plate are

$$\begin{aligned} \overline{Q}_{11}(z) = \overline{Q}_{22}(z) &= \frac{E(z)}{1-\upsilon^2}, \qquad \overline{Q}_{12}(z) = \upsilon \overline{Q}_{11}(z),\\ \overline{Q}_{66}(z) &= \frac{1-\upsilon}{2}\overline{Q}_{11}(z),\\ \overline{Q}_{44}(z) = \overline{Q}_{55}(z) &= K\frac{1-\upsilon}{2}\overline{Q}_{11}(z),\\ \overline{Q}_{16}(z) = \overline{Q}_{26}(z) &= \overline{Q}_{45}(z) = 0, \end{aligned} \tag{12}$$

where K is the material shear correction factor, $E(z)$ is the effective young's modulus, and υ is the effective Poisson's ratio of the material through the plate thickness. The convenient shear correction factor has been assumed to be given by 5/6 in our analysis of FG plates.

So, by minimizing the total potential energy (6), the equilibrium equations for the FG plate can be obtained.

2.2. Thermal Analysis. Knowledge of the temperature distribution within a body is basically important in many engineering problems. This information will be highly required in computing the capacity of the heat flow in or out the body. Further, if a body is not free to expand in all the directions, some stresses may be developed inside the body. The magnitude of these thermal stresses will influence dramatically on the design of devices such as boilers, steam turbines, and jet engines. The first step in calculating the thermal stresses is to determine the temperature distribution within the body.

FGMs are primarily used in situations where large temperature gradients are encountered. Also, FG plates are used in many applications (such as mechanical, electrical, and magnetic), where an amount of heat may be generated into the FG plate whenever other forms of energy (electrical, magnetic, etc.) are converted into thermal energy. Within our analysis, constant temperatures are imposed at the ceramic and metal surfaces, but a scalar temperature field is assumed to vary continuously along the z coordinate, such that $\partial T/\partial x = \partial T/\partial y = 0$. Furthermore, a stress free reference temperature $T_0 = 0$ is considered. The one-dimensional differential equation governing the steady state heat conduction in a FGM with heat source strength, by assuming a FG plate (ceramic/metal) with a continuous material properties distribution along its thickness, can be written as [17]

$$\frac{\partial}{\partial z}\left(k(z)\frac{\partial T}{\partial z}\right) + \dot{q} = 0, \tag{13}$$

where $k(z)$ is the thermal conductivity through the plate thickness, $T(z)$ is the temperature distribution through the plate thickness, and $\dot{q}$ is the strength of a heat source inside the body (rate of heat generated per unit volume).

The temperature distribution along the thickness can be obtained by solving the one-dimensional steady state heat transfer equation with the presence of a heat source (13), subject to the following boundary conditions:

$$T = T_U \quad \text{at } z = -\frac{h}{2}, \qquad T = T_L \quad \text{at } z = \frac{h}{2}, \tag{14}$$

by performing integration

$$k(z)\frac{dT}{dz} + \dot{q}z = C_1 \tag{15}$$

by rearranging (15) and considering neutral plane position integration

$$\int_{T(z)}^{T_U} dT = \int_z^{h/2} \frac{C_1 - \dot{q}(z+h_0)}{k(z)}dz \tag{16}$$

after solving integral

$$T_U - T(z) = C_1 \int_z^{h/2} \frac{dz}{k(z)} - \int_z^{h/2} \dot{q}(z+h_0)\frac{dz}{k(z)}. \tag{17}$$

By imposing one of the previous boundary conditions, the constant in (15) may be evaluated as follows:

$$C_1 = \frac{T_U - T_L}{\int_{-h/2}^{h/2}(dz/k(z))} + \frac{\dot{q}\int_{-h/2}^{h/2}(z+h_0)(dz/k(z))}{\int_{-h/2}^{h/2}(dz/k(z))}. \tag{18}$$

So, in (17), the temperature distribution through the plate thickness, for a steady state FG plate with heat source of strength $\dot{q}$, for any distribution of $k(z)$ is given by

$$\begin{aligned} T(z) = T_U - C_1 \int_z^{h/2} \frac{d\xi}{k(\xi)} + \int_z^{h/2} \dot{q}z\frac{d\xi}{k(\xi)}\\ + h_0\dot{q}\int_z^{h/2}\frac{d\xi}{k(\xi)}. \end{aligned} \tag{19}$$

If the plate is in a steady state without any heat sources, (13) reduces to the one-dimensional steady state heat transfer equation [18]

$$\frac{\partial}{\partial z}\left(\gamma(z)\frac{\partial T}{\partial z}\right) = 0. \tag{20}$$

So, the temperature distribution through the plate thickness for any distribution of $k(z)$, where in our upcoming thermal analyses a power law distribution (the linear rule of mixtures) of thermal conductivity $k(z)$ is assumed, can be written as

$$T(z) = T_U - \frac{T_U - T_L}{\int_{-h/2}^{h/2} (dz/k(z))} \int_z^{h/2} \frac{d\xi}{k(\xi)}, \tag{21}$$

where

$$k(z) = k_U + (k_L - k_U)\left(\frac{z + (h/2)}{h}\right)^n, \tag{22}$$

where k_U and k_L are the thermal conductivity of the upper and lower surfaces of the FG plate, respectively [19]. The grading material parameter n can be any nonnegative real number. In the case of a thermally homogenous plate; that is, when k does not depend on z, the temperature distribution is linear through the thickness. Excursions from the linear distribution are obtained by changing the grading parameter n.

It is convenient here to mention that, in general, there are many approaches for homogenization of FGMs. The choice of the approach should be based on the gradient of gradation relative to the size of a typical representative volume element. One of such approaches is the approximation approach. The linear rule of mixtures and the modified rule of mixtures by Tamura are convenient methods for estimating the equivalent material properties of the FGMs based on the approximation approach. Previous studies predicted that the linear rule of mixtures cannot reflect the detailed constituent geometry and the microstructure and provides a highly questionable accuracy compared to the modified rule of mixtures. On the other hand, the modified rule of mixtures by Tamura provides a convenient accuracy for a wide range of volume fractions and loading conditions. But, the modified rule of mixtures is restricted to the Young's modulus, so any appropriate averaging method must be used to estimate the other thermo-mechanical properties. Usually the linear rule of mixtures is being conventionally employed [20].

2.3. Position of Neutral Surface. For the analyses of the flexural behavior of a functionally graded plate, subjected only to transversal applied load, we have to determine the location of the neutral plane before solving the equilibrium equation of the plate. Clearly, due to the varying of Young's modulus of the FG plate through the thickness, the neutral plane is no longer located at the midplane but shifted from it. To determine the position of the neutral plane, we construct a new coordinate system such that the new x-axis is placed at the neutral axis, which will be determined in the following (see Figure 1). Then we have [16]

$$x = x_1, \qquad z = z_1 - h_0, \tag{23}$$

where h_0 is the distance of the neutral plane from the midplane of the plate.

In this case, similar to the usual treatment in the FSDT, the axial force for an infinitely wide FG plate subjected to transverse mechanical load is given by

$$N_{xx} = B_{11}\varphi_{x,x}. \tag{24}$$

By putting the axial force equal to zero to determine the position of the neutral surface, where the position of the neutral plane can be determined by choosing h_0, such that the axial force at the cross-section vanishes

$$B_{11} = \int_{-(h/2)+h_0}^{(h/2)+h_0} \frac{z_1 E(z_1)}{1 - \upsilon^2} dz_1 = 0. \tag{25}$$

By changing the interval of integral we have

$$\int_{-h/2}^{h/2} \frac{(z + h_0) E(z)}{1 - \upsilon^2} dz = 0. \tag{26}$$

Then, assuming υ is constant across the thickness

$$\left(\int_{-h/2}^{h/2} zE(z)\,dz\right) + \left(h_0 \int_{-h/2}^{h/2} E(z)\,dz\right) = 0. \tag{27}$$

The position of neutral plane for FG plates can be determined from

$$h_0 = -\left(\frac{\int_{-h/2}^{h/2} zE(z)\,dz}{\int_{-h/2}^{h/2} E(z)\,dz}\right). \tag{28}$$

Equation (28) provides an applicable way to manage and control the position of neutral plane for FG plates. For design considerations, sometimes we have to adapt the neutral plane position with the required design constraints. Changing the grading continuous function of the FG plate controls the position of the neutral plane.

3. The Finite Element Model

The displacements and normal rotations at any point into a finite element e may be expressed, in terms of the n nodes of the element, as follow

$$\begin{Bmatrix} u_0(x,y) \\ v_0(x,y) \\ \omega_0(x,y) \\ \emptyset_x(x,y) \\ \emptyset_y(x,y) \end{Bmatrix} = \sum_{i=1}^{n} \begin{bmatrix} \psi_i^e & 0 & 0 & 0 & 0 \\ 0 & \psi_i^e & 0 & 0 & 0 \\ 0 & 0 & \psi_i^e & 0 & 0 \\ 0 & 0 & 0 & \psi_i^e & 0 \\ 0 & 0 & 0 & 0 & \psi_i^e \end{bmatrix} \begin{Bmatrix} u_j \\ v_j \\ \omega_j \\ S_j^1 \\ S_j^2 \end{Bmatrix}, \tag{29}$$

where ψ_i^e is the Lagrange interpolation function at node i. The Lagrange interpolation functions for nine-node rectangular

element (see Figure 2) are given by in terms of the natural coordinates [15]

$$\begin{Bmatrix} \psi_1 \\ \psi_2 \\ \psi_3 \\ \psi_4 \\ \psi_5 \\ \psi_6 \\ \psi_7 \\ \psi_8 \\ \psi_9 \end{Bmatrix} = \frac{1}{4} \begin{bmatrix} (1-\xi)(1-\eta)(-\xi-\eta-1) + \left(1-\xi^2\right)\left(1-\eta^2\right) \\ (1+\xi)(1-\eta)(\xi-\eta-1) + \left(1-\xi^2\right)\left(1-\eta^2\right) \\ (1+\xi)(1+\eta)(\xi+\eta-1) + \left(1-\xi^2\right)\left(1-\eta^2\right) \\ (1-\xi)(1+\eta)(-\xi+\eta-1) + \left(1-\xi^2\right)\left(1-\eta^2\right) \\ 2\left(1-\xi^2\right)(1-\eta) - \left(1-\xi^2\right)\left(1-\eta^2\right) \\ 2(1+\xi)\left(1-\eta^2\right) - \left(1-\xi^2\right)\left(1-\eta^2\right) \\ 2\left(1-\xi^2\right)(1+\eta) - \left(1-\xi^2\right)\left(1-\eta^2\right) \\ 2(1-\xi)\left(1-\eta^2\right) - \left(1-\xi^2\right)\left(1-\eta^2\right) \\ 4\left(1-\xi^2\right)\left(1-\eta^2\right) \end{bmatrix}. \tag{30}$$

The nodal bending strain can be written as follows:

$$\left\{e_b^0\right\} = \begin{Bmatrix} u_{0,x}(x,y) \\ v_{0,y}(x,y) \\ u_{0,y}(x,y) + v_{0,x}(x,y) \\ \emptyset_{x,x}(x,y) \\ \emptyset_{y,y}(x,y) \\ \emptyset_{x,y}(x,y) + \emptyset_{y,x}(x,y) \end{Bmatrix}$$

$$= \sum_{j=1}^{9} \begin{bmatrix} \psi_{j,x}^e & 0 & 0 & 0 & 0 \\ 0 & \psi_{j,y}^e & 0 & 0 & 0 \\ \psi_{j,y}^e & \psi_{j,x}^e & 0 & 0 & 0 \\ 0 & 0 & 0 & \psi_{j,x}^e & 0 \\ 0 & 0 & 0 & 0 & \psi_{j,y}^e \\ 0 & 0 & 0 & \psi_{j,y}^e & \psi_{j,x}^e \end{bmatrix} \begin{Bmatrix} u_j \\ v_j \\ \omega_j \\ S_j^1 \\ S_j^2 \end{Bmatrix} \tag{31}$$

$$\text{or} \quad \left\{e_b^0\right\} = \sum_{j=1}^{n=9} \left[B_{bj}\right]\left\{u_j^0\right\},$$

$$\left\{e_s^0\right\} = \begin{Bmatrix} \omega_{0,x}(x,y) + \emptyset_x(x,y) \\ \omega_{0,y}(x,y) + \emptyset_y(x,y) \end{Bmatrix}$$

$$= \sum_{j=1}^{9} \begin{bmatrix} 0 & 0 & \psi_{j,x}^e & \psi_j^e & 0 \\ 0 & 0 & \psi_{j,y}^e & 0 & \psi_j^e \end{bmatrix} \begin{Bmatrix} u_j \\ v_j \\ \omega_j \\ S_j^1 \\ S_j^2 \end{Bmatrix} \tag{32}$$

$$\text{or} \quad \left\{e_s^0\right\} = \sum_{j=1}^{n=9} \left[B_{sj}\right]\left\{u_j^0\right\},$$

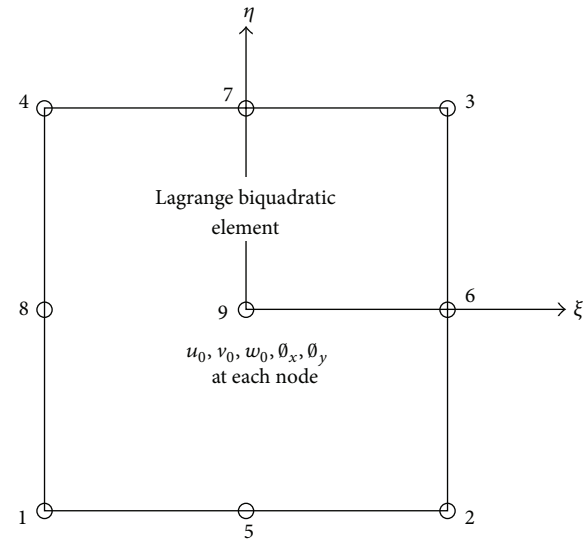

Figure 2: Nine-node quadratic Lagrange rectangular element.

where $[B_{bj}]$ is the curvature-displacement matrix, $[B_{sj}]$ is the shear strain-displacement matrix, and $\{u_j^0\} = \{u_j\ v_j\ \omega_j\ S_j^1\ S_j^2\}^T$ are the nodal degrees of freedom.

So, the total potential energy can be obtained, and (6) can be written as follow:

$$\begin{aligned} \Pi = & \left(0.5\int_A \left\{u^0\right\}^T \left[B_b\right]^T \left[DE_b\right]\left[B_b\right]\left\{u^0\right\} dA \right. \\ & \left. - \int_A \left\{u^0\right\}^T \left[B_b\right]^T \left\{DT_b\right\} dA\right) \\ & + \left(0.5\int_A \left\{u^0\right\}^T \left[B_s\right]^T \left[DE_s\right]\left[B_s\right]\left\{u^0\right\} dA \right. \\ & \left. - \int_A \left\{u^0\right\}^T \left[B_s\right]^T \left\{DT_s\right\} dA\right) - \sum \left\{u^o\right\}^T \{p\}. \end{aligned} \tag{33}$$

The minimum potential energy principle states that

$$\begin{aligned} \delta\Pi = & \left(\int_A \left[B_b\right]^T \left[DE_b\right]\left[B_b\right] dA\right)\left\{u^0\right\} \\ & + \left(\int_A \left[B_s\right]^T \left[DE_s\right]\left[B_s\right] dA\right)\left\{u^0\right\} \\ & - \int_A \left\{DT_b\right\} dA - \int_A \left\{DT_s\right\} dA \\ & - \sum_{i=1}^{n} \left[\psi_i^e\right]^T \{p\} = 0. \end{aligned} \tag{34}$$

In another form

$$\left[\left[K_b\right] + \left[K_s\right]\right]\left\{u^0\right\} = \left\{F_T\right\} + \{P\}, \tag{35}$$

where $[K_b]$, $[K_s]$ are the element bending and shear stiffness matrices, respectively, defined as

$$[K_b] = \int_A [B_b]^T [DE_b] [B_b] \, dA,$$
$$[K_s] = \int_A [B_s]^T [DE_s] [B_s] \, dA \tag{36}$$

and $\{F_T\}$, $\{P\}$ are the element thermal and mechanical load vectors, respectively, defined as

$$\{P\} = \int_A [\psi_i^e]^T \{p\} \, dA,$$
$$\{F_{Tb}\} = \int_A [B_b]^T \{DT_b\} \, dA, \tag{37}$$
$$\{F_{Ts}\} = \int_A [B_s]^T \{DT_s\} \, dA.$$

So by substitution of (31) and (32), into (4) and (5) the bending and shear strain vectors can be obtained. The normal stress components can be determined as follow:

$$\begin{Bmatrix} \sigma_{xx} \\ \sigma_{yy} \\ \sigma_{xy} \end{Bmatrix} = \begin{bmatrix} \overline{Q}_{11}(z) & \overline{Q}_{12}(z) & 0 \\ \overline{Q}_{12}(z) & \overline{Q}_{22}(z) & 0 \\ 0 & 0 & \overline{Q}_{66}(z) \end{bmatrix} \times \left\{ \begin{Bmatrix} e_{xx} \\ e_{yy} \\ \gamma_{xy} \end{Bmatrix} - \begin{Bmatrix} \alpha(z) \delta T(z) \\ \alpha(z) \delta T(z) \\ 0 \end{Bmatrix} \right\} \tag{38}$$
$$\text{or} \quad \{\sigma_b\} = [D_b] \{\varepsilon_b\},$$

and the shear stress components are

$$\begin{Bmatrix} \sigma_{yz} \\ \sigma_{xz} \end{Bmatrix} = \begin{bmatrix} \overline{Q}_{44}(z) & 0 \\ 0 & \overline{Q}_{55}(z) \end{bmatrix} \left\{ \begin{Bmatrix} \gamma_{yz} \\ \gamma_{xz} \end{Bmatrix} - \begin{Bmatrix} 0 \\ 0 \end{Bmatrix} \right\} \tag{39}$$
$$\text{or} \quad \{\sigma_s\} = [D_s] \{\varepsilon_s\}.$$

4. Numerical Result

In this section we present several numerical simulations in order to assess the behavior of functionally graded plates subjected to thermo-mechanical loads. A simple supported plate is considered for the investigation. The plate is made up of a ceramic material at the top and a metallic at the bottom. The simple power law with different values of $n = 0 : 2$ is used for the through-the-thickness variation. The plate is subjected to mechanical loadings in addition to a temperature gradient through its thickness.

4.1. A Functionally Graded Plate Subjected to a Steady State Thermomechanical Load. The analysis of FG plates is performed for a combination of materials of type ceramic-metal. The lower plate surface is assumed to be aluminum, while the top surface is assumed to be zirconia. Material properties parameter $n = [0, 2]$ is considered. Physical material properties are given in Table 1. An all edges simply supported square plate, of side $a = 0.2$ m and thickness $h = 0.01$ m, is taken for study. The plate is subjected to a uniformly distributed mechanical transverse load on the top surface, in addition to a temperature gradient along the thickness, where the temperature of the ceramic rich top surface is 300°C and the temperature of the metal rich bottom surface is 20°C (see Figure 3).

To investigate the thermo-mechanical behavior of the plate, the temperature distribution through the FG plate thickness should be firstly determined. Figure 4 shows the steady state temperature distribution given by (21), for the aforementioned FG plate. The results are highly consistent with that given at [18]. It is obviously noticed that the resulted temperature distribution within FG plates of ceramic and metallic constituents is usually smaller than those of

Table 1: Material properties.

Property	Aluminum	Zirconia
Young's modulus	$E_L = 70$ Gpa	$E_U = 151$ Gpa
Poisson's ratio	$\nu_L = 0.3$	$\nu_U = 0.3$
Thermal conductivity	$k_L = 204$ W/mK	$k_U = 2.09$ W/mK
Thermal expansion	$\alpha_L = 23 \times 10^{-6}$/C	$\alpha_U = 10 \times 10^{-6}$/C

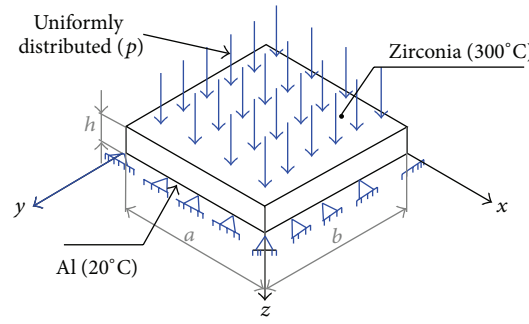

Figure 3: A simply supported FG plate subjected to a uniformly distributed mechanical load and thermal loading.

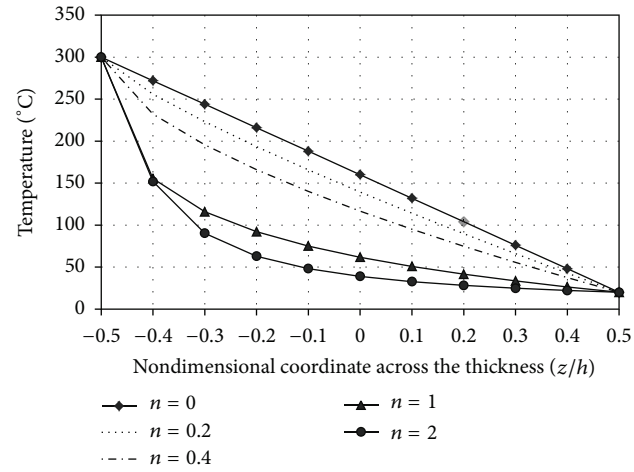

Figure 4: Temperature distribution through the FG plate thickness for various values of grading parameter n (without heat source).

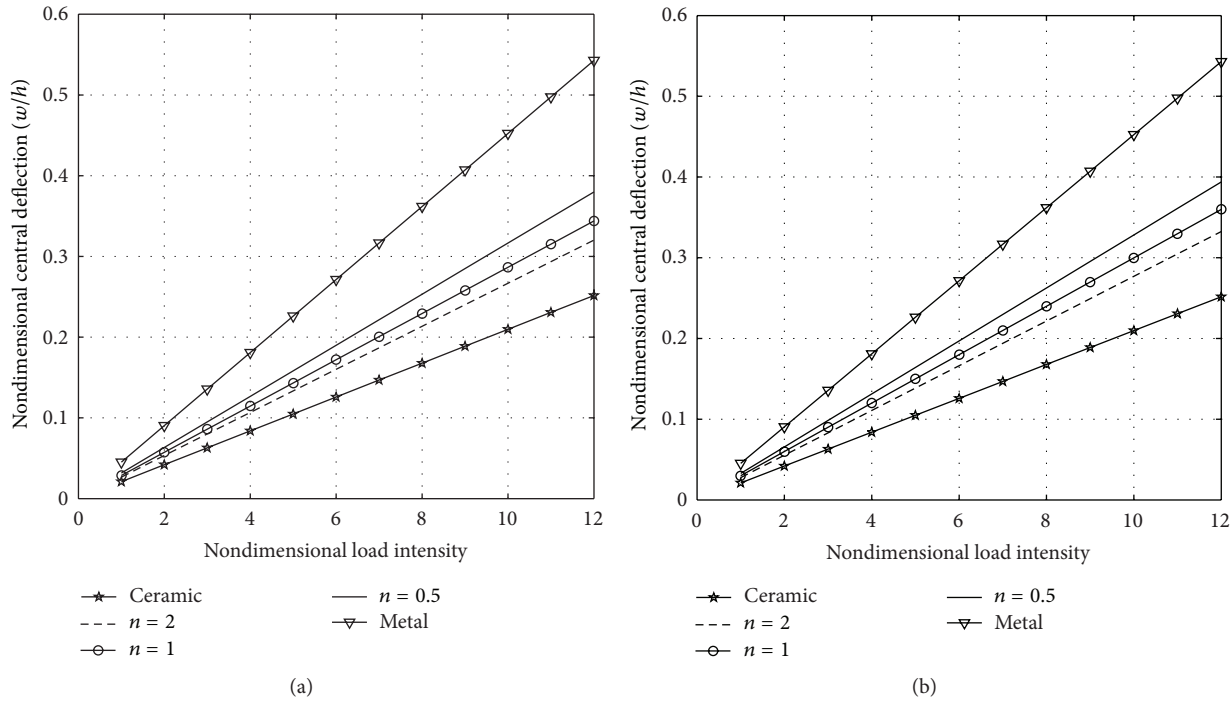

Figure 5: Nondimensional center deflection of P-FGM plate versus nondimensional load intensity (mechanical load): (a) neglecting neutral plane position, (b) considering neutral plane position.

homogeneous plates, either purely ceramic or purely metallic plates. The material parameter n has dominant effect on the thermal behavior of the FG plates, where the temperature distribution depends basically on the equivalent thermal conductivity of the constituents and the temperatures of both the upper and lower surfaces.

To investigate the elastostatic behavior of FG plates, with aluminum and zirconia material constituents, several numerical simulations are performed, for different values of the grading parameter n. The following nondimensional parameters have been manipulated throughout the numerical simulations:

$$\text{central deflection } \overline{\omega} = \omega/h;$$
$$\text{nondimensional load intensity } \overline{P} = a^4 p/E_L h^4;$$
$$\text{thickness } \overline{h} = h/a,$$

where p denotes the intensity of the applied mechanical load and E_L is the Young's modulus of the aluminum bottom face.

Figure 5, shows the nondimensional central deflection of a uniform temperature FG plate, subjected to a mechanical load and free of any thermal excitation. From Figure 5, it can be noticed that the central deflection of the FG plate (of the previous example) decreases noticeably by raising the value of the material index (n), because of the increasing of the material rigidity. The rigidity of the material increases by increasing the volume fraction of ceramic, as a consequence of raising the value of (n). Table 2 shows the numerical results of a set of numerical simulations with different values of (n). The table shows a difference in central deflection while considering and neglecting neutral plane position. The plate provides a higher central deflection when considering neutral plane position rather than the midplane of the plate. The results of Figure 5(a) are consistent with those presented in [18].

Figure 6 shows the central deflection $\overline{\omega} = \omega/h$ due to a sequence of mechanical loads for different values of n. The nondimensional load $\overline{P}$ takes values in the interval [0, 12]. In addition to the uniformly distributed mechanical transverse load on the top surface, the plate is subjected to a thermal field where the ceramic rich top surface is held at 300°C and the metal rich bottom surface is held at 20°C (see Figure 1). One may see that all the plates with intermediate material properties experience intermediate values of deflection. This was expected since the metallic plate is the one with the lowest stiffness and the ceramic plate is the one with the highest stiffness. Also, the figure shows that the contribution of the thermal load is higher than that of the mechanical load, which reduces with increasing of the mechanical load intensity. Table 3 shows the numerical results of the simulations. The results of Figure 6(a) are in excellent agreement with those presented in [18, 21].

The variation of the axial stress σ_{xx} at the center of the FG plate and along the thickness direction, for different values of the material parameter n, is shown in Figure 7. The stress of power law FGM (P-FGM) plate can be represented as a cubic function of z for material parameter $n = 2$. The maximum tensile stress along the thickness of the FG plate is located at the bottom edge ($z = h/2$) and increases as the ratio E_U/E_L increases. However, the maximum compressive stress is occurred at the top surface ($z = -h/2$) and is high for small E_U/E_L. For the ratio $E_U/E_L = 1$ in which

Table 2: Nondimensional deflection of midpoint versus nondimensional load intensity ($\overline{P}$).

$\overline{P}$	Nondimensional central deflection ($\overline{\omega}$)							
	Metal	$n = 0.5$		$n = 1$		$n = 2$		Ceramic
		Midplane	Neutral plane	Midplane	Neutral plane	Midplane	Neutral plane	
1	0.0452	0.0317	0.0328	0.0287	0.03	0.0267	0.0277	0.021
2	0.0905 (**0.089**)*	0.0633 (**0.061**)	0.0656	0.0573 (**0.056**)	0.06	0.0534 (**0.052**)	0.0554	0.042 (**0.0413**)
3	0.1357	0.095	0.0985	0.086	0.09	0.0801	0.0831	0.0629
4	0.181 (**0.1804**)	0.1266 (**0.124**)	0.1313	0.1146 (**0.113**)	0.119	0.1067 (**0.103**)	0.1108	0.0839 (**0.083**)
5	0.2262	0.1583	0.1641	0.1433	0.149	0.1334	0.1385	0.1049
6	0.2714 (**0.269**)	0.1899 (**0.185**)	0.1969	0.172 (**0.1695**)	0.179	0.1601 (**0.154**)	0.1662	0.1258 (**0.126**)
7	0.3167	0.2216	0.2298	0.2006	0.209	0.1868	0.1939	0.1468
8	0.3619 (**0.361**)	0.2532 (**0.248**)	0.2626	0.2293 (**0.228**)	0.239	0.2135 (**0.208**)	0.2216	0.1678 (**0.166**)
9	0.4072	0.2849	0.2954	0.2579	0.269	0.2402	0.2493	0.1888
10	0.4524 (**0.452**)	0.3166 (**0.308**)	0.3282	0.2866 (**0.285**)	0.299	0.2669 (**0.261**)	0.277	0.2097 (**0.206**)
11	0.4979	0.3482	0.361	0.3153	0.329	0.2935	0.3047	0.2307
12	0.5428 (**0.54**)	0.3799 (**0.365**)	0.3939	0.3439 (**0.343**)	0.359	0.3202 (**0.313**)	0.3324	0.2517 (**0.252**)

*The consistent results of Croce and Venini [18].

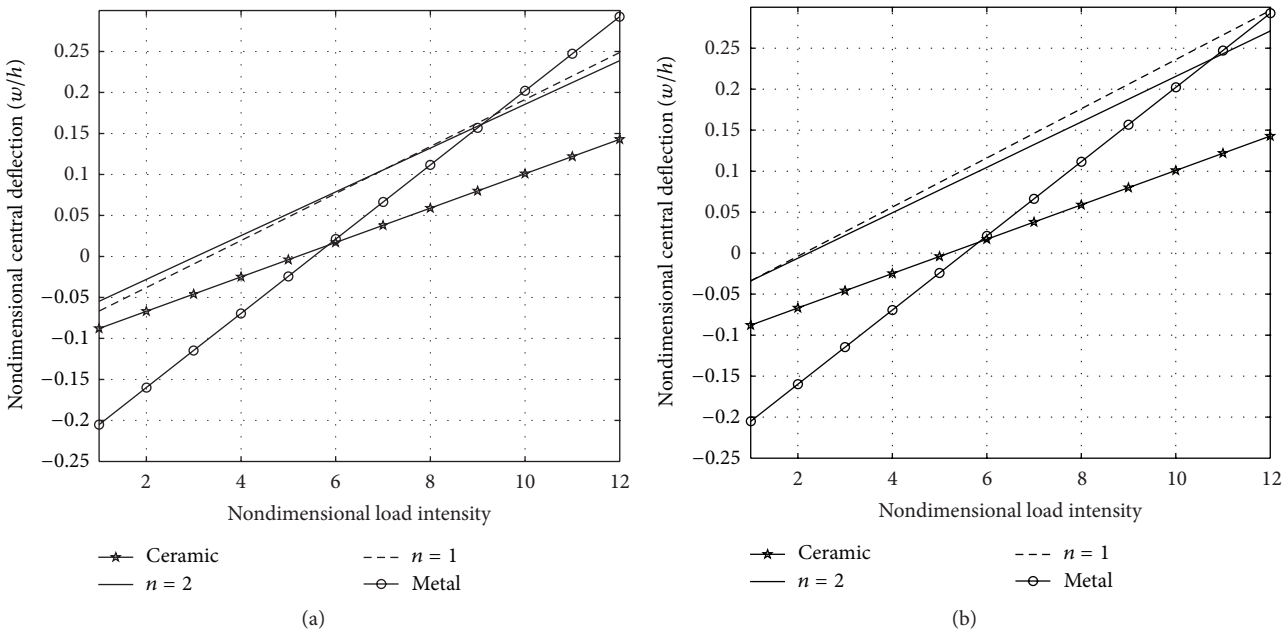

Figure 6: Nondimensional center deflection of P-FGM in steady state without heat source present versus nondimensional load intensity ($\overline{P}$) (thermo-mechanical load): (a) neglecting neutral plane position, (b) considering neutral plane position.

the FGM plate becomes a homogenous isotropic plate, the stress distribution is a linear function of z, and the maximum stress value is occurred at the top and bottom surfaces of the plate. The neutral plane—where zero axial stress is located—is shifted from the midplane to the top surface, (Figure 7(b)), by variation of grading parameter n, while for isotropic homogenous plate, the zero stress is located at the midplane. The results of Figure 7(a) are consistent with those presented by Croce and Venini [18], where they assumed that neutral plane coincides with the midplane.

Figure 8 illustrates the through-the-thickness maximum axial stress along the center line of the plate on the centroidal axis (midplane). We observe in Figure 8 that the stresses are compressive both at the top and at the bottom surfaces. The profiles of the compressive stress for the graded plates are close to each other, and their magnitude is less than the one of the homogeneous plates. All the results of Figure 8(a) are in agreement with those presented in [18, 21].

4.2. A Functionally Graded Plate Subjected to a Steady State Thermomechanical Load and Including a Heat Source. The plate considered at the previous section is used to simulate a FG plate in a steady state with heat source strength (rate of heat generated per unit volume) $\dot{q} = 100 \times 10^6$ watt/m^3.

Table 3: Nondimensional deflection of midpoint versus nondimensional load intensity ($\overline{P}$) (thermo-mechanical load without heat source).

$\overline{P}$	($\overline{\omega}$) Nondimensional central deflection for					
	Metal	$n = 1$		$n = 2$		Ceramic
		Midplane	Neutral plane	Midplane	Neutral plane	
1	−0.205 (**−0.2**)*	−0.0665 (**−0.0654**)	−0.0338	−0.0547 (**−0.0595**)	−0.0338	−0.0879 (**−0.083**)
2	−0.1598 (**−0.1547**)	−0.0379 (**−0.0345**)	−0.0038	−0.028 (**−0.0298**)	−0.0061	−0.0669 (**−0.0654**)
3	−0.1146 (**−0.1083**)	−0.0092 (**−0.0095**)	0.0262	−0.0013 (**−0.0015**)	0.0216	−0.0459 (**−0.0452**)
4	−0.069 (**−0.0654**)	0.0195 (**0.0189**)	0.0562	0.0254 (**0.0226**)	0.0493	−0.025 (**−0.0238**)
5	−0.024 (**−0.0214**)	0.0481 (**0.0476**)	0.0862	0.0521 (**0.0571**)	0.077	−0.004 (**−0.0038**)
6	0.021	0.0768	0.1161	0.0788	0.1047	0.017
7	0.066	0.1054	0.1461	0.1054	0.1324	0.038
8	0.1115	0.1341	0.1761	0.1321	0.1601	0.0589
9	0.1568	0.1628	0.2061	0.1588	0.1878	0.0799
10	0.202	0.1914	0.2361	0.1855	0.2155	0.1009
11	0.2473	0.2201	0.2661	0.2122	0.2432	0.1219
12	0.2925	0.2487	0.296	0.2389	0.2709	0.1428

*The consistent results of Croce and Venini [18].

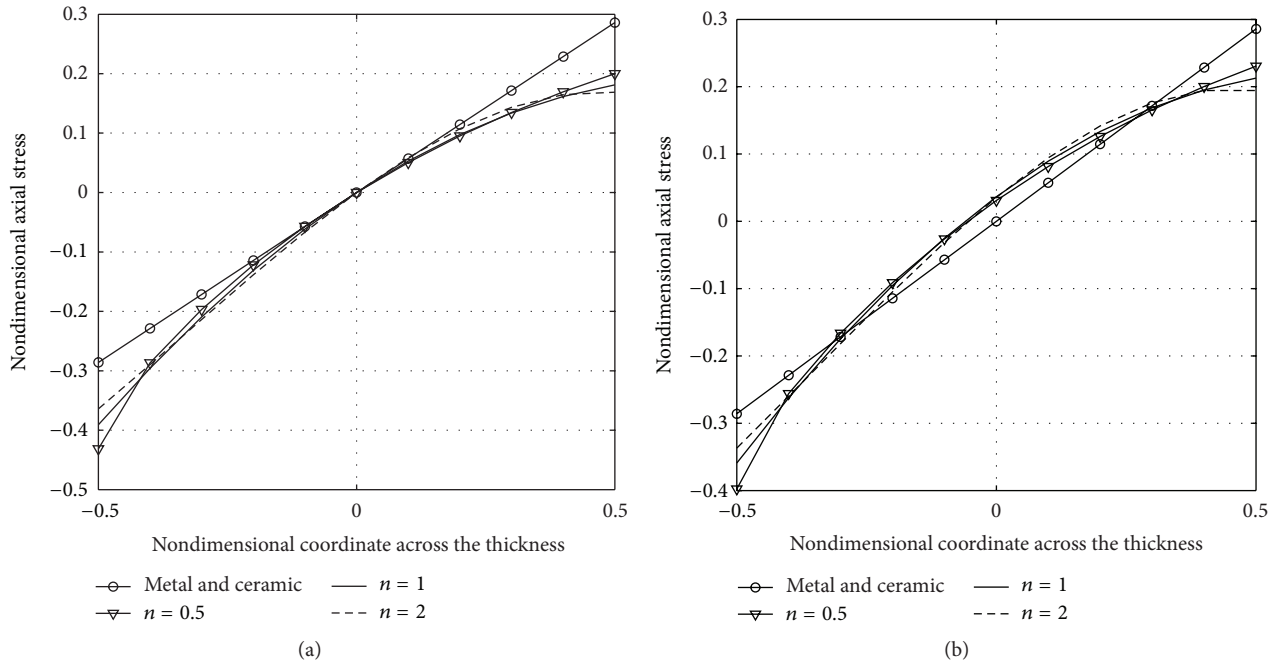

Figure 7: Nondimensional axial stress distribution through the thickness of FG plate subjected to mechanical loads: (a) neglecting neutral plane position, (b) considering neutral plane position (*nondimensional axial stress $\overline{\sigma_{xx}} = \sigma_{xx}(h^2/a^2 p)$, *nondimensional coordinate across the thickness $\overline{h} = z/h$).

In addition to a uniformly distributed mechanical transverse load on the top surface, the plate subjected to a thermal field where the ceramic rich top surface is held at 300°C and the metal rich bottom surface is held at 20°C.

Figure 9 shows the temperature distribution for the considered FG plate. It is observed that temperature within the FGM plates of ceramic and metallic constituents is always smaller than that corresponding to a purely ceramic or metallic plate. Figure 4 shows the temperature distribution for a steady state behavior of the FG plate, without heat source, where the temperature distribution for the isotropic material is a linear function of the plate thickness coordinate. However, in Figure 9, the temperature distribution for metal through the plate thickness is nearly a linear function, although it is exactly not a linear function. The reason for the extreme difference of the temperature distributions for isotropic materials (zirconia and aluminum) is due to the extreme difference in the thermal conductivity for the two materials, where the temperature distribution depends on the thermal conductivity of the material. While increasing

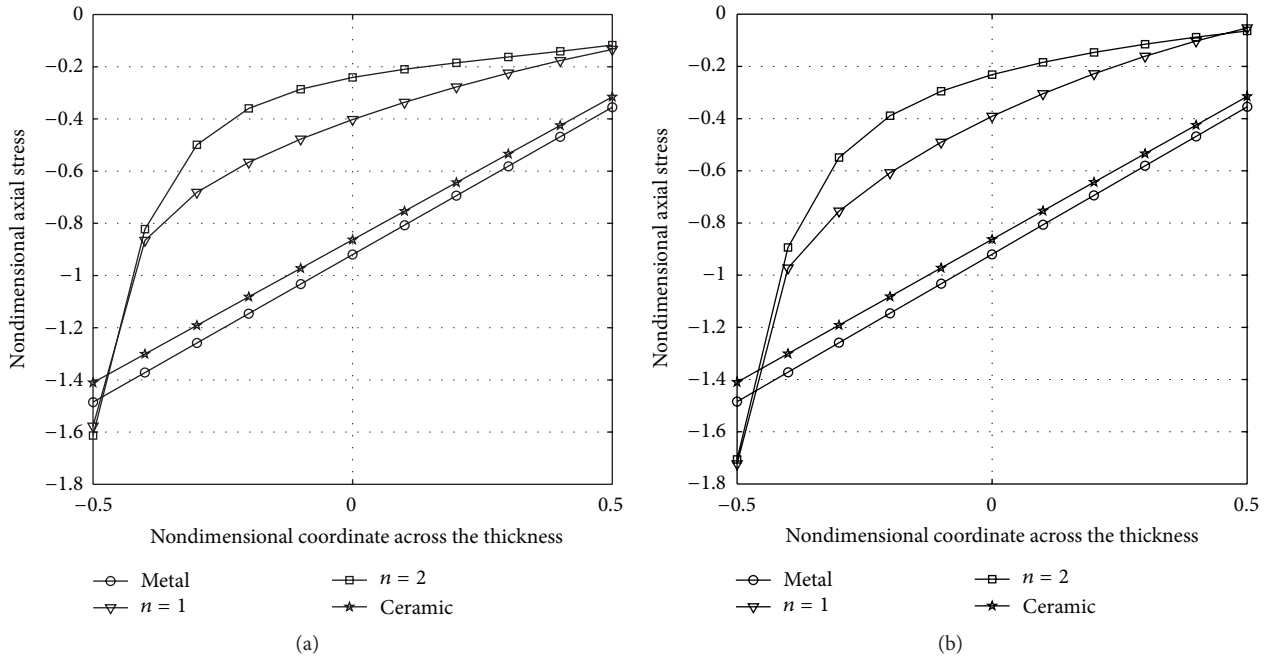

Figure 8: Nondimensional axial stress distribution, through the plate thickness, for steady state thermo-mechanical loads: (a) neglecting actual neutral plane position. (b) Considering the location of the neutral plane position (*nondimensional axial stress $\overline{\sigma_{xx}} = \sigma_{xx}(h^2/a^2 p)$, *nondimensional coordinate across the thickness $\overline{h} = z/h$).

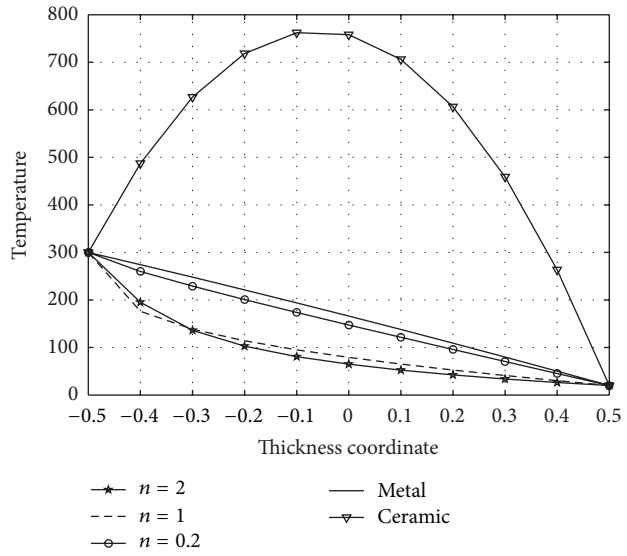

Figure 9: Temperature distributions through the plate thickness for various values of grading parameter n (with heat source present).

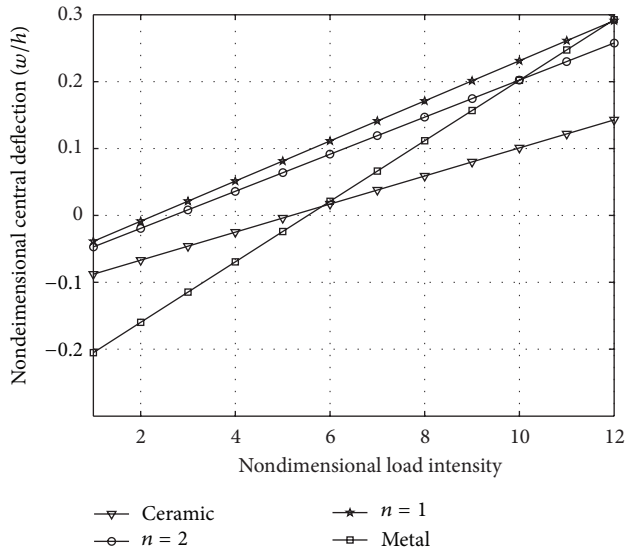

Figure 10: Nondimensional center deflection of P-FG plate in steady state with heat source present versus nondimensional load intensity ($\overline{P}$) (thermo-mechanical load).

the value of material parameter n, the FG plate becomes more sensitive for the amount of heat delivered from the heat source.

Figure 10 and Table 4 show the central deflection $\overline{\omega} = \omega/h$ due to a sequence of mechanical loads for different values of n.

Figure 11, shows the maximum axial stress σ_{xx} distribution through the plate thickness for different material parameter n. The plate is expected to be a steady state heat conductive plate subjected to an amount of generated heat of strength ($\dot{q} = 100\times10^6$ W/m^3) and thermo-mechanical loads. Figure 12 shows the axial stress distribution through the plate thickness for a steady state plate in which an amount of heat is generated from heat source ($\dot{q} = 100\times10^6$ W/m^3) and only thermal load. Figure 13 shows the nondimensional deflection of the FG steady state plate versus the heat source strength.

Table 4: Nondimensional deflection of midpoint versus nondimensional load intensity ($\overline{P}$) (thermo-mechanical load with heat source present).

$\overline{P}$	($\overline{\omega}$) Non dimensional central deflection for			
	Metal	$n = 1$	$n = 2$	Ceramic
1	−0.2051	−0.0387	−0.0471	−0.0879
2	−0.1599	−0.0087	−0.0194	−0.0669
3	−0.1146	0.0213	0.0083	−0.0459
4	−0.0694	0.0513	0.036	−0.025
5	−0.0241	0.0813	0.0637	−0.004
6	0.0211	0.1112	0.0914	0.017
7	0.0663	0.1412	0.1192	0.038
8	0.1116	0.1712	0.1469	0.0589
9	0.1568	0.2012	0.1746	0.0799
10	0.2021	0.2312	0.2023	0.1009
11	0.2473	0.2612	0.2300	0.1219
12	0.2925	0.2911	0.2577	0.1428

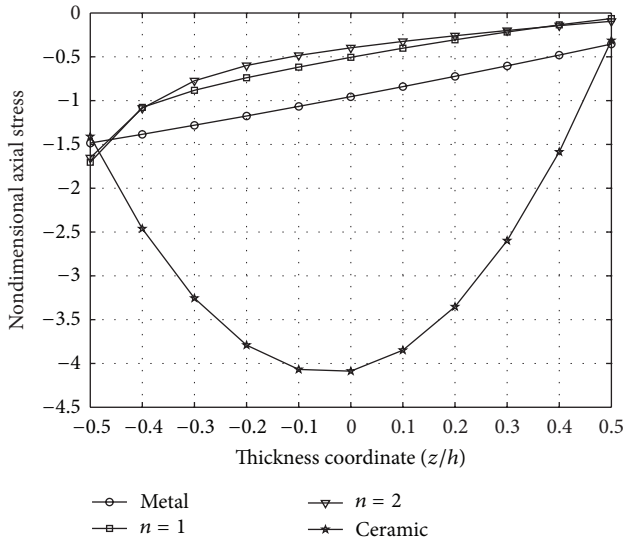

Figure 11: Nondimensional axial stress distributions through the thickness of a steady state plate, with heat source present, for thermo-mechanical loads.

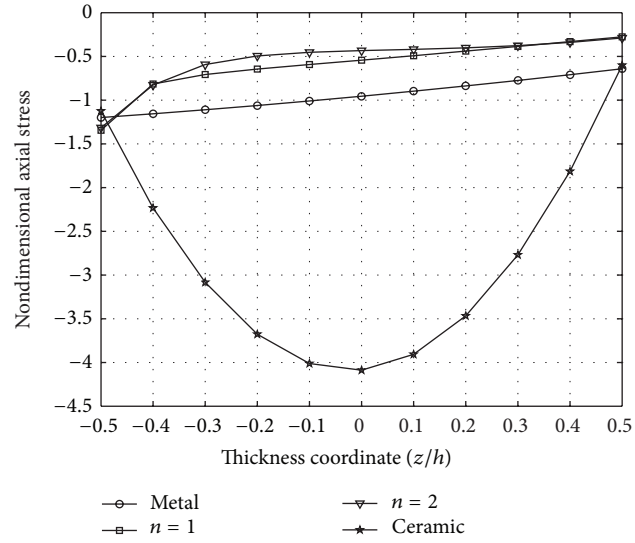

Figure 12: Nondimensional axial stress distributions through the thickness of a steady state plate, with heat source present, for thermal loads.

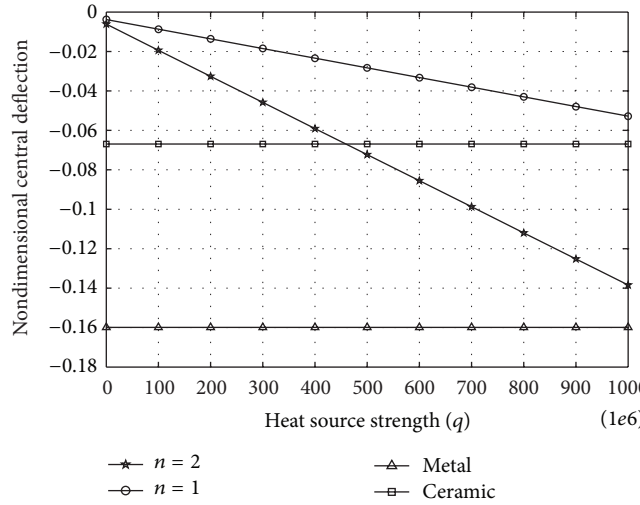

Figure 13: Non dimensional deflection of the central point of a steady state plate versus the heat source strength ($\overline{P} = 2$).

Figures 6 and 10 show that the isotropic homogenous materials experience nearly the same deflection, independent on the amount of strength of the heat source. However, for FGMs, it is observed that they are more sensitive for the heat strength change. Also, Figure 13 proves that isotropic material provides a very lack sense for heat strength change. But FGMs provide a changeable deflection by changing the amount of heat source strength.

Figures 11 and 12 show that the stress distribution through the plate thickness depends mainly on the material properties more than any other parameter. The reason for the extreme difference of the stress profiles for isotropic materials (zirconia and aluminum) is due to the extreme difference in the thermal conductivity for the two materials, where the temperature distribution and consequently the thermal strains depend on the thermal conductivity of the material. Figures 11 and 12 show that the ceramic material is subjected to the highest thermal stresses because of its low thermal conductivity. Metal material is subjected to thermal stresses that are less than the ceramic material due to its high thermal conductivity, while the FGMs are subjected to thermal stresses that are less than the isotropic materials due to their moderate thermal conductivity. Also, Figures 11 and 12 show the high ability of FGMs to withstand thermal stresses, which reflects its ability to operate at elevated temperatures.

5. Conclusions

In this study, a finite element model based on the first-order shear deformation plate (FSDT) theory is developed for

the investigation of thermo-mechanical behavior of functionally graded plates. Different numerical simulations have been developed to investigate the thermoelastic behavior of a simply supported FG plate, with different material distributions along the thickness. The numerical results lead to the following conclusions:

(1) there is a difference in plate deflection while considering the effect of shifting the neutral plane position;

(2) the neutral plane of the FG plate is shifted towards the surface with the higher young's modulus. Also, the position of the neutral plane depends mainly on the ratio of the young's modulus of the two plate constituents;

(3) FG plates provide a high ability to withstand thermal stresses, which reflects its ability to operate at elevated temperatures;

(4) the FGMs are more sensitive to the variation of the intensity of the heat flow, in or out of the structure, than that may be happened in the case of the isotropic material structures. The FGMs provide a highly stable response for the thermal loading comparing to that of the isotropic materials;

(5) due to the continuity of the material properties distribution along the thickness of the plates, the strains and stresses are varied smoothly without any sort of singularities and on contrary to what may be happened in the conventional laminated plates.

References

[1] M. Koizumi, "FGM activities in Japan," *Composites Part B: Engineering*, vol. 28, no. 1-2, pp. 1–4, 1997.

[2] S. S. Alieldin, A. E. Alshorbagy, and M. Shaat, "A first-order shear deformation finite element model for elastostatic analysis of laminated composite plates and the equivalent functionally graded plates," *Ain Shams Engineering Journal*, vol. 2, no. 1, pp. 53–62, 2011.

[3] Z. Q. Cheng and R. C. Batra, "Three-dimensional thermoelastic deformations of a functionally graded elliptic plate," *Composites Part B: Engineering*, vol. 31, no. 2, pp. 97–106, 2000.

[4] Y. Tanigawa, T. Akai, R. Kawamura, and N. Oka, "Transient heat conduction and thermal stress problems of a nonhomogeneous plate with temperature-dependent material properties," *Journal of Thermal Stresses*, vol. 19, no. 1, pp. 77–102, 1996.

[5] G. N. Praveen and J. N. Reddy, "Nonlinear transient thermoelastic analysis of functionally graded ceramic-metal plates," *International Journal of Solids and Structures*, vol. 35, no. 33, pp. 4457–4476, 1998.

[6] W. Lanhe, "Thermal buckling of a simply supported moderately thick rectangular FGM plate," *Composite Structures*, vol. 64, no. 2, pp. 211–218, 2004.

[7] A. Alibeigloo, "Exact solution for thermo-elastic response of functionally graded rectangular plates," *Composite Structures*, vol. 92, no. 1, pp. 113–121, 2010.

[8] A. M. Afsar and J. Go, "Finite element analysis of thermoelastic field in a rotating FGM circular disk," *Applied Mathematical Modelling*, vol. 34, no. 11, pp. 3309–3320, 2010.

[9] H. V. Tung and N. D. Duc, "Nonlinear analysis of stability for functionally graded plates under mechanical and thermal loads," *Composite Structures*, vol. 92, no. 5, pp. 1184–1191, 2010.

[10] M. K. Singha, T. Prakash, and M. Ganapathi, "Finite element analysis of functionally graded plates under transverse load," *Finite Elements in Analysis and Design*, vol. 47, no. 4, pp. 453–460, 2011.

[11] J. Chareonsuk and P. Vessakosol, "Numerical solutions for functionally graded solids under thermal and mechanical loads using a high-order control volume finite element method," *Applied Thermal Engineering*, vol. 31, no. 2-3, pp. 213–227, 2011.

[12] H. S. Shen and Z. X. Wang, "Nonlinear bending of FGM plates subjected to combined loading and resting on elastic foundations," *Composite Structures*, vol. 92, no. 10, pp. 2517–2524, 2010.

[13] Z. X. Wang and H. S. Shen, "Nonlinear analysis of sandwich plates with FGM face sheets resting on elastic foundations," *Composite Structures*, vol. 93, no. 10, pp. 2521–2532, 2011.

[14] M. Shaat, F. F. Mahmoud, A. E. Alshorbagy, S. S. Alieldin, and E. I. Meletis, "Size-dependent analysis of functionally graded ultra-thin films," *Structural Engineering and Mechanics*, vol. 44, no. 4, pp. 431–448, 2012.

[15] J. N. Reddy, *Mechanics of Laminated Composites Plates: Theory and Analysis*, CRC Press, Boca Raton, Fla, USA, 1997.

[16] H. Yaghoobi and A. Fereidoon, "Influence of neutral surface position on deflection of functionally graded beam under uniformly distributed load," *World Applied Sciences Journal*, vol. 10, no. 3, pp. 337–341, 2010.

[17] S. S. Rao, *The Finite Element Method in Engineering*, Pergamon Press, Oxford, UK, 2nd edition, 1989.

[18] L. D. Croce and P. Venini, "Finite elements for functionally graded Reissner-Mindlin plates," *Computer Methods in Applied Mechanics and Engineering*, vol. 193, no. 9–11, pp. 705–725, 2004.

[19] A. H. Muliana, "A micromechanical model for predicting thermal properties and thermo-viscoelastic responses of functionally graded materials," *International Journal of Solids and Structures*, vol. 46, no. 9, pp. 1911–1924, 2009.

[20] J. R. Cho and D. Y. Ha, "Averaging and finite element discretization approaches in the numerical analysis of functionally graded materials," *Materials Science and Engineering A*, vol. 302, pp. 187–196, 2001.

[21] C. Chinosi and L. Della Croce, "Approximation of functionally graded plates with non-conforming finite elements," *Journal of Computational and Applied Mathematics*, vol. 210, no. 1-2, pp. 106–115, 2007.

Hindawi Publishing Corporation
Mathematical Problems in Engineering
Volume 2013, Article ID 515792, 8 pages
http://dx.doi.org/10.1155/2013/515792

Research Article

Thermoelastic Characteristics in Thermal Barrier Coatings with a Graded Layer between the Top and Bond Coats

Seokchan Kim,[1] Jaegwi Go,[1] Yeon-Gil Jung,[2] and Je-Hyun Lee[2]

[1] *Department of Mathematics, Changwon National University, 9 Sarim-dong, Changwon 641-773, Republic of Korea*
[2] *School of Nano and Advanced Materials Engineering, Changwon National University, 9 Sarim-dong, Changwon 641-773, Republic of Korea*

Correspondence should be addressed to Jaegwi Go; jggo@changwon.ac.kr

Received 6 December 2012; Accepted 20 February 2013

Academic Editor: Abdelouahed Tounsi

Copyright © 2013 Seokchan Kim et al. This is an open access article distributed under the Creative Commons Attribution License, which permits unrestricted use, distribution, and reproduction in any medium, provided the original work is properly cited.

A graded layer was introduced at the interface between the top and bond coats to reduce the risk of failure in a thermal barrier coating (TBC) system, and the thermoelastic behavior was investigated through mathematical approaches. Two types of TBC model with and without the graded layer, subject to a symmetric temperature distribution in the longitudinal direction, were taken into consideration to evaluate thermoelastic behaviors such as temperature distribution, displacement, and thermal stress. Thermoelastic theory was applied to derive two governing partial differential equations, and a finite volume method was developed to obtain approximations because of the complexity. The TBC with the graded layer shows improved durability in thermoelastic characteristics through mathematical approaches, in agreement with the experimental results. The results will be useful in discovering technologies for enhancing the thermomechanical properties of TBCs.

1. Introduction

The deposition process for thermal barrier coatings (TBCs) exerts a critical influence on the determination of the thermomechanical properties, such as elastic modulus, thermal conductivity, and coefficient of thermal expansion. Moreover, failure phenomena usually occur at the interface between the top and bond coats because of the mismatch of mechanical and thermal properties as the TBC system cools from a high operating temperature to ambient temperature. To improve the thermal durability of TBCs for protecting hot components such as combustors and turbine parts, functionally graded materials (FGMs) and composite materials (CMs) are widely employed [1–9]. FGMs consist of two or more distinct material phases whose volume fractions continuously vary with space variables, thus yielding continuously varying mechanical and thermal properties in the FGM system. CMs are products composed of two or more distinct constituent materials involving different physical or chemical properties such that their constituents remain still distinguishable at the macroscopic or microscopic scale within the structure. The original purpose of these materials is, simultaneously, to resist high temperature and ensure low thermal conductivity through TBC techniques.

CMs make use of improved characteristics such as strength, fatigue life, stiffness, temperature-dependent behavior, thermal insulation, thermal conductivity, and weight. For example, TBCs are applied in building aircraft to obtain light and strong materials in surfacing while insulating against hazardous physical factors such as heat and lightning. In aircraft, aerospace, automotive, and shipping applications, fiber-reinforced and resin-matrix CMs contribute to the improvement through their higher strength and stiffness benefits [10–12]. However, owing to different macroscopic or microscopic scales within the structure, CMs are exposed to the risk of delamination during service. On the other hand, FGMs represent improved bonding strength, toughness, wear and corrosion resistance, and reduced residual and thermal stresses because of the graded material properties. These outstanding advantages of FGMs over conventional composites and monolithic materials have led to extensive study for potential applications as structural elements, such as FGM beams [13, 14], plates [15, 16], shells [17], and cylinders [18, 19], and have provoked the interest of researchers toward

the development of potential new structural and functional applications. Therefore, FGMs and CMs are being explored to determine their characteristics from various points of view.

The microstructural characterizations of TBCs are greatly influenced by the size, shape, and density of the feedstock powder [20–23]. In addition, the deposition process parameter is an essential element in determining its microstructure. Cernuschi et al. [24] and Jung et al. [25] analyzed the microstructure features of TBCs manufactured using the air plasma spray process, and the effects of thermal annealing on the microstructure of TBCs deposited by electron beam physical vapor deposition have been investigated by Kulkarni et al. [26] and Schulz and Schmücker [27]. Moreover, the study of microstructural behavior has been extended to functionally graded (FG) TBC materials. The microstructure and phase stability of FG TBCs based on $LaMgAl_{11}O_{19}$ (LaMa)/YSZ have been investigated by Chen et al. [28], and the results indicated that all of the LaMa and LaMa-containing intermediate composite coatings suffer irreversible phase transformations induced by the recrystallization of amorphous LaMa coating. Schulz et al. [29] tried to optimize the thermal, wear, and corrosion properties of FGMs and found that TBCs deposited onto Cu substrates by pulsed laser deposition showed improved spallation behavior by a graded lamella microstructure with improved interface fracture toughness. Shaw [30] studied the thermal residual stresses in multilayered and compositionally graded plates and coatings.

In the present paper, the thermoelastic characteristics of circular disk TBC specimens with and without an FG layer between the top and bond coats are analyzed through mathematical approaches. Two partial differential equations are derived based on thermoelastic theory, and the thermoelastic characteristics, such as temperature distribution profiles, displacement, and stresses, are determined through mathematical approaches. Because of the complexity of the governing equations, a finite volume approach is adopted to analyze the thermoelastic characteristics.

2. Mathematical Modeling

2.1. Thermoelastic Formulation. According to the assumption that the temperature profiles pressure the circular disk to the longitudinal direction only, all quantities are independent of circumferential θ-direction. Equilibrium equations in polar coordinates thus are

$$\frac{\partial \sigma_r}{\partial r} + \frac{\partial \tau_{rz}}{\partial z} + \frac{\sigma_r - \sigma_\theta}{r} = 0,$$
$$\frac{\partial \tau_{rz}}{\partial r} + \frac{\partial \sigma_z}{\partial z} + \frac{\tau_{rz}}{r} = 0. \tag{1}$$

Let u be the displacement to the radial direction, and let w be the displacement to the longitudinal direction. The strain-displacement relations are as follows:

$$\varepsilon_r = \frac{\partial u}{\partial r}, \quad \varepsilon_\theta = \frac{u}{r}, \quad \varepsilon_z = \frac{\partial w}{\partial z},$$
$$\gamma_{r\theta} = 0, \quad \gamma_{z\theta} = 0, \quad \gamma_{rz} = \frac{\partial u}{\partial z} + \frac{\partial w}{\partial r}. \tag{2}$$

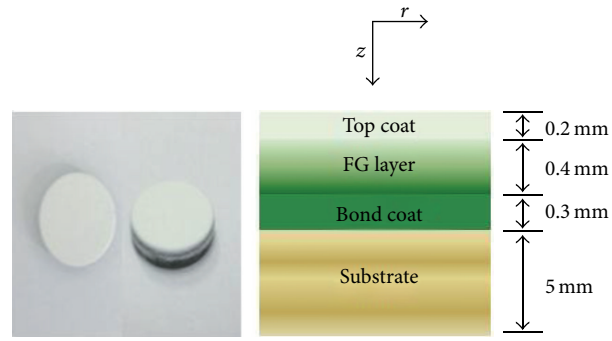

Figure 1: Schematic diagram of a circular disk model for thermoelastic characteristics of TBCs.

In addition, the strain-stress relations due to the action of thermal loading can be expressed as

$$\varepsilon_r = \frac{1}{E}\left[\sigma_r - \nu\left(\sigma_\theta + \sigma_z\right)\right] + \alpha T,$$
$$\varepsilon_\theta = \frac{1}{E}\left[\sigma_\theta - \nu\left(\sigma_r + \sigma_z\right)\right] + \alpha T,$$
$$\varepsilon_z = \frac{1}{E}\left[\sigma_z - \nu\left(\sigma_r + \sigma_\theta\right)\right] + \alpha T, \tag{3}$$
$$\tau_{r\theta} = G\gamma_{r\theta} = 0, \qquad \tau_{\theta z} = G\gamma_{\theta z} = 0,$$
$$\tau_{rz} = G\gamma_{rz},$$

where $G = 2E(1+\nu)$.

The combination of (1)–(3) leads to the following governing equations:

$$-K(1-\nu)\, r\frac{\partial}{\partial r}\left(r\frac{\partial u}{\partial r}\right) + Gr^2\frac{\partial}{\partial z}\left(\frac{\partial u}{\partial z}\right) + K(1-\nu)\, u = 0, \tag{4a}$$

$$-K(1-\nu)\, r\frac{\partial}{\partial z}\left(\frac{\partial w}{\partial z}\right) + (G - K\nu)\, r\frac{\partial}{\partial r}\left(\frac{\partial u}{\partial z}\right) + (G - K\nu)\frac{\partial u}{\partial z} + K\alpha(1+\nu)\, r\frac{\partial T}{\partial z} = 0, \tag{4b}$$

where $K = E/(1+\nu)(2\nu - 1)$.

2.2. Temperature Distribution Formulation. Since the circular disk is subject to a uniform temperature loading in the longitudinal z-direction only (see Figure 1), the differential equation for the temperature distribution profile is

$$\frac{\partial^2 T}{\partial z^2} = 0. \tag{5}$$

The general solution of (5) is

$$T(z) = c_{i1}z + c_{i2}, \tag{6}$$

where c_{i1} and c_{i2} are integration constants for the ith layer temperature distribution. The integration constants will be determined based on the following boundary conditions:

$$T(z_0) = T_{\text{in}}, \qquad T(z_1) = T_1, \qquad T(z_2) = T_2, \qquad T(z_3) = T_3, \qquad T(z_b) = T_{\text{out}}, \tag{7}$$

but only two boundary values T_{in} and T_{out} are known, and so heat flux at each layer point is considered. The heat flux at ith layer point is expressed as

$$q_i = \frac{k_i}{L_i}\left(T_{i-1} - T_i\right), \qquad q_i = q_{i+1}, \tag{8}$$

where q_i is the heat flux into ith layer, k_i is the conductivity, and L_i is the length of ith layer. At each ith layer point, the integral constants for the temperature distribution profile are determined uniquely by solving the following linear system:

$$\begin{aligned} c_{i1}z_{i-1} + c_{i2} &= T_{i-1}, \\ c_{i1}z_i + c_{i2} - T_i &= 0, \\ q_i = \frac{k_i}{L_i}\left(T_{i-1} - T_i\right), &\qquad q_i = q_{i+1}, \\ q_{n-1} = \frac{k_{n-1}}{L_{n-1}}\left(T_{n-2} - T_{n-1}\right), &\qquad q_{n-1} = q_n, \\ q_n - \frac{k_n}{L_n}T_{n-1} = -\frac{k_n}{L_n}T_{\text{out}}, &\quad i = 1, 2, \ldots, n-1. \end{aligned} \tag{9}$$

The T_{i-1} is a known value solved by $(i-1)$th layer linear system and T_{out} is a given initial value, and thus the number of $2(n-i)+3$ equations will determine $2(n-i)+3$'s unknown coefficients. Here, n is the number of layers. The temperature distribution profiles obtained through this process will be applied to (4a) and (4b) for the thermoelastic characteristics.

2.3. FG Layer Formulation. The elastic modulus E, Poisson's ratio ν, thermal expansion coefficient α, and thermal conductivity k are assumed to vary exponentially with the variable z; that is,

$$E = E_0 e^{\delta_1 z}, \tag{10a}$$

$$\nu = \nu_0 e^{\delta_2 z}, \tag{10b}$$

$$\alpha = \alpha_0 e^{\delta_3 z}, \tag{10c}$$

$$k = k_0 e^{\delta_4 z}. \tag{10d}$$

The inner area of the circular disk ($z = z_1$) consists of 100% of the top coat material, whereas the outer area of the disk ($z = z_2$) has 100% of the bond coat material; that is, the properties in (10a), (10b), (10c), and (10d) have values equal to those of the materials in the top and bond coats, respectively, at the inner and outer areas of the disk. Thus, the constants in (4a) and (4b) can be determined as

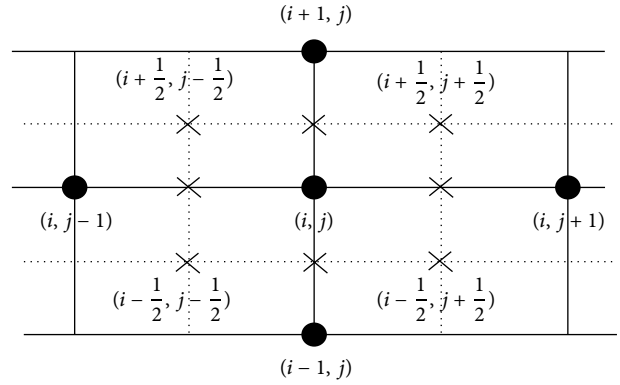

Figure 2: Finite volume mesh for a two-dimensional domain.

$$E_0 = E_T e^{-\delta_1 z_1}, \tag{11a}$$

$$\nu_0 = \nu_T e^{-\delta_2 z_1}, \tag{11b}$$

$$\alpha_0 = \alpha_T e^{-\delta_3 z_1}, \tag{11c}$$

$$k_0 = k_T e^{-\delta_4 z_1}, \tag{11d}$$

$$\delta_1 = \frac{1}{z_1 - z_2}\ln\left(\frac{E_T}{E_B}\right), \tag{12a}$$

$$\delta_2 = \frac{1}{z_1 - z_2}\ln\left(\frac{\nu_T}{\nu_B}\right), \tag{12b}$$

$$\delta_3 = \frac{1}{z_1 - z_2}\ln\left(\frac{\alpha_T}{\alpha_B}\right), \tag{12c}$$

$$\delta_4 = \frac{1}{z_1 - z_2}\ln\left(\frac{k_T}{k_B}\right). \tag{12d}$$

The subscripts T and B on a variable represent the properties of the constituent materials in the top and bond coats, respectively. The mechanical and thermal properties obtained through this process will be used to analyze the thermoelastic characteristics of graded layer between the top coat and bond coat.

2.4. Discretization of the Governing Equation Based on a Finite Volume Method. The governing equations for the microstructural characterization of TBCs are too complicated to be solved analytically, and a finite volume method is adopted for numerical approximations. The model is divided up into control volumes and integrates the field equations over each control volume (see Figure 2). In formulating a numerical approximation for the present problem, the finite

surface mesh is denoted by (i, j), and the discretizations for the governing equations are developed based on the following relations at the adjacent locations:

$$\left(\frac{\partial u}{\partial r}\right)_{i,j+1/2} = \frac{u_{i,j+1} - u_{i,j}}{\Delta r},$$

$$\left(\frac{\partial u}{\partial r}\right)_{i,j-1/2} = \frac{u_{i,j} - u_{i,j-1}}{\Delta r},$$

$$\left(\frac{\partial u}{\partial r}\right)_{i,j-1} = \frac{u_{i,j+1} - u_{i,j-1}}{2\Delta r},$$

$$\left(\frac{\partial w}{\partial z}\right)_{i,j} = \frac{1}{2\Delta z}\left(3w_{i,j} - 4w_{i-1,j} + w_{i-2,j}\right),$$

$$w_{m+1/2,j+1} = w_{m,j+1} + \frac{1}{4}\left(3w_{m,j+1} - 4w_{m-1,j+1} + w_{m-2,j+1}\right),$$

$$w_{m-1/2,j+1} = w_{m-1,j+1} + \frac{1}{4}\left(w_{m,j+1} - w_{m-2,j+1}\right),$$

$$\phi_{i+1/2,j+1/2} = \frac{1}{2}\left(\phi_{i+1/2,j+1} + \phi_{i+1/2,j}\right). \tag{13}$$

In the previous equations a subscript 1/2 implies the value of the displacement at the boundary of the control surface. According to the above relations at the adjacent locations, (4a) is discretized as follows:

$$\begin{aligned} &u_{i+1,j}\left[G_i r_j^2 \frac{\Delta r}{\Delta z}\right] + u_{i,j+1}\left[K_i(1-\nu_i) r_j r_{j+1/2} \frac{\Delta z}{\Delta r}\right] \\ &+ u_{i,j-1}\left[K_i(1-\nu_i) r_j r_{j-1/2} \frac{\Delta z}{\Delta r}\right] + u_{i-1,j}\left[G_i r_j^2 \frac{\Delta r}{\Delta z}\right] \\ &+ u_{i,j}\left[K_i(1-\nu_i) \times \left(\Delta r \Delta z - r_j\left(r_{j+1/2} + r_{j-1/2}\right)\frac{\Delta z}{\Delta r}\right) - 2G_i r_j^2 \frac{\Delta r}{\Delta z}\right] = 0. \end{aligned} \tag{14a}$$

Similar process is adjusted to (4b) and arrives at

$$\begin{aligned} &u_{i,j+1}\left[\frac{1}{8}(G_i - K_i\nu_i)\left(5r_j + 4\Delta r\right)\right] \\ &- u_{i,j}\left[\frac{1}{8}(G_i - K_i\nu_i)\left(10r_j + 8\Delta r\right)\right] \\ &+ u_{i,j-1}\left[\frac{1}{8}(G_i - K_i\nu_i)\left(5r_j + 4\Delta r\right)\right] \\ &- u_{i-1,j+1}\left[(G_i - K_i\nu_i) r_j\right] \\ &+ u_{i-1,j}\left[2(G_i - K_i\nu_i) r_j\right] \\ &- u_{i-1,j-1}\left[(G_i - K_i\nu_i) r_j\right] \\ &+ u_{i-2,j+1}\left[\frac{3}{8}(G_i - K_i\nu_i) r_j\right] \\ &- u_{i-2,j}\left[\frac{1}{8}(G_i - K_i\nu_i) r_j\right] \\ &+ u_{i-2,j-1}\left[\frac{3}{8}(G_i - K_i\nu_i) r_j\right] \\ &- w_{i+1,j}\left[K_i(1-\nu_i) r_j \frac{\Delta r}{\Delta z}\right] \\ &+ w_{i,j}\left[2K_i(1-\nu_i) r_j \frac{\Delta r}{\Delta z}\right] \\ &- w_{i-1,j}\left[K_i(1-\nu_i) r_j \frac{\Delta r}{\Delta z}\right] \\ &= K_i\alpha_i(1+\nu_i) r_j \Delta r\left[T_{i-1/2} - T_{1+1/2}\right]. \end{aligned} \tag{14b}$$

The finite volume model is developed based on the following boundary conditions:

$$u(0,z) = 0, \quad u(R,z) = 0, \quad \sigma_r(R,z) = 0, \quad \sigma_z(r,0) = 0, \quad \sigma_z(r,z_b) = 0. \tag{15}$$

3. Results and Discussion

The temperature distribution profiles and thermoelastic characteristics were investigated based on the mechanical and thermal properties shown in Table 1 using the processes in Sections 2.2 and 2.3. The mechanical and thermal properties of the FG layer are obtained based on (11a), (11b), (11c), and (11d). The temperature distribution profiles of the TBCs with and without the FG layer are shown in Figure 3. At the top coat of the TBC without the FG layer (hereafter CM), the decrease in temperature is linear, while the TBC with the FG layer (hereafter FGM) exhibits an exponential decrease.

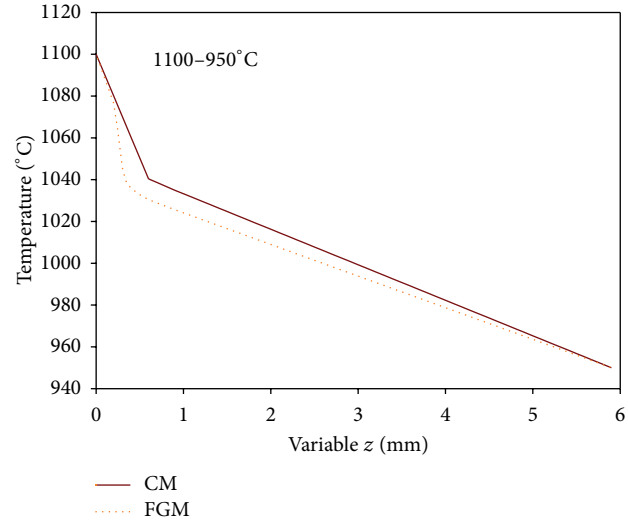

Figure 3: Temperature distribution profiles under the symmetric temperature distribution of 1100–950°C.

Table 1: Mechanical and thermal properties used in this study for analyzing thermoelastic characteristics.

Material/property	Elastic module (GPa)	Poisson's ratio	Thermal expansion coefficient (10^{-6}/°C)	Thermal conductivity (W/m °C)
Top coat* (8 wt% Y_2O_3 doped ZrO_2)	100	0.2	9.5 (20–1300°C)	2.0
Bond coat (AMDRY 995C)	200	0.3	14	11
Substrate (NIMONIC 263)	221	0.3	11.1 (20–100°C)	11.7

* Properties of the top coat prepared using an air plasma spray with METCO 204 NS-G powder.

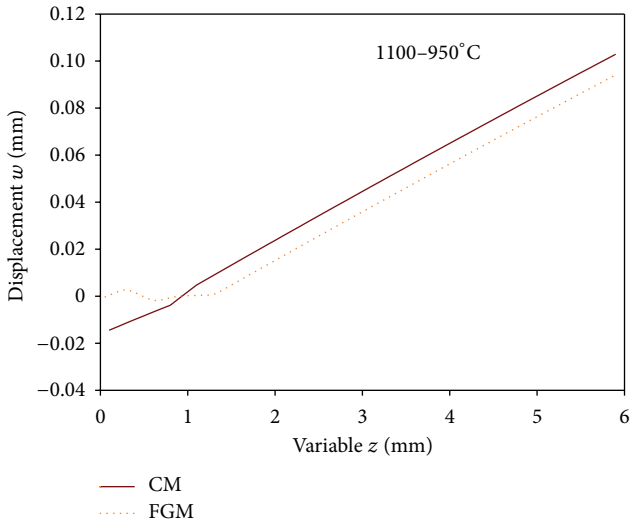

Figure 4: Displacement in the longitudinal direction of TBCs under the symmetric temperature distribution of 1100–950°C.

Over the entire domain, the circle with the FG layer is under a loading from a lower temperature, which implies an improved durability for the FGM. The rate of temperature decrease becomes slower as the metal concentration increases along the longitudinal direction and demonstrates that the mathematical approach is reliable and reasonable.

The longitudinal and radial displacement profiles are presented in Figures 4 and 5, respectively. Unlike the displacement profile of the CM at the top and bond coats, the longitudinal displacement of the FGM fluctuates at the top coat, the FG layer, and the bond coat (see Figure 4). At the substrate, the two models exhibit similar behavior, although a lower displacement develops along the z-direction in the FGM. The radial displacement profiles of each layer in the FGM are displayed in Figure 5(a). At the top coat, a larger fluctuation appears near the center, while the magnitude of the radial displacement at the FG layer is almost constant for the interval $0 < r < 7$, which implies that the durability is increased through the FG layer. A small radial displacement develops at the bond coat because of the relaxation of delamination. The radial behaviors at the bond coat in both the CM and the FGM are compared in Figure 5(b). The magnitude of the radial displacement of the FGM is almost negligible, whereas the bond coat of the CM undulates with a large magnitude in comparison with the FGM.

Figure 6 represents the longitudinal and circumferential stresses. The tensile longitudinal stress appearing at the interface between the bond coat and the substrate of the CM converts into a compressive stress in the FGM, and the FGM experiences larger compressive longitudinal stress at the top coat, the FG layer, and the bond coat (see Figure 6(a)), indicating that the FGM will improve the thermal stability of the TBC system during service. A tensile longitudinal stress develops at the substrate in the FGM. In the circumferential stress, the magnitude is larger at the top coat, the FG layer, and the bond coat in the FGM; on the other hand, a smaller magnitude appeared at the substrate (see Figure 6(b)). Both models are influenced by the compressive circumferential stress over the entire domain.

The radial stress profiles are displayed in Figure 7. At the top coat, the largest undulation occurs near the center and the magnitude decreases as the radius r increases (see Figure 7(a)). A fluctuation with the smallest magnitude develops at the bond coat because of the alleviation of stress at the FG layer. A comparison of the radial stress at the bond coat between the CM and the FGM is shown in Figure 7(b). For the interval $3 < r < 6$, a large fluctuation is produced in the CM, while the influence of the radial stress is negligible in the FGM, showing the superiority of the FGM.

Overall, as compared with the models, the FG layer in TBCs provides buffer zone interactions between the top coat and the bond coat and absorbs critical shocks. This phenomenon is shown through the thermoelastic behavior at the bond coat of the FGM: (i) the magnitude of the radial displacement is trivial in comparison with that of the CM, (ii) the tensile longitudinal stress at the interface between the bond coat and the substrate in the CM converts into a compressive stress, and (iii) a negligible fluctuation is developed along the radius in comparison with that of the CM. The results demonstrate that the thermal durability of the TBC can be improved by introducing an FG layer between the top coat and the bond coat, and the mathematical analysis presented is a reasonable approach. The results and analysis performed here contribute further understanding to the behavior of TBCs.

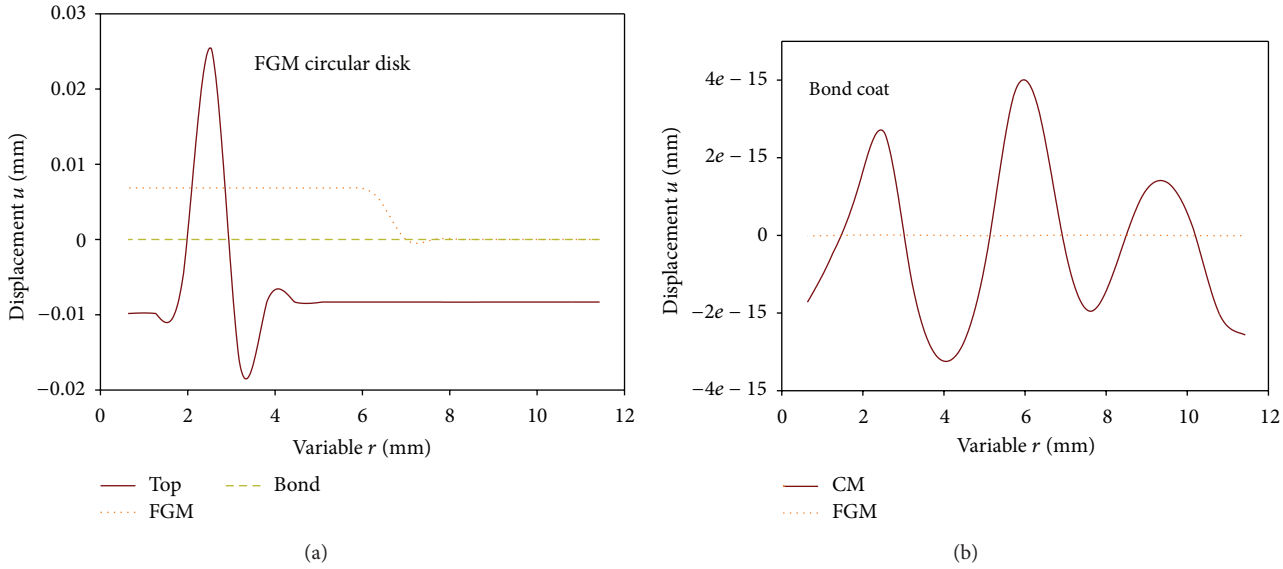

Figure 5: Displacement in the radial direction of TBCs under the symmetric temperature distribution of 1100–950°C: (a) TBC with FG layer and (b) comparison at the bond coat.

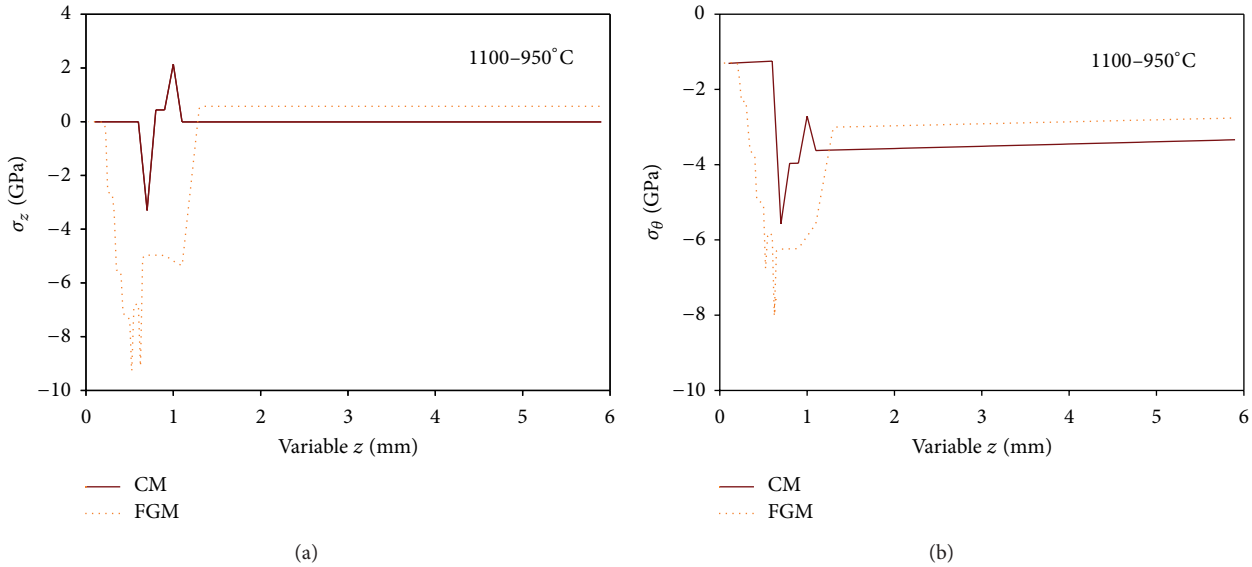

Figure 6: Stresses in TBCs under the symmetric temperature distribution of 1100–950°C: (a) longitudinal stress and (b) circumferential stress.

4. Conclusion

The thermoelastic behavior of the FGM (circular disk TBC with FG layer) was investigated and compared with that of the CM (circular disk TBC without FG layer). The FGM is subject to a lower temperature loading over the entire domain, which reduces the magnitude of the longitudinal displacement. The FG layer in the FGM converts the tensile longitudinal stress appearing at the interface between the bond coat and the substrate of the CM into a compressive stress and increases the magnitude of the compressive stress at the top coat, the FG layer, and the bond coat. Moreover, an insignificant radial stress is developed at the bond coat in the FGM, contributing to the improved performance of the FG layer. Consequently, the thermoelastic characteristics obtained for temperature, displacements, and stresses demonstrate that the FG layer will decrease the risk of failure in the TBC system and the thermal durability of the TBC system can be improved during the lifetime cycle.

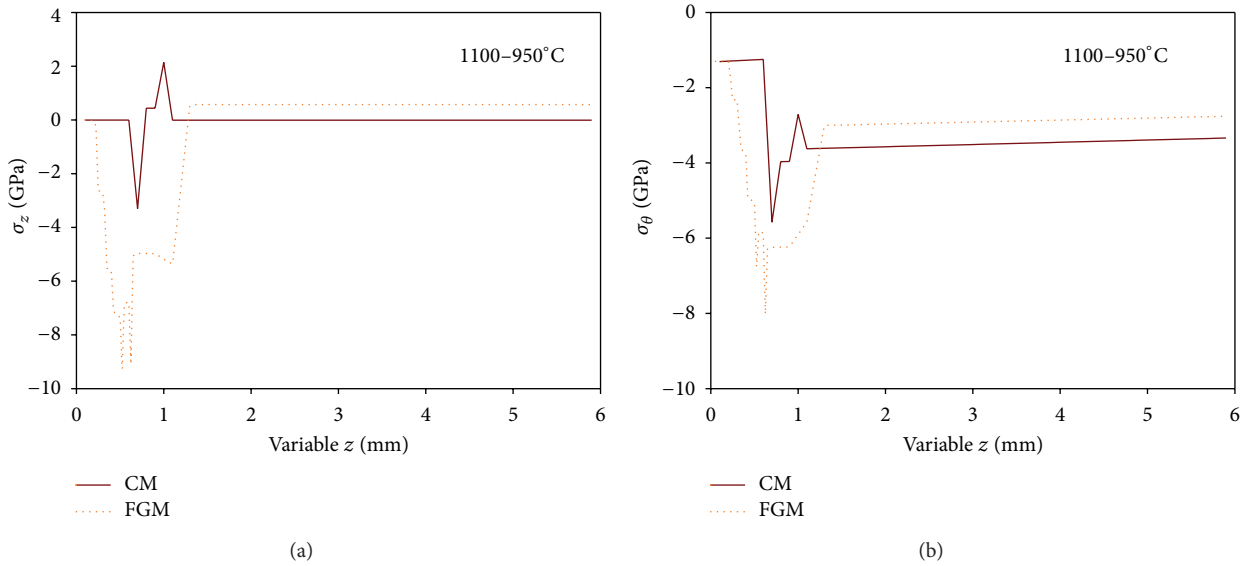

Figure 7: Radial stresses in TBCs under the symmetric temperature distribution of 1100–950°C: (a) TBC with FG layer and (b) comparison at the bond coat.

Acknowledgments

This research was supported by the Basic Science Research Program through the National Research Foundation of Korea (NRF) funded by the Ministry of Education, Science and Technology (2010-0024178). This work was supported by a National Research Foundation of Korea (NRF) grant funded by the Korean Government (MEST) (2012-0009450) and by a grant from the Fundamental R&D Program for Core Technology of Materials funded by the Korean Ministry of Knowledge Economy (10041233).

References

[1] X. Cao, F. Jin, I. Jeon, and T. J. Lu, "Propagation of Love waves in a functionally graded piezoelectric material (FGPM) layered composite system," *International Journal of Solids and Structures*, vol. 46, no. 22-23, pp. 4123–4132, 2009.

[2] M. L. Pines and H. A. Bruck, "Pressureless sintering of particle-reinforced metal-ceramic composites for functionally graded materials: part I. Porosity reduction models," *Acta Materialia*, vol. 54, no. 6, pp. 1457–1465, 2006.

[3] E. Ercenk, U. Sen, and S. Yilmaz, "Structural characterization of plasma sprayed basalt-SiC glass-ceramic coatings," *Ceramics International*, vol. 37, no. 3, pp. 883–889, 2011.

[4] S. Das, A. K. Mukhopadhyay, S. Datta, G. C. Das, and D. Basu, "Hard glass-ceramic coating by microwave processing," *Journal of the European Ceramic Society*, vol. 28, no. 4, pp. 729–738, 2008.

[5] L. Zhao, W. Q. Chen, and C. F. Lü, "Symplectic elasticity for bi-directional functionally graded materials," *Mechanics of Materials*, vol. 54, pp. 32–42, 2012.

[6] A. J. Goupee and S. S. Vel, "Transient multiscale thermoelastic analysis of functionally graded materials," *Composite Structures*, vol. 92, no. 6, pp. 1372–1390, 2010.

[7] G. J. Nie, Z. Zhong, and S. Chen, "Analytical solution for a functionally graded beam with arbitrary graded material properties," *Composites B*, vol. 44, no. 1, pp. 274–282, 2013.

[8] R. F. Gibson, "Modal vibration response measurements for characterization of composite materials and structures," *Composites Science and Technology*, vol. 60, no. 15, pp. 2769–2780, 2000.

[9] K. Y. Maalawi, "Use of material grading for enhanced buckling design of thin-walled composite rings/long cylinders under external pressure," *Composite Structures*, vol. 93, no. 2, pp. 351–359, 2011.

[10] I. M. Daniel and O. Ishai, *Engineering Mechanics of Composite Materials*, Oxford University Press, New York, NY, USA, 2nd edition, 2006.

[11] X.-H. Zhao and W. F. Chen, "The effective elastic moduli of concrete and composite materials," *Composites B*, vol. 29, no. 1, pp. 31–40, 1998.

[12] K. B. Shin and S. H. Hahn, "Evaluation of the structural integrity of hybrid railway carriage structures including the ageing effects of composite materials," *Composite Structures*, vol. 68, no. 2, pp. 129–137, 2005.

[13] Y. Li, H. Zhang, N. Zhang, and Y. Dai, "Stress analysis of functionally gradient beam using effective principal axes," *International Journal of Mechanics and Materials in Design*, vol. 2, no. 3-4, pp. 157–164, 2005.

[14] Z. Zhong and T. Yu, "Analytical solution of a cantilever functionally graded beam," *Composites Science and Technology*, vol. 67, no. 3-4, pp. 481–488, 2007.

[15] X. L. Chen and K. M. Liew, "Buckling of rectangular functionally graded material plates subjected to nonlinearly distributed in-plane edge loads," *Smart Materials and Structures*, vol. 13, no. 6, pp. 1430–1437, 2004.

[16] E. Feldman and J. Aboudi, "Buckling analysis of functionally graded plates subjected to uniaxial loading," *Composite Structures*, vol. 38, no. 1–4, pp. 29–36, 1997.

[17] K. D. Kim, Gilson Rescober Lomboy, and S. C. Han, "Geometrically non-linear analysis of Functionally Graded Material (FGM) plates and shells using a four-node quasi-conforming

shell element," *Journal of Composite Materials*, vol. 42, no. 5, pp. 485–511, 2008.

[18] Y. Obata and N. Noda, "Steady thermal stresses in a hollow circular cylinder and a hollow sphere of a functionally gradient material," *Journal of Thermal Stresses*, vol. 17, no. 3, pp. 471–487, 1994.

[19] K. M. Liew, S. Kitipornchai, X. Z. Zhang, and C. W. Lim, "Analysis of the thermal stress behaviour of functionally graded hollow circular cylinders," *International Journal of Solids and Structures*, vol. 40, no. 10, pp. 2355–2380, 2003.

[20] X. Wang, R. T. Wu, and A. Atkinson, "Characterisation of residual stress and interface degradation in TBCs by photo-luminescence piezo-spectroscopy," *Surface and Coatings Technology*, vol. 204, no. 15, pp. 2472–2482, 2010.

[21] A. C. Karaoglanli, E. Altuncu, I. Ozdemir, A. Turk, and F. Ustel, "Structure and durability evaluation of YSZ+Al_2O_3 composite TBCs with APS and HVOF bond coats under thermal cycling conditions," *Surface and Coatings Technology*, vol. 205, no. 2, pp. S369–S373, 2011.

[22] Y. H. Sohn, E. Y. Lee, B. A. Nagaraj, R. R. Biederman, and R. D. Sisson Jr., "Microstructural characterization of thermal barrier coatings on high pressure turbine blades," *Surface and Coatings Technology*, vol. 146-147, pp. 132–139, 2001.

[23] C. Batista, A. Portinha, R. M. Ribeiro, V. Teixeira, M. F. Costa, and C. R. Oliveira, "Morphological and microstructural characterization of laser-glazed plasma-sprayed thermal barrier coatings," *Surface and Coatings Technology*, vol. 200, no. 9, pp. 2929–2937, 2006.

[24] F. Cernuschi, P. Bison, and A. Moscatelli, "Microstructural characterization of porous thermal barrier coatings by laser flash technique," *Acta Materialia*, vol. 57, no. 12, pp. 3460–3471, 2009.

[25] S.-I. Jung, J. H. Kim, J. H. Lee, Y. G. Jung, U. Paik, and K. S. Lee, "Microstructure and mechanical properties of zirconia-based thermal barrier coatings with starting powder morphology," *Surface and Coatings Technology*, vol. 204, no. 6-7, pp. 802–806, 2009.

[26] A. Kulkarni, A. Goland, H. Herman et al., "Advanced neutron and X-ray techniques for insights into the microstructure of EB-PVD thermal barrier coatings," *Materials Science and Engineering A*, vol. 426, no. 1-2, pp. 43–52, 2006.

[27] U. Schulz and M. Schmücker, "Microstructure of ZrO_2 thermal barrier coatings applied by EB-PVD," *Materials Science and Engineering A*, vol. 276, no. 1-2, pp. 1–8, 2000.

[28] X. Chen, L. Gu, B. Zou, Y. Wang, and X. Cao, "New functioanlly graded thermal barrier coating system based on LaMgAl11O19/YSZ prepared by air plasma spraying," *Surface and Coatings Technology*, vol. 206, no. 8-9, pp. 2265–2274, 2012.

[29] U. Schulz, M. Peters, F. W. Bach, and G. Tegeder, "Graded coatings for thermal, wear and corrosion barriers," *Materials Science and Engineering A*, vol. 362, no. 1-2, pp. 61–80, 2003.

[30] L. L. Shaw, "Thermal residual stresses in plates and coatings composed of multi-layered and functionally graded materials," *Composites B*, vol. 29, no. 3, pp. 199–210, 1998.